Tampere University

Nonna Nurmi

DEBINDING OF STEREOLITHOGRAPHICALLY PRINTED CERAMIC PARTS

Supercritical carbon dioxide as solvent

Master's thesis
Faculty of Engineering and
Natural Sciences
D. Sc. Erkka Frankberg
Prof. Erkki Levänen
December 2022

ABSTRACT

Nonna Nurmi: Debinding of stereolithographically printed ceramic parts: Supercritical carbon dioxide as solvent
Master's thesis
Tampere University
Master's programme in Materials Engineering
December 2022

Cleaning, pre-conditioning and thermal debinding of 3D-printed ceramic parts takes a significant amount of time and ways to shorten the manufacturing time are scarce. The thermal debinding could be made more economical by extracting some of the slurry substances prior to thermal debinding, creating flow channels for gases to exit.

Supercritical carbon dioxide ($scCO_2$) was used with different chemicals to find out which ones dissolve from the stereolithographically printed part without cracking and part deformation. The $scCO_2$ extracted samples were tested with TGA, DSC, FTIR, stereomicroscope, SEM, and the sample mass and dimensions were measured before and after the extraction test. The $scCO_2$ extraction testing time, co-solvent, monomer fractions and slurry contents were varied.

PEG400, PEG200 difunctional methacrylate, uncured 3,4-Epoxycyclohexylmethyl 3,4-epoxycyclohexanecarboxylate, uncured 1,10-decanediol diacrylate, and paraffin oil were successfully extracted. With these substances included in the recipe and removed using $scCO_2$, as a result of extraction the parts shrank. The substance removal rate was enhanced with ethanol as a co-solvent in polymeric samples, but in samples containing alumina, the rate was decreased, and co-solvent caused delamination between the print layers. Isopropanol showed better extraction results with less delamination in ceramic samples.

Keywords: supercritical carbon dioxide, debinding, additive manufacturing, stereolithography, monomers

TIIVISTELMÄ

Nonna Nurmi: Sideaineen poisto keraamisista 3D-stereolitografiaprinteistä: ylikriittinen hiilidioksidi liuottimena
Diplomityö
Tampereen yliopisto
Materiaalitekniikan diplomi-insinöörin tutkinto-ohjelma
Joulukuu 2022

3D-printattujen keraamikappaleiden puhdistus, esikäsittely ja terminen sideaineenpoisto ovat hitaita ja keinoja valmistuksen nopeuttamiseen on vähän. Termistä sideaineenpoistoa voitaisi nopeuttaa liuottamalla osa lietteen ainesosista ennen polttoa, jolloin rakenteeseen voi muodostua virtauskanavia nopeuttamaan kaasujen poistumista.

Ylikriittistä hiilidioksidia (scCO$_2$) käytettiin liuottimena lietekemikaaleille ja tutkittiin, mitkä kemikaalit liukenevat ja poistuvat rakenteesta aiheuttamatta stereolitografialla tulostettuun kappaleeseen säröjä. scCO$_2$-käsitellyt näytteet analysoitiin termogravimetrisen analyysin, differentiaalisen pyyhkäisykalorimetrian, Fourier infrapunaspektroskopian ja pyyhkäisyelektronimikroskopian keinoin. Lisäksi näytteiden massa ja dimensiot mitattiin ennen ja jälkeen liuotuskokeen. Liuotuksen testiaikaa, apuliuotinta, monomeerien osuuksia ja reseptien kemikaalisisältöä vaihdeltiin.

PEG400, PEG200 difunktionaalinen metakrylaatti, kovettumaton 3,4-epoksisykloheksyylimetyyli 3,4- epoksisykloheksaanikarboksylaatti, kovettumaton 1,10-dekaanidioli diakrylaatti, sekä parafiiniöljy liukenivat näytteistä ylikriittisellä hiilidioksidilla. Näiden kemikaalien avulla kehitetyillä sideaineresepteillä ylikriittinen hiilidioksidikäsittely aiheutti kappaleiden kutistumista, kun taas kaupallisesti käytössä olevan lietteen näytteet turposivat. Liuotusnopeus kasvoi, kun etanolia käytettiin apuliuottimena polymeerinäytteille, mutta alumiinioksidinäytteissä se aiheutti tulostuskerrosten välistä delaminaatiota ja liuotus hidastui. Isopropanolista apuliuottimena aiheutui vähemmän kerrosten irtoamista alumiinioksidinäytteissä.

Avainsanat: ylikriittinen hiilidioksidi, sideaineen poisto, materiaalia lisäävä valmistus, stereolitografia, monomeerit

PREFACE

This thesis was done in the Research Group of Ceramic Materials at Tampere University from March to December 2022, and it was a part of Business Finland-funded cerAM project and a double degree agreement between Tampere University and Universidad Politècnica de Madrid.

I want to thank my thesis instructors D.Sc. Erkka Frankberg and Prof. Erkki Levänen for honest feedback, professional support, and endless research ideas. Many thanks to Prof. Jose María Ulloa for supervision from Madrid’s side.

Thanks to Stella Zakeri, Aaretti Kaleva, Piie Konnunaho, Arnold Ismailov, Milla Rinne, Teemu Vastamäki and Jorma Vihinen for help with experiments and devices.

Thanks to Dominique Hautcoeur and Karo for brainstorming and problem-solving sessions, and Niko for proofreading and emotional support.

Tampere, 22. December 2022

Nonna Nurmi

CONTENTS

LIST OF FIGURES

LIST OF SYMBOLS AND ABBREVIATIONS

AM	additive manufacturing
BAPO	phenylbis(2,4,6-trimethylbenzoyl) phosphine oxide
CAD	computer-aided design
CO_2	carbon dioxide
CQ	camphorquinone
DDDA	1,10-decanediol diacrylate
DSC	differential scanning calorimetry
ECC	3,4-Epoxycyclohexylmethyl 3,4-epoxycyclohexanecarboxylate
FEM	finite element model
FEP	fluorinated ethylene propylene
FTIR	Fourier transformation infrared spectroscopy
HA	hydroxyapatite
HDDA	1,6-hexanediol diacrylate
HIP	hot isostatic pressing
LED	light-emitting diode
PEG	polyethylene glycol
PEGMA	poly(ethylene glycol) dimethacrylate
PGTA	propoxylated glycerol triacrylate
PI	photoinitiator
$scCO_2$	supercritical carbon dioxide
SEM	scanning electron microscope
SLA	stereolithography
TGA	thermogravimetric analysis
TMPTA	trimethylolpropane triacrylate
UV	ultraviolet
a	absorption coefficient
A	geometrical model constant for sintering densification
b	width
$\mathrm{C_d}$	curing depth
$\mathrm{C_w}$	curing width
$\mathrm{D_p}$	1/e penetration depth
D	diffusion coefficient
E	energy
$\mathrm{E_c}$	critical energy
G	grain size
$\Delta \mathrm{G}$	change in Gibbs energy
H	function for initial stage sintering
$\Delta \mathrm{H}$	change in enthalpy
h	height
I	intensity
K	consistency factor
k	Boltzmann constant
L	length/ traveled distance
m%	mass percentage
m	empirical constant for sintering neck growth and shrinkage
n	refractive index, empirical constant for sintering neck growth and shrinkage
Q	quadrupole moment

P	power
r	pore radius
ΔS	change in entropy
sp^2	atomic hybridization
T	transmittance/ absolute temperature
t	time
ΔU	change in internal mixing energy
v_s	scanning speed
v%	volume percentage
w_0	light beam radius
α	pore geometry constant or polarizability
Γ	attractive part of intermolecular potential energy
λ	wavelength
γ	interfacial tension or surface energy
ρ	density
θ	radiation wave path angle
η	viscosity
μ	dipole moment
τ	shear stress
$\dot{\gamma}$	shear rate
Ω	atomic volume

1. INTRODUCTION

Ceramics are challenging to manufacture or machine due to their hardness, brittleness, and low fracture resistance. Their melt casting is difficult due to high melting temperatures and poor resistance to thermal shock. Ceramics are therefore often processed from powders, and during heating, the powder particles fuse together. [1]–[3] The strength of ceramics is determined by the largest cracks and pores present in the material [4]. During debinding, the thermal pyrolysis done before sintering, other substances (carbon dioxide, water, methane, hydrogen, and hydrocarbons) leave the structure and only ceramic remains [1]. This thermal pyrolysis phase with possible preconditioning and the following sintering are slow and make the production of advanced ceramic parts less efficient and economical [5]. For example, the recommendation from Lithoz GmbH for pre-conditioning, thermal debinding and sintering of an alumina part takes altogether 215 h, and the thermal debinding takes 95 h of this time.

Dental prostheses and implants are an increasingly important field for ceramics manufacturing. They are needed to maintain patients' ability to chew food once a natural tooth has broken or needs to be removed. Nowadays, ceramic dental replacements are mostly milled into final shape from ceramic blocks. Milling can cause cracks and scratches to the material, ceramic material choices are limited, and the unrecyclable material waste percentage may be even 95%. [6]–[8] Additive manufacturing (AM) methods have become an alternative for milling and other subtractive methods, providing less waste and stresses within the part, better user safety and increasingly lower price range due to increasing popularity of AM methods. However, milling is still significantly faster due to the lack of debinding and sometimes in case of glass ceramics, even sintering phases in manufacturing. [6] AM methods, such as stereolithography (SLA), may include requirement for support structures during printing and post-machining due to the “staircase effect” of layer structure. [9] Therefore, SLA method needs further research and optimization.

Dental applications require unique characteristics from ceramic forming to produce dense, dimensionally accurate, flawless, and strong tooth replacements that match the aesthetical requirements and the unique shape for each patient [10]. These requirements can be met by SLA [11], but the thermal treatment process needs to be sped up to make it economically reasonable. Ceramic 3D printing is also rather new a field of manufacturing; thus, processes are still largely in optimization phase. The issue with time-consuming heating phases could be overcome by removing some of the substances before pyrolysis and creating channels for gases to escape the structure without causing cracks [2]. This could be done by dissolving an uncured or inert substance with supercritical carbon dioxide ($scCO_2$) and leaving a cured polymer skeleton with ceramic particles in the structure. Similar has been done to injection molded ceramic parts with low molecular weight monomers [12] and hydroxyapatite (HA) bone replacements manufactured by laser stereolithography to remove uncured monomers [13], [14].

Solvents used for extraction are often hazardous to humans and/or environment, but $scCO_2$ has proven a way to extract substances out of the polymer matrix with less safety concerns. $scCO_2$ is easily available, cheap, weakly polar, its density and diffusivity can be varied, and it has a critical point easier to reach than e.g., water. It provides an environmentally friendly and relatively safe alternative to many toxic and hazardous solvents used in the debinding process of ceramics, providing a way to utilize carbon dioxide (CO_2) that is known as a harmful pollutant to our planet. [15]

However, not all substances can be dissolved out of the printed green body in a way that does not harm the ceramic part. Thus, slurry recipe development and understanding chemical and physical phenomena behind substance interactions are crucial. The molecular structure, molecular weight, and polarity of the molecules in ceramic slurry play an important role in solubility to $scCO_2$. A short polymer chain and weak polarity increase the similarity and solubility to $scCO_{2.}$ [16], [17]

1.1 Commercial resin trials

To find out what kind of substances could be extracted with $scCO_2$ and if an SLA print would crack during $scCO_2$ extraction, preliminary tests were done with a commercial resin (Azure Blue resin from Prusa Research). The substance mixture is called resin when it does not contain ceramic powder, and a slurry when it contains ceramic powder. Results from preliminary tests (see section 6.2 Experimental setups) for $scCO_2$ extraction are discussed here to show the importance of test parameter optimization, slurry recipe design with right substances, use of non-cured monomers/additives in solvent extraction, and use of solvents in supercritical state for efficient substance removal.

During exposure to a solvent, a polymer can swell and absorb solvent. In the case of $scCO_2$ extraction, swelling can be a result of CO_2 sorption and slow desorption, that can go on for days after exposure. [18]–[20] In the preliminary tests conducted, it was seen that $scCO_2$ was able to dissolve only samples that were not post-cured with heat and additional light exposure, but even those samples were badly cracked. It can be concluded that the substances in the Azure Blue commercial resin contents cannot be dissolved with $scCO_2$ in the conditions used without breaking the sample, and therefore slurries with recipes based on previous studies [21]–[23] were decided to be used further in this study. It was also concluded, that fully cured polymer does not easily dissolve in $scCO_2$. This was expected based on previous literature [24].

1.2 Research hypothesis and questions

CO_2 reaches supercritical state at 31.1 °C and 73.8 bars [25]. 40 °C and 100 bars were chosen as initial temperature and pressure for the $scCO_2$ extraction tests to be sure of supercritical conditions in the $scCO_2$ chamber. The importance of solvent supercritical state can be concluded from $scCO_2$ extraction tests that were made in 80 bar and 100 bar pressures for parallel samples with our own slurry recipe samples. Over 7 times more monomer was extracted in 100 bars within 24 h, compared to the same test in 80 bars. This is further discussed in Subsection 7.2.

Royer [26] removed polyethylene glycol (PEG) from ceramic parts with water debinding and $scCO_2$ extraction. In his study, the PEG removal time was reduced from 48 h to 4 h with the use of $scCO_2$ extraction. Similar was observed in this thesis in a test of immersing an SLA green part in water for 48 h. With 2 h $scCO_2$ exposure, 3 times more monomer was removed compared to 48 h immersion in water decanter, as discussed later in Subsection 7.2.

To understand why creating strong ceramic tooth restorations with SLA and $scCO_2$ extraction is so challenging and time-consuming, and yet an important topic of research, one must first understand the steps and details related to the process. Characteristics of ceramic powders, processing methods and previous research related to $scCO_2$ extraction are presented on general level first in Chapter 2. In Chapter 3, stereolithography is discussed as a method with specific light interaction and layer adhesion considerations. Mechanisms and characteristics related to successful slurry printing and $scCO_2$ extraction are discussed in Chapter 4, followed by requirements related to dental applications explained in Chapter 5. This theory part is followed by description of materials and methodology used in the experimental part of this thesis. Results are discussed in Chapter 7, followed by conclusions, Chapter 8.

Based on the previously described need to speed ceramic thermal debinding with a safe and available solvent, and challenges related to extraction, this thesis aimed to answer the following research questions:

1. Can a fraction of the monomer content in an SLA-printed part be dissolved with $scCO_2$ without breaking the part?
2. What kind of monomers can be dissolved like this?
3. Can the extraction be sped up with a co-solvent without breaking the part?

2. PROCESSING OF CERAMICS

Nowadays, technical solutions require demanding properties like high stiffness, inertness, hardness, or temperature resistance, from ceramics that are classified as nonmetallic and inorganic materials. They are divided into traditional ceramics (glasses, whiteware, clays, cements, abrasives, refractories) and advanced or engineering ceramics. Unlike traditional ceramics produced from natural sources, advanced ceramics are synthetic or modified to make their properties meet industrial requirements. Advanced ceramics are further divided into oxides (like aluminum oxide, zirconium oxide, and complex oxides) and non-oxides (carbides, nitrides, borides, halides, silicides). Oxides are versatile and commonly easier to process due to their lower sintering temperature, than extremely high-temperature-resistant and generally harder non-oxides. [2], [27]

Success in producing a ceramic part that meets the expectations for properties is a complicated process. Relationships between powder characteristics, slurry recipe chemical interactions, forming process steps and heat treatment cycles must be understood. The success is strongly dependent on completing every step carefully and understanding physical and chemical phenomena according to each processing method, as mistakes are difficult or impossible to fix during the process. Therefore, the principles of ceramic powder choice, and ceramic forming methods, are discussed in this chapter.

2.1 Ceramic powders

Particles smaller than 1 µm in diameter are called colloids. They tend to interact with each other and agglomerate more, than larger particles. Particles with similar properties accumulating in one part of a powder mixture or solution is called segregation. In small particles, van der Waals forces, electrostatic charges and forces caused by moisture are stronger than gravitational and inertial forces, thus agglomeration is more likely than segregation. Slurry sedimentation is slower with smaller particles due to the smaller magnitude of gravitational forces according to Stokes' law. Thorough mixing of ceramic slurries is important to avoid agglomerates, as they lead to inhomogeneous sintering. Small particles also densify requiring less energy and, therefore, at lower sintering temperature due to their larger surface energy. They may accumulate on the surfaces of larger particles, creating a partially ordered mixture that is less desirable than a random mixture. A partially ordered mixture creates gradients in grain size and pores, which leads to uneven densification and stresses within the final part. [2], [3] Ceramic powders are produced mechanically or chemically. The production method is chosen according to powder type, budget, required powder purity and particle size. The powder microstructure may be complex and in advanced ceramics processing, a simple microstructure is preferred to avoid large deviation in part properties. Simple microstructure consists of narrow particle and pore size distribution and particles with similar shape, with less secondary phases present. Information about powder characteristics such as:

- particle shape,
- particle size and size distribution,
- chemical composition, surface structure,
- density, porosity,

is crucial to produce the wanted properties in the final part. For instance, large size distribution may lead to different size pores and uneven densification and grain growth during sintering, reducing the microstructure simplicity. An important macroscopic level difference to polymers during heat treatments is that ceramics generally shrink less due to smaller density change because of absence of covalent bond formation and molecular chain relaxation, and pores left in the structure are larger. Larger pores and flow channels lead to easier and faster liquid flow during additive removal. [2], [28]

Regarding shape, smooth spherical or uniaxial particles are seen to produce best density, but the particles are mostly not perfect in shape and their surfaces have roughness. The more the particle shape deviates from perfectly round towards irregular, the more the packing density mostly decreases from the highest obtainable theoretical value of 0.61 for loose random packing for monosized spheres. However, the packing density increases when different size particles are mixed but can also lead to uneven density through a ceramic part. This causes internal stresses within the part, that need to be relaxed during sintering. [2]

Initially, particle surface chemistry determines the interaction with other particles. Further, atomic size line defects and point defects, surface roughness and elemental composition affect packing homogeneity during sintering. In macroscale, powder processing needs to be kept clean, as any impurities, such as dust, may create liquid phases and voids in the part during thermal treatments, causing heterogeneities. These defects magnify further in the processing, deteriorating the final ceramic part, and these heterogenous spots are mostly the initiators for mechanical failure. [2]

To ease processing, ceramic powders are often mixed with other substances to produce a slurry or a paste. A low viscosity is needed in stereolithography, and high solid content is needed to achieve high part density. Slurry viscosity is affected by the ceramic powder quantity, particle size and type. The more ceramic powder, the higher viscosity, which makes printing more difficult and dimensional resolution worse in additive manufacturing methods. Also, the smaller the particle size, the higher the surface area and more particles present, which means more likely interactions between particles. Thus, higher the viscosity, which limits the usage of smaller particle size powders in additive manufacturing. [29], [30] Though, according to Dehurtevent & al. [30] the flexural strength and shrinkage are not greatly affected by decreasing the particle size, at least with particles with size 0.46 µm or 1.56 µm. In their study, mean shrinkage of SLA-printed parts after heat treatment was 24.0 % for samples with particle size 0.46 ±0.03 µm and 24.5 % for samples with particle size 1.56 ±0.04 µm. Flexural strengths were 271.7 (sd 44.5) MPa and 273.8 (sd 41.9) MPa, respectively.

Manothan & Tesavibul [31] reported similar results regarding particle size effect on shrinkage, but they discovered better strength properties with a small particle size slurry. This may be due to better packing or less defects attained with smaller particle size. Obtained properties are strongly dependent on fabrication method and flaws present in samples. Small particle size is however a major contributor to achieve high density in the final part, together with sintering temperature profile and pressure. [29], [30]

Viscosity is an important feature especially in SLA, where polymeric resins are mixed with high content of ceramic powder. Viscosity needs to be low to print successful parts. Viscosity, the ability of a liquid to resist flow, is measured as a ratio between shear rate and shear stress:

$$\eta = \frac{\tau}{\dot{\gamma}}, \tag{1}$$

where τ is shear stress and $\dot{\gamma}$ is shear rate. The direct division is called apparent viscosity and for non-Newtonian fluids, instantaneous viscosity is calculated as the gradient in a shear stress vs. shear rate curve. [2] Viscosity behavior of a substance can be Newtonian, which means the viscosity does not change with increasing shear rate, or non-Newtonian, in which case the viscosity either decreases (shear-thinning) or increases (shear thickening) with increasing shear rate (Figure 1) [32], [33].

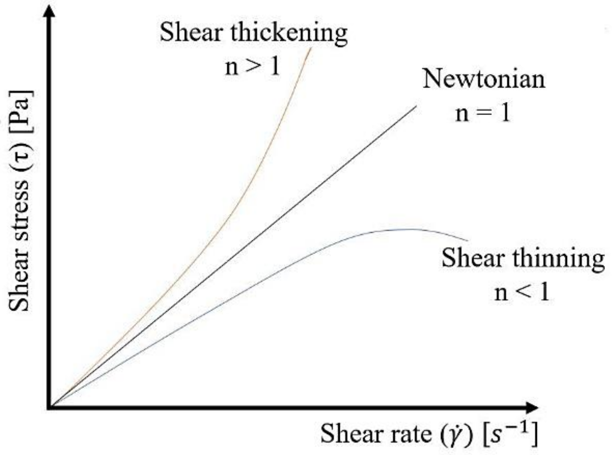

Figure 1: Shear stress vs. shear rate for Newtonian, shear thickening and shear thinning fluids [33].

An empirical equation can be used to describe the viscosity behavior:

$$\tau = K\dot{\gamma}^n, \tag{2}$$

where *K* is consistency index and *n* describes the deviation from Newtonian behavior. [2] A shear-thinning behavior is often desired to avoid agglomeration and to obtain better slurry spreading in methods like SLA, but a high solid content may lead to shear thickening. Measuring the viscosity for very low viscosity slurries can be challenging due to slurry slipping against the measuring geometry at high shear rates in a rotational rheometer. Though, there does exist a critical shear rate at which a shear-thinning behavior can change to shear-thickening, which is associated with a change from viscous flow to elastic interaction of particles. [32]–[34]

2.2 General process steps and forming methods

As mentioned in the previous subsection, ceramic powder can be prepared mechanically from mined ores or by synthesizing chemically via reactions in solid state or including a liquid or vapor phase. The processing of the obtained ceramic material may be done dry by compacting powders or wet by adding liquid substances. Pressing methods are by far the most used forming methods due to their lower price and easier processing. Powder processing methods can be divided into melt-based methods and powder sintering. Melt-based methods are mainly used for glasses due to high melting temperatures of most ceramics. Simplifying, in powder sintering methods, the powder is mixed (with other substances) and put together into a porous shape called a green body, which is then debinded and sintered by heating (Figure 2). Machining can be done to a green body or after sintering to finetune the surface and shape, if required surface quality and tolerances cannot be reached during the previous processing steps. It is critical to notice that failure in any processing step may lead to flaws that will be present in the final ceramic part. [2], [27]

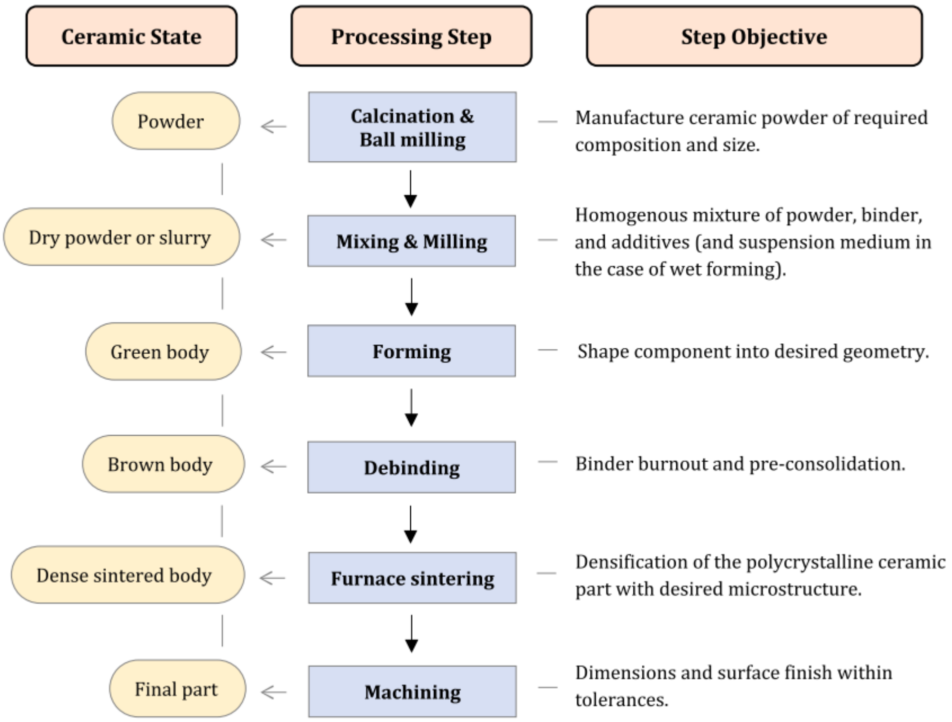

Figure 2: General ceramic processing steps for powder-based methods [27].

The goal of ceramic processing is mostly to produce dense parts with small grain size and uniform properties. To achieve this, the initial powder **mixing** phase needs to be done carefully in a way that produces a randomly distributed mixture with homogeneous properties. This requires time and thorough mixing. In addition to the powder itself, liquids can be used as solvents, dispersants, plasticizers, and binders to ease the mixture flow, strengthen the green body structure, and to ensure uniform distribution of additives and particles during forming. Solvents and binders are chosen between aqueous and non-aqueous (organic) substances. Mixing methods are based on diffusion, convection, and shear. Shearing ball mills are often chosen for their reasonable price, easy usage, and ability to break agglomerates. [2]

Powder **forming** methods can be divided into dry and semidry pressing, casting, plastic-forming and solid freeform fabrication/additive manufacturing. Pressing (die compaction and isostatic compaction) are the most widely used, producing parts from deliberately agglomerated sets of particles called granules with varying control of microstructure, dimension accuracy, or stresses. Casting (slip, pressure, tape and gel-casting) is based on removing a liquid part of a slurry leaving only the ceramic in the structure. Casting methods, such as tape casting, are often used for thin parts with relatively simple shape.

Plastic-forming methods (extrusion, injection molding) are based on moving a paste mass with ceramic powder, binders, and other processing substances, through a tube with rotating screws inside. Extrusion is used for parts with regular cross sections, such as tubes. In injection molding, the ceramic mixture is injected into a mold. Injection molding is expensive due to tooling costs. [2] These forming methods are presented in Table 1.

Table 1: Ceramic powder forming methods [2].

Method	Variations	Principle
Pressing	Die and isostatic compaction	Ceramic powder with binder is pressed into shape using a die/mold
Casting	Slip, pressure, gel and tape casting	Pressure or evaporation to remove solvent and create a ceramic part
Plastic-forming	Extrusion and injection molding	A ceramic paste mass is pushed through a nozzle/mold
Additive manufacturing	Powder bed fusion, sheet lamination, binder jetting, extrusion, material jetting, vat photopolymerization (e.g. stereolithography), directed energy deposition	Ceramic part is created layer by layer with 3D CAD model

Molds or dies are not used for green body forming in additive manufacturing methods. Instead, computer-aided-design (CAD) models are used to determine cross sections to be formed into 3D shape layer by layer. Many AM methods, injection molding and tape casting use more binder content in slurries than other ceramic forming methods, leading to additional challenges in debinding and largest obtainable part wall thickness. [2] Additive manufacturing processes can be further divided into categories based on the material used for creating the 3D shape:

- powder-based (binder jetting, powder bed fusion, directed energy deposition),
- solid-based (sheet lamination, extrusion),
- liquid-based (photopolymerization, material jetting, extrusion). [27]

These techniques have more variations under the explained titles and are presented in Figure 3 based on the amount of processing steps and usage of powder bed. Terms vat photopolymerization and stereolithography are often used as synonyms and DLP and LCM as their sub-branches. Sometimes, SLA is defined as a method with laser light source and DLP the same with a projector light source. However, considering SLA the most used term for photopolymerization printing regardless the light source or existence of ceramic powder, term SLA is used in this thesis as a synonym for vat photopolymerization.

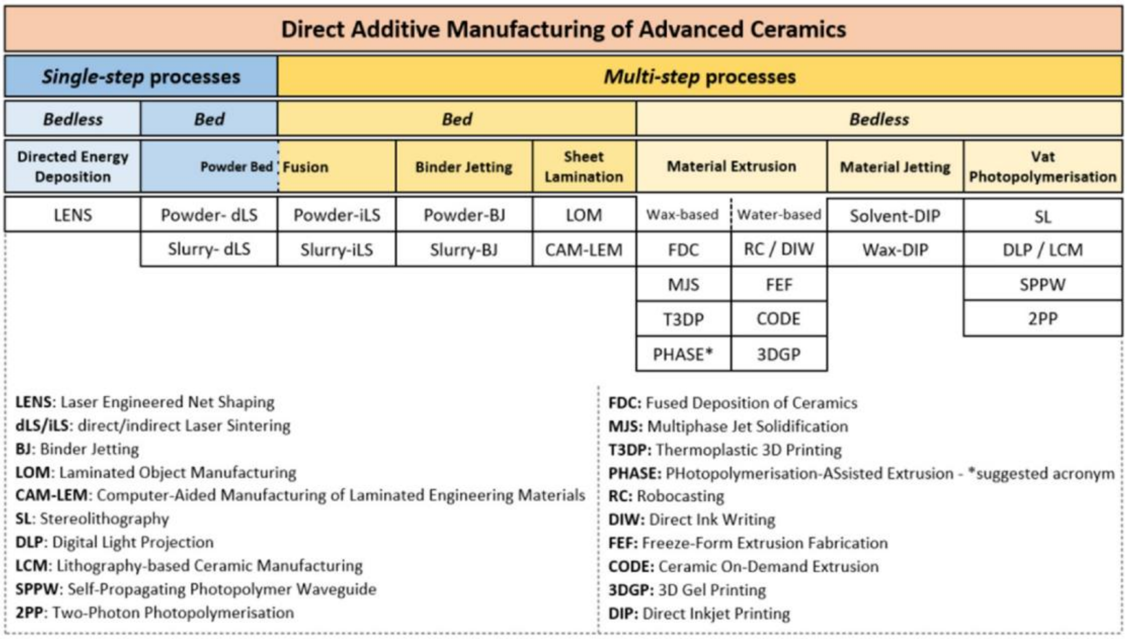

Direct Additive Manufacturing of Advanced Ceramics								
***Single-step* processes**		***Multi-step* processes**						
Bedless	***Bed***	***Bed***			***Bedless***			
Directed Energy Deposition	**Powder Bed**	**Fusion**	**Binder Jetting**	**Sheet Lamination**	**Material Extrusion**		**Material Jetting**	**Vat Photopolymerisation**
					Wax-based	Water-based		
LENS	Powder- dLS	Powder-iLS	Powder-BJ	LOM			Solvent-DIP	SL
	Slurry- dLS	Slurry-iLS	Slurry-BJ	CAM-LEM	FDC	RC / DIW	Wax-DIP	DLP / LCM
					MJS	FEF		SPPW
					T3DP	CODE		2PP
					PHASE*	3DGP		

LENS: Laser Engineered Net Shaping
dLS/iLS: direct/indirect Laser Sintering
BJ: Binder Jetting
LOM: Laminated Object Manufacturing
CAM-LEM: Computer-Aided Manufacturing of Laminated Engineering Materials
SL: Stereolithography
DLP: Digital Light Projection
LCM: Lithography-based Ceramic Manufacturing
SPPW: Self-Propagating Photopolymer Waveguide
2PP: Two-Photon Photopolymerisation

FDC: Fused Deposition of Ceramics
MJS: Multiphase Jet Solidification
T3DP: Thermoplastic 3D Printing
PHASE: PHotopolymerisation-ASsisted Extrusion - *suggested acronym
RC: Robocasting
DIW: Direct Ink Writing
FEF: Freeze-Form Extrusion Fabrication
CODE: Ceramic On-Demand Extrusion
3DGP: 3D Gel Printing
DIP: Direct Inkjet Printing

Figure 3: Additive manufacturing techniques [27].

In directed energy deposition, powders are deposited with lasers or other high energy sources to form parts. Similarly, laser or electron beam is used in powder bed fusion, but it is used selectively on a powder bed. In binder jetting, droplets of liquid binder are dropped on a powder bed layer by layer, instead of using a laser. Thin films are layered on top of each other and attached with heat or a binder in sheet lamination method. In extrusion techniques, powder mixed with wax or water is pushed through an extruder as a thread to form a part layer by layer. When using ultraviolet (UV) light for curing, in material jetting it is used to cure a sprayed liquid material, and in photopolymerization, a liquid containing ceramic powder is cured with light to form a shape layer by layer. [35]

Powder bed fusion, photopolymerization and material jetting techniques produce parts with good resolution, and in the latter two, the surface quality and mechanical properties are also good. Photopolymerization requires an extensive debinding program due to larger amount of binder substances. Powder bed fusion has advantages in easier post-processing. Sheet lamination is fast and not that expensive, but part mechanical properties are often poor. Binder jetting and extrusion-formed parts are cheaper as well, but their resolution, surface quality and mechanical properties are worse than in powder bed fusion and photopolymerization. In addition, binder jetting requires a long post-processing step like photopolymerization. [36]

After green body forming, solvents and additives, such as binders, used in the recipe must be removed to prevent deformation and cracks formed by evaporating or degrading substances. This is done by drying solvents and/or **debinding** organic substances. Pyrolysis/thermal debinding is the most common debinding method and hold time, heating rate, gas atmosphere and temperature need to be controlled to regulate exiting liquid and gas pressure gradients. Also, solvent extraction or capillary flow into a porous mold, also called wicking, can be used for debinding. In liquid immersion solvent extraction, the debinding time depends on

- part thickness,
- binder solubility in solvent,
- powder packing density,
- binder concentration,
- activation energy and
- temperature.

Thermal debinding can be done in vacuum or non-oxidizing/oxidizing atmosphere. Vacuum enhances degradation product diffusion and permeation, but temperature and heat transport control are poor. In different binders, decomposition products and decomposition temperature differ, requiring extra work in determining the heating program. [2] Vacuum debinding results in higher density and faster debinding of ceramic parts [37].

In thermal debinding, the green body is first heated to a softening point at about 150–200 °C. In this phase, moisture, trapped air or bubbles from residual solvent exit the part. Shrinkage and deformation happen especially in parts with low powder packing density, high binder content and low viscosity. Binder decomposition happens mostly at 200–400 °C. Low molecular weight substances can partly escape the part by capillary flow, but high weight polymers need to be degraded first. In non-oxidizing atmosphere, the degradation of cured polymers occurs by scission (chain breaks at random points) or depolymerization (polymer breaks into monomers). In an oxidizing atmosphere, heat partly degrades polymers, but the degradation mostly happens by oxidation starting from the part surface. These volatile degradation products must be allowed to diffuse out of the structure before reaching their boiling point to avoid bubble formation. After that, the thermal debinding program is run above 600 °C to degrade and gasify carbon residues. [2]

The diffusion and permeation time for each step can be approximately calculated, if sample thickness, particle size, powder packing density, pore and ambient pressure, burnout volume change, burnout vapor molecular weight, viscosity and volume are known. However, finding all those parameters can be challenging. The temperature program for debinding should be designed noticing that the ceramic powder may act as degradation catalyst and lower polymer decomposition temperatures significantly. [2] The program design can be done according to thermogravimetric analysis (TGA) results, as can be seen in Figure 4. In TGA, a sample is placed inside an aluminum oxide crucible on a scale that measures the mass change during heating in a furnace. This information can be used to verify e.g., the sample chemical composition, substance degradation temperatures and thermal stability. [38]

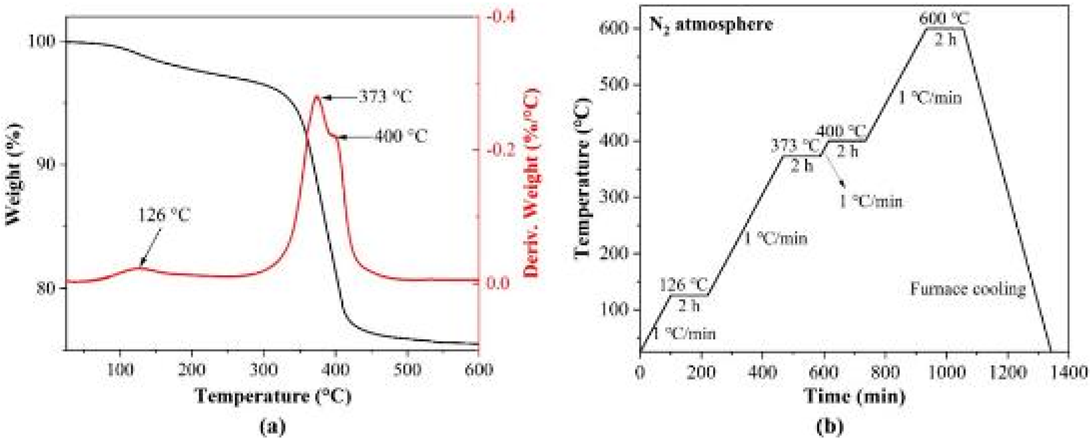

Figure 4: a) TGA results with weight loss as a function of temperature, and b) debinding program designed based on the TGA results degradation steps [39].

Debinding is followed by a final heat treatment called **sintering**. Most common sintering method is solid-state sintering. The ceramic part is heated up to 0.5–0.75 times the powder melting temperature and solid-state diffusion activates to fuse the particles together. Solid state diffusion is a complex, irreversible process, in which particles come in contact, grain size grows, and density, strength and hardness increase while porosity decreases. As it is an irreversible process, the total free energy of the system decreases. In solid state sintering, powder particles fuse directly in contact with each other. In liquid-phase sintering, a liquid is used between particles to enhance densification or to accelerate grain growth. This is mainly used for materials with properties that make solid-state sintering difficult or expensive, such as high melting temperature or strong covalent bonding, including some non-oxide ceramics such as silicon carbide and silicon nitride. Heat treatment program for sintering needs to be optimized, as too long holding times may decrease mechanical properties as well, if grain growth is favored instead of densification. [2], [40]–[42] Sintering speed could be increased with microwave sintering [35] or novel emerging high-speed sintering techniques, such as spark plasma, flash, or ultra-fast high temperature sintering [43].

In polymer processing, heat is typically used for creating chemical reactions between hydrocarbon chains or to deform the polymeric material to form a part. Ceramic particles are fused together via diffusion, in much higher temperatures instead. The particle fusion starts with powder particles coming into contact and forming necks while mass diffuses between particles and into the pores between them. Porosity reduction continues until densification stops, leaving isolated pores in the structure. Pore surface area decreases, causing free energy decrease, and grain boundary area increases, causing free energy increase. Mass transportation mechanisms during sintering vary according to the material physical and chemical properties. E.g., polymers and glasses undergo more viscous flow than most of other ceramics and metals. Sintering is a race between grain size growth and densification, as non-densifying mechanisms (vapor transport, lattice diffusion from the surface, and surface diffusion) and densifying mechanisms (lattice diffusion from grain boundary, plastic flow, and grain boundary diffusion) compete (Figure 5). [2]

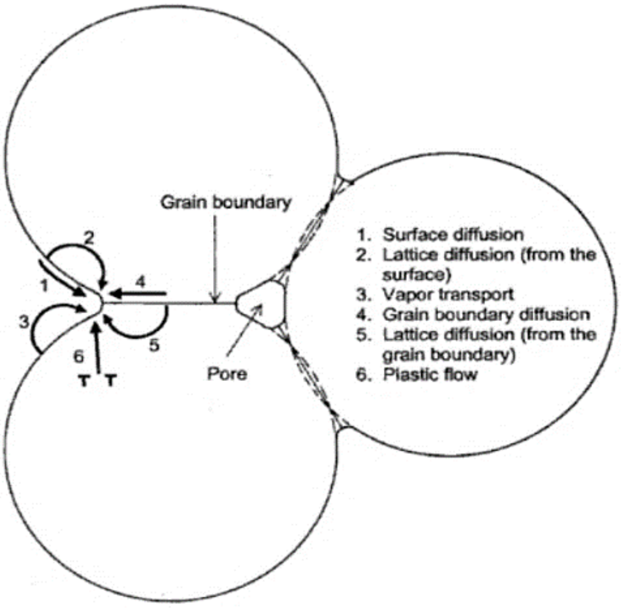

Figure 5: Mass transportation mechanisms of solid-state sintering [2].

The sintering rate is defined by the slowest active mechanism, and different ions might diffuse via different paths, changing mechanism according to changes in temperature, composition, or grain size. Due to this complexity, a comprehensive theory or equations describing sintering mechanisms for a particle system is replaced with empirical models. Even the models containing empirical constants are only valid for very uniform consolidation, particle size and arranging pattern, and simple application of for example Fick's law for diffusion flux does not accurately describe a ceramic system with multiple particles and varying diffusion mechanisms. For the initial stage of sintering, general models for neck growth ($\frac{X}{a}$, distance between neck surface and particle center per particle radius) and densifying mechanism shrinkage ($\frac{\Delta L}{L_0}$, change in length per initial length) can be presented as following [2]:

$$\left(\frac{X}{a}\right)^m = \frac{H}{a^n}t \tag{3}$$

and

$$\left(\frac{\Delta L}{L_0}\right)^{\frac{m}{2}} = -\frac{H}{2^m a^n}t, \tag{4}$$

where m and *n* are empirical constants depending on sintering mechanism, *t* is time and *H* is a function with parameters regarding geometry and material used for the ceramic part. These functions include mechanism-dependent diffusion coefficients, thicknesses, specific surface energies, vapor pressure, temperature, and viscosity dependence. [2]

Grain size growth via grain fusion is driven by the reduction of high energy grain boundary area. The grain boundary moves toward grain center as a curved front, as atoms move to the higher chemical potential side of the boundary. In normal grain growth, the grain size distribution remains narrow. Changes in grain boundary energy and mobility, caused by grain orientation, impurities and inhomogeneous particle packing, lead to abnormal grain growth of a grain much larger than other grains (Figure 6). In short sintering cycles, wide particle size distribution in the initial powder may lead to abnormal grain growth as well. On the other hand, bimodal particle size distribution offers better particle packing density and less pores in the structure prior to sintering. With long enough time in computer simulations, smaller particles grow faster, and the grain size approaches normal again, so the large particle size distribution is not enough to explain the abnormal growth. [2]

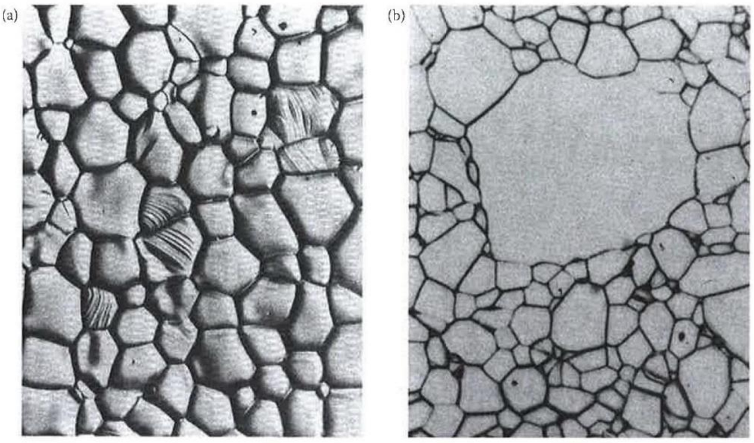

Figure 6: Alumina ceramic with a) normal grain size distribution and b) abnormal grain growth [2].

Shrinkage/growth of the pores depends on pore side curvature against the grain boundary, and pores larger than grain size are difficult to remove because the change in pore surface energy is smaller than in grain boundary energy. Narrow particle size distribution generally results in narrow size distribution in pore size as well. Therefore, a good green body density is important. A part with green density less than 40–45 % of the theoretical value can be difficult to sinter into a dense part, due to lower probability of pores being smaller than grains. In the intermediate and final stages of sintering, the pore geometry and chemical potential on their surfaces are expected to be uniform, and therefore only lattice and grain boundary diffusion are expected to be significant. Coble has expressed the polycrystalline system sintering as densification [2]:

$$\frac{1}{\rho}\frac{d\rho}{dt} = A\left(\frac{D\Omega}{G^m kT}\right)\left(\frac{\alpha\gamma_{SV}}{r}\right). \tag{5}$$

In the equation, ρ is relative density at time *t*, *A* is a geometrical constant, *D* is diffusion coefficient dependent on mass transport mechanism, Ω is atomic volume, *G* is grain diameter, α is a pore geometry constant, γ_{SV} is surface energy, *r* is pore radius, *T* is the absolute temperature, *k* is Boltzmann constant and *m* is the constant presented in Equation 4. *A, m* and α vary depending on diffusion mechanism and/or sintering phase. Thermal debinding and sintering heating phases need to be slow, so that gases formed during pyrolysis can escape the structure without causing cracks. This is a challenging and time-consuming step in parts that contain much binder, i.e., injection molded and most AM-formed parts. Debinding rates over 1 K/min have been studied to cause cracking and blistering in ceramic parts. In sintering, the heating rates are usually higher than in debinding (0.5–15 K/min), higher rates often leading to smaller grain size but also lower density. [2] Lower sintering temperature leads to smaller grain size [44], but higher temperature increases the sintering rate. Therefore, a compromise needs to be made, and a temperature too high or too low will lead to a density lower than optimum. [2]

As stated in this chapter, ceramic processing methods and powder choice include many variables and steps that need to be optimized well to avoid flaws that cause mechanical failure of the ceramic part. Thermal debinding is time-consuming due to slow heating rates required by the low resistance to thermal shock, that is typical for ceramic materials. Solvent extraction as a debinding method also has its challenges. An alternative solvent extraction method with supercritical carbon dioxide is presented in the next subsection.

2.2.1 Supercritical carbon dioxide ($scCO_2$) as a debinding solvent in injection molding

When carbon dioxide is heated and pressurized above its critical temperature 31.1°C and critical pressure 73.8 bars, it reaches supercritical state (Figure 7) [25]. Supercritical carbon dioxide ($scCO_2$) has simultaneously properties of a fluid and a liquid: it presents great diffusivity, liquid-like density, and low viscosity with no surface tension. Due to these properties, $scCO_2$ can penetrate solid structures and act like a hydrocarbon solvent for weakly polar and low molecular weight substances. [25], [45]

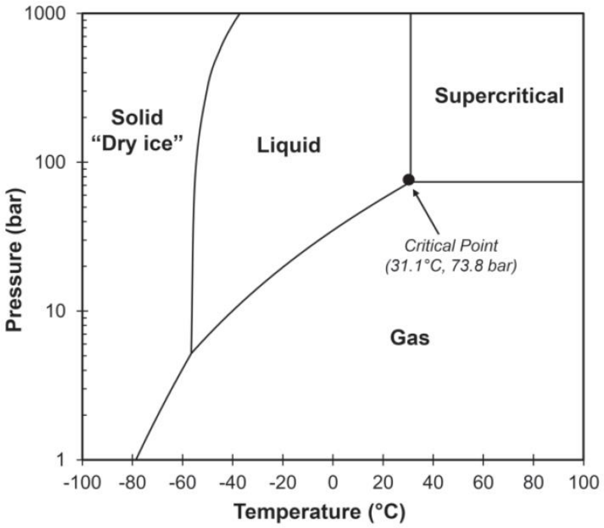

Figure 7: Carbon dioxide phase diagramme [46].

Motivation to use carbon dioxide comes also from its availability, reasonable price, chemical inertness, non-flammability, and non-toxicity [25], [45]. Many other substances used as solvents, such as ethers, hydrocarbons, acids, amines, halogenated and aprotic polar compounds are either hazardous for health or dangerous to handle. Among water, alcohols, ketones and esters, CO_2 is quite safe to use, and its critical point is reasonably easy to reach as observed in Figure 8. [16]

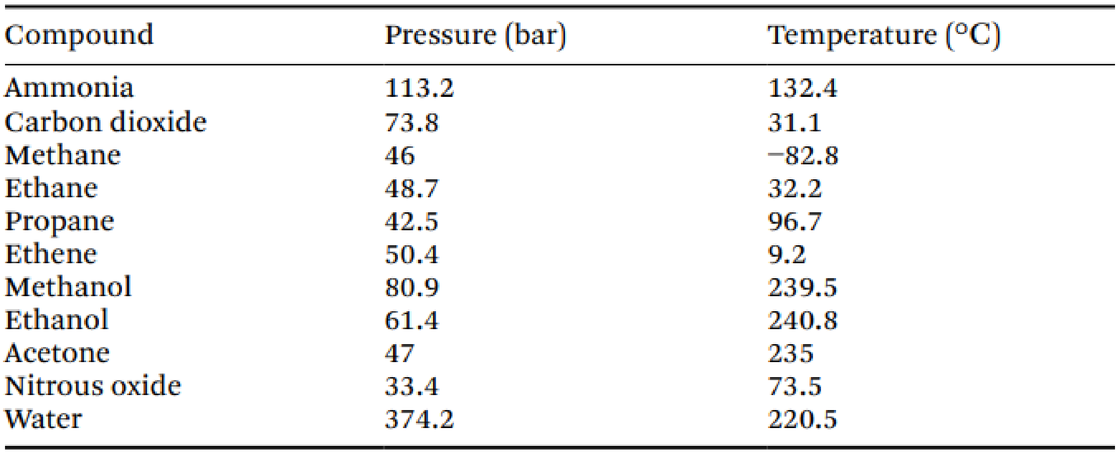

Compound	Pressure (bar)	Temperature (°C)
Ammonia	113.2	132.4
Carbon dioxide	73.8	31.1
Methane	46	−82.8
Ethane	48.7	32.2
Propane	42.5	96.7
Ethene	50.4	9.2
Methanol	80.9	239.5
Ethanol	61.4	240.8
Acetone	47	235
Nitrous oxide	33.4	73.5
Water	374.2	220.5

Figure 8: Critical points of different solvent substances [16].

Use of $scCO_2$ extraction has benefits in less decomposition product diffusion and binder redistribution induced defect formation compared to thermal debinding methods, and less solvent hazards compared to solvent immersion [47], [48]. Few polymers are soluble in $scCO_2$, but $scCO_2$ is soluble in various polymers [49]. In addition to solute extraction, $scCO_2$ can also be used to impregnate additives and dyes to polymers, to produce polymer blends and foams by swelling, polymer synthesis, coatings, food processing, production of pharmaceutical products and bone scaffolds [50]. The characteristics of $scCO_2$ change remarkably with increasing pressure, as can be seen in Figure 9. The change in density is greatest when conditions are altered in low temperature or pressure.

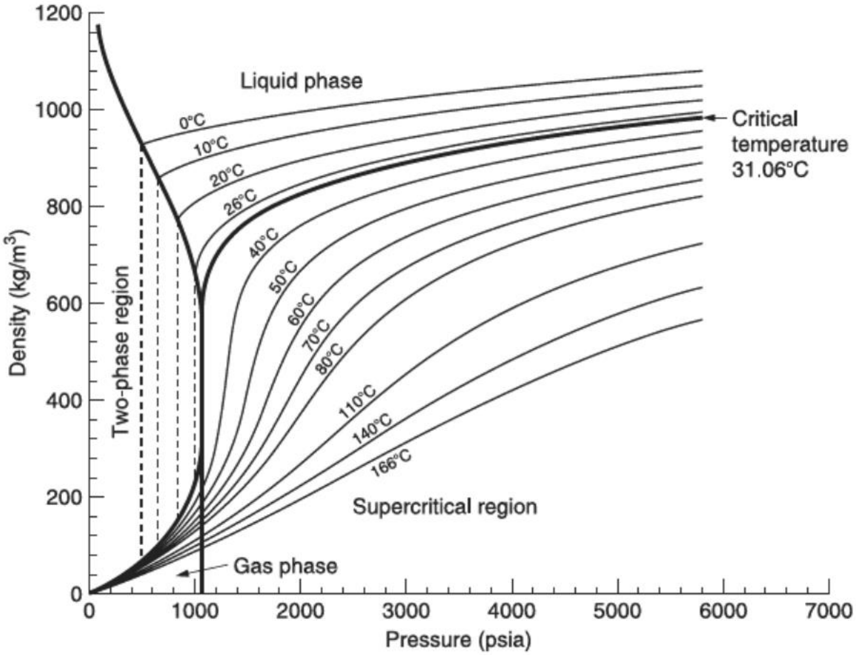

Figure 9: Density vs. pressure of CO_2. 1000 psi is equal to 68.75 bars. [15]

Nishikawa & al. [12] discovered already in 1991 that light-weight organic binders may be removed from a ceramic injection-molded part with $scCO_2$ and that co-solvents may ease the process by altering the solubility parameters of substances. They explored that high-molecular weight thermoplastics were not removed from the ceramic part structure. 80 % of light-weight organic binders were removed within 14 h in 195 bar and 60 °C conditions. In another example, Chartier & al. [51] used solubility parameters and calculated diffusivity (that have opposite pressure and temperature dependencies) to determine best conditions for $scCO_2$ extraction of paraffin wax. During the $scCO_2$ exposure, removable material dissolves into $scCO_2$ and diffuses out of the structure. If $scCO_2$ is used for debinding, it is important to create a recipe that also contains binders that do not dissolve in $scCO_2$. The part shape will not remain in green body shape if all binder is removed in the debinding. [47]

In the study of Nishikawa & al. [12], the removable binders were unsaturated higher alcohols and fatty acids and increasing the pressure from 100 bar to 200 bar had a dramatic increase in binder removal in a test of 3 h. In addition to alcohols, fatty acids and paraffin wax, $scCO_2$ has also been used to extract PEG from green bodies without crack creation [12], [26], [52]–[54]. Besides injection molding, $scCO_2$ has been used to extract dioctyl phthalate binder from tape casted barium titanate capacitors [20]. In the dioctyl phthalate (DOP) removal (Figure 10), increasing temperature (decreasing density) had more dramatic an effect on binder extraction amount than increasing pressure.

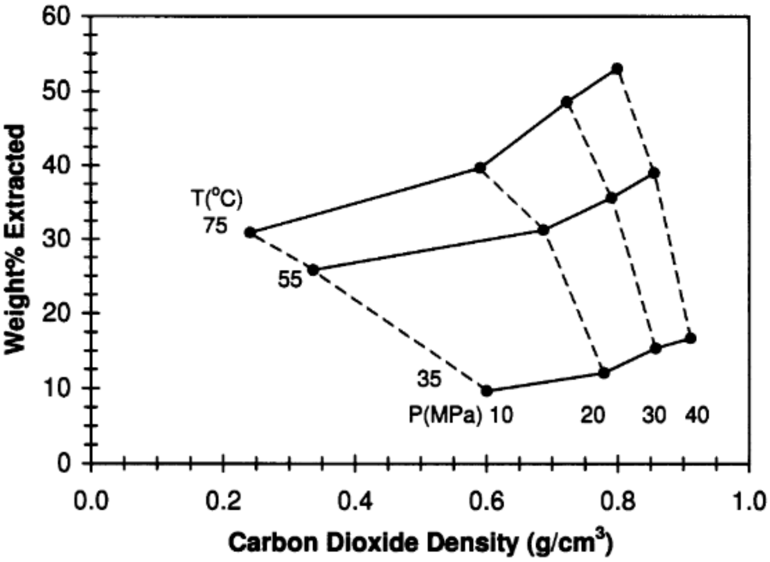

Figure 10: CO_2 extraction efficiency vs. density for dioctyl phthalate extraction in 3 h test [20].

$scCO_2$ extraction was used for hydroxyapatite parts resulting in microporous structure that is clean of remaining uncured monomers or additives [13], [14], increasing biocompatibility that is crucial also in dental applications. If a solvent is removed from the green body by evaporation, the remaining capillary forces between pores may collapse the structure. But the pores are filled with solvent during $scCO_2$ extraction depressurization phase and thus the collapse and cracks are more unlikely. [55], [56] As mentioned in Section 2.1, pores in ceramic parts are large, thus binder removal with $scCO_2$ can be assumed to create flow channels for gases to evaporate during the latter thermal debinding phase [2].

In binder removal of injection molded ceramic parts, flexural strength was better with $scCO_2$ debinded parts than thermally debinded parts. Also, the defects were smaller, and their size had less deviation. [48] Depressurization rate must be slow enough not to create too high a gradient between pressures outside and inside the part to avoid cracking [20]. Following the previous research on $scCO_2$ extraction of injection molded and SLA-printed hydroxyapatite parts, $scCO_2$ extraction could be used for SLA-printed alumina and zirconia parts for dental applications.

This chapter aimed to create a general view of the complexity related to ceramic processing and method-specific aspects. Challenges and requirements for powder characteristics, and processing steps have been discussed. The characteristics of stereolithography method, requirements for successful layer adhesion, and powder choice requirements related to light interactions are presented in the next chapter.

3. STEREOLITHOGRAPHY (SLA)

SLA was still 10 years ago used mostly for prototyping and research purposes, but the manufacturing industry has over the last decades turned towards demands in higher product complexity, uniqueness, and short lead times over the production of large number of fewer product variables. Regarding this change, SLA has advantages. [34] In 2022, already various companies produce industrial ceramic SLA printers: Lithoz, 3DCeram, Tethon 3D, Admatec, Formlabs, and Aon Inni (specialized on dental restorations). Ceramic 3D printing is expected to double its market value from 2020 to 2025, especially growing in medical, aerospace and defense fields. [57], [58]

Additive manufacturing methods have advantages over traditional ceramic processing methods regarding shape limitations, resolution, processing time (on the other hand every layer needs to be cured separately, slowing down the process [1]) and investment costs for molds and post-machining. In addition, SLA provides dense parts with good surface finish, high bending strength, high density, and less defects than methods requiring high energy laser beam. [59], [60] Crack-free parts without major pores can present similar characteristics to those prepared with conventional methods. To achieve this, process parameter and recipe optimization, use of colloidal processes, or extra densification via infiltration or hot isostatic pressing (HIP) might be needed due to inhomogeneities in prints. [2], [4] The main challenge regarding mechanical properties of SLA-produced parts is delamination between print layers [61].

3.1 Method and principle

A CAD model is needed to tell the stereolithography printer software how to create the 3D structure for the ceramic part. The CAD model designing includes its variables as well. For instance, printing orientation and geometry affect mechanical properties of the final ceramic part. [62] Once the CAD model is made, it is sliced into layers of desired thickness (min. 25 µm) to form the 3D shape by curing one horizontal surface at a time. The method is based on photopolymerization/photocrosslinking, and UV or visible light radiation at 200–700 nm (Figure 11) wavelength is used to activate photoinitiators (PI) in a liquid resin to cure the liquid slurry into solid form in the shape determined with a monochromatic light source, such as light-emitting diodes (LEDs), laser or LEDs with a projector. [34], [63] Based on literature reviews done by Zakeri & al. and Bove & al., the most typical wavelength range used is 350–460 nm at UV-A and blue light wavelengths [33], [41]. I.e., Prusa SL1S plastic printer uses 405 nm wavelength with about 2 mW/cm^2

light intensity and Lithoz CeraFab7500 uses 450 nm with 65 mW/cm^2 maximum intensity [64]. LEDs have benefits of not heating the slurry too much, being easy to handle and having a long lifespan compared to for example halogen lamps [65].

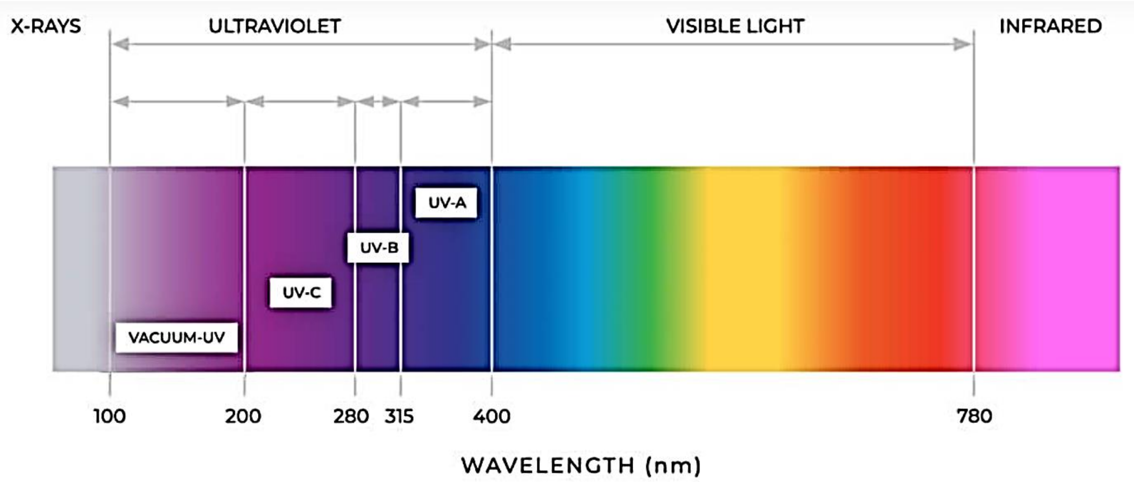

Figure 11: Ultraviolet and visible light in electromagnetic spectrum [66].

The SLA printer consists of a moving printing platform, resin tank, light source, and electronics. The printing can be done in a bottom-up or top-down orientation. In a bottom-up printer the resin tank has a transparent bottom (usually a fluorinated ethylene propylene, FEP, film or a glass) and the light source is situated under it. In the beginning of the printing, the resin is poured to the tank and the platform lowers down 1 layer height away from the tank bottom. There the first layer is cured, and the platform moves up detaching the cured layer from the tank bottom. This continues, until the whole 3D structure is printed. [67] To reduce slurry viscosity, heating can be used [68]. In top-down printer type (Figure 12), the light source is situated above the resin tank and the part is cured by moving the printing platform down. Controlling layer thickness is difficult in top-down stereolithography and it requires a very low viscosity slurry to be used. It is also slower than bottom-up method, and therefore bottom-up is often preferable, even though challenges with insufficient part adhesion to the platform may occur. [41]

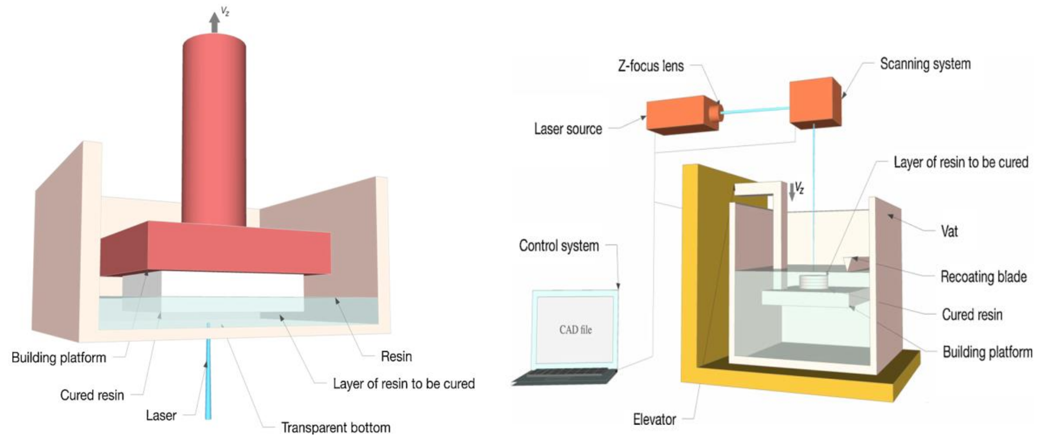

Figure 12: Bottom-up (left) and top-down (right) SLA printer schematics [41].

The acceptable viscosity limit for SLA slurries is considered to be 3000 mPa*s at 10 1/s shear rate [69], or 2000-5000 MPa*s at 30 1/s [33] or 5000 mPa*s at 100 1/s shear rate [68]. 5000 mPa*s is roughly the viscosity of a cooking syrup. Thus, the viscosity needs to be quite low for SLA to ensure easy cleaning of the printer and green bodies, but some tackiness is allowed due to the spreading blades and adjustable printer parameters. [70], [71]

Once the part is printed, it is cleaned from residual resin/slurry. The cleaning agent must be chosen wisely not to damage the green body. For example, ethanol may swell the polymers in the green body causing delamination and destroy the part surface, and ethylene glycol and glycerin may leave residues on the structure. [72] Dibasic ester [73] and later supercritical carbon dioxide can also be used for the cleaning without residuals in the green body [13], [14]. Carbon dioxide extraction will be further discussed in Chapter 4.

3.2 Light interactions and the slurry

SLA involves challenges in slurry recipe designing due to light interactions with matter. Several phenomena need to be considered especially when a ceramic powder is introduced to the slurry. If the printing parameters, light wavelength, and slurry components are not chosen accordingly, the slurry may not cure at all, or the part may be formed with weak mechanical properties or deformed shape.

As radiation travels from material to another, i.e., from air to a liquid resin, its path and energy change. Some of the radiation (light) is **reflected** away from the surface, **transmitted** through the material, and some is **refracted** or **absorbed**. In refraction, the light wave changes direction depending on the refractive index difference between two materials according to Snell's law, but does not lose energy:

$$n_1 sin\theta_1 = n_2 sin\theta_2, \tag{6}$$

where n_1 and n_2 are the refractive indices of the involved materials and $\theta_1$and θ_2 are the incident and refracted angles of light wave path. [74] Following Snell's equation, it can be seen that the more similar the refractive indices between the materials are, the less refraction is involved. Therefore, to limit refraction in SLA printing, the resin matrix and ceramic powder should have refractive indices close to each other. Consequently, using alumina and silicon oxide that have refractive indices closer to monomers, instead of silicon carbide or zirconia that have high refractive indices, is easier in printing with SLA. [4] Refractive indices of common ceramic powders and monomers used for SLA are presented in Table 2 later in Subsection 3.2.1. Different light interactions with matter are presented in Figure 13.

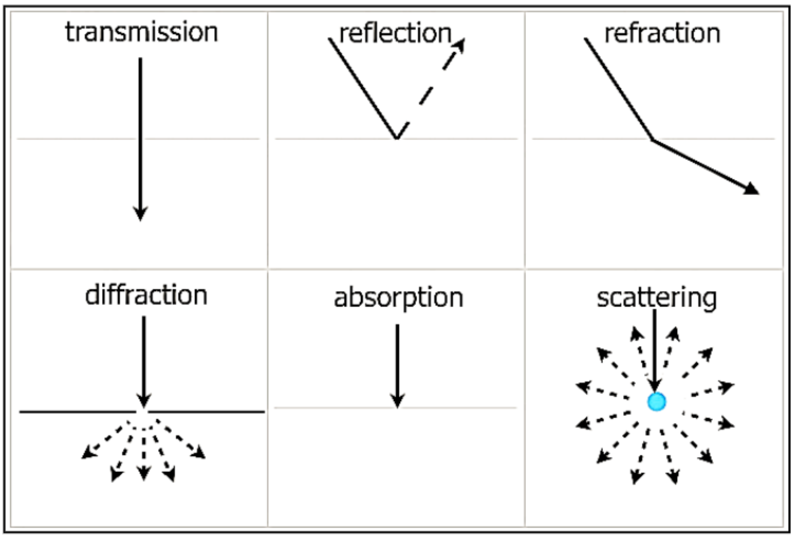

Figure 13: Interactions between light and matter [75].

The light intensity diminishes depending on traveled distance and absorption coefficient. This phenomenon is called absorption. Absorption coefficient depends on light wavelength and refractive index. This is due to the differing speed of light in materials due to changes in permittivity and permeability: in matter, light travels slower than in vacuum, depending on refractive index. The energy decrease associated with light traveling in matter follows Lambert-Beer law:

$$I = I_0 e^{-aL}, \tag{7}$$

where I is reduced intensity, I_0 is initial intensity, a is the absorption coefficient and L is the traveled distance. [74] The shorter the traveled distance, the less absorption is involved. Therefore, the smaller the layer thickness in SLA print geometry, the less light absorption happens. The higher the total refractive index of the slurry, the more light radiation is absorbed by the slurry, affecting the penetration depth of light. Also, larger refractive index of a powder leads to decrease in curing depth. [4], [76]

Absorption is also related to the energy-band structure of the material. Metals, that act as conductors, do not have an energy gap between valence and conduction bands and they appear as opaque due to photon absorption. In semiconductors, such as titanium oxide or silicon carbide, the band gap energy is rather small, thus photon absorption is likely. Insulators, such as alumina and zirconia, have a large band gap energy, which leads to reflection and diffraction rather than absorption. [77]

Ceramic particles cause refraction and scattering of light radiation in the slurry. Higher powder content diminishes the polymerization process and light traveling [4], [76], but it is crucial to achieve high density and good mechanical properties without flaws, so a compromise needs to be made. When the traveling light wave meets particles and passages between them, it **diffracts** and **scatters**. Diffraction means change in the wave front curvature and breakage into several beams that change their path, as illustrated in Figure 13. Scattering happens with an impact between a particle and the light wave, changing wave path. The elastic scattering associated with ceramic slurries is Rayleigh type when the particles are much smaller than the chosen light wavelength, in few nanometers scale. When the particles are larger, Mie scattering occurs. [74], [78], [79]

The most typical ceramic powder particle size used in SLA is 0.2–5 μm [33], [41]. Scattering is largest when the light wavelength and particle size are approximately equal. The scattering maximum wavelength depends on the refractive index difference between powder and matrix. Based on Rayleigh, Mie, and diffraction theories, when particle size is smaller or larger than light wavelength, Ilies [79] study predicts longer mean free path for photon travel (Figure 14) than when they are approximately equal. [74], [78], [79] Some studies [4], [76], [80] conclude that smaller particle size leads to more scattering, but they have used particles larger than the light wavelength, not exceeding the scattering maximum presented in Figure 14 and proceeding to particles that would be significantly smaller than used light wavelength.

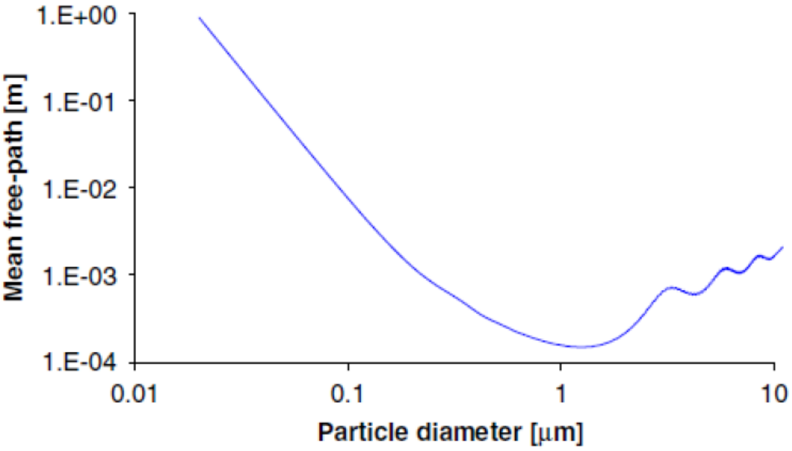

Figure 14: Mean free path vs. particle diameter with 808 nm wavelength, 0.1 vol% solid content, 1.8 and 1.49 refractive indices for powder and matrix [79].

Mie theory assumes homogeneous particle size and particle distribution. These results are modeled with 0.1 vol-% solid content, which does not correspond to solid contents used in true ceramic slurries and thus do not present the real situation, in which the distance between ceramic powder particles is smaller and interactions that depend on each other are more likely. The scattering attenuation is dependent on particle density, which increases with increasing solid loading in a slurry. [74], [78]

Curing depth and width of a slurry depend semilogaritmically on the total energy dose (light exposure time) and their critical energy doses, and sensitivity to light attenuation. The sensitivity, D_p, depends on ceramic powder content, scattering length, photoinitiator and dye concentrations and extinction coefficients. [81] The light exposure time per layer and the exposed surface area affect the print resolution, as scattered light will cure slurry also around the actual part if parameters are not set according to curing depth measurements [36]. The empirical cured depth can be presented with Jacob's equation, a modification of Lambert-Beer law:

$$C_d = D_p \ln\left(\frac{E}{E_c}\right), \tag{8}$$

in which D_p is the sensitivity, light penetration depth at which the light intensity has dropped to 1/e (36.8%) of initial, E_c is the critical energy needed for curing and E is the light intensity at slurry surface. D_p and E_c are exposure-independent slurry parameters, and a typical value for critical energy for resins without ceramic powder is 1–10 mJ/cm^2 [82]. E depends on light source power P, scanning speed v_s and light beam radius w_0, in the following manner:

$$E = \sqrt{\frac{2}{\pi}\frac{P}{w_0 v_s}} \tag{9}$$

and changing radiation parameters thus changes the curing depth. [41], [69], [73] The effect of the light intensity and refractive index difference between ceramic powder and matrix is shown in Figure 15. With a high contrast and/or too strong intensity, the horizontal resolution is worse than with a low contrast and/or low intensity. [33]

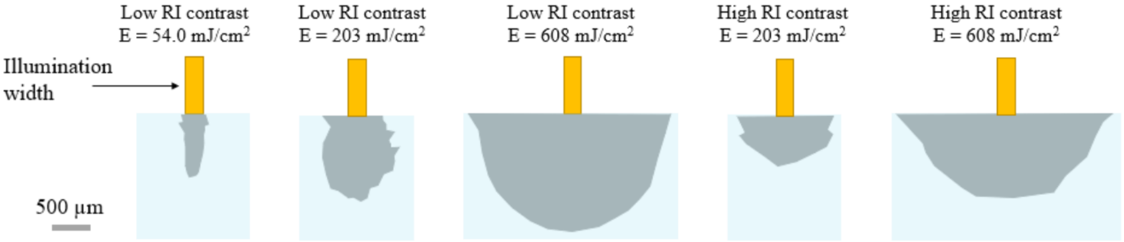

Figure 15: Cured slurry shape in relation with intensity and refractive index difference between powder and matrix [33].

The critical energy to be overcome to start the polymerization process is affected by the amount of photoinitiator and its absorbance at light source wavelength, and radiation path disturbances such as scattering, and absorption caused by ceramic particles. To ensure efficient adhesion between print layers, printing parameters should be set to irradiate more than 3 times the measured curing depth. [69], [83] Also, the scattering and absorption phenomena worsen the lateral resolution of the printing. Curing width is dependent on light beam size, curing depth and sensitivity to penetration depth [41]:

$$C_w = w_0 \sqrt{\frac{2C_d}{D_p}} \tag{10}$$

3.2.1 Ceramic powders in SLA

Alumina, zirconia, and silicon oxide (silica) are often used ceramic powders in SLA due to their suitable light penetration and scattering properties discussed in Subsection 3.2. SLA-printed alumina parts are used in i.e., applications for aerospace, automotive and thermal processing industries, whereas zirconia parts (Figure 16) are used for instance for jewelry, cutting tools and metal forming. They are both used also in electronics and medical applications. [33] In medical applications, alumina is nowadays common in hip bearings and zirconia in dental restorations [7]. Silica is a common material for electronics [84]. Barium titanate, lead zirconate titanate and silicon carbide have high refractive indices [33] and are therefore challenging to print with SLA. As can be seen in Table 2, silicon carbide needs a higher light wavelength to avoid photon excitation and absorption with the light energy close to its band gap energy [77].

Figure 16: SLA-printed zirconia tooth crown restoration after printing (left), debinding (middle), sintering and coloring (right) [85].

Some slurry compositions with common powders, their particle sizes, refractive indices (RI), refractive index differences (ΔRI) compared to the matrix and wavelengths (λ) are presented in Table 2. Alumina and zirconia have good mechanical resistance and are therefore often chosen for process optimization and research purposes in additive manufacturing [30]. Especially zirconia presents great fracture toughness, flexural strength, and easy machining of the green body. However, the use of zirconia is limited by its high refractive index that limits the curing depth, and its tendency to increase slurry viscosity and to show considerable shrinkage of parts during thermal treatments. Therefore, alumina is often chosen especially for preliminary studies with SLA. [30], [33], [44]

Table 2: Literature review of common slurry recipes used for SLA [33].

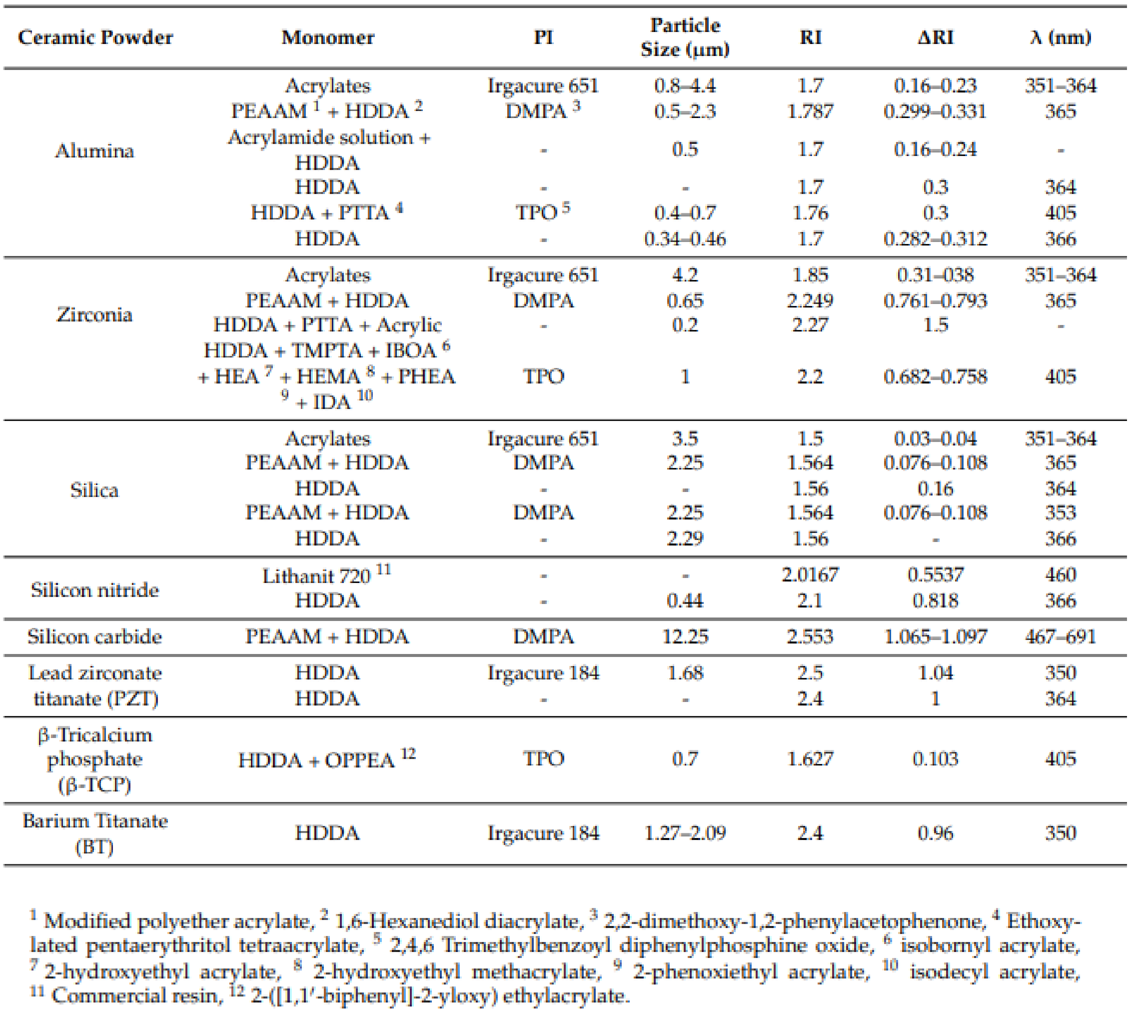

Ceramic Powder	Monomer	PI	Particle Size (μm)	RI	ΔRI	λ (nm)
Alumina	Acrylates	Irgacure 651	0.8–4.4	1.7	0.16–0.23	351–364
	PEAAM [1] + HDDA [2]	DMPA [3]	0.5–2.3	1.787	0.299–0.331	365
	Acrylamide solution + HDDA	-	0.5	1.7	0.16–0.24	-
	HDDA	-	-	1.7	0.3	364
	HDDA + PTTA [4]	TPO [5]	0.4–0.7	1.76	0.3	405
	HDDA	-	0.34–0.46	1.7	0.282–0.312	366
Zirconia	Acrylates	Irgacure 651	4.2	1.85	0.31–038	351–364
	PEAAM + HDDA	DMPA	0.65	2.249	0.761–0.793	365
	HDDA + PTTA + Acrylic	-	0.2	2.27	1.5	-
	HDDA + TMPTA + IBOA [6] + HEA [7] + HEMA [8] + PHEA [9] + IDA [10]	TPO	1	2.2	0.682–0.758	405
Silica	Acrylates	Irgacure 651	3.5	1.5	0.03–0.04	351–364
	PEAAM + HDDA	DMPA	2.25	1.564	0.076–0.108	365
	HDDA	-	-	1.56	0.16	364
	PEAAM + HDDA	DMPA	2.25	1.564	0.076–0.108	353
	HDDA	-	2.29	1.56	-	366
Silicon nitride	Lithanit 720 [11]	-	-	2.0167	0.5537	460
	HDDA	-	0.44	2.1	0.818	366
Silicon carbide	PEAAM + HDDA	DMPA	12.25	2.553	1.065–1.097	467–691
Lead zirconate titanate (PZT)	HDDA	Irgacure 184	1.68	2.5	1.04	350
	HDDA	-	-	2.4	1	364
β-Tricalcium phosphate (β-TCP)	HDDA + OPPEA [12]	TPO	0.7	1.627	0.103	405
Barium Titanate (BT)	HDDA	Irgacure 184	1.27–2.09	2.4	0.96	350

[1] Modified polyether acrylate, [2] 1,6-Hexanediol diacrylate, [3] 2,2-dimethoxy-1,2-phenylacetophenone, [4] Ethoxylated pentaerythritol tetraacrylate, [5] 2,4,6 Trimethylbenzoyl diphenylphosphine oxide, [6] isobornyl acrylate, [7] 2-hydroxyethyl acrylate, [8] 2-hydroxyethyl methacrylate, [9] 2-phenoxiethyl acrylate, [10] isodecyl acrylate, [11] Commercial resin, [12] 2-([1,1′-biphenyl]-2-yloxy) ethylacrylate.

Alumina and zirconia have strong covalent and ionic bonds between aluminum and oxygen ions, that lead to characteristic properties of ceramics: chemical resistance, high melting point, low conductivity, and high hardness. Zirconia is often stabilized with yttria, magnesium oxide or calcium oxide to produce a metastable tetragonal matrix with a minor fraction of cubic phase to enhance fracture toughness and strength. The tetragonal matrix can transform from tetragonal to monoclinic under external stress, including volume expansion that creates internal stresses that act as a toughening mechanism. Alumina, on the other hand, suffers strength degradation from inappropriate contents of calcium oxide, sodium oxide or silicon dioxide. Calcium oxide and alkalis segregate at grain boundaries, and silicon dioxide hinders densification. Zirconia is softer than alumina and is therefore easier to machine in green body state. [7]

According to several references [30], [37], [60], [86], [87], there needs to be more than 50 vol-% of ceramic powder in the SLA slurry to avoid cracking and deformation during thermal debinding, as in low powder content slurries the particles are not close enough to each other in the green body. This is supported by literature reviews done by Zakeri & al. [41] and Bove & al. [33], in which the general solid loading is 40–60 vol-% for SLA slurries. Large volumetric shrinkage leads to internal stresses in the part as well [88].

3.3 Layer adhesion

To be able to print a 3D shape, the initial layer needs to adhere to the printing platform and to avoid delamination between print layers, the cured layers need to adhere to each other. Both consisting mainly of Van der Waals forces, adhesion means molecular force attraction between two substances [89] and cohesion means substance internal strength, where the valence forces keep particles close to each other [90]. The complementary theories explaining adhesion phenomena are related to:

- chemical bonds,
- mechanical interlocking,
- diffusion,
- adsorption,
- electrostatic forces [91].

Often adhesion between two materials (or in this case print layers) is a combination of these [92]. Molecular attraction, chemical ion bonds, covalent and metal bonds are stronger and shorter than Van der Waals forces (Figure 17) [90] thus it is beneficial to create chemical bonds between print layers. This is done by using printing parameters that cure more than 1 layer thickness, so the layers would be better adhered to each other, and ceramic particles are closer to each other.

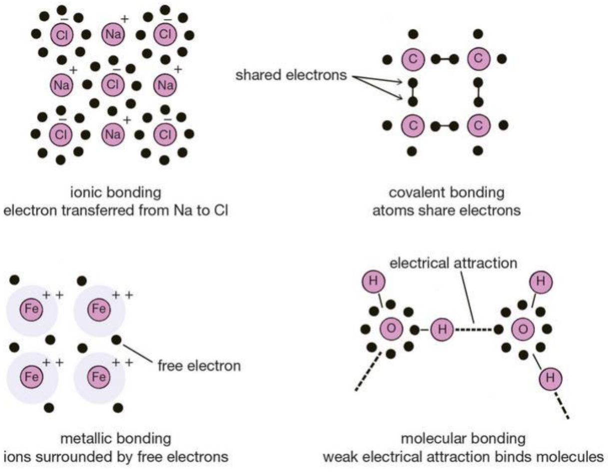

Figure 17: Types of chemical bonding [94].

In mechanical interlocking, one substance sinks into the surface roughness of another substance and as a rough surface has large surface area and energy, adhesion compared to flat surfaces can be improved with surface roughening [89]. For instance, adhesion strength between aluminum and epoxy or aluminum and acrylate may be improved even by 2 to 4 times by sanding, grit blasting or etching the aluminum surface [93]. Therefore, sanding could be used to improve adhesion of the cured slurry to print platform in bottom-up SLA in the case of poor initial adhesion.

A basic requirement for good adhesion in addition to time, chemically appropriate adhesives, adequate surface wetting and right environmental conditions, is adhesive joint geometry [94]. A straight butt joint, which is often not strong [95], is a challenge with SLA as the layers are cured on top of each other and ripped off the FEP film or glass. Good surface wetting is determined based on contact angle as θ:

$$\cos(\theta) = \frac{(\gamma_{SV} - \gamma_{SL})}{\gamma_{LV}}, \tag{11}$$

where γ_{SV} is interfacial tension between solid and vapor, γ_{SL} between solid and liquid and γ_{LV} between liquid and vapor. The lower the contact angle between the surface and liquid, the better wetting. Water has higher surface tension than most organic liquids and therefore organic binders are often preferred in slurries. [2]

Material and printing parameter choices and their relation to successful SLA printing were discussed. To get a deeper understanding of successful SLA printing for specific applications with supercritical solvent extraction, further details about polymer chemistry, material interactions in slurries and dental applications need to be discussed in the two next chapters.

4. CHEMISTRY IN SLA

As stated in the previous chapters, ceramic powder mostly needs processing aids from other substances to ease forming and to create strong parts with minor defects. A single substance does not generally satisfy all needs to maintain a stable slurry, in which the ceramic particles are divided homogeneously without agglomeration. In addition, the slurry needs to cure fast and with minimal shrinkage upon exposure to light in SLA and to be processed, viscosity needs to be low enough. The requirements for slurry characteristics regarding $scCO_2$ extraction are quite different than for SLA, some even opposite (Table 3). As discussed in Chapter 1, crosslinked substances do not dissolve in $scCO_2$, whereas high crosslinking density is required for SLA. Solubility in $scCO_2$ is further discussed in Subsection 4.2.1.

Table 3: Requirements for the slurry for SLA and $scCO_2$ extraction. Data from [15], [24], [96]–[98].

SLA	$scCO_2$
low viscosity	weak polarity
good particle dispersion	low molecular weight
hardening under light exposure	carbonyl groups
fast curing reaction	amorphous
low curing shrinkage	high free volume
strong 3D polymer network	high chain flexibility
strong and elastic, not too brittle	exposed functional group
user safe	resistant to pressure
low refractive index difference	non-crosslinked

On top of the topics discussed so far, understanding and considering parameters and requirements set by $scCO_2$ are essential for successful $scCO_2$ extraction prior to thermal debinding. In this chapter, photopolymerization and photocrosslinking mechanisms are presented with the most common polymeric materials and slurry components used in SLA printing, together with solubility aspects with $scCO_2$.

4.1 Polymer chemistry in SLA

Without understanding polymerization and the function of other process additives, the final ceramic part is likely to fail due to flaws, if even possible to print. This subsection begins with the explanation of terms related to polymerization and crosslinking, followed by introduction to monomers and additives used in SLA slurries.

4.1.1 Polymerization and functionality

Monomer is the simplest unit of repeatable molecule to produce polymers. When these molecules react to form longer molecular chains (polymerize), oligomers and polymers are formed. Oligomers are short chain polymers that are used in plastic resins, but mostly not in ceramic slurries due to their higher viscosity compared to monomers. [41], [99]

Terms polymerization, curing, and crosslinking are often mixed. In this thesis, polymerization means attaching monomers chemically to each other to form a longer molecular chain, a polymer. Crosslinking means creating chemical bonds between monomers/oligomers/polymers to form a 3D network. Crosslinking of thermosets can also be called curing (opposed to vulcanization of rubbers). When the reaction is initialized by light, terms photopolymerization and photocrosslinking are used. [100]–[103]

Thermoset polymers crosslink/cure forming a network that may not be melted with repetitive heating, whereas **thermoplastic** polymers remain as linear polymer chains that may be reformed once they are melted. A thermoset may be created by crosslinking existing polymer chains or from monomers with a crosslinker substance. The simplified structure of monomers, oligomers, thermoplastics, elastomers, and thermosets are presented in Figure 18. Due to strong chemical crosslinks, thermosets do not dissolve in solvents easily and they generally also resist higher temperatures and mechanical stress, than thermoplastics. [94], [104]

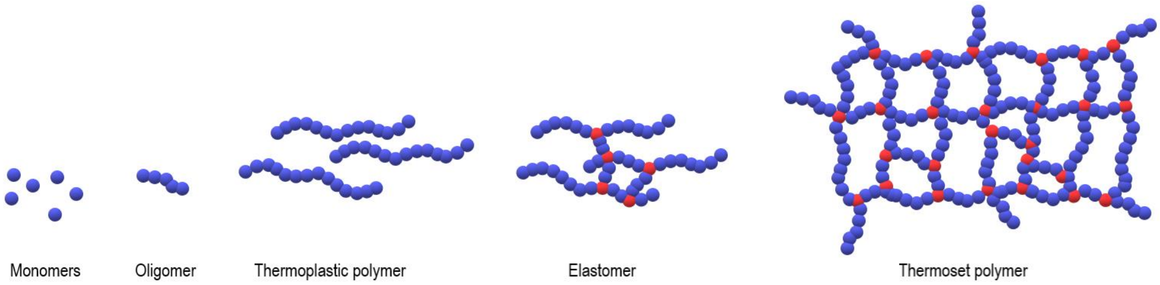

Figure 18: Simplified structures of a monomer, oligomer, thermoplastic, elastomer, and a thermoset. Data from [94], [99].

The most common ways of polymerization are addition/chain growth and condensation/step-growth (two different functional groups react releasing a by-product). **Addition polymerization/crosslinking**, that is used in UV-curing systems, has 3 stages. They are called initiation, propagation, and termination. The initiation of the addition reaction can be achieved by a stimulus, such as heat, pressure, or radiation (light, microwaves, X-rays etc.), forming a species that attaches to another monomer. [105], [106] In photopolymerization, the light dose (irradiation time) and chosen wavelength affect the degree of polymerization and crosslinking density [107]. Usually, a photoinitiator (PI) that is excited to a higher energy level by a photon, is needed to form the reaction-initiating free radical, anion/acid or cation/base. [105], [108] These crosslinking mechanisms are called **free radical** and **ionic photocrosslinking**. Cationic crosslinking is more popular in SLA than anionic. [103]

Radical photoinitiators are classified as one-component (type 1) photoinitiators that undergo a bond cleavage to form radicals, and two-component (type 2) that need a co-initiator or a co-sensitizer. [105] The difference between the degradation of these radical PI types due to light energy (*hv*) is presented in Figure 19.

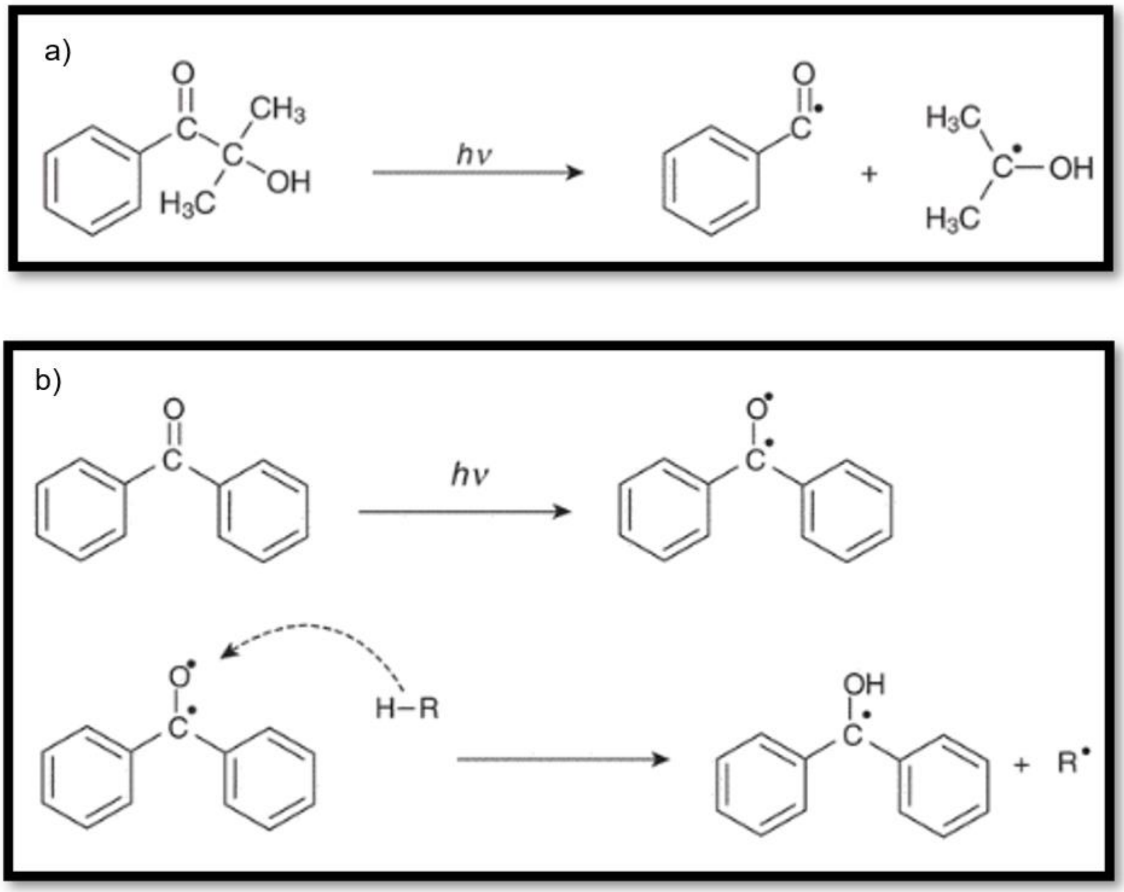

Figure 19: Type 1 (a) hydroxyl-phenyl-ketone and type 2 (b) benzophenone radical photoinitiators (PI) [102]. Dot presents a radical and R is the abbreviation for the chemical structure, that can be in this case any molecule that has a hydrogen (H) available to react with the oxygen radical.

In cationic polymerization/crosslinking, a hydrogen ion Brönsted acid is formed, and it bonds with monomer double bonds [102]. The schematic example of cationic initiation is presented in Figure 20.

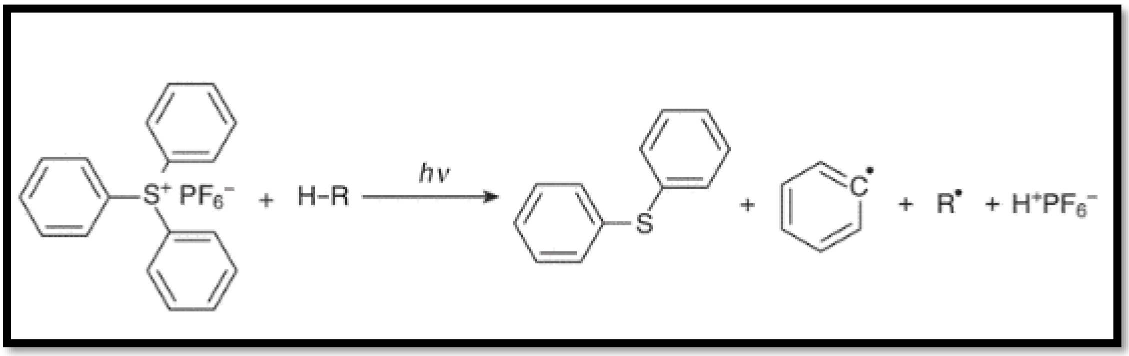

Figure 20: Cationic photocrosslinking initiation with phosphate tri-aryl sulphonium salt [102]. Dot represents a radical and R is the abbreviation for the chemical structure, that can be in this case any molecule that has a radical.

After the initiation, the radical/cation (*R**) reacts with a double bond in a monomer (*M*), leaving a radical/cation in the monomer, as presented in (a) in Figure 21. This proceeds to propagation (b), in which the reaction goes on creating a polymer network. Radical reaction is often terminated by two radicals combining (c) or by disproportionation (d), but cationic reaction may go on after the light source is removed. This is called dark curing. [69], [87]

a) $\mathrm{R}^* + \mathrm{M} \rightarrow \mathrm{RM}^*$

b) $\mathrm{RM}_n^* + \rightarrow \mathrm{RM}_{n+1}^*$

c) $\mathrm{RM}_n^* + \mathrm{R'M}_m^* \rightarrow \mathrm{RM}_n\mathrm{M}_m\mathrm{R'}$

d) $\mathrm{RM}_n^* + \mathrm{R'M}_m^* \rightarrow \mathrm{RM}_n + \mathrm{R'M}_m$

Figure 21: Photopolymerization/-crosslinking a) initiation, b) propagation and termination by c) combination or d) disproportionation [86].

An example of common type 1 radical photoinitiator is phenylbis(2,4,6-trimethylbenzoyl) phosphine oxide (BAPO) and a type 2 ketone-hydrogen donor system camphorquinone with a hydrogen donor amine, ethyl 4-(dimethylamino)benzoate. Their molecular structures can be seen in Figure 22 and their absorption properties are discussed later in Subsection 4.1.3.

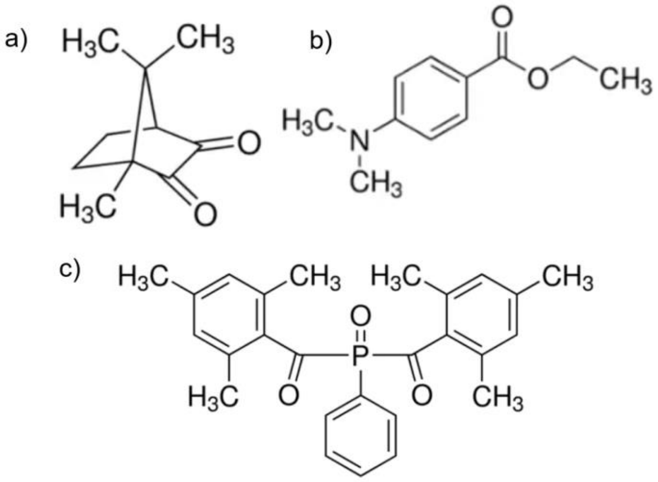

Figure 22: Radical photoinitiators a) camphorquinone, b) ethyl 4-(dimethylamino) benzoate, and c) phenylbis(2,4,6-trimethylbenzoyl) phosphine oxide BAPO [109].

Photopolymerization/crosslinking has advantages over multicomponent polymerization/crosslinking done by hand by adding a hardener to the resin, as no air bubbles are formed due to mixing and the reaction is often faster. [107] Polymerization process is driven by diffusion, and once started, resin viscosity increases. This causes less mobility of the reacting chains and affects final conversion. [87] The solidification steps included in crosslinking/polymerization are called gelation, where the liquid turns into a flexible rubbery state, and vitrification, where the rubbery polymer solidifies into a stiff solid. [110] Higher amount of ceramic powder, PI concentration and temperature affect the conversion as well, and as stated before, the slurry rheological behavior should be shear thinning to neglect effects of sedimentation [41], [60], [68].

4.1.2 Monomers in SLA

Materials usable in slurries for SLA are limited. Viscosity must be low, but after UV-curing the green body must have adequate green strength to withstand handling and further processing. All substances also need to be compatible with each other regarding unwanted chemical reactions and effects on print characteristics. [2] A monomer incompatible with another can for instance inhibit the polymerization reaction of another monomer [111]. Another important point of view is user safety. Most of the common acrylates, methacrylates and epoxies cause irritation and sensitization. Perhaps photocurable caprolactone or lactic acid, or plant-derived epoxies could be used instead of acrylates and epoxies to decrease health hazard concerns regarding monomers [174], [175].

Some monomers may remain uncured in the green body after printing. Uncured residual monomers result in green bodies with lower strength and macroscopic cracking during thermal debinding, if the remaining monomers and photoinitiators crosslink and the part shrinks before pyrolysis. [60], [112] As stated in Bae & Halloran's study [112], it is important that the uncured monomers are removed or cured before the thermal debinding. This can be done by post-curing with light or heat, or by the before described solvent/scCO$_2$ extraction. Thermogravimetric analysis (TGA) and differential scanning calorimetry (DSC) can be used to study the quantity of uncured monomers after the light curing step. DSC is used to study temperature change-related endothermic and exothermic transitions (like crystallization, melting, glass transition) in the form of heat flow. [38]

As showed in Figure 23, the heat exchange related to curing is seen as an enthalpy heat flow peak, which diminishes when less uncured monomer is left in the sample. The temperature shift in glass transition temperature is seen as a notch pointed with arrows. In heat-flux DSC furnace, the crucible with a sample is accompanied with an empty reference crucible on a separate thermoelectric disk and difference in temperatures between the sample and reference are measured [113].

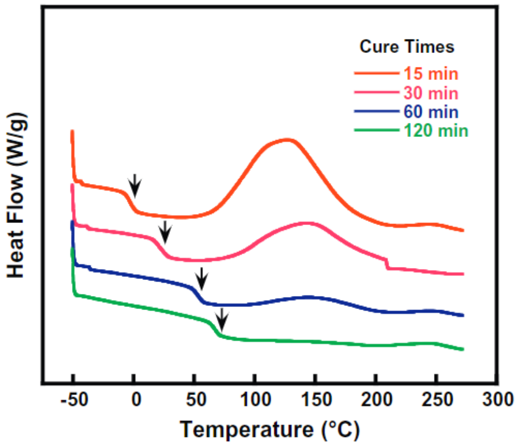

Figure 23: Heat flow vs. temperature curves of epoxy resins cured for different times. Glass transition temperatures are presented with arrows [114].

When designing a slurry recipe, major binders should be chosen in a way that they don't have a significant overlap in their decomposition temperatures during debinding. The binders must also have properties suitable for debinding to be removed before sintering, and they should not react with the powder. Inorganic substances may be difficult or impossible to remove before sintering. Often a compromise needs to be made regarding price, viscosity, and user/environmental safety. Due to these reasons, the slurry often consists of many substances and as their chemical structure and reactions are frequently complex, many recipes have been developed by trial and error. [2] To reduce delamination, cracking, and polymerization shrinkage, a non-reactive component may be added to the slurry. If the same non-reactive component also decomposes during debinding, instead of evaporating, it may reduce part porosity and create channels for diffusion. For instance, PEG could be used as such a component. [83]

As discussed in the previous subsection, radical photocrosslinking is the most common polymerization type used in SLA. It occurs in monomers that have an unsaturated vinyl (alkene with 2 sp^2 carbon atoms) in their molecular structure, such as acrylates and methacrylates. [87], [115] Acrylates and methacrylates are used as thermosets in 3D-printing technologies, and their chemical difference is only one methyl group (Figure 24) [41], [90].

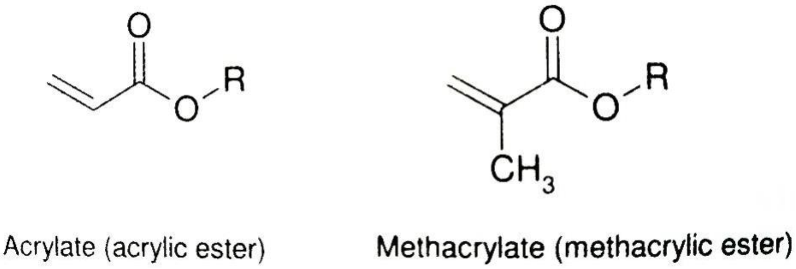

Figure 24: Acrylate and methacrylate chemical structures [90]. R represents the rest of the molecular chain.

Based on literature reviews done by Bove & al. [33], Zakeri & al. [41], and Camargo & al. [116], acrylates with different functionalities are by far the most used monomers for SLA. The most popular acrylates seem to be:

- isobornyl acrylate (IBOA),
- 1,6-hexanediol diacrylate (HDDA),
- trimethylolpropane triacrylate (TMPTA),
- (ethoxylated) pentaerythritol tetra-acrylate (EPTTA),
- polyethylene glycol diacrylate 200-400 (PEGDA).

Also, some methacrylates and dimethacrylates, like 2-hydroxyethyl methacrylate (HEMA) and poly(ethylene glycol) dimethacrylate (PEGMA), are used. Curing rate of methacrylates is often slower than acrylates, but they are used for obtaining good flexibility and lower shrinkage. Often, acrylates and methacrylates are based on ethylene glycol or propylene glycol to reduce cracking. Acrylamide and N-N’-methylenebisacrylamide have been used in aqueous slurries as well. Monomers are mono-, di-, tri- or tetra-functional based on how many functional groups they have in their molecular structure. The most popular acrylates with functionality numbers 1–4 are presented in Figure 25. Monofunctional monomers polymerize forming entangled linear polymer chains. Multi-functional monomers crosslink instead, which results in a stiffer and tougher polymer matrix and reduces the challenge with remaining uncured monomers in green body. [33], [41], [69], [82], [116], [117]

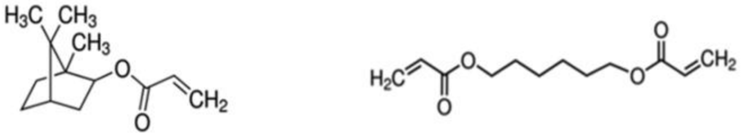

Isobornyl acrylate (monofunctional)

1,6-Hexanediol diacrylate (difunctional)

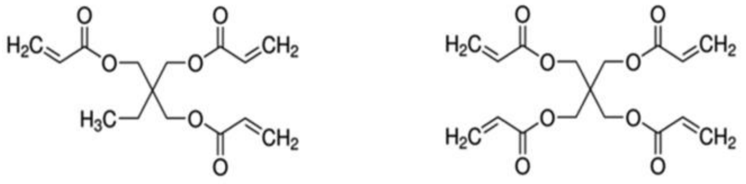

Trimethylolpropane triacrylate (trifunctional)

Pentaerythritol tetraacrylate (tetrafunctional)

Figure 25: Molecular structures of most popular mono-, di-, tri- and tetrafunctional monomers in SLA [69].

Acrylates are generally quite brittle and fast curing [82] which can generally cause print delamination, but they are popular in SLA due to their curing speed and availability in many different chemical structures; thus, their mechanical properties can be adjusted. They can be combined to form copolymers via radical polymerization. [69] The brittleness of acrylates comes from high crosslinking density and inhomogeneity, which can be modified to produce tougher parts with e.g., addition-fragmentation chain transfer agents, or generating interpenetrating networks of 2 different curing systems [118]. In general, linear polymer chains such as acrylics, vinyls, and PEGs are flexible and have lower viscosity than stiff chains with heavy side groups or ring structures, such as polystyrene or epoxies [2], [119], [120]. Higher functionality also leads to higher viscosity, as the molecule is larger and heavier [116].

The combination of different monomers in slurry recipes is often a compromise between reactivity and low viscosity [60] and a mixture of two monomers to form an interpenetrating polymer network with one glass transition temperature, is commonly used [121]. Two monomers with the same curing mechanism can also be combined. For instance, HDDA is often combined with TMPTA to reduce shrinkage and to increase green body hardness. As ceramic particle surfaces are hydrophilic due to the hydroxyl groups, hydroxylated monofunctional acrylates may be used to enhance dispersion [116]. To improve green part biodegradability, softness and to reduce polymerization shrinkage, step-growing thiol-ene monomers could be used as a combination with acrylates, but their shelf life is short and causes extra challenges in slurry handling [118].

Epoxies are a group of thermosets that have a molecular structure with two or more oxirane rings and in light-curing resins, they undergo cationic polymerization. In general, they are used for their strength properties and high crosslinking density, and great adhesion. Their photocuring is often slow and continues even after light source removal, and they increase the slurry viscosity, but they shrink less due to the oxirane ring opening during their curing. [122], [123] 3,4-epoxycyclohexylmethyl 3,4-epoxycyclohexanecarboxylate (ECC) seems to be the most popular epoxy used in SLA slurries. Its' chemical structure is presented in Figure 26 with the structure of PEG.

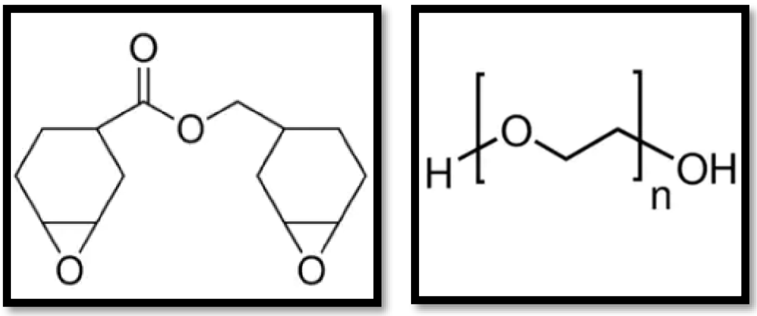

Figure 26: Molecular structures of ECC (left) and PEG400 (right) [109].

In addition to organic slurries with acrylates and epoxies, aqueous water-based slurries for SLA also exist. They have low viscosity, good affinity to ceramic powders, and toxic solvents are not a concern, but green body strength is low and the parts crack easily. [8], [37], [116], [124]–[126]

4.1.3 Additives in SLA

Monomers are not enough to allow transforming the ceramic powder into the printed green body. Photoinitiators, dispersion agents, plasticizers and inert diluents or solvents are used in the slurry recipe in addition to curable monomers (binders). [2], [60], [87]

Photoinitiator types were discussed in the previous Subsection 4.1.1. There are various photoinitiators available for different wavelengths and constant research is done to create new ones [105]. Choice needs to be made according to the monomer curing type and radiation wavelength used in the printer. For example, BAPO for type 1 radical systems has maximum absorbance in the wavelength range of 360-400 nm and CQ for type 2 radicals works best at 450–475 nm, as can be seen in Figure 27. [127] The initiators need to be sensitive enough to light to keep the part production time reasonable [60]. Photoinitiator content must be optimized as unreacted photoinitiators may affect the final properties of the printed part [128].

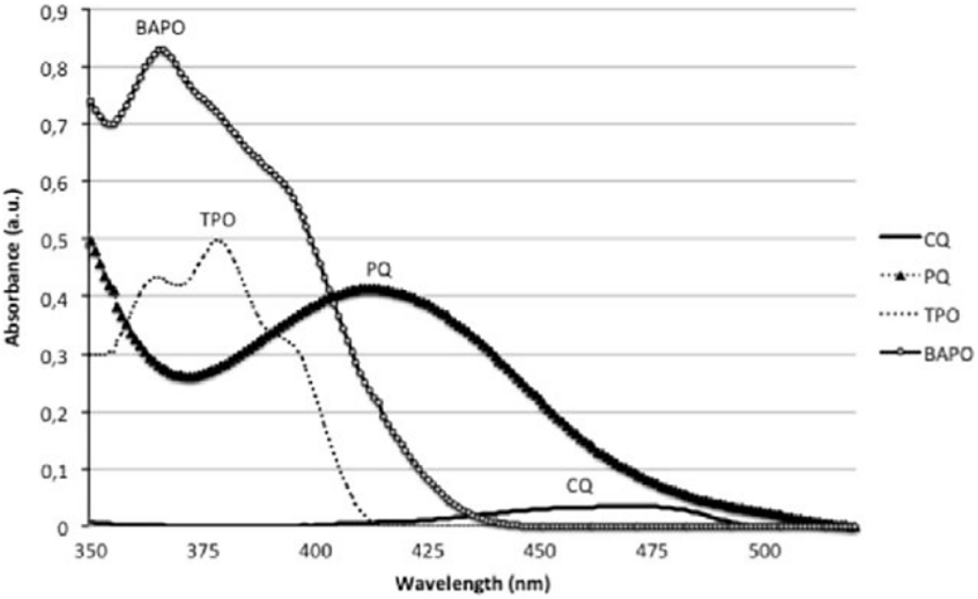

Figure 27: Absorbance of different radical photoinitiators at wavelength range 350–550 nm [127].

Dispersion agents are used to ensure homogeneity and to prevent reagglomeration of the slurry once the slurry has gone through mixing, to break initial powder agglomerates. They may also decrease slurry viscosity due to electrostatic interactions with the monomers. [68] Attention must be paid to polarity when choosing a binder, as it should not replace the dispersion agent on particle surfaces. For oxides, dispersant should be more polar than the binder, and often substances with amine, carboxyl, silane, or phosphoric acid functional groups are used. [2], [116] If the binder is more polar than the dispersant, there is a stronger attractive force between binder and powder, leading to replacement of dispersant.

Most raw and non-functionalized ceramic powders are lyophobic (“liquid-hating”); thus, they tend to interact with other ceramic particles instead of a liquid, causing flocculation, and as there is no affinity between the liquid and particles, the solution Gibbs energy increases. Therefore, to achieve solution stability within the slurry, electrostatic (charging particles), steric (attaching noncharged polymer chains on particle surface) or electrosteric (attaching charged polymer chains on particles) stabilization (Figure 28) is used in the form of dispersion agents. Inorganic acid salts are used for electrostatic stabilization, but if used in excess quantities, they may leave significant residues on the powder surfaces, which may lead to liquid phase formation during sintering. [2]

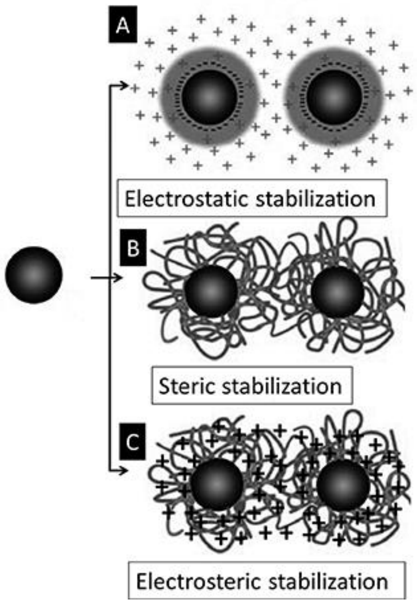

Figure 28: Schematics of a) electrostatic, b) steric, and c) electrosteric stabilization of ceramic particles [129].

Diluents can be used to lower slurry viscosity, to tune refractive index of the slurry matrix, and to lower polymerization shrinkage, but care needs to be taken not to affect the UV-curability of the slurry. [68], [116] Most common diluents used in SLA are water, low molecular weight alcohols (methanol, ethanol, isopropanol, 1-octanol), glycerin and PEG [116]. Plasticizers may be used as well. A low-molecular weight plasticizer occupies space between binder polymer chains, decreasing their interaction and thus decreasing the binder glass transition temperature, hardness, and strength. In fact, using a plasticizer may be necessary to produce crack-free green bodies by reducing elastic modulus and increasing polymer flexibility. PEG has been used as a plasticizer, as a part of steric stabilization for aqueous ceramic slurries and as a binder. Due to the –OH groups in its structure, it works for stabilization only in hydrogen bonding liquids. [2], [61] PEG was used also in this work as both a binder and a plasticizer.

4.2 Chemical debinding with $scCO_2$

As described earlier in Chapter 2, $scCO_2$ has been used for solvent extraction for decades. However, literature regarding monomer extraction for SLA-printed dental ceramics parts was not found during this thesis. As seen in Chapter 2, $scCO_2$ can ease thermal debinding, but also creation of ceramic parts with less defects. “Like dissolves like”, due to opposite partial electric molecular charges clustering and surrounding each other, causing solvation [115]. The schematic of water molecule partial negative charges attracting to positively charged sodium ion, and positive partial charges attracting to negative chlorine ion, is presented in Figure 29.

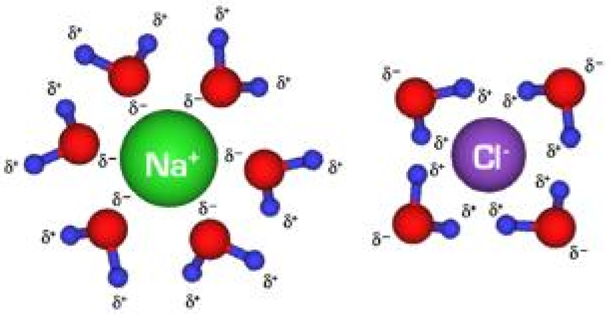

Figure 29: Sodium and chlorine ions surrounded by water molecules in solvation [130].

Solubility depends on polarity, temperature, solvent density, and pressure [130]. Success in solvent extraction depends on finding the right temperature and pressure conditions, and substances that are soluble in each other. $scCO_2$ solubility to other substances is discussed in this subsection.

4.2.1 Solubility and polarity

$scCO_2$ has a polarity similar to hexane and toluene and is therefore a very weakly polar solvent for dissolving other non-polar or weakly polar substances. Solubility between 2 substances can be modified by changing pressure, temperature, or co-solvent. [16] At a certain pressure and temperature, the two substances are not completely soluble and above this point, they are miscible. This is called the “cloud point”. [131] To achieve solvation, the change in Gibbs energy ΔG_{mix} needs to be negative:

$$\Delta G_{mix} = \Delta H_{mix} - T\Delta S_{mix}. \tag{12}$$

Enthalpy change ΔH_{mix} depends mostly on density and polymer-solvent intermolecular and intramolecular interactions, whereas ΔS_{mix}, change in entropy, depends on combinatorial entropy of mixing and noncombinatorial contribution to mixing volume change. [15]

ΔH_{mix} is approximately equal to change in internal mixing energy ΔU_{mix}, which depends on:

- mole fractions of substances,
- intermolecular potential energy,
- spatial distribution of molecules related to each other,
- distance between molecules,
- solution density, and
- Boltzmann constant.

As the internal mixing energy depends on density, one can generalize that solubility may improve by increasing pressure, using high-density co-solvent, or decreasing slurry density. However, the interactions between polymer and $scCO_2$ need to be more favorable than intramolecular interactions. The intermolecular potential energy's attractive part between small, free molecules in substances *i* and *j*, can be presented as:

$$\Gamma_{ij}(r,T) \approx -\left[C_1 \frac{\alpha_i \alpha_j}{r^6} + C_2 \frac{{\mu_i}^2 {\mu_j}^2}{r^6 kT} + C_3 \frac{{\mu_i}^2 {Q_j}^2}{r^8 kT} + C_4 \frac{{\mu_j}^2 {Q_i}^2}{r^8 kT} + C_5 \frac{{Q_i}^2 {Q_j}^2}{r^{10} kT} + complex\ formation\right]. \quad (13)$$

In the equation, α is polarizability, μ is dipole moment, *Q* is quadrupole moment and $C_{1\text{-}5}$ are constants. The effect of induction is so much smaller than dispersion and polarity, that it is neglected. Also, the effect of polymer chain connections is not included. [15]

$scCO_2$ solvent properties change if pressure or temperature are altered. The first term in Equation 13 does not depend on temperature, and CO_2 dispersion forces that depend on polarizability, are weak in pressures that are not very high. Thus, CO_2 with polarizability $26.5 \cdot 10^{-25}\mathrm{cm}^3$ is not an efficient solvent in very high temperatures, where dispersion dominates, and polar interactions are negligible. At low temperatures, polar molecular interactions and complex formation dominate, and polar polymer's dipole interactions are strong. CO_2 molecule has no dipole moment due to its symmetry, but its short-distance quadrupole moment (Figure 30) is strong ($-4.3 \cdot 10^{-20}$ esu cm^2) because it is dense in modest pressures and temperatures, which on the other hand makes nonpolar polymers less soluble to CO_2 in low temperatures. [15], [132]

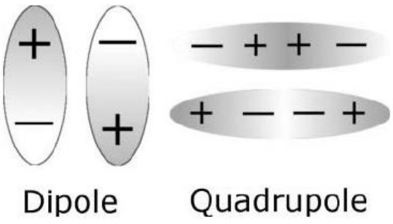

Figure 30: Dipole and quadrupole charge distribution [133].

As seen in terms 2–5 in Equation 13, polar moments are inversely dependent on temperature, which means that in high temperatures they are negligible and polar molecules act like nonpolar molecules. CO_2 ability to dissolve depends on its density and internal energy, and at moderate temperature and pressure its density is high. [15] The longer the polymer chain, the less soluble it becomes to $scCO_2$ [17] and the upper limit of molecular weight to dissolve in $scCO_2$ is assumably 500-1000 g/mol [45], [134]. Increasing temperature above solute melting point may worsen solubility to $scCO_2$, as even if the solute free volume increases, $scCO_2$ density decreases [53]. Hence, CO_2 has polar and nonpolar nature and temperature and pressure needed for $scCO_2$ extraction depend on solute and CO_2 free volume difference and intermolecular interactions [15], [134].

According to McKeen [106], epoxies and acrylates have quite high polarity, whereas silicone and fluoropolymers have low polarity. However, in addition to fluoropolymers and dimethyl siloxane, some

- acrylates,
- methacrylates,
- styrenics,
- olefins and
- free radical initiators

are soluble in $scCO_2$ [15], [135]. In fact, $scCO_2$ is a good solvent for many monomers [25]. Fluoropolymers are the most soluble in $scCO_2$, but they are expensive, often not biodegradable, and hazardous in monomer state [97], [98], [136]. According to Sarbu & al. [97], a combination of 2 monomers with one presenting high chain flexibility, low cohesive energy density, high free volume, and another containing Lewis base functional groups (preferably a carbonyl), can work as a more CO_2-philic substance in lower pressures than either monomer does alone. If the solute, such as paraffin wax, has wide molecular mass distribution, some of the substance may not dissolve during extraction as the longer chains remain in the structure [17].

$scCO_2$ does not dissolve crystalline or crosslinked polymers, but amorphous phases and materials. Therefore, the polarity and polymer structure determine whether $scCO_2$ can be used as a solvent. [24] As $scCO_2$ can act as a solvent for low molecular weight components, instead of crosslinking two monomers creating an interpenetrating network, one monomer could be left uninitiated in a slurry and dissolved with $scCO_2$ [96].

$scCO_2$ is used for extracting oils, that often contain fatty acids like oleic, linoleic, and palmitic acid, that are aliphatic hydrocarbons with good solubility to $scCO_2$, as suggested by Hyatt [45], [137]. According to Hyatt [45], esters (such as in HDDA), alcohols (such as ethanol), halocarbons (such as fluoroethylene), aldehydes, ketones, and short aliphatic hydrocarbons (found in ECC and oils) are soluble in $scCO_2$. Paraffin oil is refined mineral oil, that consists of a complex structure of linear and cyclic paraffins, mainly 15-40 carbon atoms [138]. On the contrary, Hyatt [45] claims that glycol (such as PEG), glycerol, phenols (used in Prusa Azure Blue resin), amides, urethane, urea, and polyhydroxy aromatic substances have poor or non-existent solubility to $scCO_2$. The substances discussed are listed in Table 4.

Table 4: Monomer solubility to $scCO_2$ [45].

Miscible or good solubility	Poor solubility or immiscible
halocarbons	glycol
aldehydes	glycerol
esters	phenols
ketones	amides
alcohols	urea, urethane
aliphatic hydrocarbons up to 20 carbons	polyhydroxy aromatics

The special interaction of CO_2 with carbonyl groups and fluorine atoms may be explained with more exposed surface area of these atoms in molecular structure, for example compared to sterically hindered ether oxygen (found for example in PEG) [98]. It is shown in Figure 31, that a carbonyl group and hydrogen atoms of an alkene are more exposed than the ether oxygen. I.e., fluoroethylene is an alkene with fluorine atoms instead of hydrogen. [136]

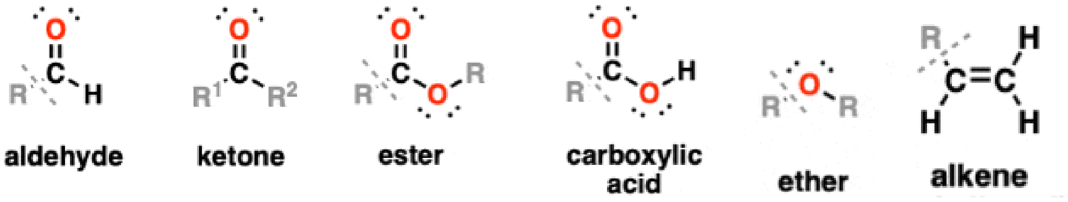

Figure 31: Aldehyde, ketone, ester, and carboxylic acid have carbonyl groups, whereas ether and alkenes do not [139].

Acrylates, methacrylates, and epoxies have carbonyl groups, which could indicate that they can be soluble in $scCO_2$ in uncured state. Based on the hindrance of ether oxygen, PEG or PEGMA would be expected to have lower solubility to $scCO_2$, but PEG has been used for extraction of ceramic parts, as discussed in Chapter 2, and low molecular weight PEG with M_w 400 g/mol has a cloud point with $scCO_2$ at 40.6 °C and 1026.6 bars, as can be seen in Figure 32. [132]

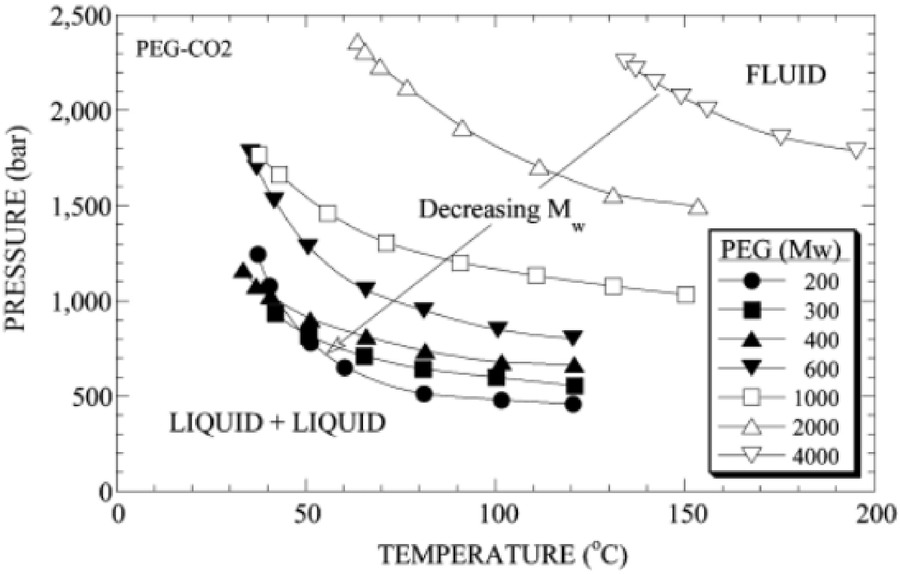

Figure 32: Phase behavior of PEG with different molecular weights in $scCO_2$ [132].

Co-solvent can be used for extraction aid. Co-solvents are used i.e., for caffein extraction of coffee beans with $scCO_2$. Caffein is polar, thus the use of polar co-solvents, such as water, ethanol, or isopropyl alcohol, enhances solubility to $scCO_2$. With a co-solvent, the diffusion coefficient was increased by double and substance removal by 13 % in experiments by Nishikawa & al. [12], once the co-solvent concentration was sufficient. The co-solvent must be chosen according to the solute polarity, as it can worsen the extraction rate if it makes the solvent solubility parameter more different from the solute than it was without a co-solvent [53]. As PEG, used in recipes of this study, is soluble in water, water could be experimented as a co-solvent, but water is only fairly soluble in $scCO_2$ [15]. The effect of ethanol and isopropyl alcohol on the extraction rate of caffein is presented in Figure 33.

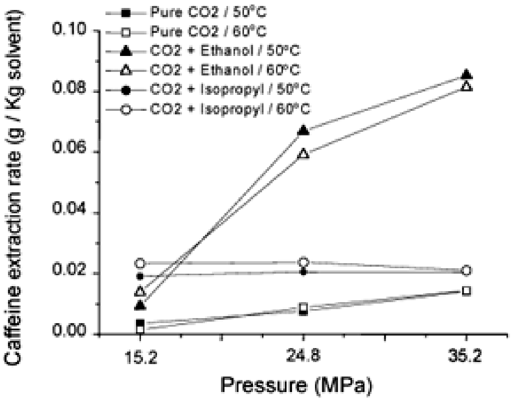

Figure 33: Caffein extraction rate vs. pressure with $scCO_2$ and co-solvents [140].

The changes in dominating forces can be seen as a non-linear behavior with increasing pressure and temperature. In certain pressure, the extraction rate curves obtained in different temperatures, can cross. This means that e.g., in 15.2 MPa with $scCO_2$ with ethanol, the better extraction rate can be obtained in 60 °C temperature, but when the pressure is increased to 24.8 MPa, the rate is faster in 50 °C. [140]

It is also possible that uncured monomers polymerize, or polymers degrade in $scCO_2$, thus process parameters must be optimized. Other chemical reactions often need carefully chosen catalysts. [25] To study if a substance has been fully extracted with $scCO_2$ or to see if any chemical reactions have happened during the extraction, elemental analysis could be conducted. Fourier transformation infrared (FTIR) spectroscopy can be used for this purpose. The basic interpretation of peaks emitted by organic groups are presented in Figure 34.

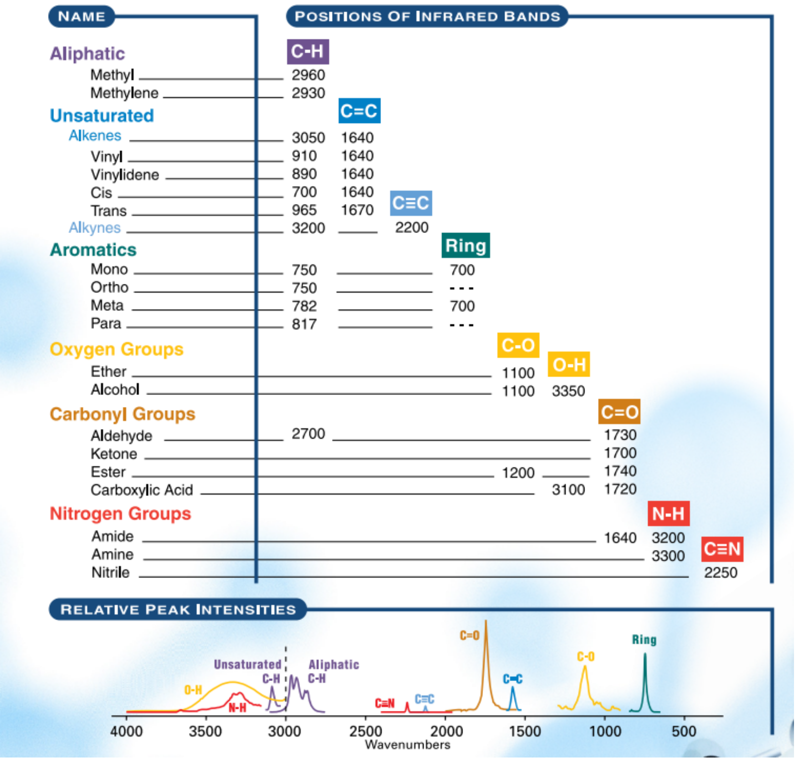

Figure 34: FTIR reference chart for organic functional groups [141].

Fourier transform infrared spectroscopy is used to characterize molecular bonds and furthermore, chemical compositions in a sample. Each molecular linkage vibration has a unique frequency that can be recorded as an interference in an infrared radiation beam in form of absorption of light at a certain energy. [142]

4.2.2 Diffusion

The scCO_2 extraction process consists of solubilization and diffusion (and capillary flow if the binder melts). The diffusion starts from the ceramic part surface. In Figure 35, the solvation of a binder is presented in the beginning of the extraction, at time t_1, and at t_2. At t_1, some of the binder has dissolved from the part surfaces and concentration gradient between the part center and edges is large. At t_2, most of the binder is removed and even if the inner part contains only half on the binder content from initial, there is still some binder left in the outer parts. Thus, the concentration gradient is smaller. Gas diffusion flux during substance extraction depends on solute concentrations, solid density, and diffusion parameters. In addition to solubility, the effective diffusivity through a porous structure needs to be accounted for. Porosity and tortuosity affect the amount, size, and length of flow channels. Diffusivity of a substance depends on the ongoing dissolved substance diffusion itself and substance solubility, that change over the process as binder is removed. [12], [51]

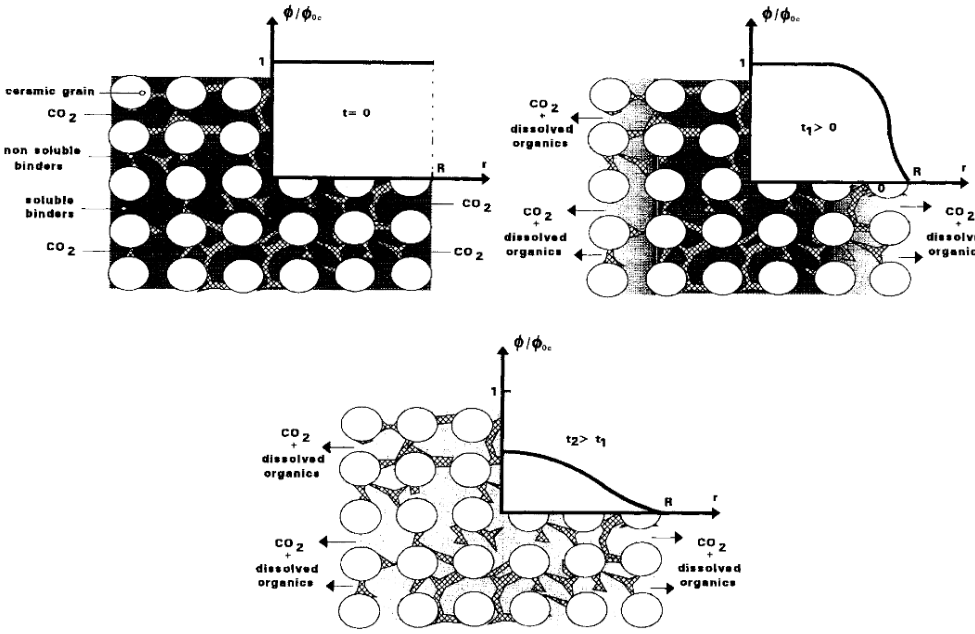

Figure 35: Presentation of remaining polymer content Φ/Φ_0 at $t=0$, $t=t_1$, and $t=t_2$ during solvent extraction [51].

Diffusion rate increases with decreasing pressure or increasing temperature and solubility changes in an opposite manner [52] . When $scCO_2$ flow rate is increased, the equilibrium phase thickness between $scCO_2$ and solute becomes smaller, thus resistance to mass transfer lowers. This results in higher extraction rate, but too high a rate may result in conditions that do not achieve equilibrium; thus, less mass is extracted. When diffusion path is short, resistance to diffusion is also smaller, therefore smaller molecules and parts with smaller dimensions are extracted faster. The extraction is fastest in the beginning, but in the end when less solute is left, the extraction rate decreases. [25]

If the pressure gradient between a polymer surface and $scCO_2$ is too high, the polymer can swell. Like decaffeination of coffee or tea, the swelling effect may be used to extract impurities or non-cured monomers. As the matrix swells, the supercritical solvent diffuses into the structure to dissolve the removable substances and during depressurization it diffuses out, taking the dissolved impurity away. $scCO_2$ can also act as a polymer plasticizer. [55] Especially, interactions between carbonyl and CO_2 can cause swelling in acrylates [135]. Swelling may also be a result of bubble formation and expansion during depressurization phase [20].

5. DENTAL APPLICATIONS

Due to the inability of a body to restore a damaged tooth, dental restorations, such as prostheses and implants, are needed. The most common ways to make dental restorations are pressing or casting pre-sintered blocks that are milled into final shape. Dental implant is an implantable screw plugged into the jawbone. Implant will combine with natural bone and is in contact with blood tissue, and therefore material selection is even more crucial than with prostheses. Prostheses are placed on remaining tooth tissue or as a removable denture on a missing tooth without jawbone contact. Processing methods that cause internal stresses, voids, porosity, agglomerates, or inhomogeneous structure, may lead to mechanical failure. [7] Therefore, understanding details related to biocompatibility and required mechanical properties, are discussed in this chapter.

5.1 Tooth structure and dental restorations

A human tooth consists of a root, crown, and a neck between them. Soft tissue called pulp is the innermost tissue, covered by hard tissues called dentin, cementum, and enamel. Tooth structure is presented in Figure 36. Enamel is the hardest substance in a human body consisting 95 % of rod-shaped hydroxyapatite crystals and prisms, inorganic ions, and minorities of organic matter and water. Its color depends on the degree of mineralization and layer thickness. High mineralization degree produces more transparency, and the yellowness of dentin can be seen through the enamel layer. Enamel does not contain living cells, and therefore, once damaged, is not repaired by the body. Dentin instead can grow in case of abrasion or decay. Dentin contains 70 % carbonated hydroxyapatite and has smaller, less regular, and less crystallized crystals. Tooth root covering cementum keeps the tooth attached. [7]

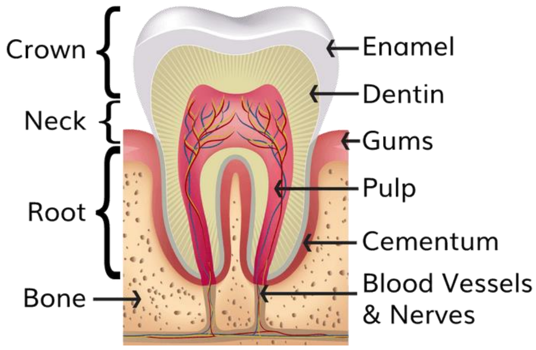

Figure 36: Parts and materials of a human tooth [143].

In dental restorations, color and transparency are important factors. As tooth crowns are multilayer structures, light is reflected, absorbed, and transmitted through the layers differently than in the case of a one-layer structure. Organic compounds in dentin cause yellowish appearance due to reflection of long wavelengths of light, and dentin has more role in the color appearance of a tooth than enamel. Enamel and air have refractive indices quite close to each other, so light is transmitted without major refraction. Due to uneven distribution of tissues, a gradient in color can be seen along an individual tooth surface. [7]

Regardless the importance of aesthetic appearance, the most important purpose of a tooth restoration is to withstand forces related to chewing and cutting food. The main goal is to retain the masticatory function in a way, that the prosthesis shape matches the remaining tooth and the opposite tooth surface. The restoration should be strong and resistant to intraoral ageing, and fatigue, but not cause too much abrasion on the remaining natural teeth. The prosthesis material must be biocompatible. Teeth must withstand stresses and pressure of 20 MPa from multiple directions when cutting, grinding, and crushing food or in occlusion, about 3000 times per day. Dentin is tough and flexible, with hardness in the range of 0.13–0.51 GPa. Enamel is rigid and has hardness in the range of 3–6 GPa. These structures support each other. Because of entangled HA crystal bundles, enamel is tougher than synthetic crystalline HA. [7] Hydroxyapatite has been used as a prosthesis coating due to its similarity to natural bone [125], [144], [145], but its low mechanical properties, low resistance to chemical conditions in a mouth, and porosity make it challenging for HA to be used as the only material for a dental prosthesis using SLA [146]. Mechanical properties of enamel and dentin are presented in Table 5 together with alumina and yttria-stabilized zirconia. [7]

Table 5: Mechanical properties of zirconia, alumina, enamel, and dentin [7], [146]–[149].

Property	**Unit**	**Y-TZP**	**Alumina**	**Enamel**	**Dentin**
Density	g/cm^3	6.0	3.9	2.96	2.1
Grain size	µm	0.3–0.5	1.75	nanorods	nanorods
Flexural strength	MPa	900–1200	350–650	60–90	245–280
Young's modulus	GPa	100–210	210–410	60–120	18–24
Fracture toughness	MPa*m$^{1/2}$	7–9	3.3–5	0.52–1.36	2.0–2.5
Hardness	GPa	5.5–15.8	20–21	3–6	0.13–0.51

A prosthesis may be intracoronal if there is enough tooth left to support the structure. An intracoronal prosthesis is placed in a pit surrounded by the remaining healthy tooth. For a minor pit-like injury, a hardening resin may be used. Direct filling is fast and easy, but the restoration is not long-lasting and as a polymer is not inert, bacteria and viruses may enter the restoration. If intracoronal restoration or filling are not sufficient, an extracoronal replacement is used as a partial or full crown as an onlay on the remaining tooth. [7] Full-ceramic crown and implant post are presented in Figure 37.

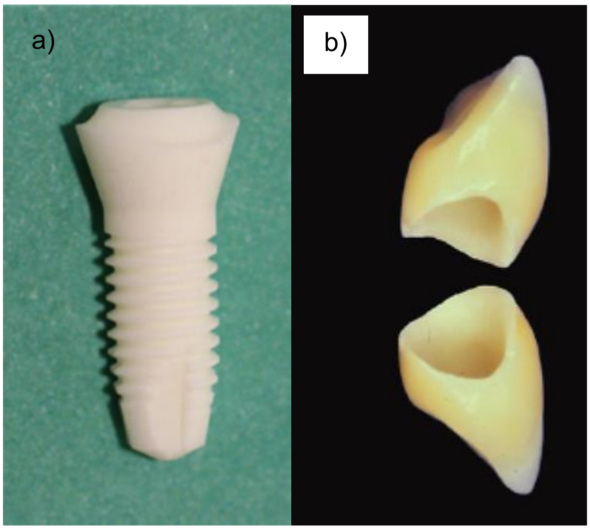

Figure 37: A ceramic tooth implant (a) and tooth crown prostheses (b) [7].

In the case where no natural tooth remains for attaching the crown, an implantable post can be inserted in the root canal and a ceramic crown attached on top of it. Fixed prostheses are supported by the tooth or an implant and attached with adhesion or mechanical interlocking. [7] Due to the clinical requirements for biocompatibility, combined with requirements for mechanical and chemical properties, the material choices for dental restorations are rather limited. Possible material choices and their development are discussed in the next subsection.

5.2 Material property requirements for dental restorations

Prostheses and implants have been made from ceramics, metals, polymers, and their composites. Each class has their own advantages and disadvantages, that are generalized and summarized in Table 6. In dental applications, the use of ceramics over metals, e.g., titanium, is justified with their better chemical inertness, biocompatibility, and natural similarity with human teeth. Current challenges related to ceramic dental prostheses are related to long-term mechanical properties, aesthetical requirements and clinical requirements regarding bacterial accumulation and bone loss. Clinical challenges are often solved with antibacterial coatings. [10] Polymers may exhibit good mechanical properties comparing with dentin and enamel but are still often weak comparing to metals and ceramics. They also age faster than ceramic materials in the harsh oral environment. Metal-ceramics present a combination of good ceramic aesthetics and metals mechanical properties, but also the problem of metal allergy and porcelain chipping. [150]

Table 6: Advantages and disadvantages of the materials used for dental restorations, data from [150].

Material class	**Content**	**Biocompatibility**	**Longterm durability**	**Mechanical strength**	**Fracture toughness**	**Color**	**Translucency**
Traditional ceramics	porcelain	+	+	-	-	+	+
Glass-ceramics	mica, leucite, lithium disilicate	+	+	+	-	+	+
High-strength ceramics	alumina, zirconia, glass-infiltrated	+	+	++	-	+	+
Metal ceramics	metal core with porcelain veneer	-	+	-	+	+	-
Base metals	titanium, nickel, cobalt, chromium	-	+	+	++	-	-
Noble metals	gold, palladium-silver, platinum	+	+	+	++	-	-
Amalgam	silver, mercury, zinc, copper	-	-	+	+	-	-
Polymers	PE, PMMA, PEG, PEEK	+	-	-	-	+	+
Composites	glass ionomers, resin composites	-	-	-	-	+	+

Glass ceramics and porcelain present lower strength properties than high-strength ceramics [10]. Porcelains are brittle and prone to chipping. Therefore, the strongest and most popular ceramic choices for prostheses are alumina (Al_2O_3) and zirconia (ZrO_2), and their composites. For implants, titanium and zirconia are the most popular according to Reinhardt & Beikler in 2014. [7]

As can be seen in Table 6, high-strength ceramics present advantages that are not generally found in polymers or metals: a combination of great aesthetics, mechanical properties, and chemical inertness. Alumina has been used in implants since 1960s, but as alumina has lower resistance to tensile stress and is prone to fractures, it was replaced by titanium and nowadays zirconia is preferred. Development of high purity alumina has led to better results in novel prostheses. Zirconia's fracture toughness (9 MPa*m$^{1/2}$) and bending strength (900–1200 MPa) are superior compared to other bioceramics, and it presents high elastic modulus, low interaction with tissues and bacteria and does not cause allergy like some metals. [7] In Figure 38, aesthetic appearance of metallic and metal-ceramic restoration crowns is presented.

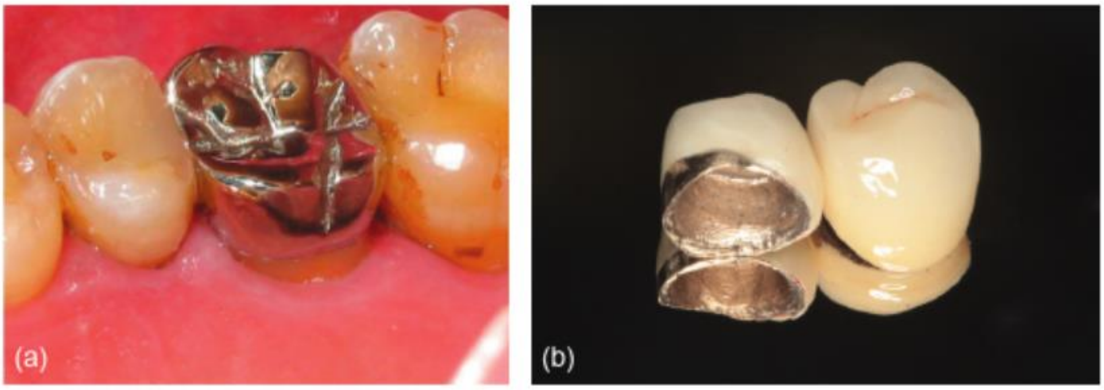

Figure 38: Metallic crown (a) and metal-ceramic crown (b) [7].

Polycrystalline yttria-stabilized tetragonal zirconia, that has been used in bone replacements since 1990s, can change crystalline phase under stress, hindering the propagation of cracks and leading to higher strength. Zirconia implants cause less stresses on the bone than alumina implants, due to the low elastic modulus. Although, zirconia has lower thermal conductivity with high thermal expansion coefficient and is more sensitive to thermal shocks in metal alloy composites. The benefits of both zirconia and alumina may be combined by producing a composite with both materials, but the result is opaque without the desired translucency. [7] In dental applications, the appearance of the ceramic tooth crown is important. Coloring zirconia to right shades and translucency is challenging and therefore the use of zirconia is still developing despite its satisfactory mechanical properties. [44] Regarding mechanical properties, silicon nitride would be an option from other ceramic materials, but due to its grey color it does not fit the aesthetic requirements. [7]

The use of ceramics in dental industry has been limited due to the difficulty of manufacturing parts with minor deviation in properties [150]. Thermal debinding decreases strength and increases the porosity of a ceramic part, which is not suitable for dental crown applications [1], even though for dental implants some porosity is needed to allow bone growth into the implant [7].

To be used in dental applications, the 3-point flexural strength of the material needs to be over 300 MPa to withstand masticatory strains over time and the deviation in properties should be small. Usually, Weibull modulus and Weibull characteristic strength (both describing material characteristic variability and defect uniformity [151]) are used to determine the reliability and homogeneity of the materials. Often it is difficult to evaluate the material long-term durability properties corresponding to a real-life situation, as strains in a human mouth are not uniaxial. Simulation methods, such as finite element model (FEM), are used to predict prosthesis failure behavior. [30]

5.3 SLA in dental applications

Additive manufacturing is seen as a promising alternative to pressing and milling in producing high-strength ceramic restorations. However, the research results comparing ceramic prostheses to metallic ones and AM manufactured prostheses to traditionally milled ones are not straightforward. Especially with ceramics, some studies show that better mechanical properties can be achieved with AM methods [152], some show no significant difference [153] and some, worse properties than conventionally prepared [154]. AM methods also differ from each other significantly and even within one method, process parameters affect the result significantly. [6], [7] For example, robocasting may leave porosity in the ceramic part, resulting in lower strength [155]. With ceramic materials, the final properties are strongly dependent on the whole process from material choice to sintering program, and promising results have been shown as well. The challenge is, that ceramic AM printing is a rather new field that does not have a largely developed industrial market yet and most of the results are limited to scientific research with few parallel samples. [6], [7], [156]

Milling is cost effective and requires little human labor due to automated computer-aided techniques and is therefore popular. Yet, milling also causes microcracks throughout the ceramic surface, and SLA-printed parts are often free of post-process machining and produces little unrecyclable waste, reducing costs required for molds, materials, and tools. If printed with right parameters and processed carefully, SLA can be used to print prostheses that meet dental standards. Tolerances required for dental prostheses are small, and here SLA has advantage over conventional methods, as the lateral resolution of SLA devices for ceramics is about 40–60 µm. [156]–[158] Polymerization shrinkage decreases with increasing ceramic powder content and is generally higher in SLA than in subtractive-manufactured parts. Dental parts need to be dense to allow good mechanical properties, which can be achieved with a high ceramic powder content resulting in a high particle packing density that is crucial prior to sintering. [10], [30]

Dental application characteristics, human teeth, and material property requirements for restorations were discussed in this chapter. The experimental part of this work is presented next. The used materials and methods are described first, followed by results and discussion.

6. MATERIALS AND RESEARCH METHODOLOGY

Azure Blue Tough UV-sensitive resin (Prusa Research) was used for preliminary $scCO_2$ extraction tests. Monomers used in the recipes of this work were difunctional 1,10-Decanediol diacrylate (Sarbio 5201), PEG200 difunctional methacrylate (Sarbio 6201), and trifunctional propoxylated glyceryl triacrylate (Sarbio 5300) from Arkema Sartomer Europe. Binders to be removed with $scCO_2$ were 3,4-Epoxycyclohexylmethyl 3,4-epoxy cyclohexane carboxylate and polyethylene glycol 400 from Sigma Aldrich Co LLC, paraffin oil from GVK Coating Technology Oy and as a diluent EasyClean Resin Cleaner from FormFutura BV. Molecular structures of the Sarbio monomers are presented in Figure 39.

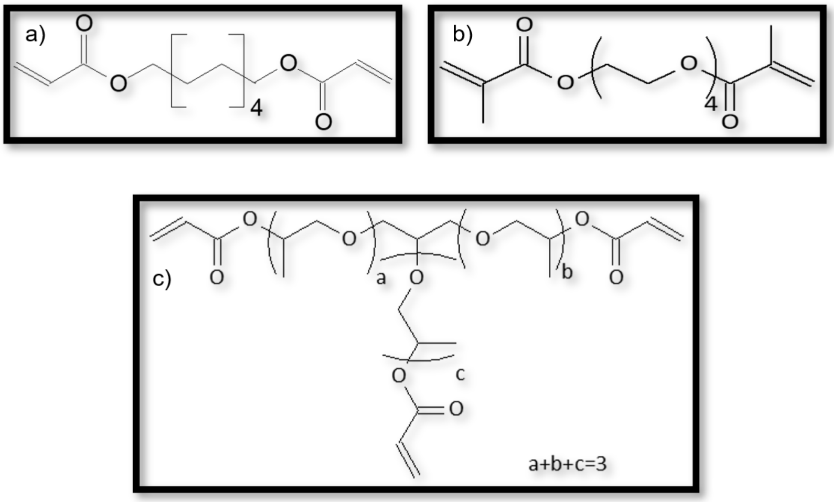

Figure 39: Molecular structures of 1,10-decanediol diacrylate (a), PEG200 dimethacrylate (b) and propoxylated glyceryl triacrylate (c) [159].

As radical photoinitiators, phenylbis(2,4,6-trimethylbenzoyl) phosphine oxide was used for resins without ceramic powder with Prusa SL1S printer, and camphorquinone with ethyl 4-(dimethylamino) benzoate for slurries with Lithoz CeraFab7500. Photoinitiators were provided by Sigma Aldrich.

Alkyloammonium salt Disperbyk-180 was used as a dispersion agent from BYK Altana Chemie GmbH, and SMA6 high purity alumina powder from Baikowski France. The reported particle size distribution of SMA6 was d50 0.23 µm and d100 2.3 µm, and the average specific surface area was 6.3 m^2/g. The substances with purposes and abbreviations used in this thesis are summarized in Table 7.

Table 7: Substances used in the recipes of this thesis, with abbreviations, suppliers, and purposes.

Substance	Abbreva-tion	Supplier	Purpose
1,10-Decanediol diacrylate	DDDA	Sartomer	binder
PEG200 dimethacrylate	PEGMA 200	Sartomer	binder
Propoxylated glyceryl triacrylate	PGTA	Sartomer	binder
3,4-Epoxycyclohexylmethyl 3,4-epoxycyclohexanecarboxylate	ECC	Sigma Aldrich	plasticizer, binder
Polyethylene glycol 400	PEG400	Sigma Aldrich	plasticizer, binder
Paraffin oil		GVK	binder
EasyClean Resin Cleaner		FormFutura	diluent, solvent
Phenylbis(2,4,6-trimethylbenzoyl) phosphine oxide	BAPO	Sigma Aldrich	radical photoinitiator type 1
Camphorquinone	CQ	Sigma Aldrich	radical photoinitiator type 2
Ethyl 4-(dimethylamino)benzoate	A	Sigma Aldrich	co-initiator for type 2
Disperbyk-180, alkylomammonium salt	BYK180	BYK	dispersion agent
Aluminum oxide, grade SMA6	Al2O3	Baikowski	ceramic powder

6.1 General methods

The general procedure with experiments with our own recipes was chemical weighing into opaque plastic bottles, mixing with planetary mill, printing, print washing, weighing, measuring dimensions, optical imaging, $scCO_2$ extraction and observing changes in mass, dimensions, and appearance. In addition, thermal analysis methods and FTIR spectrometry were used to characterize changes.

6.1.1 Sample preparation by SLA

Resin/slurry chemicals were weighed into opaque brown plastic bottles with ±1 % accuracy. Zirconium oxide pearls were added into the bottles for mixing to break agglomerates and photoinitiator crystals. Resins without ceramic powder were mixed for 1 h with 105 rpm speed in a planetary mill and slurries with alumina were mixed for 12 h in a custom ball mill before adding photoinitiators and 1 more hour in the planetary mill after adding initiators.

Printing was done by adding the resin/slurry in the printer resin tank and using a sliced 3D-model for rectangles with 15 mm length, 4 mm thickness and 5 mm height. The printer used for samples without ceramic powder was Prusa SL1S and for ceramic samples

Lithoz CeraFab7500. The printing platform in Prusa SL1S was made of aluminum and in CeraFab7500 it was glass. UV exposure time was chosen according to curing depth measurements (Appendix 4). Once the print was ready, resin samples were washed with Form Futura resin cleaner for 3 min and ceramic samples were dipped in dibasic ester and immersed in ultrasonic bath (Bandelin Sonorex) for 1 min.

Once the samples were dried by blotting with paper, they were weighed (scale Sartorius Quintix613-1S), and their dimensions measured with a micrometer. Stereomicroscopy images were taken with Leica MZ7.5 to observe the color and surface structure of the samples and a scanning electron microscope (Jeol JSM-IT500) was used with 15 kV voltage and with secondary electron and back scattered electron settings. The samples were coated with carbon prior to imaging with SEM.

6.1.2 Curing depth and viscosity

Curing depth was measured by exposing uncured resin to LED light with radiation wavelength of 405 nm and slurries to LED with wavelength 460 nm, and intensity 2.8 mW/cm^2, for a variety of times to draw a slope to count the critical energy and sensitivity.

Viscosity was measured with an Anton Paar MCR 301 rotational rheometer, with a shear rate sweep from 0.1 to 1000 1/s at 25 and 40 °C, using a plate-plate geometry due to scarcity of chemicals.

6.1.3 scCO$_2$ extraction

Thar Technologies Inc. RESS 250 supercritical carbon dioxide apparatus was utilized in the scCO$_2$ experiments of this study. The apparatus has a high-pressure pump that builds CO$_2$ pressure up from the CO$_2$ cylinder. The CO$_2$ then goes through a pre-heater and to the pressure chamber, where the samples are placed in a decanter or another crucible. The preheated CO$_2$ is further heated within the chamber. The system also includes a co-solvent pump. A schematic of the scCO$_2$ system is presented in Figure 40.

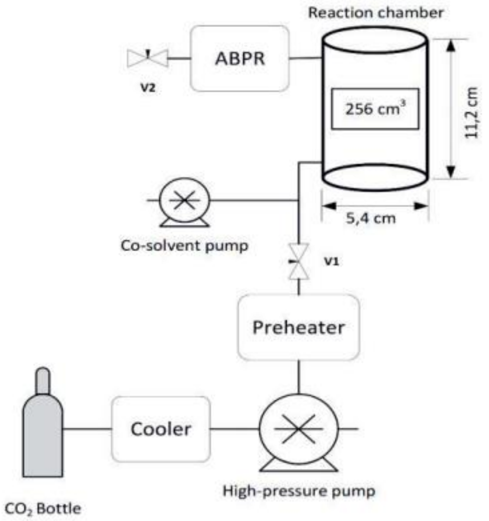

Figure 40: Schematic of Thar RESS 250 $scCO_2$ system [46].

Dynamic CO_2 flow through the test chamber with 5 g/min flow rate was used to circulate the $scCO_2$ through a stainless-steel chamber of 256 cm^3 in volume. The samples were kept in the chamber under $scCO_2$ exposure for 2, 4, 5, or 24 h in 40 °C and 100 bars. Pressurization speed was not controllable as the CO_2 was led to the chamber via a manual needle valve, but the depressurization phase was set to a rate with desired change per minute (6 bar/min) and controlled with an automated back-pressure regulator and needle valves.

6.1.4 Thermal analyses and spectroscopy

To study which substances and in what quantity or temperature left the samples during the $scCO_2$ extraction, a combination of TGA, DSC and Fourier-transformation infrared spectroscopy (FTIR) were used for samples before and after $scCO_2$ extraction. TGA was run with Netzsch TGA 209F3 Tarsus from room temperature to 800°C with 10 K/min heating rate in nitrogen gas atmosphere. DSC was run with Netzsch DSC 214 Polyma from -20 to 200 °C with the same heating rate and gas atmosphere. FTIR scan was taken with PerkinElmer Spectrum 2 with wave number range 500-4000 cm^{-1} with 24 scans.

6.2 Experimental setups

To find out which parameters to use for $scCO_2$ extraction and if substances could be dissolved into $scCO_2$ from an SLA printed part, test runs were first done with a commercial Azure Blue Tough resin from Prusa Research. The samples with 25 mm length, 10 mm height and 5 mm thickness were printed with Prusa SL1S stereolithography printer with 2 s UV-exposure time and washed with Form Futura EasyClean resin cleaner for 3 min, rinsing with water. Azure Blue resin consisted of 40–50 % 4-[4-(4-chlorophenyl)-4-hydroxypiperidin-1-yl]-1-(4-fluorophenyl) butan-1-one, 20–40 % 1,6-hexanediol diacrylate, 3–5% 1-hydroxycyclohexyl phenyl ketone and 3–5 % color pigment [64].

A Taguchi array [160] (Table 8) was made to study the effects of pressure, temperature, time and post-curing regarding changes in sample mass, dimensions or appearance. 3 parallel samples were made for each run and the post-curing was done by drying the sample for 7 min and exposing to UV-light for 40 min with Original Prusa CW1S Curing and Washing Machine.

Table 8: scCO$_2$ extraction test parameters for Azure Blue samples.

Run	Pressure /bar	Time/ h	Temperature/ °C	Post-curing
1	100	2	40	no
2	100	2	40	yes
3	100	24	60	yes
4	100	24	60	no
5	200	2	60	yes
6	200	2	60	no
7	200	24	40	no
8	200	24	40	yes

Based on the theory presented in Chapter 4, uncured 1,10-decanediol diacrylate (DDDA) and ECC monomers, and EasyClean Resin Cleaner were tested in the scCO$_2$ chamber to see if they dissolve and could be used in slurry recipes. Thar RESS250 was used for this purpose with 100 bar pressure, 40 °C temperature, 1,5 h time and 5 g/min CO$_2$ flow. Depressurization rate was set to 6 bar/min. Furthermore, a commercial printed green body from a Lithoz Lithalox HP500 slurry was put into the chamber with same test parameters. Conclusions were drawn from these preliminary tests, which are presented in the next chapter.

To study the solvation ability of scCO$_2$ without challenges followed by adding ceramic powder into the resin, recipes without ceramic powder were tested first. These 8 resin recipes (printed with Prusa SL1S) and slurry recipes including alumina powder (9-10, printed with CeraFab7500) are presented below in Table 9. Part dimensions were changed from the initial commercial Prusa Azure Blue resin tests to ease the adhesion to printing platform and to observe mass removal in parts with smaller thickness. Otherwise, the printing parameters and sample preparation was kept the same for recipes 1-8. The recipe contents were based on previous research and theory discussed in Chapter 4. They were combinations of fast-curing acrylates with different functionalities, and a slowly curing methacrylate to create flexibility. The $scCO_2$ extractable additives were chosen based on assumptions of extraction capability of $scCO_2$.

Table 9: Recipe list for $scCO_2$ extraction testing. DDDA: 1,10-decanediol diacrylate, PEGMA200: PEG200 dimethacrylate, PGTA: propoxylated glyceryl triacrylate, ECC: 3,4-Epoxycyclohexylmethyl 3,4-epoxycyclohexanecarboxylate, PEG: polyethylene glycol, Al_2O_3: aluminum oxide.

	MONOMERS/ vol-%				INERT ADDITIVES/ vol-%			CERAMIC/ vol-%
Recipe	**DDDA**	**PEGMA200**	**PGTA**	**ECC**	**PEG**	**Easy-Clean**	**paraffin oil**	**Al_2O_3**
1	35		35	30				
2	42.5	5	42.5			10		
3	85	5			10			
4	75	5					20	
5	75	5			20			
6	37.5	5	37.5		20			
7	40		40		20			
8	25		25	30	20			
9	75	5			20			50
10	25		25	30	20			50

The monomers + additives were weighed based on volume percentage to produce a resin of 50 ml volume. In the mixing of ceramic slurries, the ceramic powder was weighed to correspond to the desired volume percentage based on theoretical density and dispersion agent was added according to 2 w-% of ceramic powder content. All recipes contained 3 w-% radical photoinitiator of the total monomer + inert additives mass. ECC was left uninitiated.

To compare the ability of water and $scCO_2$ to dissolve PEG, recipe 5 sample was immersed in water decanter for 48h. Recipe 6 sample was tested in 80 bar and 100 bar to study the importance of supercritical conditions in the test chamber. All recipes except recipe 4 were tested in $scCO_2$ for 24 h. In addition, recipes 5 and 8 were tested for 2 h and recipe 8 with the most promising results was tested further for 5 h and with ethanol and EasyClean as co-solvents. The conducted $scCO_2$ experiments for each recipe are listed in Table 10.

Table 10: scCO2 experiments list. All were done in 100 bar and 40 °C except the 24 h test in 80 bars and water immersion in atmospheric pressure and room temperature.

Recipe	2 h	5 h	24 h	2h with ethanol	4h with ethanol	2h with Easy-Clean	2h with IPA	24h 80 bar	48h water immersion
1			x						
2			x						
3			x						
4	x								
5	x		x						x
6			x					x	
7			x						
8	x	x	x	x	x	x			
9	x	x	x	x					
10	x	x	x	x			x		

The co-solvent flow was set to 0.2 ml/min and CO_2 flow to 5 g/min. Based on changes in sample mass, dimensions, density, TGA curves and FTIR results, conclusions were made on which substances had been removed from the structure with $scCO_2$. TGA and DSC were analyzed to find out, if residuals of those substances were left in the sample structures. Further, cracks and shape deviation were observed with optical microscopy.

The recipes with alumina (9 and 10) were developed based on the results from resins 5 and 8, which had the most promising results regarding mass extraction, delamination, and faster extraction with co-solvent. Alumina was chosen for the studies instead of zirconia, to avoid additional printability challenges of zirconia, due to light interaction. Recipes 9 and 10 with alumina powder were studied with similar analysis methods as the resins 1–8.

7. RESULTS AND DISCUSSION

Experimental test results are presented and analyzed in this chapter. Results from the preliminary tests done with commercial Prusa resin, Lithoz Lithalox HP500 green body and pure monomers are presented first, followed by results from actual resin and slurry development. TGA, FTIR, and physical change data for recipes 1–10, which led to conclusions of substances suitable for $scCO_2$ debinding of ceramic SLA prints, are discussed after preliminary test results. Challenges with variables and error sources are discussed in the end of the chapter.

7.1 Preliminary tests

There was no mass loss caused by $scCO_2$ exposure in the post cured Prusa Azure Blue samples (runs 2, 3, 5 and 8). In fact, the post cured samples only gained mass and swelled during the $scCO_2$ extraction tests. In the case of runs 2, 3, 5, and 8, after the $scCO_2$ treatment followed by several days' observation, sample mass decreased back towards the initial mass. The only samples with mass decrease of 5–6% were samples from runs 4 and 7, which had been in the $scCO_2$ chamber for 24h in either elevated temperature or pressure compared to the other tests. Even these samples swelled at first due to the $scCO_2$ extraction. The most significant changes in Azure Blue samples were seen when changing the $scCO_2$ test time from 2 h (runs 1 and 6) to 24 h (runs 4 and 7), these test times were chosen to be used in the following tests with our own resin recipes. The changes in mass and sample length in environmental conditions after test runs 1–8 are presented in Figure 41 a. The graphs for average change of thickness *b* and height *h* can be found in Appendix 1.

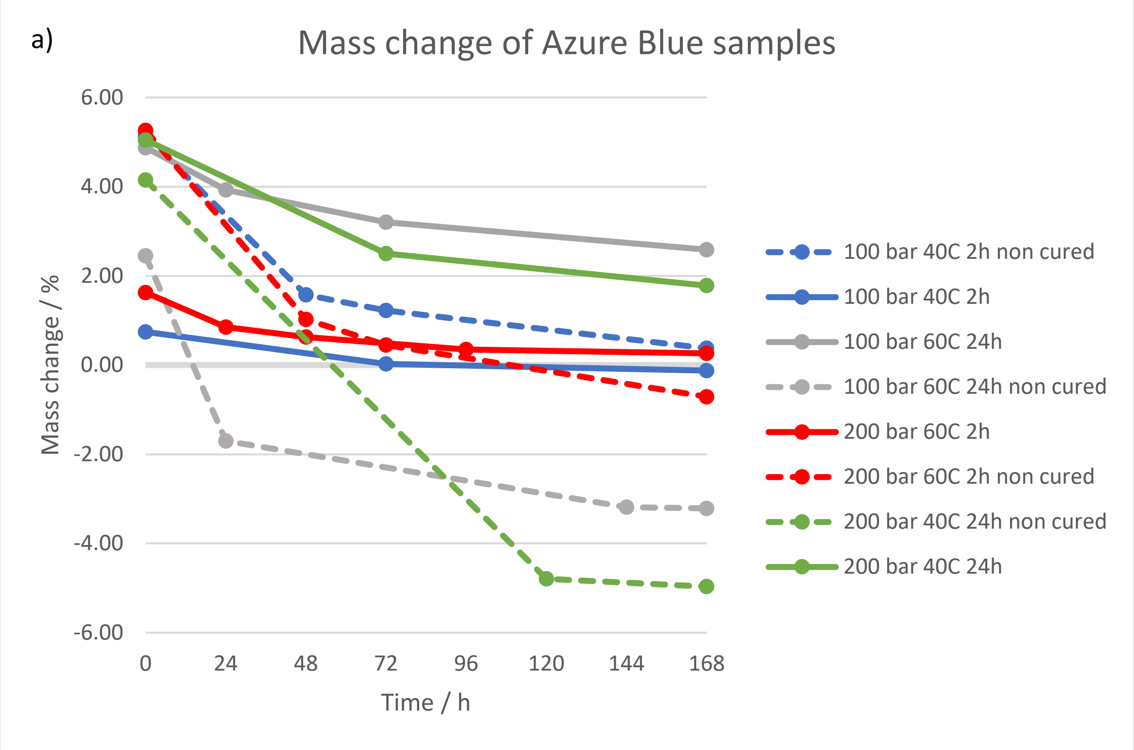

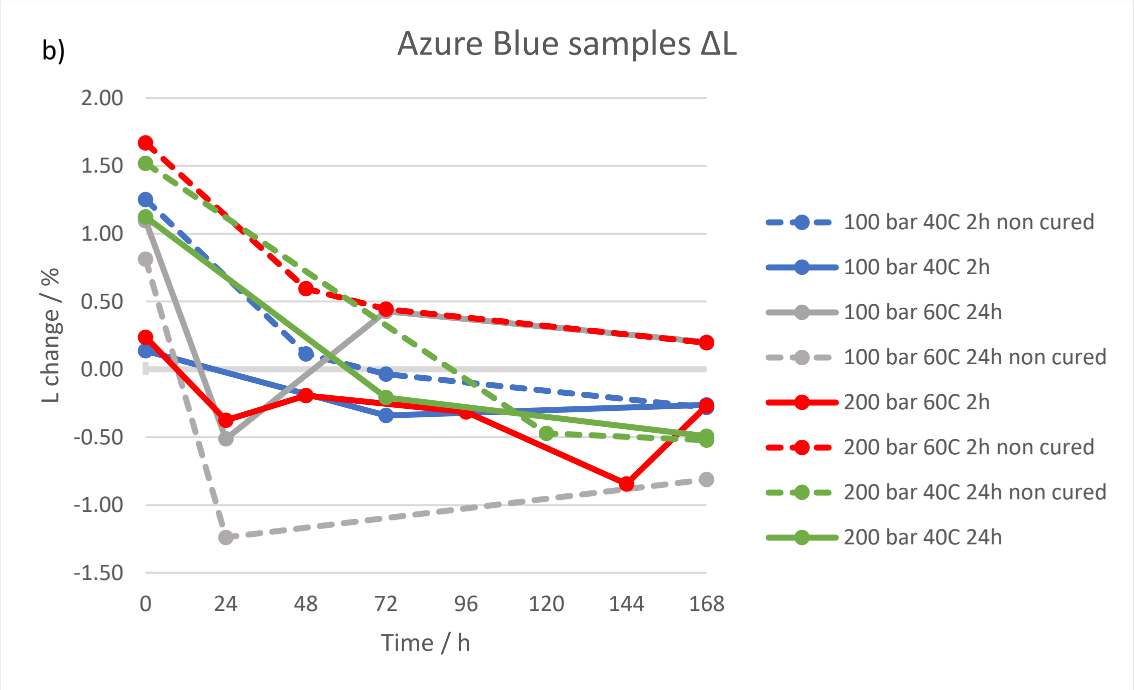

Figure 41: a) mass change of non-post cured and post cured Azure Blue samples after $scCO_2$ exposure and b) length change of non-post cured and post cured Azure Blue samples after $scCO_2$ exposure. t=0 is the mass and length immediately after $scCO_2$ exposure.

The shrinkage of Azure Blue samples was also largest for samples of runs 4 and 7, as seen in Figure 41 b. Non-post cured samples swelled more than post cured samples. As already stated in the Introduction, all non-post cured Azure Blue samples (runs 1, 4, 6 and 7) were cracked after $scCO_2$ testing, whereas the post cured samples (runs 2, 3, 5 and 8) were not. Post-cured samples only swelled, and the non-cured ones cracked badly, even if only small amount of mass was lost with exposure time of 24 h in either elevated pressure or temperature compared to other samples (Figure 42). The difference in appearance between non-post cured and post cured samples, both for 24 h in 200 bar and 40 °C, are presented below.

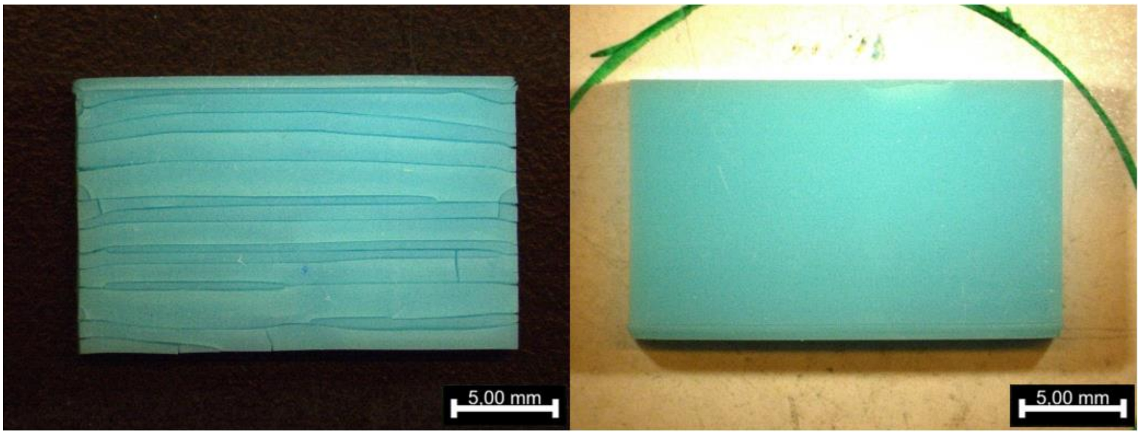

Figure 42: Microscopy images of non-post cured Azure Blue sample from run 7 (left) and post cured sample from run 8 (right).

The substances used in Azure Blue commercial resin did not leave the structure with $scCO_2$ efficiently despite major swelling, even though the average molecular mass of those substances is similar to the ones used in our own slurries, all between 200 and 430 g/mol [109], [161]–[166]. These results of Azure Blue test runs indicate that the substances used in the Azure Blue resin are not highly soluble to $scCO_2$, however the solubility can slightly be modified by changing the temperature and pressure of $scCO_2$. Thus, resin recipe development is important to be extractable with $scCO_2$. This conclusion was used to develop the recipes presented in Table 9.

In addition, non-cured DDDA, ECC and FormFutura EasyClean were tested in $scCO_2$. DDDA and ECC showed -40% and -43% decrease in mass after the initial 1.5h $scCO_2$ extraction, respectively (Table 11). ECC foamed vigorously in the very end of the depressurization back to atmospheric pressure at 6 bar/min rate. A Lithoz Lithalox HP500 green body was also tested with $scCO_2$ extraction.

Table 11: $scCO_2$ extraction test mass changes after 1.5 h in 100 bar and 40 °C.

Substance	Mass decrease / %
DDDA	-40
ECC	-43
FormFutura	-100
Lithoz Lithalox HP500 green body	-0.2

FormFutura EasyClean resin cleaner dissolved totally, but Lithoz Lithalox HP500 green body sample did not dissolve. It cracked throughout the structure (Figure 43).

Figure 43: Lithoz Lithalox HP500 green body sample after 1.5h in 100bar and 40°C in scCO_2.

The above-described DDDA and ECC monomer and Lithalox HP500 green body samples were taken to FTIR to study if major chemical changes had happened during scCO_2 extraction. The FTIR results for all samples before and after scCO_2 extraction seemed similar (Figure 44), indicating that no major molecular bond changes, and therefore no major chemical reactions, happened during the extraction with these substances. FTIR results of DDDA and Lithoz green body are listed in Appendix 1.

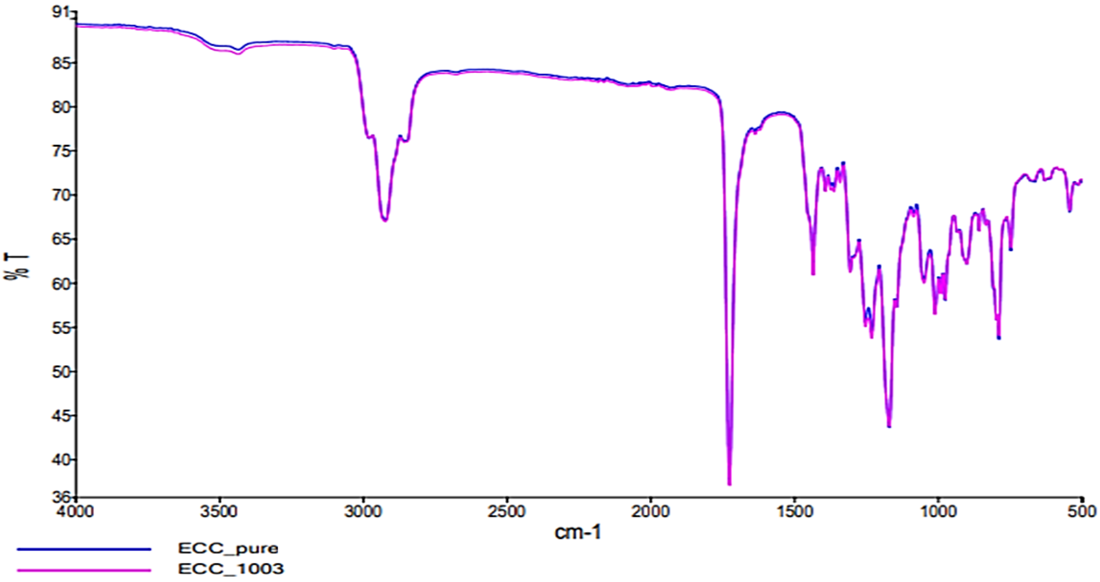

Figure 44: FTIR transmittance graphs of ECC before and after 1.5 h $scCO_2$ extraction test.

Based on the mass loss and FTIR results, it was concluded that uncured DDDA, ECC and FormFutura EasyClean resin cleaner are soluble in $scCO_2$ and could be used as components in the recipes, and that a cured Lithoz Lithalox HP500 was not soluble in the conditions used and that the $scCO_2$ treatment can cause cracks to the part structure.

7.2 Studies of the importance of supercritical conditions

Recipe 6 was tested with $scCO_2$ for 24 h at 40 °C and 80 bars and at 40 °C and 100 bars. The sample mass decreased 2.79 % in 80 bars and 20.89 % in 100 bars. The difference in sample appearance is presented in Figure 45. The sample extracted with 100 bars was cracked, but other recipes could be printed and extracted without causing cracks, as will be discussed later in this chapter. This result of significant increase in mass extraction with 100 bars vs. 80 bars indicates that ensuring supercritical conditions and sufficient pressure for higher solvent solubility are crucial to succeed with the extraction process.

Figure 45: Microscopy images of recipe 6 (37.5 vol-% DDDA, 5 vol-% PEGMA200, 37.5 vol-% PGTA, 20 vol-% PEG) after 24 h scCO$_2$ exposure in 80 bars (up) and 100 bars (down) at 40 °C.

Recipe 5 sample with 20 vol-% PEG content was immersed in a decanter filled with water for 48 h. The sample mass decreased 5.62 % during this test and within the scCO$_2$ extraction of same recipe sample for 2 h at 100 bars and 40 °C, the mass decrease was 15.76 %. This 15.76 % is 63-79 % of the total PEG content in that recipe, assuming that most of the 5 vol-% PEGMA200 stays in monomer state and is also extractable with scCO$_2$.

Dugauguez [167] was able to remove 80–90% of PEG content with water immersion of 48 h on nickel-chrome superalloy component produced by metal injection molding, so the process seems to be system and material dependent. From these tests it may be concluded that the supercritical conditions speed the solvation process of certain substances into CO$_2$, and that supercritical conditions may have not been present at 80 bars due to uncertainty in measuring the pressure inside the chamber. Another possibility for higher mass extraction in 100 bars may be due to the difference in scCO$_2$ density, which increases significantly when pressure is increased from 80 bars to 100 bars, as was discussed in subsection 2.2.1 in Figure 9.

In many scCO$_2$ extraction tests [12], [20], [26], the pressure and temperature used was higher than in the experiments of this study. The temperature and pressure for tests in this study would be the lowest ensuring supercritical chamber conditions, and therefore most economical and safe to use, and if needed they could be increased later. In fact, in many earlier studies the pressure and temperature used were about 200–400 bars and 50–150 °C [9], [10], [17], [23], [24], so an interesting comparison between required conditions could be done. Dugauguez [167] used 20 bar per minute for depressurization rate to avoid part damage, which is much faster than the depressurization rate (6 bar/min) used in this study.

7.3 Visual inspection

Figure 46a-j shows the visual condition of printed samples treated with $scCO_2$. Recipe 1 could not be printed without cracks and severe delamination with same printing parameters as the other recipes or even with a double light exposure time. The result was fully delaminated and cracked after the $scCO_2$ exposure. Also, recipe 2 which contained EasyClean resin cleaner as an additive delaminated badly during $scCO_2$ extraction, as seen in Figure 46.b. Resins from recipe 3 and 4 resulted in badly cracked results with the chosen printing parameters as well, as seen in Figure 46.c and 47.d. Therefore, these 4 recipes were excluded from further experiments with FTIR and printing with ceramic powders. DSC and TGA was done to recipe 4 to analyze which substances were extracted with $scCO_2$. More optical microscopy images of samples can be found in Appendix 2.

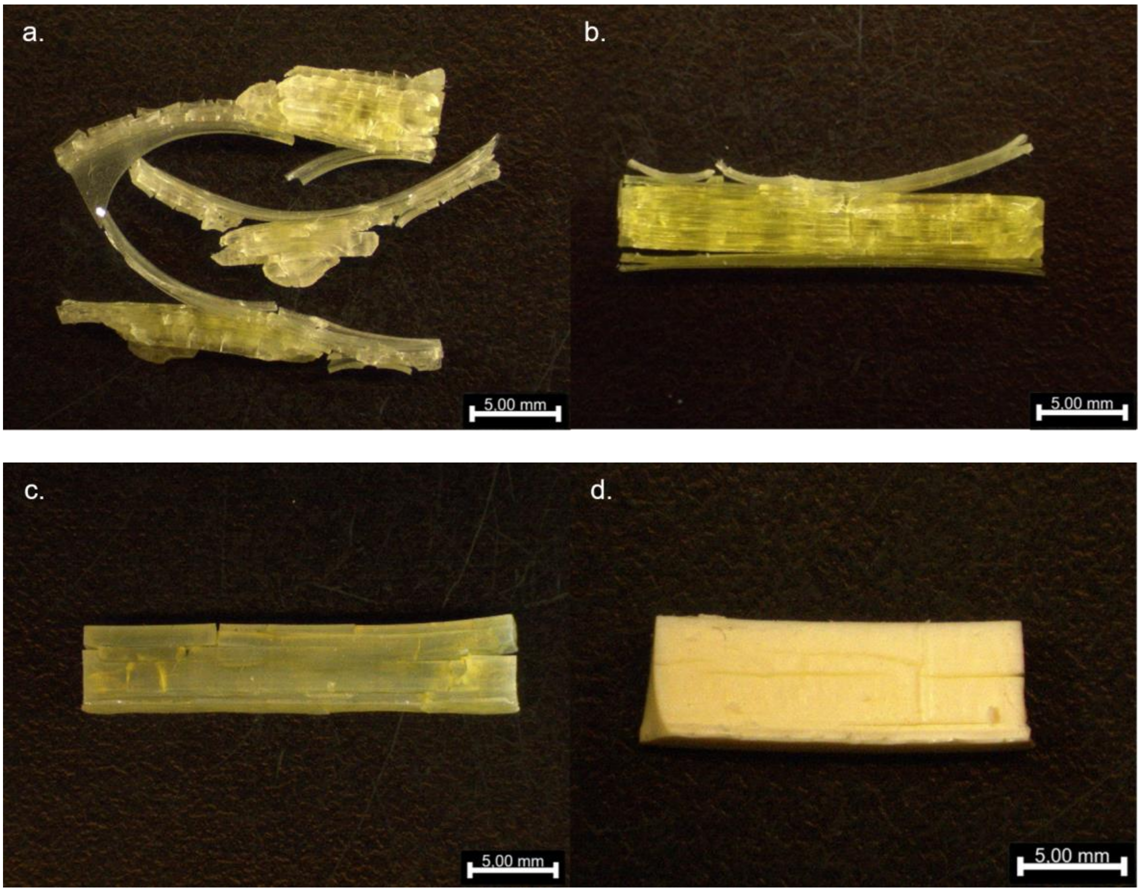

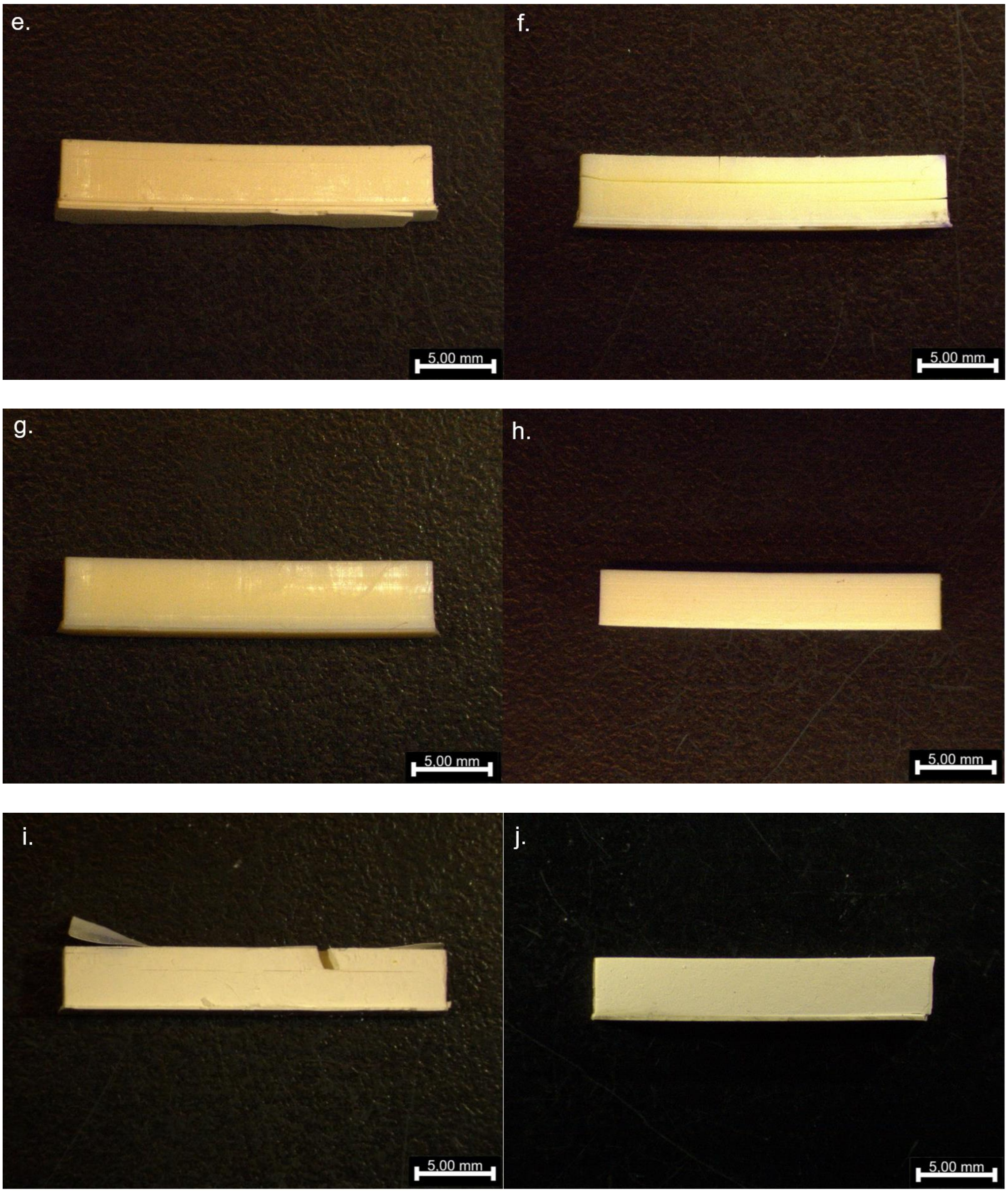

Figure 46: Microscopy images of a) recipe 1, b) recipe 2, c) recipe 3, d) recipe 4, e) recipe 5, f) recipe 6, g) recipe 7, h) recipe 8, i) recipe 9 and j) recipe 10. Recipes 1-3 and 5-10 after 24h and recipe 4 after 2 h $scCO_2$ extraction test in 100 bar and 40 °C.

Polymeric recipes 5, 7 and 8 (Figure 46 e, g and h) were printed without cracks or delamination. Recipe 10 containing DDDA, ECC, PGTA and PEG (as recipe 8) and alumina seemed to be the most suitable with the tested printing and extraction parameters, as no cracks were seen in the samples after 2 h and 5 h (Figure 77 a and b), or 24 h $scCO_2$ exposure (Figure 46 j). The absence of cracks is better seen in microscopy images with larger magnification in Figure 47 a and b.

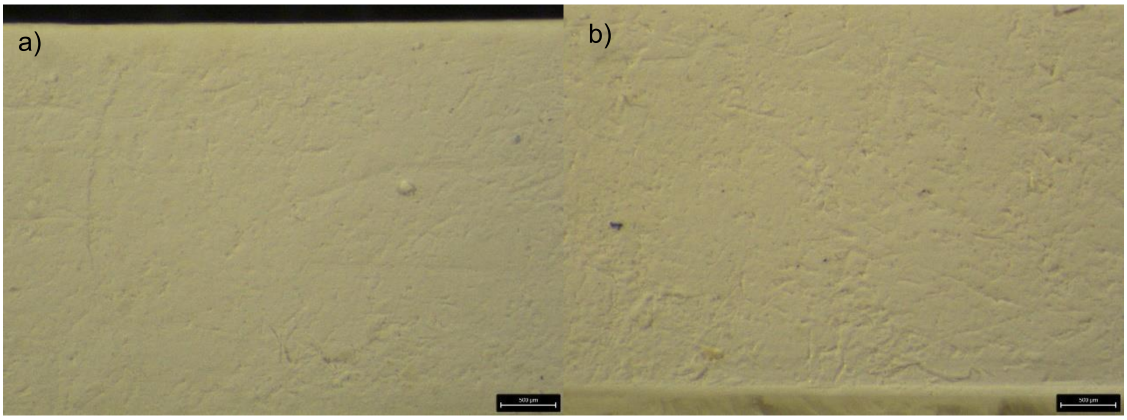

Figure 47: Microscopy images of recipe 10 (50 vol-% alumina, 12.5 vol-% DDDA, 12.5 vol-% PGTA, 15 vol-% ECC, 10 vol-% PEG) after a) 2 h scCO$_2$ exposure, 85x magnification and b) 24 h scCO$_2$ exposure, 85x magnification.

Recipe 9 with 50 vol-% (80 w-%) alumina was also printed with Lithoz CeraFab7500 and samples were exposed to scCO$_2$ for 2, 5 and 24 h. The appearance of recipe 9 after 5 h scCO$_2$ extraction can be seen in Figure 76 in Appendix 2, but a better view of the closeup is presented in Figure 48 a and b. These samples had some cracks, but it is also visible from the notches pointed with an arrow in Figure 48a that the printing process has not been completely successful, and parameter optimization should be done in further experiments.

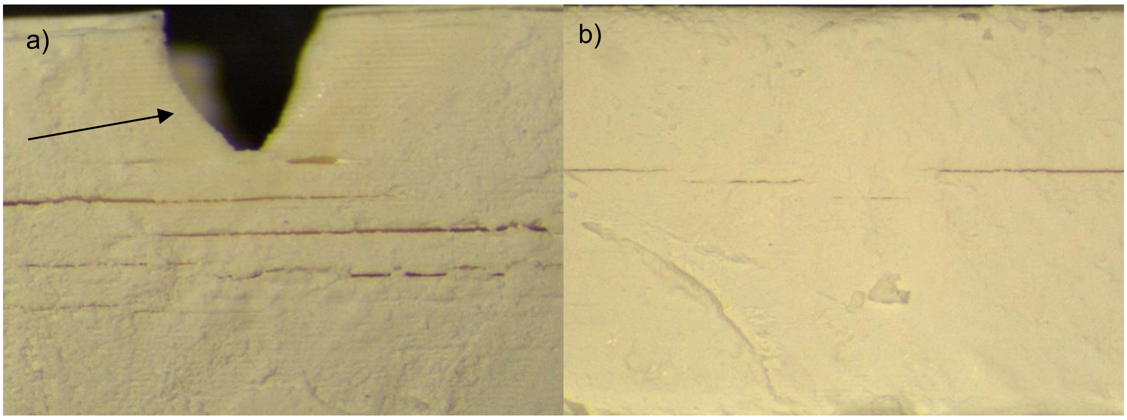

Figure 48: Microscopy images of recipe 9 (50 vol-% alumina, 37.5 vol-% DDDA, 2.5 vol-% PEGMA200, 10 vol-% PEG) a) after 2 h scCO$_2$ exposure, 107x magnification and b) after 24 h scCO$_2$ exposure, 85x magnification.

PEG (and ECC) acted as a plasticizer in the recipes. The difference between recipes 3 (10 vol-% PEG) and 5 (20 vol-% PEG) are presented below in Figure 49 a before and Figure 49 b after 24 h exposure to scCO$_2$ in 100 bars and 40 °C. Recipe 5 had no visible cracks, whereas recipe 3 delaminated already before testing. The opacity generated during the scCO$_2$ extraction may be a result of different light diffraction due to porosity changes [161]. Based on this observation, higher amount of PEG reduced delamination in recipe 5.

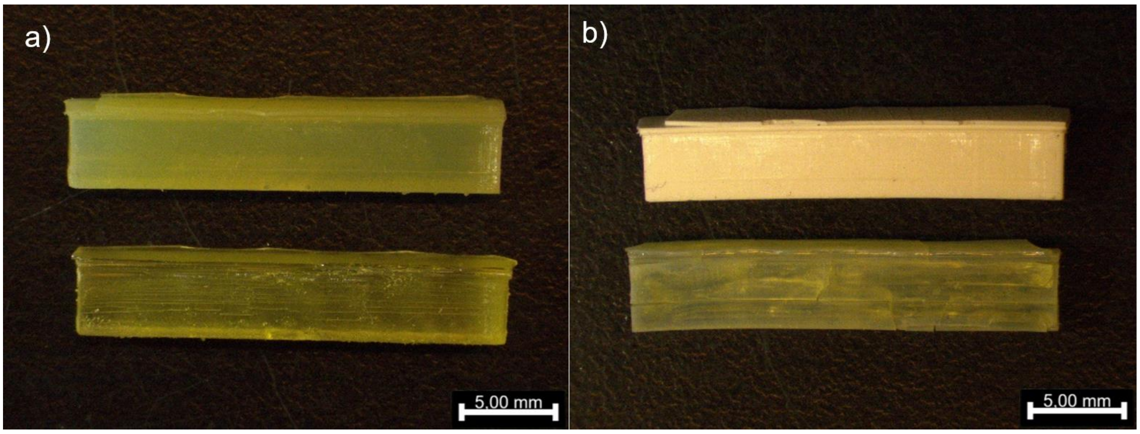

Figure 49: Microscopy images of recipes 3 (85 vol-% DDDA, 5 vol-% PEGMA200, 10 vol-% PEG) and 5 (75 vol-% DDDA, 5 vol-% PEGMA200, 20 vol-% PEG) a) before $scCO_2$ extraction, recipe 5 with PEG 20% up and recipe 3 with PEG 10% down. b) after 24h $scCO_2$ extraction, recipe 5 with PEG 20% up and recipe 3 with PEG 10% down.

Recipe 6 (37.5 vol-% DDDA, 5 vol-% PEGMA, 37.5 vol-% PGTA, 20 vol-% PEG) print was also cracked after 24 h $scCO_2$ extraction. Recipes 5, 7, and 8 maintained their shape without cracks after 24h exposure to $scCO_2$. The greatest dimension decrease between different recipes was observed in recipe 8, which also had the greatest mass loss. Their appearance are presented in Figure 50 and numerical changes in mass and dimensions are listed in the next subsection. It seems that crack-free prints with the chosen process parameters are easier to produce with a recipe that has a combination of fast and slow-curing monomers, or a larger amount of uninitiated/uncured plasticizer (PEG, ECC, paraffin oil).

Figure 50: Microscopy image of recipes 5 (75 vol-% DDDA, 5 vol-% PEGMA200, 20 vol-% PEG) (a), 7 (40 vol-% DDDA, 40 vol-% PGTA, 20 vol-% PEG) (b) and 8 (25 vol-% DDDA, 25 vol-% PGTA, 30 vol-% ECC, 20 vol-% PEG) (c) samples after 24h $scCO_2$ extraction.

Appearance of the samples after different exposure times to $scCO_2$ was compared with recipe 8. The changes in dimensions and appearance can be observed comparing the samples printed with the same resin recipe and after exposing them to $scCO_2$ for 2, 5 and 24 h (Figure 51). The extraction starts from the sample surface as was discussed in Subsection 4.2.2, and the sample warps if exposure time is too short to extract all or most of the soluble substances. All the samples have been placed in the crucible for $scCO_2$ extraction in similar direction; the surface attached to printing platform facing the crucible bottom (pointed with a red arrow in Figure 51). This, together with substance extraction starting from the surfaces of the part may cause the bending seen in Figure 51. The bending is not seen to the same extend in recipes 9 and 10 samples which contain ceramic powder (Figure 46 i–j).

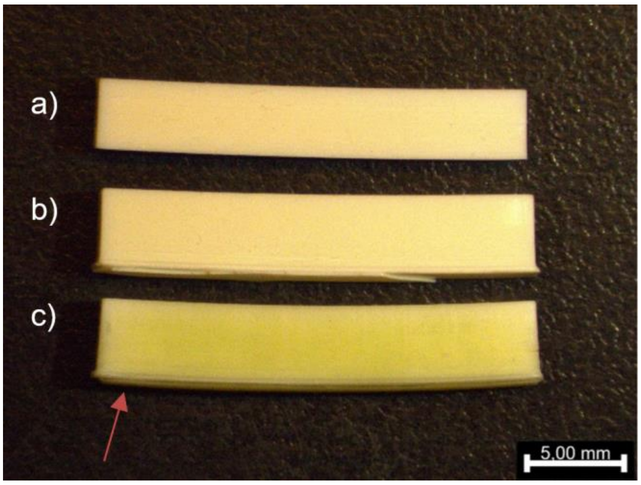

Figure 51: Recipe 8 (25 vol-% DDDA, 25 vol-% PGTA, 30 vol-% ECC, 20 vol-% PEG) after a) 24h, b) 5h and c) 2h exposure to $scCO_2$. The red arrow indicates the surface placed against sample crucible inside the CO_2 chamber during extraction.

The changes in density based on mass and dimension loss (next subsection) indicated that there could be some porosity or voids left in the structure of $scCO_2$-exposed samples. This was examined with optical stereomicroscopy and scanning electron microscopy from fracture surfaces of the samples. However, no porosity or voids were detected in the optical microscopy images (Appendix 3) and the presence of porosity could not be confirmed based on the SEM images taken from fracture surfaces of recipe 5 samples. In images taken from the recipe 8 sample outer surface, pits and grooves were seen. Further conclusions based on the SEM images (Appendix 4) could not be made, as it was not clear if the pattern was caused by the light source in printing or something else. This could be studied further with an SEM with better resolution and samples containing ceramic powder, which has more interactions with the electron beam used in SEM imaging, than polymers.

However, the layer delamination in recipe 9 and its' absence in recipe 10 sample could be seen in the fracture surface images presented in Figure 52 below. The smoothness of recipe 10 fracture surface indicates, that the printing has been successful and there is likely sufficient bonding between print layers in order to avoid cracks in further thermal debinding step.

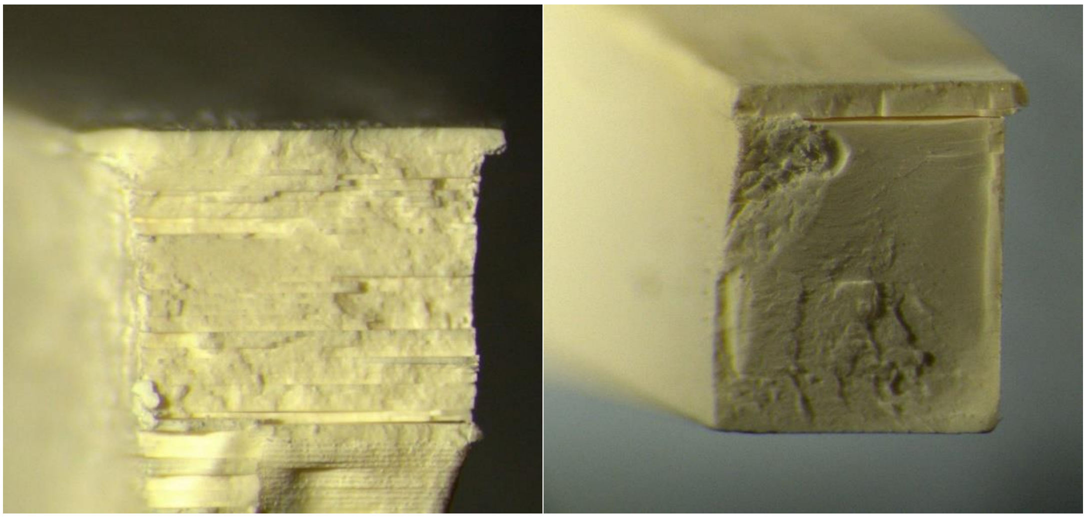

Figure 52: Recipe 9 (50 vol-% alumina, 37.5 vol-% DDDA, 2.5 vol-% PEGMA200, 10 vol-% PEG) (left) and recipe 10 (50 vol-% alumina, 12.5 vol-% DDDA, 12.5 vol-% PGTA, 15 vol-% ECC, 10 vol-% PEG) (right) fracture surface after 24h exposure to $scCO_2$. 64x magnification.

As a conclusion based on sample appearance, the development of polymeric recipe 8 into ceramic recipe 10 lead to the best printing results without visible delamination. The polymeric recipe 5 print result was also crack free, but delamination was seen in recipe 9 print that was based on recipe 5. Recipe 7 could be tried with a ceramic powder in the future.

7.4 Mass and dimension changes

The recipes 2-8 listed in Table 9 and further recipes 9 and 10 based on recipes 5 and 8 were developed considering the observation that both cured and uncured monomer components are needed to remove substances while a cured polymer network remains in the part holding its' 3D shape. Recipe 1 was too deformed after printing to measure dimension changes, as seen in the previous subsection. Thus, this recipe was excluded from mass and dimensions analysis.

To produce parts without cracks and to choose the right printing parameters, especially when changing the printer from Prusa, used for polymeric resins, to Cerafab7500 used for ceramic powder filled slurries, the curing depths of all recipes and viscosity of recipes 5, 8, 9, and 10 were measured prior to printing. An additional batch of recipe 9 with 25 vol-% alumina instead of 50 vol-% was also prepared for viscosity measurements and used in the comparison with recipe 9 with 50 vol-% alumina. As can be seen in Figure 53, recipes 5 and 8 without ceramic powder had lower viscosity than recipes 9 and 10 with alumina, as expected. Even though the alumina powder filled recipes 9 and 10 have a viscosity that is much larger than resins without alumina powder, they were still approximately 10 times lower than the viscosity of Lithoz Lithalox HP500. Recipes 8 and 10 contain ECC, which has a viscosity higher than acrylates DDDA and PGTA, thus the viscosity of resin 8 was higher than resin 5. However, the same difference was not seen in slurries 9 and 10.

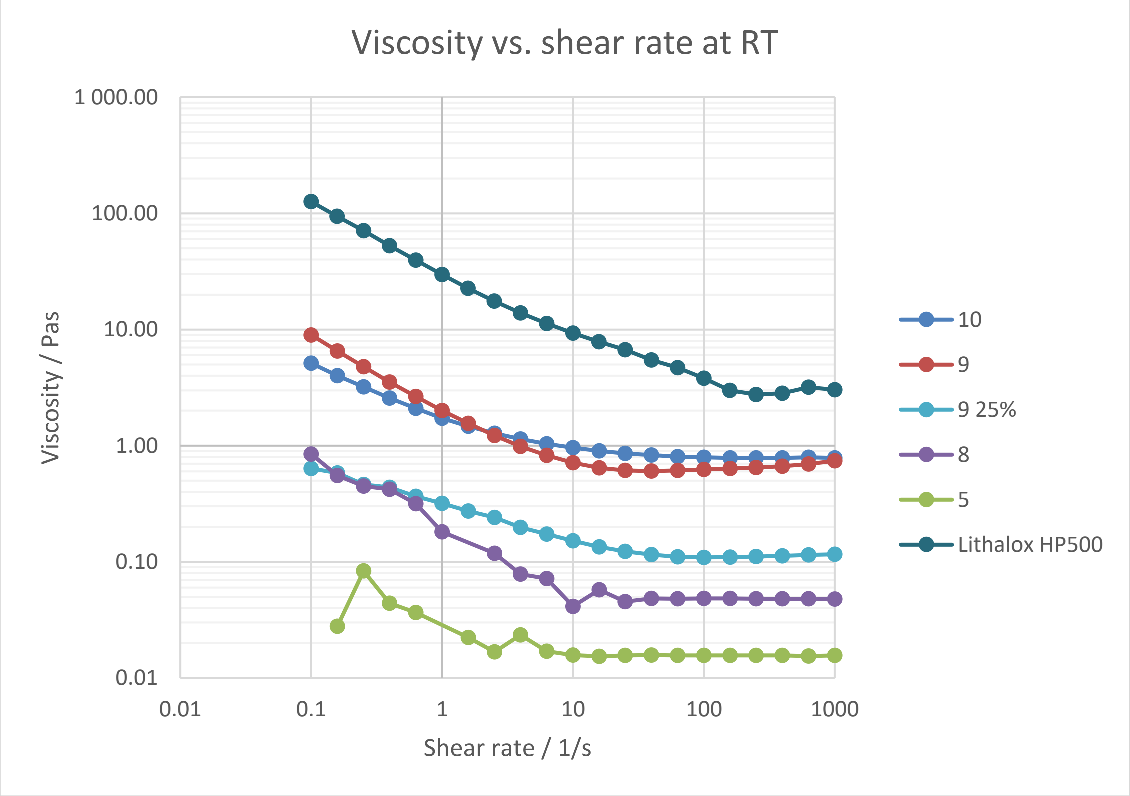

Figure 53: Rotational rheometer viscosity vs. shear rate data obtained from recipes 5 (75 vol-% DDDA, 5 vol-% PEGMA200, 20 vol-% PEG), 8 (25 vol-% DDDA, 25 vol-% PGTA, 30 vol-% ECC, 20 vol-% PEG), 9(50 vol-% alumina, 37.5 vol-% DDDA, 2.5 vol-% PEGMA200, 10 vol-% PEG), 10 (50 vol-% alumina, 12.5 vol-% DDDA, 12.5 vol-% PGTA, 15 vol-% ECC, 10 vol-% PEG), Lithoz Lithalox HP500, and an additional batch of recipe 9 with 25 vol-% alumina.

Recipe 9 seems to have shear-thinning behavior, with apparent thickening at high shear rates due to slippage, which is typical for rotational rheometer studies with low-viscosity slurries. [32] The same is not seen in recipes 5, 8 or 10. As expected, the slurry 9 with only 25 vol% alumina had lower viscosity than the recipe with 50 vol%.

The effect of heating the slurry to 40 °C was studied with the same rotational rheometer device. It can be seen in Figure 54, that the viscosity can be lowered by heating, as the viscosity for recipes 9, 10 and Lithalox HP500 were lower for each recipe slurries in 40 °C than room temperature. Nevertheless, heating may create other challenges, such as polymerization of monomers prior to printing.

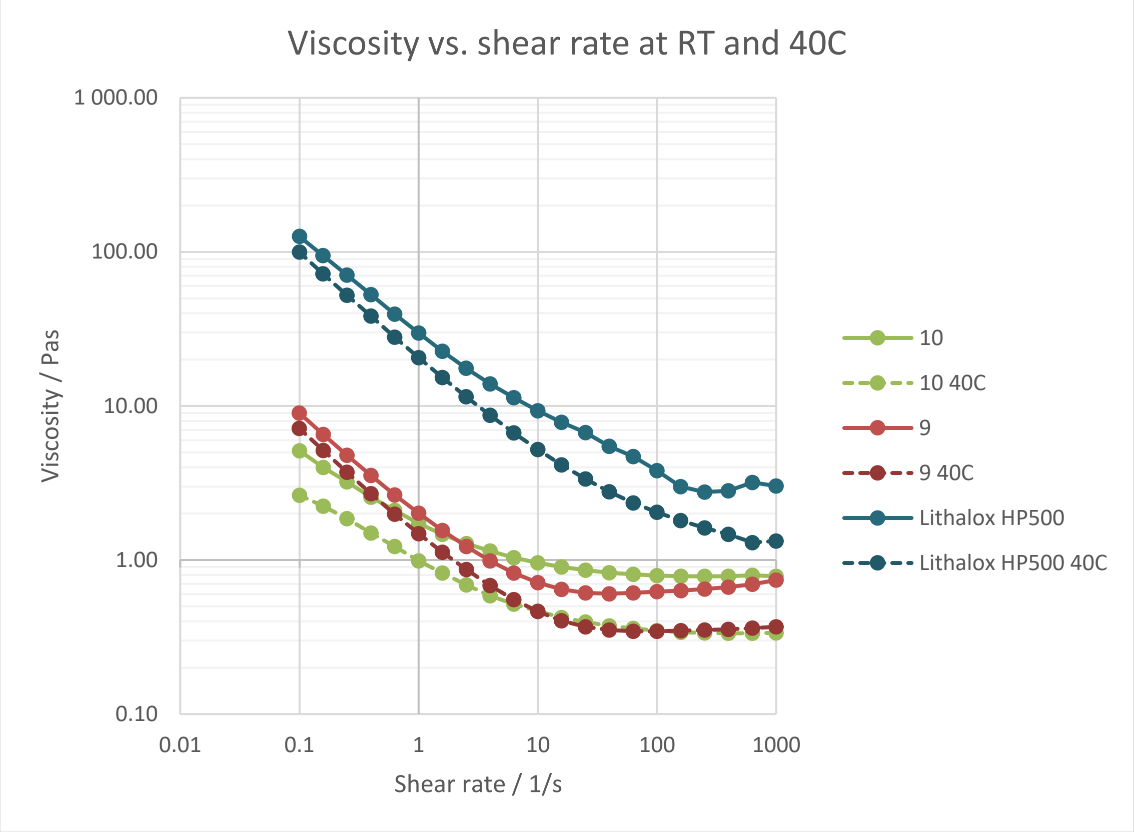

Figure 54: Viscosity vs. shear rate of recipes 9 (50 vol-% alumina, 37.5 vol-% DDDA, 2.5 vol-% PEGMA200, 10 vol-% PEG), 10 (50 vol-% alumina, 12.5 vol-% DDDA, 12.5 vol-% PGTA, 15 vol-% ECC, 10 vol-% PEG) and Lithalox HP500 at room temperature and at 40 °C.

The effects of temperature and ceramic powder content on viscosity and the curing behaviors can be further observed in the graphs in Appendix 5. Based on the viscosity measurements, slurries 9 and 10 are well suitable for SLA printing and have a shear thinning viscosity that is significantly lower than that of Lithoz Lithalox HP500.

The mass changes (out of initial monomer mass) due to $scCO_2$ exposure are presented in are illustrated in Figure 55 below and as a list in Table 15 in Appendix 5. It may be seen that all samples from recipes 2–10 underwent mass decrease during the $scCO_2$ extraction, which indicates that all recipes had a component that is soluble to $scCO_2$.

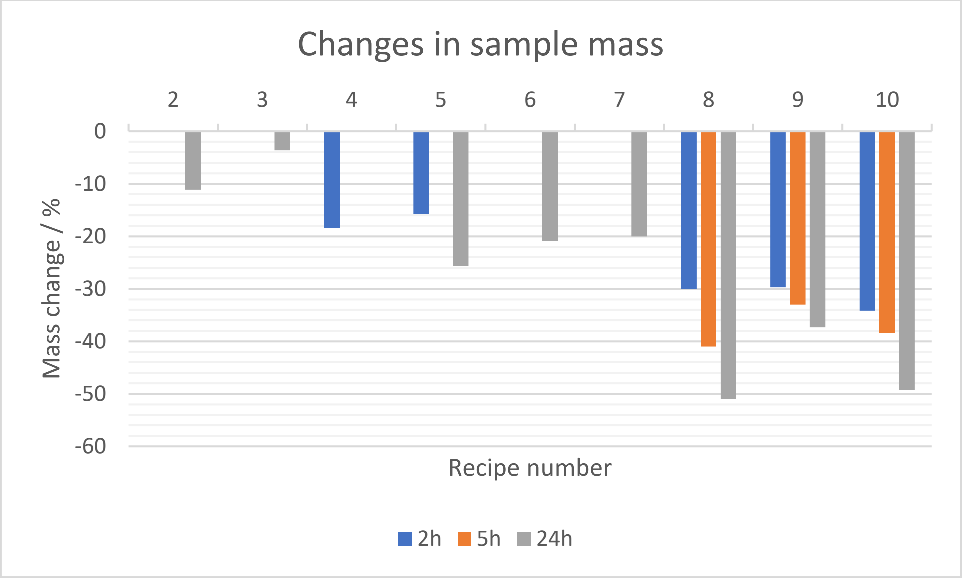

Figure 55: Mass changes (out of monomer mass) of recipes 2-10 after exposing to $scCO_2$ for 2, 5, or 24 h.

It was showed in Table 11 that EasyClean resin cleaner is soluble to $scCO_2$, and the mass decrease of recipe 2 was 11.1 w-%. As will be later discussed in Subsection 7.5, also PEGMA200 is expected to be soluble to $scCO_2$, thus it is likely that most of the EasyClean and/or some PEGMA200 has been extracted. The mass decrease of recipe 3 was 3.65 w-%.

Recipe 4 was developed to experiment $scCO_2$ extraction of paraffin oil. As presented in Figure 55, 18.36% of initial sample mass left the print structure during 2h $scCO_2$ extraction. Recipe 4 density also decreased by 12.51 % and -2.53, -1.94 and -2.32 % decreases in h, b and L were seen, respectively. If we assume that fast-curing DDDA has fully cured during light exposure, most of the paraffin oil and some PEGDMA200 were successfully extracted. However, the recipe 4 would need optimization as the samples were cracked, and therefore 24h test was not done on these samples, excluding recipe 4 from the following numerical evaluations of dimensions and density.

As seen in Figure 55, the mass decrease of recipe 6 (37.5 vol-% DDDA, 5 vol-% PEGMA200, 37.5 vol-% PGTA, 20 vol-% PEG) was 20.88 w-% and 20.00 w-% for recipe 7 (40 vol-% DDDA, 40 vol-% PGTA, 20 vol-% PEG). As will be presented in Subsection 7.5, it is likely that the PEG and some slowly curing PEGMA200 has been extracted from recipes 6 and 7 structures.

As expected, the mass decrease in 2 h and 5 h extraction tests was less than in 24 h tests for recipes 8, 9 and 10. This indicates, that 5 h was not enough to extract all the extractable substances from these recipes with the used 100 bars and 40 °C test parameters. Further studies with e.g., 10 h and 15 h extraction time, could be made to find out the optimum extraction time. The mass loss of recipe 9 samples was significantly higher in 2 h and 24 h tests than mass loss of recipe 5. As the recipes were same except for alumina content, this indicates that the recipe 9 samples were not fully cured during the printing. The mass losses with 2 h, 5 h and 24 h extraction tests with recipes 8 and 10 are similar, indicating that the prints in both cases were successful and that the same substances were extracted. These recipes contained 30 vol-% ECC of the monomer content and comparing to the weight losses of all the other recipes and the TGA results discussed in Subsection 7.5, it can be assumed that the ECC has been extracted in addition to PEG.

Figure 56 below and Table 16 in Appendix 5 present the average changes in *h* height, *b* thickness, *L* length and ρ density of all recipes after 24 h exposure to $scCO_2$, excluding recipe 4. Samples of recipes 2 and 3 were severely cracked after $scCO_2$ exposure, as was seen in Figure 46 a and b. This may have caused error to dimension measuring and seem like the thickness of recipe 2 and the height of recipe 3 increased instead of shrinkage. The main difference between recipe 5 (75 vol-% DDDA, 5 vol-% PEGMA200, 20 vol-% PEG) and recipes 6 (37.5 vol-% DDDA, 5 vol-% PEGMA200, 37.5 vol-% PGTA, 20 vol-% PEG) and 7 (40 vol-% DDDA, 40 vol-% PGTA, 20 vol-% PEG) is the content of PGTA. Recipes 6 and 7 shrank more in thickness and length, than recipe 5. Based on this observation, trifunctional PGTA shrinks more than difunctional DDDA. As expected, the shrinkage was largest in recipe 8, which also contained most extractable material. The density decrease of recipe 8 was also largest, which indicates there might be pores in the structure. However, as discussed in Subsection 7.3, the presence of pores was not confirmed.

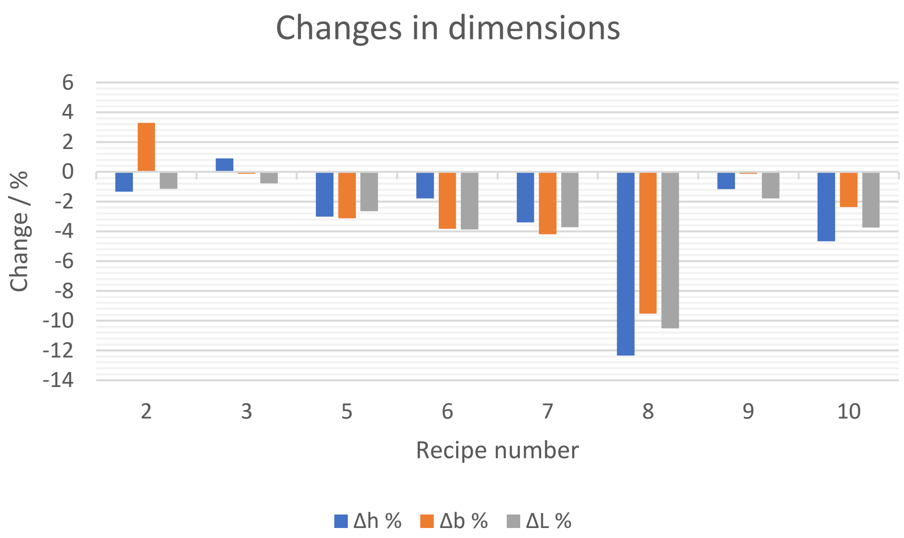

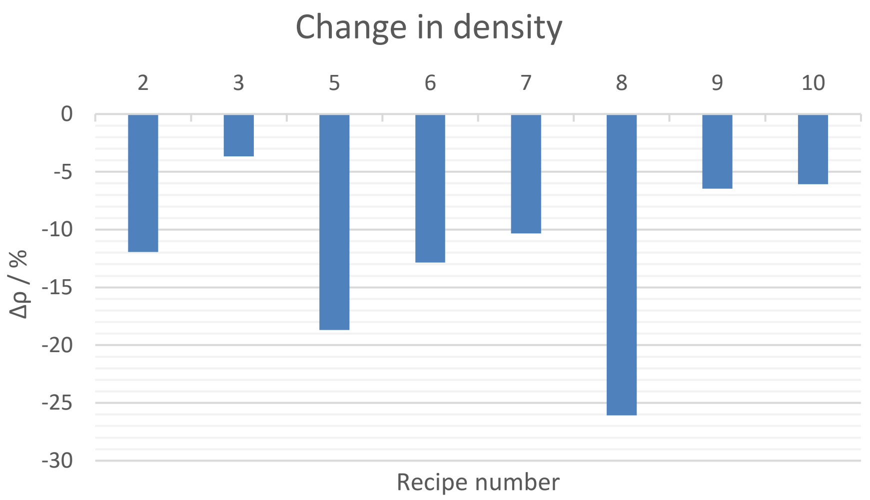

Figure 56: Above: recipes 2-3 and 5-10 changes in dimensions after 24 h scCO$_2$ extraction. Below: recipes 2-3 and 5-10 changes in density after 24 h scCO$_2$ extraction. Recipes 9 and 10 contain alumina powder.

It may be observed in Figure 56 that the density, counted based on the change in mass and dimensions, decreased in all samples. As expected, based on the theory in Chapter 2, the shrinkage and density decrease were smaller in the ceramic versions (recipes 9 and 10) than polymeric recipe versions (recipes 5 and 8).

7.5 Thermogravimetric analysis (TGA)

The degradation onset temperatures of pure monomers, PEG and paraffin oil were determined with TGA. They are summarized in Table 12 and the TGA graphs can be found in Appendix 6. The TG analysis begins with polymeric resin recipes 4 and 5, as they have similar content except for the extractable additive (PEG/paraffin oil). The analysis of TGA results after $scCO_2$ extraction of recipes 4 and 5 is also simpler than those of the other recipes, that contain PGTA and/or ECC, which add additional degradation steps in the curve to interpret.

Table 12: Degradation steps amount and onset temperatures of substances used in recipes 1-10.

Substance	Degradation steps	Degradation onset temperatures / °C
DDDA	2	181, 399
PGTA	2	165, 346
PEGMA200	3	144, 240, 377
ECC	2	264, 313
PEG	1	314
paraffin oil	1	236

It may be observed in Table 12 that the degradation of monomers used has 1, 2 or 3 steps and some of them overlap with each other, which makes the analysis of graphs challenging. For quantitative analysis, more parallel samples should be measured, and recipes should be designed in a way that no overlapping in degradation temperatures is significant. Comparison between recipe 5 sample as printed and a sample exposed to $scCO_2$ for 24 h (Figure 57) shows, that the first degradation steps of DDDA at 181 °C and PEGMA200 at 144 and 240 °C are not visible after $scCO_2$ extraction. Also, the PEG degradation at 314 °C is missing. This observation together with the -25.60 w-% mass loss presented in Table 15 indicates that PEG (20 vol-% in the recipe) and PEGMA200 (5 vol-% in the recipe) can be extracted with $scCO_2$.

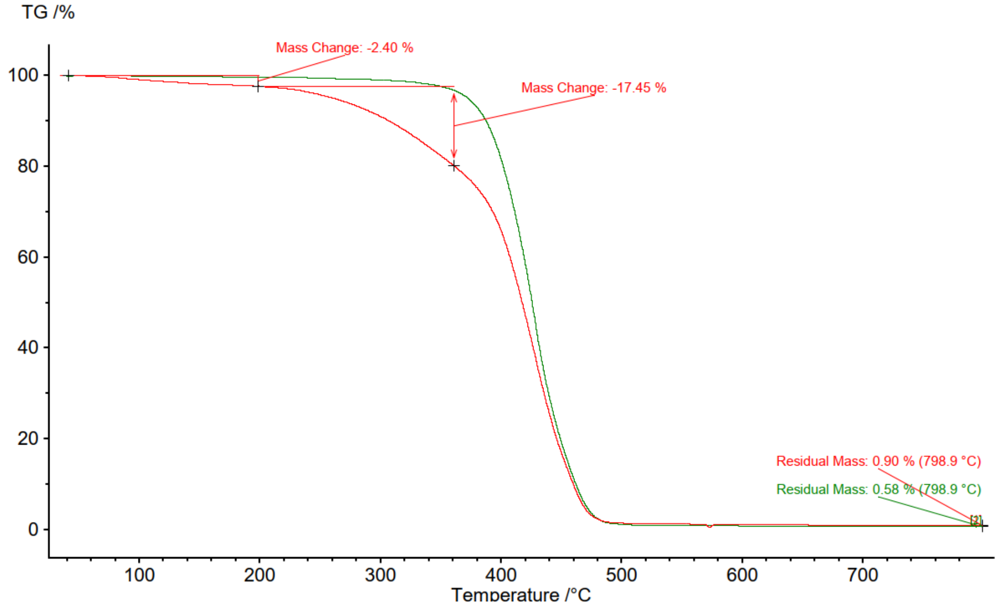

Figure 57: Recipe 5 (75 vol-% DDDA, 5 vol-% PEGMA200, 20 vol-% PEG) TGA curves (nitrogen atmosphere) of a sample as printed (red) and a sample exposed to $scCO_2$ for 24 h (green).

Residual mass of up to 1 w-% can be found in all the TGA samples. This most probably consists of carbon residual and photoinitiators, that are inorganic substances that have very high degradation temperature. Recipe 4 contained the same substances as recipe 5, but paraffin oil replaced PEG. As was seen in Figure 57, also in Figure 58 the initial degradation step of PEGMA200 is missing after $scCO_2$ extraction. As 18.36 % of sample mass was lost during the 2 h $scCO_2$ extraction, probably some of both PEGMA200 and paraffin oil are still left in the structure, as it was seen in the previous subsection that 2 h was not enough to remove all the extractable substances for other recipes used. Thus, it can be concluded that when using recipe 4, likely 2 hours was not enough to remove all uncured and dissolvable material either, but further experiments should be made with longer exposure time to see if all paraffin oil can be extracted from the structure. As seen in the green curve in Figure 58, the mass loss consists of 2 steps, of which the first one has 4.46 w-% loss that starts approximately at 240 °C. This is possibly the remaining paraffin oil in the structure.

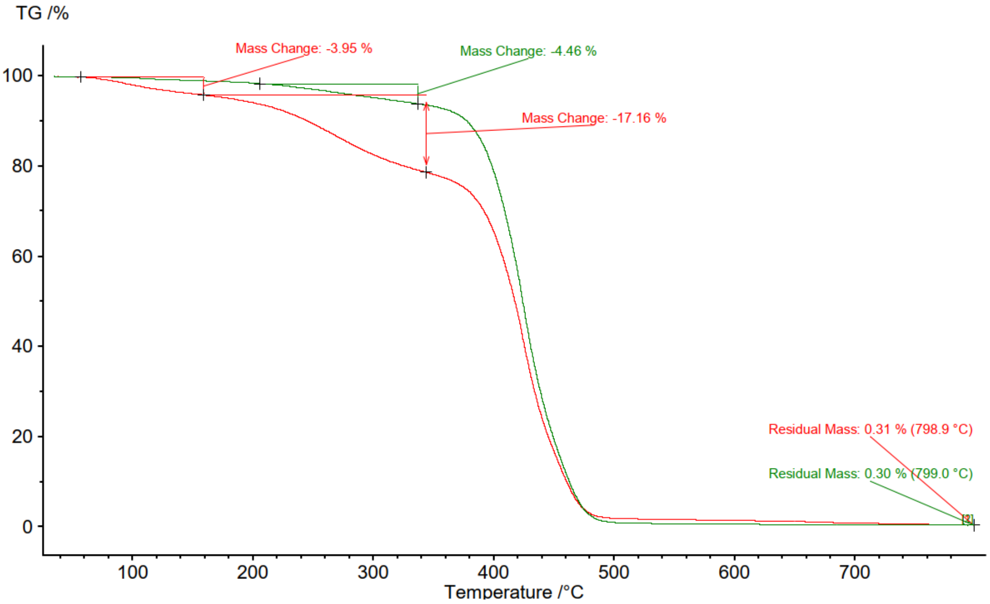

Figure 58: TGA curves of recipe 4 in nitrogen atmosphere (75 vol-% DDDA, 5 vol-% PEGMA200, 20 vol-% paraffin oil) sample as printed (red) and sample exposed to scCO$_2$ *for 2 h (green).*

Recipe 7 shows a smaller difference between the as printed and 24 h scCO$_2$ exposed samples. This recipe consisted of 40 vol-% DDDA and 40 vol-% PGTA with 20 vol-% PEG. The presence of the first degradation step (indicated with a black arrow) in the red TGA curve in Figure 59 and supplementary DSC results of recipe 7 in Appendix 7 indicate that some uncured DDDA and/or PGTA are present in the print, but they are either extracted or cured during the 24 h scCO$_2$ extraction. The total mass loss during scCO$_2$ extraction presented in Table 11 was -20.0 %. Assuming that the PEG was evenly distributed in the resin, and only PEG was extracted, it could be hypothesized the DDDA and PGTA monomers can crosslink further during the scCO$_2$ extraction, as the first degradation is not present in the scCO$_2$ extracted sample. Another meaning for the first degradation step could be a stabilizer degrading during that step.

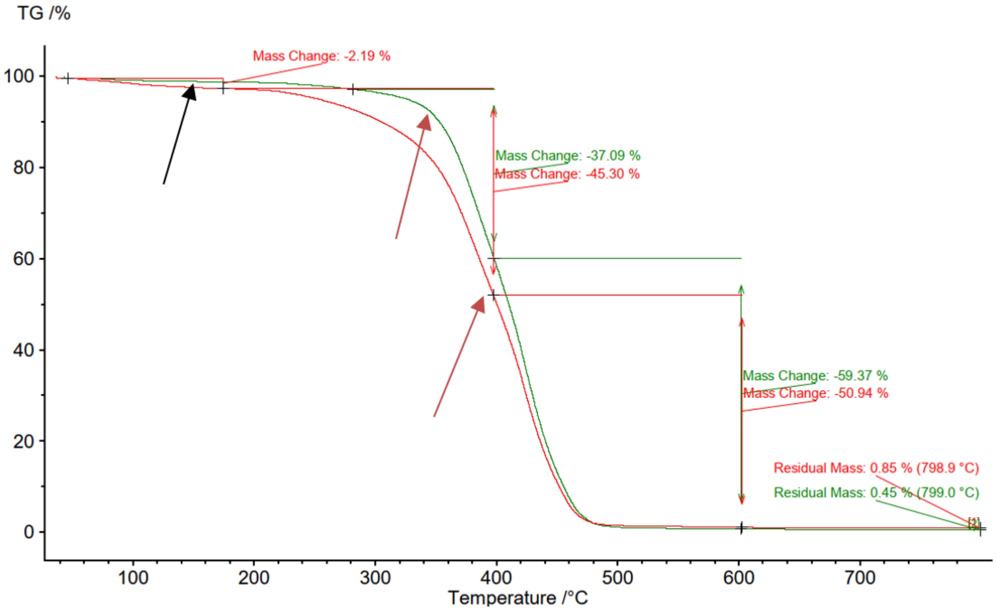

Figure 59: Recipe 7 (40 vol-% DDDA, 40 vol-% PGTA, 20 vol-% PEG) TGA curves (nitrogen atmosphere) of a sample as printed (red) and a sample after 24h exposure to scCO$_2$ (green). Black arrow indicates the 1st degradation step of DDDA/PGTA, and red arrows the 2nd steps.

In Figure 59, the degradation steps of DDDA and PGTA can be seen around 346 °C and 399 °C (indicated with red arrows) in the green curve, as expected based on the mass losses of this recipe discussed in the previous subsection at Figure 55. DDDA and PGTA are fast-curing acrylates, so this result is expected and further proves that PEG is extracted.

Recipes 6 and 8 are more challenging to interpret, as they contain 4 major substances instead of 3, and as seen in i.e., Figure 59, the combination of two substances degrading in temperatures close to each other may appear as one and in a combination of substances, the degradation temperature may shift when comparing to pure chemicals. Nevertheless, evaluating the comparison between the as-printed sample, and samples that underwent 2 h and 24 h extraction in Figure 60 a and b, it can be observed that the more time used for extraction, the closer the curve is to the remaining degradation steps of PGTA at 346 °C and DDDA at 399 °C. As presented in Subsection 7.2, several extraction tests have been done in higher temperatures and pressures, than the tests of this thesis. Trying different pressure and temperature parameters would perhaps increase the solubility rate and shorten the time needed for complete extraction of uncured substances.

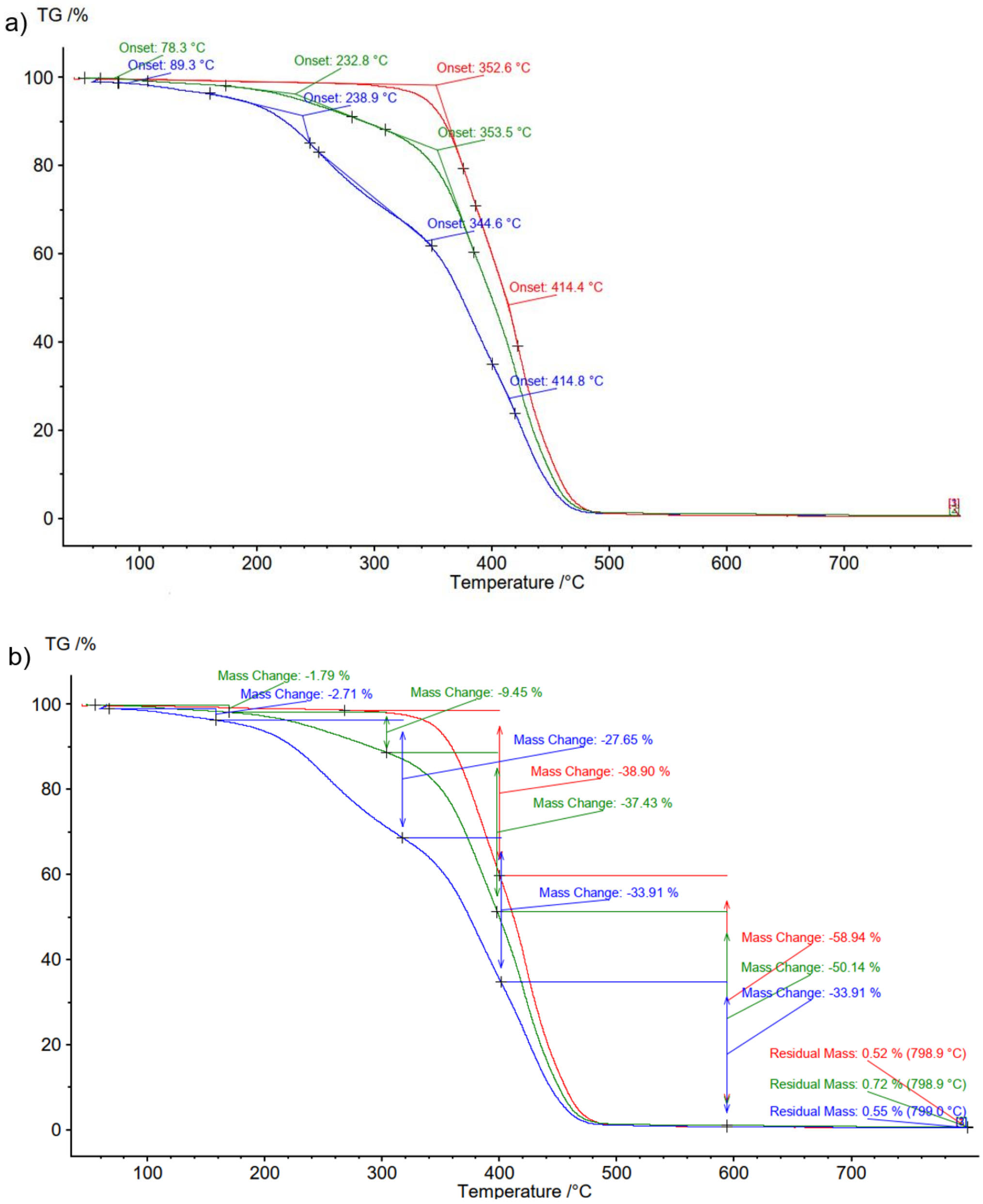

Figure 60: a) TGA curves of recipe 8 as printed (blue), 2h (green) and 24h scCO$_2$ exposed (red) samples with degradation onset temperatures. b) recipe 8 as printed (blue), 2h (green) and 24h scCO$_2$ exposed (red) samples with mass loss steps. All curves in nitrogen atmosphere.

The large ECC degradation step at 240-300 °C also diminishes and cannot be seen in the data using 24 h extraction time. Thus, also uninitiated ECC can be dissolved in scCO$_2$. This trend is supported by the mass loss data in Table 15, as 30 vol-% ECC and 20 vol-% PEG were used in recipe 8 and within 24 h, 51 % of the resin total mass was extracted. The extra 1 % may originate from uninitiated BAPO or uncured DDDA or PGTA. Samples were not dried before TGA or DSC measurements, which may cause the mass to decrease due to moisture evaporation already below 100 °C. In Figure 60, the as printed and 2h extracted samples, the degradation can be seen starting from the beginning of the measurement. To avoid this, samples should be dried prior to testing, but as monomers are delicate and may suffer from heating, it can be challenging.

Mass change results of recipes 3–8 and TGA curves seen in this subsection and Appendix 6 indicate that PEG, paraffin oil, ECC, PEGDMA200 and FormFutura EasyClean resin cleaner can be extracted from the structure with $scCO_2$, but the cured DDDA or PGTA do not. This conclusion is further supported by comparing the computed average and a real sample degradation curve. This is demonstrated in Figure 61, where the purple curve is a computed average of TGA data from pure monomers that are present in recipe 8 (DDDA, PGTA, ECC, PEG), and the black curve is the computed average of only DDDA and PGTA, which are assumed to be left in the structure after $scCO_2$ extraction. It can be seen that the blue TGA data curve of an as printed sample of recipe 8 fits the computed purple curve in an acceptable manner. The green curve of a recipe 8 sample that has undergone 24 h $scCO_2$ extraction also fits the computed average of DDDA and PGTA, except for the 1st degradation step that was already discussed in Figure 59.

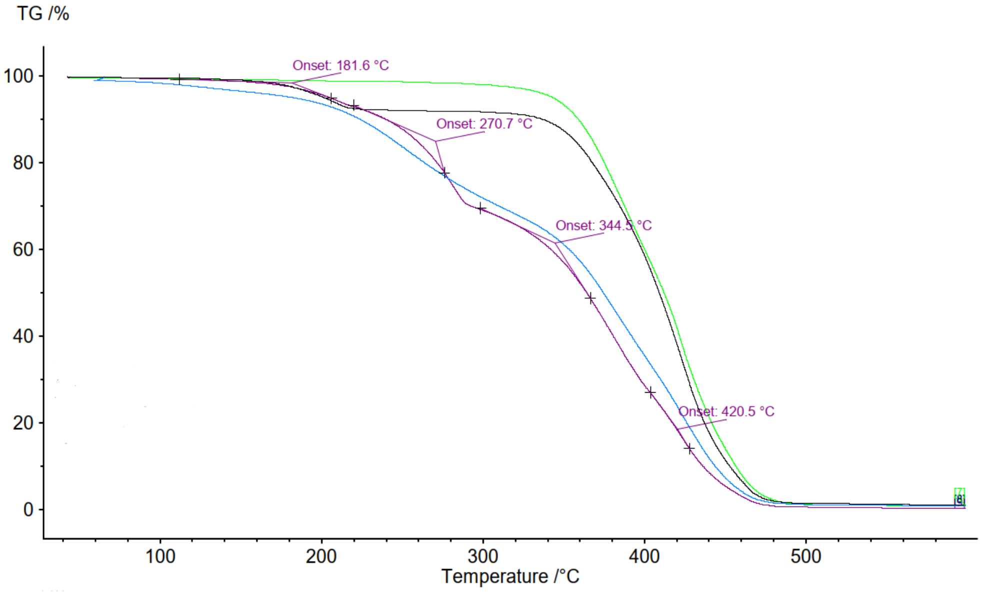

Figure 61: TGA data of recipe 8 (25 vol-% DDDA,25 vol-% PGTA, 30 vol-% ECC, 20 vol-% PEG) before (blue) and after 24 h $scCO_2$ extraction (green) with computed averages of pure chemicals: DDDA, PGTA, ECC, PEG (purple) and DDDA + PGTA (black).

In 24h tests with recipes 5 and 8, the mass loss (Figure 55) was slightly higher than the expected value based on the mass of non-cured substances in the recipe. This is likely due to the unreacted photoinitiator or uncured DDDA or PGTA that are also extracted with $scCO_2$. Similar changes can be seen in the samples of recipes 9 and 10, but with the alumina content remaining as residual mass at 800 °C. This is demonstrated in Figure 62 a and b.

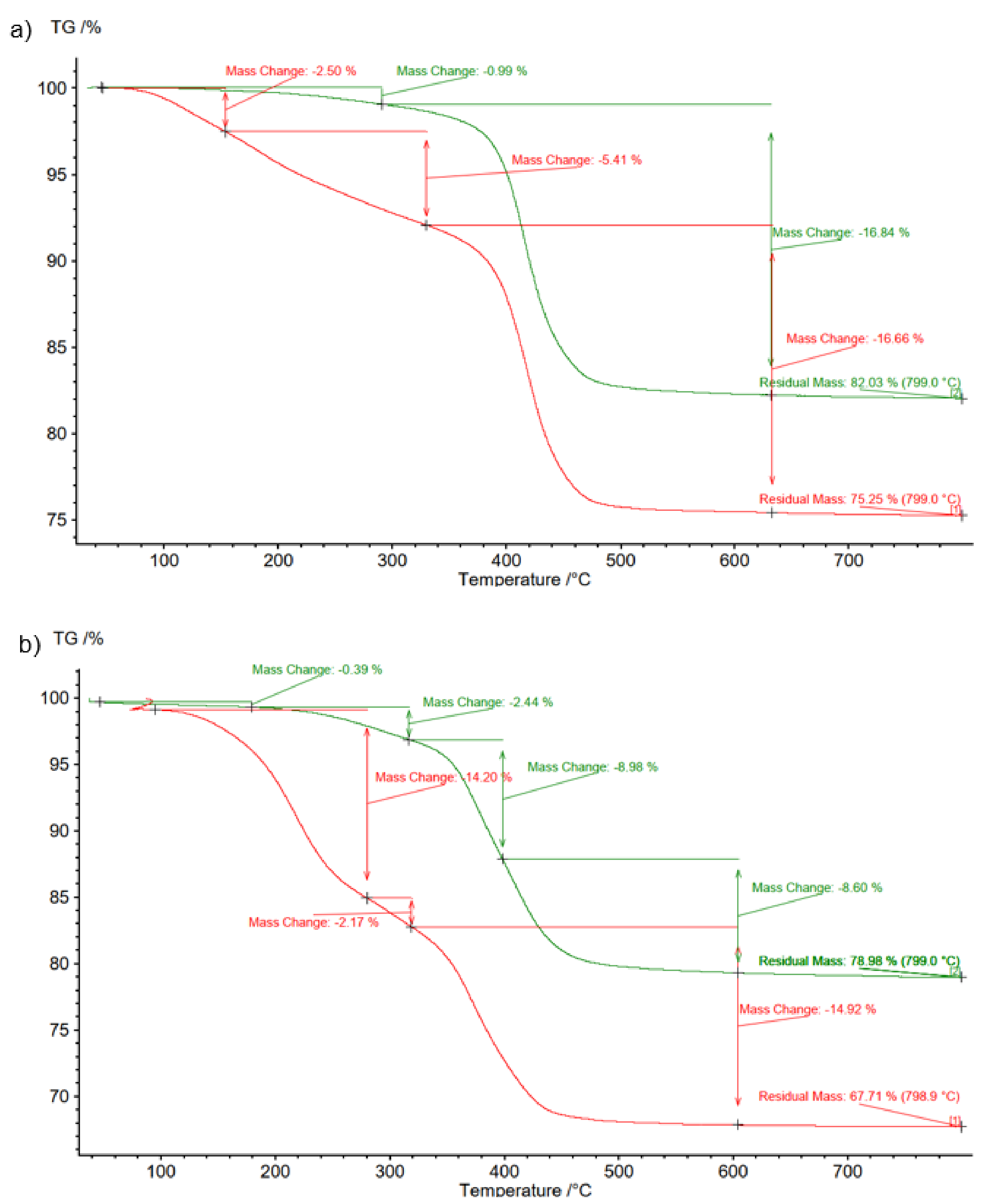

Figure 62: TGA curves in nitrogen atmosphere. a) recipe 9 (50 vol-% alumina, 37.5 vol-% DDDA, 2.5 vol-% PEGMA200, 10 vol-% PEG) as printed (red) vs. 5 h (green) $scCO_2$ exposed sample. b) recipe 10 (50 vol-% alumina, 12.5 vol-% DDDA, 12.5 vol-% PGTA, 15 vol-% ECC, 10 vol-% PEG) as printed (red) and 5 h (green) $scCO_2$ exposed sample curves.

The degradation step starting at around 265 °C indicates that after 5 h extraction, there is still some ECC left in recipe 10 structure. In recipe 9, the degradation starts at 180 °C, indicating uncured DDDA. It can also be seen from the red recipe 10 as printed sample data, that instead of intended 75 w-% alumina, 67.7 w-% is found, which is most likely due to a user mistake during weighing.

7.6 Differential scanning calorimetry (DSC)

DSC was used to study if there are uncured monomers left in the samples after the printing or after the $scCO_2$ extraction. The DSC data of pure substances and samples not presented in this subsection can be found in Appendix 7. All samples had a minor sharp exothermic peak at 56 °C (Figure 63, indicated with an arrow). This is a common artifact caused by the movement of aluminum pan inside the furnace while heating, due to expansion coefficient gradient [168] and can be seen even in the sample that has been through a thermal debinding cycle in air atmosphere, and thus contains only ceramic powder and minorities of carbon residue.

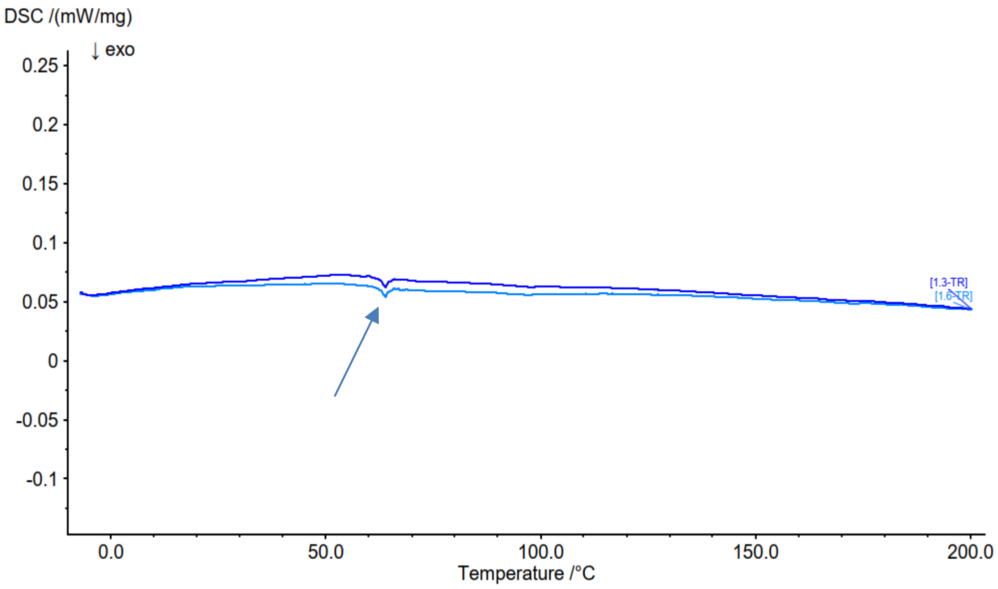

Figure 63: DSC curves of 2 consequent heatings in nitrogen atmosphere of a recipe 9 (50 vol-% alumina, 37.5 vol-% DDDA, 2.5 vol-% PEGMA200, 10 vol-% PEG) sample that has been exposed to $scCO_2$ for 5h and thermally debound. The arrow indicates the artifact caused by crucible movement inside the furnace.

To study true thermal behavior of polymers, 2. heating is often used for evaluation, but in case of monomers and solvents it is not beneficial as irreversible curing and evaporation are not seen in the 2. heating.

There is a difference in the reactions happening during DSC experiment between recipes 4–8 (printed with Prusa SL1S) and 9–10 (printed with CeraFab7500). The difference is demonstrated between recipe 5 and 10 samples in Figure 64. Recipes 9 and 10 containing alumina and printed with CeraFab7500 seem to have cured better, as there are no major endothermic evaporation/reorganization or exothermic curing steps seen in the print or scCO$_2$ extracted samples. In recipes 4–8 printed with Prusa SL1S, some uncured monomers are seen especially in the prints that have not been extracted with scCO$_2$. This can be observed in the blue curve in Figure 64 a, where the endothermic peak at -1.5 °C is likely the crystallization of uncured DDDA and the exothermic peak at approximately 155 °C is uncured PEGMA200 and at 165 °C in the red curve of a 2 h extraction sample. These peaks can be found comparing to the DSC data of pure monomers found in Appendix 7. As expected, after 24 h scCO$_2$ extraction in the pink curve in Figure 64 a, there is less uncured monomer left in the structure.

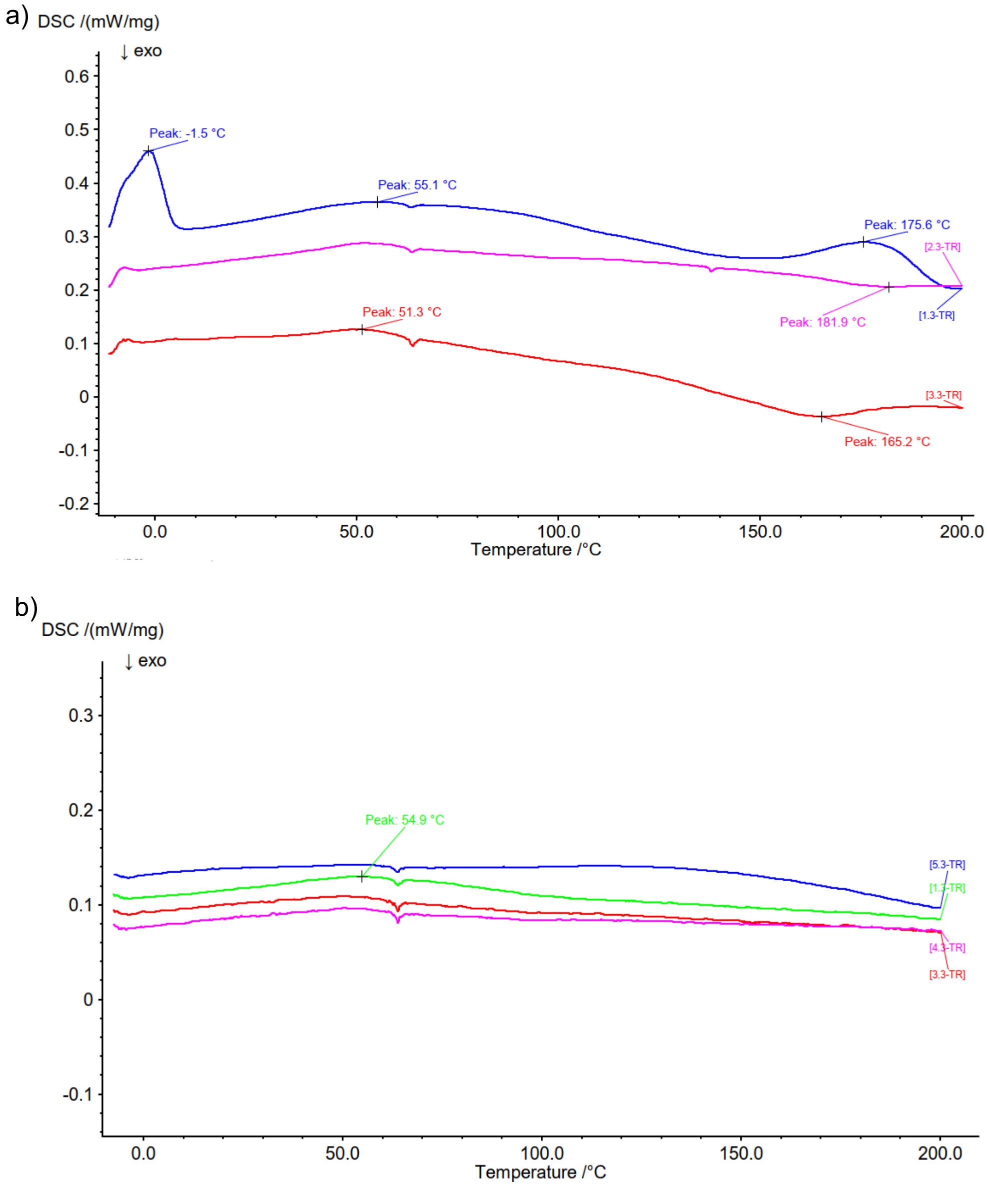

Figure 64: DSC data of first heatings in nitrogen atmosphere. a) recipe 5 (75 vol-% DDDA, 5 vol-% PEGMA200, 20 vol-% PEG) as printed (blue), 2h (red) and 24h (pink). b) recipe 10 (50 vol-% alumina, 12.5 vol-% DDDA, 12.5 vol-% PGTA, 15 vol-% ECC, 10 vol-% PEG) as printed (blue), 2h (green), 5h (red), 24h (pink).

The assumed crystallization peak of DDDA can be seen in recipes 5–7 prints at approximately 0 °C. It is possible that the peak is shifted due to the lower percentage of uncured DDDA compared to the data obtained from the pure chemical (Appendix 7). The same DDDA peak is not seen in any samples made with slurry recipe 9 or 10. Also, the recipe 4–8 curves with or without $scCO_2$ extraction show a trend towards exothermic degradation similar to what is seen in the pure PGTA curve. Based on these observations, the printing parameters and/or light intensity used in the Prusa SL1S printer are not enough to fully cure the resin, which could be beneficial for $scCO_2$ extraction purposes if the printing with ceramic powder with the same printer could be possible.

However, printing a ceramic slurry with a such low light intensity would significantly increase curing time per layer and therefore printing time would increase significantly, and in addition possibly resulting in decreased resolution of prints due to overpolymerization. The exothermic peak of ECC starting at 134 °C for the as printed sample (indicated with a blue arrow) and revealing the PEGMA200 peak under it in the $scCO_2$ extracted samples can be seen in the recipe 8 sample. The large exothermic peak diminishes with the exposure time of $scCO_2$, as seen in Figure 65. This further supports the earlier conclusions made in mass decrease and TGA results; uncured ECC is left in the structure and can be extracted with $scCO_2$.

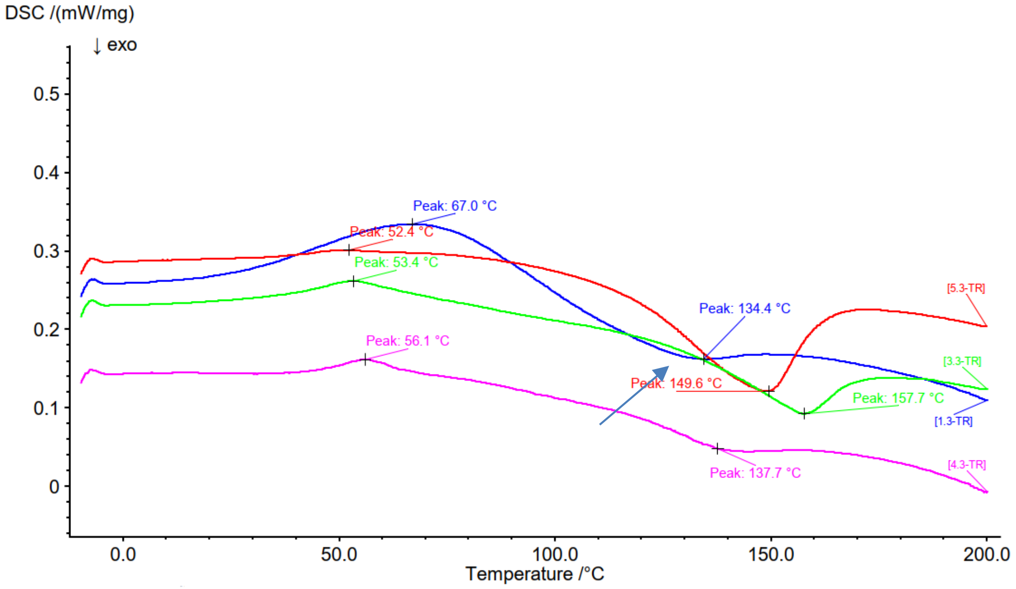

Figure 65: DSC curves of first heatings in nitrogen atmosphere of recipe 8 (25 vol-% DDDA, 25 vol-% PGTA, 30 vol-% ECC, 20 vol-% PEG) as printed (blue), 2h (red), 5h (pink) and 24 h (green).

The endothermic peak at 67 °C seen in Figure 65 is seen only in the recipe 8 as printed samples, which are the only polymeric samples containing ECC. The peak also diminishes once the sample is extracted with $scCO_2$, which indicates that the peak could be related to epoxy that is extracted from the structure. The same peak is not seen in the data obtained from pure ECC, which can mean that the ECC goes through relaxation, or some moisture evaporates, or residual EasyClean, used for print cleaning, evaporates instead. For a more quantitative study of each monomer residual should be done by heating the DSC to a higher temperature than 200 °C. Also, if further studies are made with DSC and TGA, it can be beneficial to use air atmosphere instead of nitrogen to determine the thermal debinding program, since thermal debinding is typically done in air atmosphere.

7.7 Fourier transformation infrared spectroscopy (FTIR)

FTIR measurements were made for the samples of recipes 5–8 before and after 24h $scCO_2$ exposure to study the changes in atomic bonds. Based on [169]–[173], the peaks used for the interpretation of the samples are as presented in Table 13. The FTIR data obtained for pure DDDA, PGTA, ECC and BAPO can be found in Appendix 8.

Table 13: FTIR peak types and wave numbers [169]–[173].

Wavenumber	Bond	Type
500	C=O	Bend
790	C–O–C	Stretch
810	C–C	Stretch
885-895	C=C	Bend
909-915	C–O	Stretch
1050-1085	C–O	Stretch
1102	C–O	Stretch
1162	C–H	Bend
1196	P=O	Stretch
1648-1658	C=C	Stretch
1725	C=O	Vibration
2349	O=C=O	Stretch
2856	C–H	Stretch
2925	C–H	Stretch
3436	O–H	Stretch

The challenge of interpreting the FTIR results comes from the similarity of some of the monomer hydrocarbon and carbon-oxygen bonds, such as the C=O (peak 1723 cm^{-1}), C–O (peak 1102 cm^{-1}), and C–H (peaks 1162, 2856 and 2925 cm^{-1}). These bonds are found in all the monomers used in our recipes and the vinyl C=C double bond in acrylates and methacrylate and indicated with arrows in Figure 66. As the vinyl double bond opens during the radical photocrosslinking, a substantial change in the 810 cm^{-1} or 1648–1658 cm^{-1} peak could indicate polymerization or removal of uncured monomer during scCO$_2$ extraction. However, no significant change in these peaks can be seen in the FTIR results, as shown in Figure 66 and Figure 67, indicating that most of the acrylates were cured.

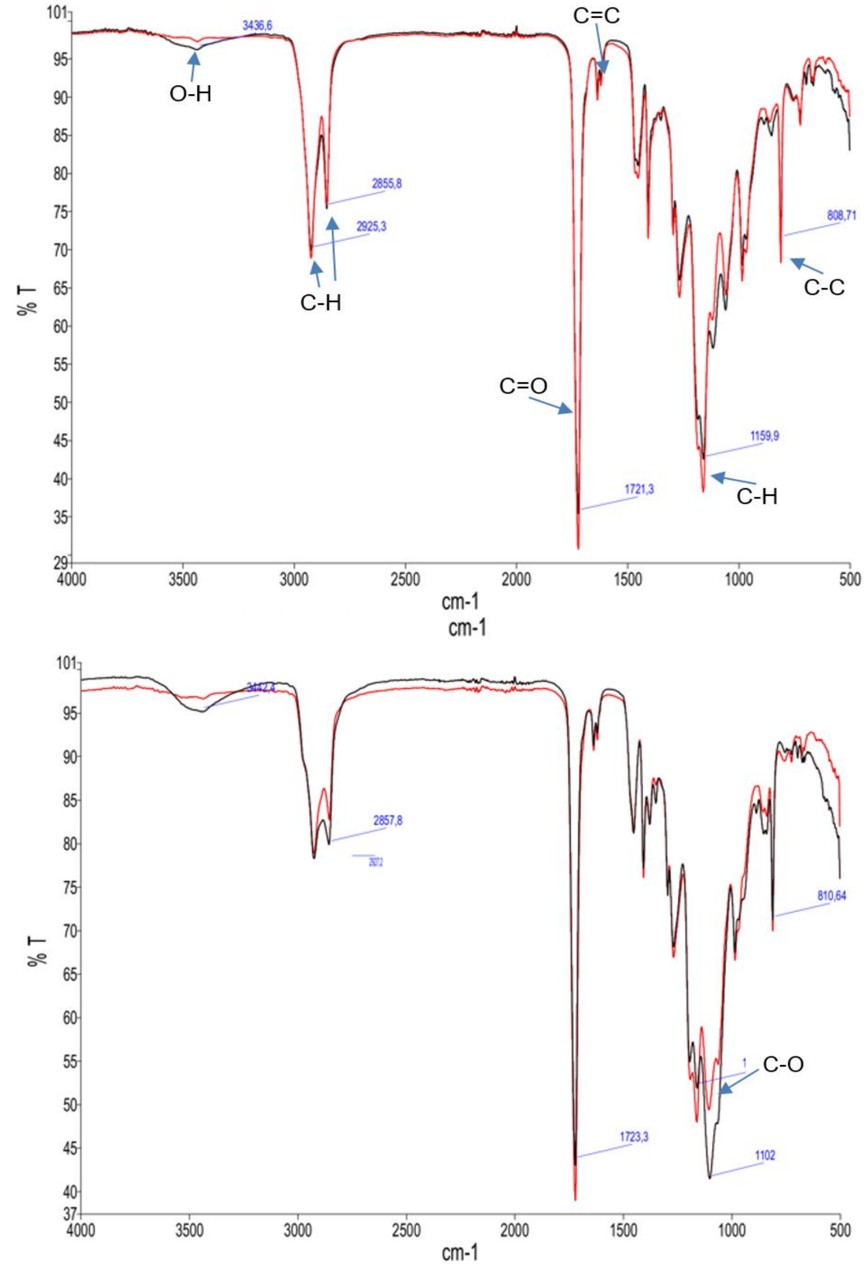

Figure 66: FTIR curves, up: recipe 5 (75 vol-% DDDA, 5 vol-% PEGMA200, 20 vol-% PEG) before (black) and after 24 h (red) scCO$_2$ extraction. Down: recipe 6 (37.5 vol-% DDDA, 5 vol-% PEGMA200, 37.5 vol-% PGTA, 20 vol-% PEG) before (black) and after 24 h (red) scCO$_2$ extraction. The most significant peaks are indicated with arrows.

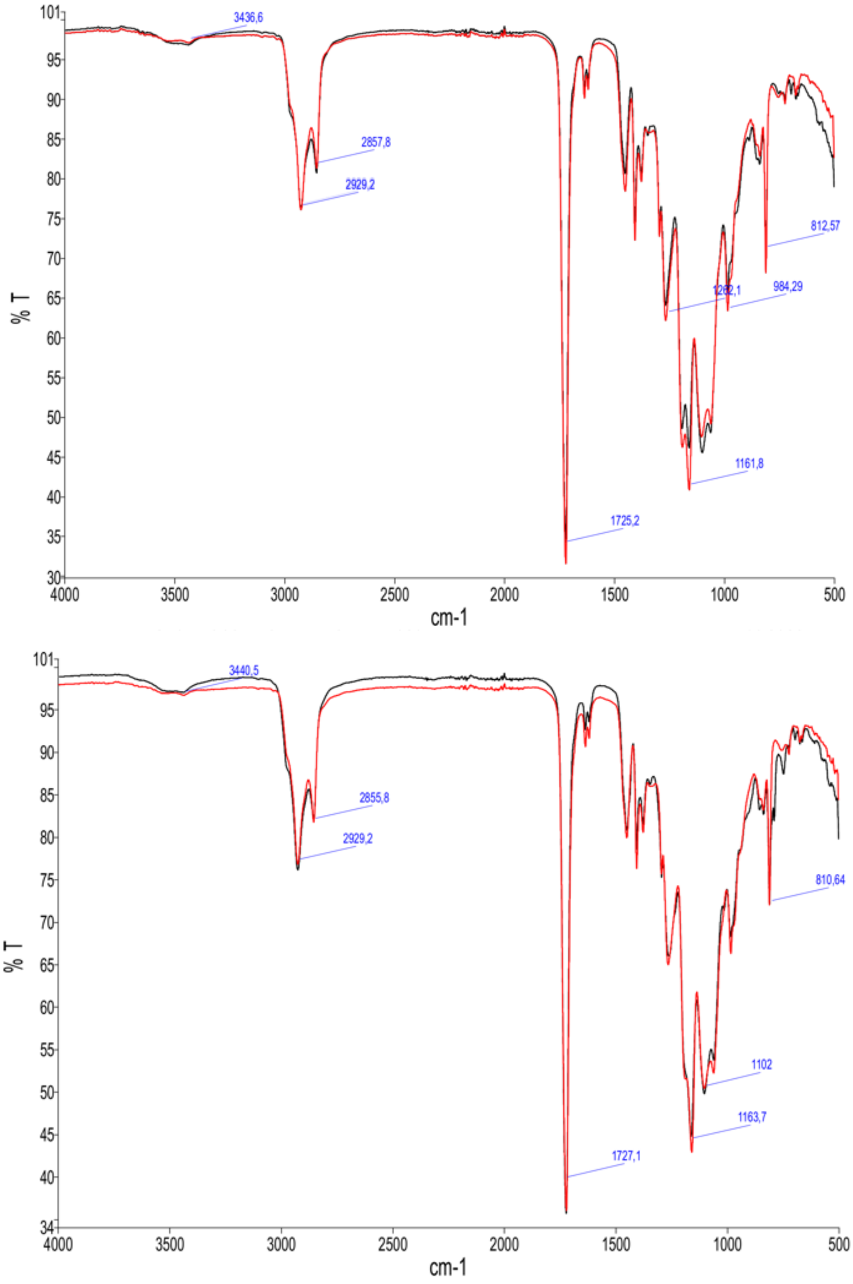

Figure 67: FTIR curves, up: recipe 7 (40 vol-% DDDA, 40 vol-% PGTA, 20 vol-% PEG) before (black) and after 24 h (red) $scCO_2$ extraction. Down: recipe 8 (25 vol-% DDDA, 25 vol-% PGTA, 30 vol-% ECC, 20 vol-% PEG) before (black) and after 24 h (red) $scCO_2$ extraction.

Due to the similarity of the used substances, the FTIR results are mainly useful for estimating changes in the presence of PEG, CO_2, uncured ECC and BAPO, which have atomic bonds that are different from the main hydrocarbon chains. For example, the ethanol peak at 3436 cm^{-1} belonging to PEG was decreased in the $scCO_2$ exposed samples, as seen in Figure 66. This indicates that PEG amount has diminished as seen in the previous TGA results but has not totally been extracted, but the minor alcohol peak may also be a residual from FTIR crystal cleaning with isopropanol. The primary alcohol (PEG) C–O stretching bond peak at 1050–1085 cm^{-1} is smaller in all samples after $scCO_2$ extraction, which supports the assumption.

Also, the 1102 cm^{-1} aliphatic ether C–O stretching bond peak was smaller after $scCO_2$ extraction, but this bond can be found in all the used monomers as well. Comparing recipe 5 to recipes 6–8, that have a larger amount of PGTA and PEDMA200, it may be observed that the ether C–O stretching bond peaks are larger as there are more of those bonds in the structures of recipes 6-8.

CO_2 stretching peak at 2349 cm^{-1} is not seen in any FTIR results, which could indicate that $scCO_2$ has fully desorbed from the sample structures after the $scCO_2$ treatment. Based on this, $scCO_2$ does not build up in the polymers used in the recipes, in a manner it did in the case of Azure Blue commercial resin. The 909–916 cm^{-1} peak of oxirane ring stretching belonging to ECC is hindered under the larger peaks next to it, but visible in the before and after comparison in recipe 8, and the oxirane C–O–C stretching peak at 790 cm^{-1} seems to have disappeared or at least diminished during $scCO_2$ extraction, as seen in Figure 68.

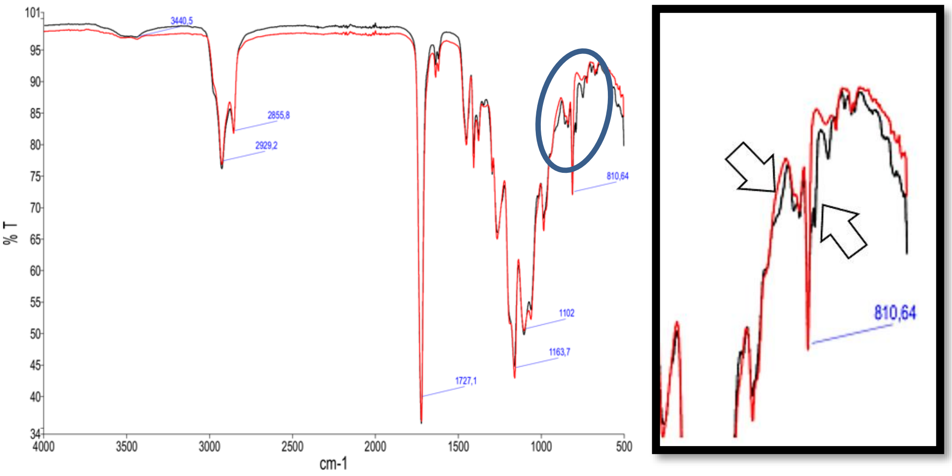

Figure 68: Recipe 8 (25 vol-% DDDA, 25 vol-% PGTA, 30 vol-% ECC, 20 vol-% PEG) ECC oxirane ring FTIR peaks at 790 and 915 cm^{-1}, indicated with an arrow.

Unfortunately, the characteristic peak between phosphorus and oxygen at 1196 cm^{-1}, related to photoinitiator BAPO, is hindered under the 1186 cm^{-1} peak of DDDA and 1194 cm^{-1} peak of ECC, and as the amount of BAPO comparing to the monomers is small, the peak would be smaller as well. Thus, the existence of BAPO cannot be evaluated from these results.

As a conclusion based on the FTIR data, the decrease of O–H transmission peak at 3436 cm^{-1} and C–O stretching bond peak at 1050–1085 cm^{-1} support the assumption that PEG is extracted from the printed samples with $scCO_2$, and the decrease of ECC oxirane ring FTIR peaks at 790 and 915 cm^{-1} indicate that ECC is extracted. The missing CO_2 stretching peak at 2349 cm^{-1} indicates that no CO_2 is absorbed into the samples.

7.8 Effect of co-solvent in $scCO_2$ extraction

The effect of co-solvent on solvation of monomers and PEG was studied with recipes 8, 9 and 10. All of them were extracted with ethanol as co-solvent for 2 h and recipe 8 for 4 h in addition. As FormFutura EasyClean was seen to totally dissolve in $scCO_2$, it was also experimented as co-solvent for recipe 8. With recipe 10, isopropanol (IPA) was tried as well, as seen in Table 14.

Table 14: Recipes 8–10 mass changes (out of monomer content) with and without (WO) co-solvents. EtOH: ethanol, IPA: isopropanol.

Recipe	2 h WO	2 h EtOH	2 h EasyClean	2 h IPA	4 h EtOH	5 h WO	24 h WO
8	-30.0	-39.9	-9.6		-42.9	-41.0	-51.0
9	-29.68	-24.06				-32.98	-37.30
10	-34.15	-19.32		-30.21		-38.37	-49.25

According to earlier conclusions made based on mass loss, TGA, DSC and FTIR, recipes 8 and 10 should have approximately 50 % of monomer mass (30 % uninitiated ECC and 20 % PEG) that could be extracted with $scCO_2$ in an ideal situation and with sufficient time. Recipe 9 should have max. 25 % (20 % PEG and max. 5 % PEGMA200). Based on the obtained mass losses of recipe 9 in Table 14, there has been uncured DDDA in the structure.

The mass removal during $scCO_2$ extraction with the selected co-solvents performs worse than without co-solvents, except for recipe 8. It seems that adding ceramic powder decreases the efficiency of ethanol as a co-solvent for recipes 9 and 10, but further repetitions should be made to make conclusions. Isopropanol seems to be more efficient than ethanol for recipe 10, but both resulted in smaller mass decrease than 2 h test without co-solvent. EasyClean resulted in the worst mass decrease. The changes in the appearance of recipe 8 samples after extraction with $scCO_2$ and co-solvents is presented in Figure 69 a–c. Based on the results in Table 14 and the appearance of Figure 69 b, it seems that EasyClean resin cleaner may be absorbed into the sample. It can also be noted that the Figure 69 c sample color remains similar to the as printed sample, unlike in most of the samples that did not have a co-solvent during extraction, like Figure 69 a.

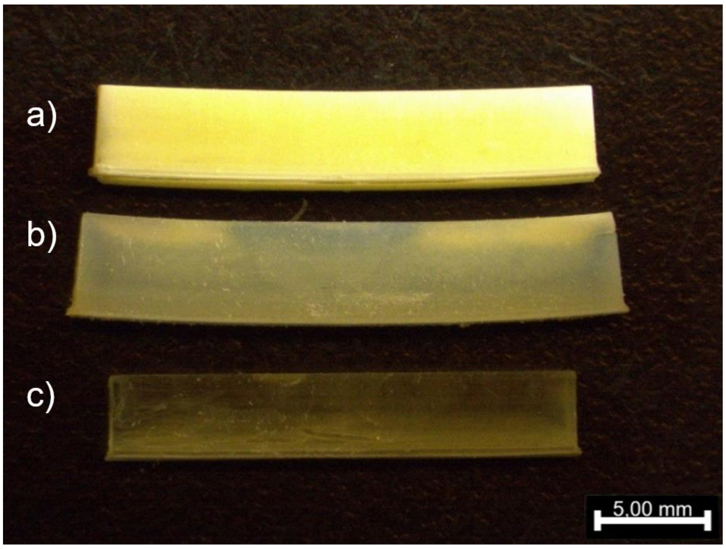

Figure 69: Microscopy images of recipe 8 (25 vol-% DDDA, 25 vol-% PGTA, 30 vol-% ECC, 20 vol-% PEG) after 2h $scCO_2$ without solvent (a), 2h with EasyClean (b) and 2h with ethanol as co-solvent (c).

In addition to worse extraction, the use of ethanol with recipes 9 and 10 resulted in delamination between print layers, as seen in Figure 70 a–b. Use of isopropanol did not cause laminar cracks (Figure 70 c); however, it did cause delamination off the initial layer that is printed for better adhesion to the print platform. This indicates that the choice of co-solvent is important also regarding possible delamination, and the best choice may not be the same for polymeric samples and samples containing ceramic powder.

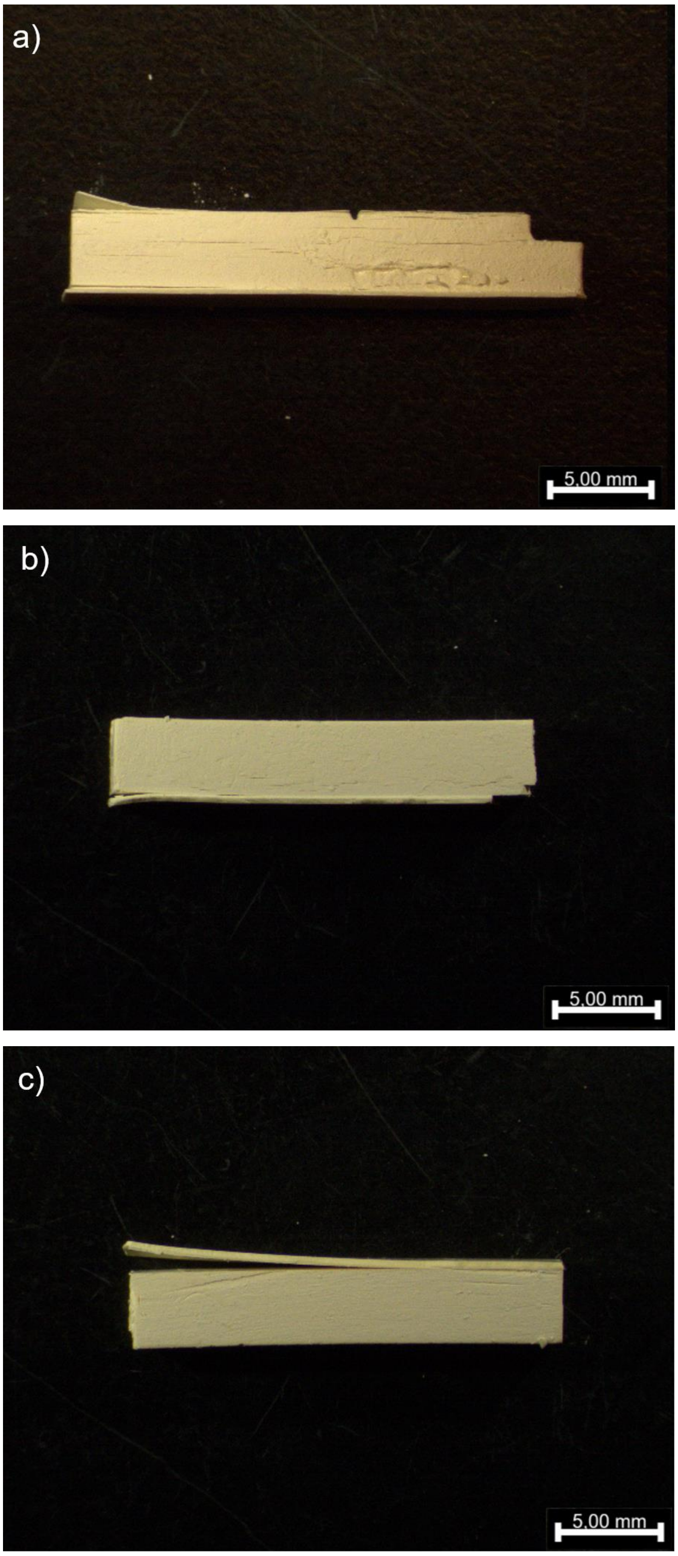

Figure 70: Microscopy images of a) recipe 9 (50 vol-% alumina, 37.5 vol-% DDDA, 2.5 vol-% PEGMA200, 10 vol-% PEG) after 2 h scCO$_2$ extraction with ethanol b) recipe 10 (50 vol-% alumina, 12.5 vol-% DDDA, 12.5 vol-% PGTA, 15 vol-% ECC, 10 vol-% PEG) after 2 h scCO$_2$ extraction with ethanol and c) recipe 10 after 2 h scCO$_2$ extraction with isopropanol as co-solvent.

DSC and TGA were also used to experiment differences between samples with and without co-solvents. With recipe 8, it seems that use of ethanol (pink curve) or EasyClean (red curve) diminishes the exothermic peak at 140 °C (Figure 71 a, indicated with an arrow). No major differences were seen in the DSC curves of samples produced with recipes 9 and 10, which was already seen in the DSC results of those recipes without co-solvent and is repeated in Figure 71 b.

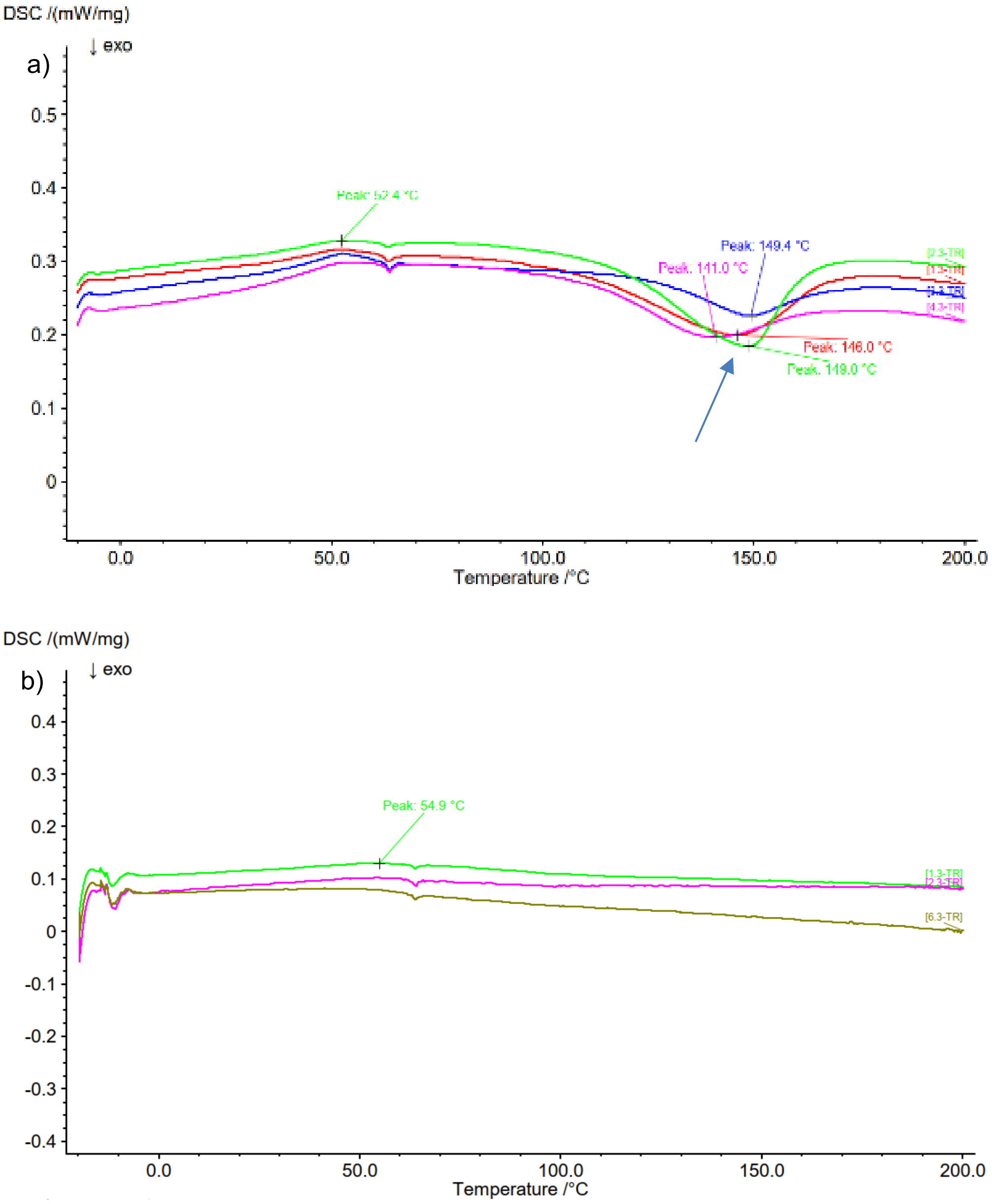

Figure 71: DSC data. a) recipe 8 (25 vol-% DDDA, 25 vol-% PGTA, 30 vol-% ECC, 20 vol-% PEG) sample with 2 h $scCO_2$ extraction without co-solvent (green), 2 h extraction with ethanol (pink), 2 h extraction with EasyClean (red) and 4 h extraction with ethanol (blue). b) Recipe 10 (50 vol-% alumina, 12.5 vol-% DDDA, 12.5 vol-% PGTA, 15 vol-% ECC, 10 vol-% PEG) sample after 2 h extraction without co-solvent (green), 2 h extraction with isopropanol (pink), 2 h extraction with ethanol (dark green).

TGA results together with the mass loss results in Table 14 show that the use of co-solvent can decrease the extraction efficiency. As discussed in the theory part in Chapter

4, co-solvent can change the substance's solubility to $scCO_2$. The co-solvent may also build up in the sample. In Figure 72 a, the extraction result of recipe 8 sample is worse with EasyClean (green curve) and better with ethanol (blue curve), comparing to 2 h extraction without co-solvent (red curve). It may be seen that the blue curve with ethanol as co-solvent is the closest to the degradation of DDDA+PGTA, as was discussed in Figure 61, indicating that most of the uncured substances are extracted.

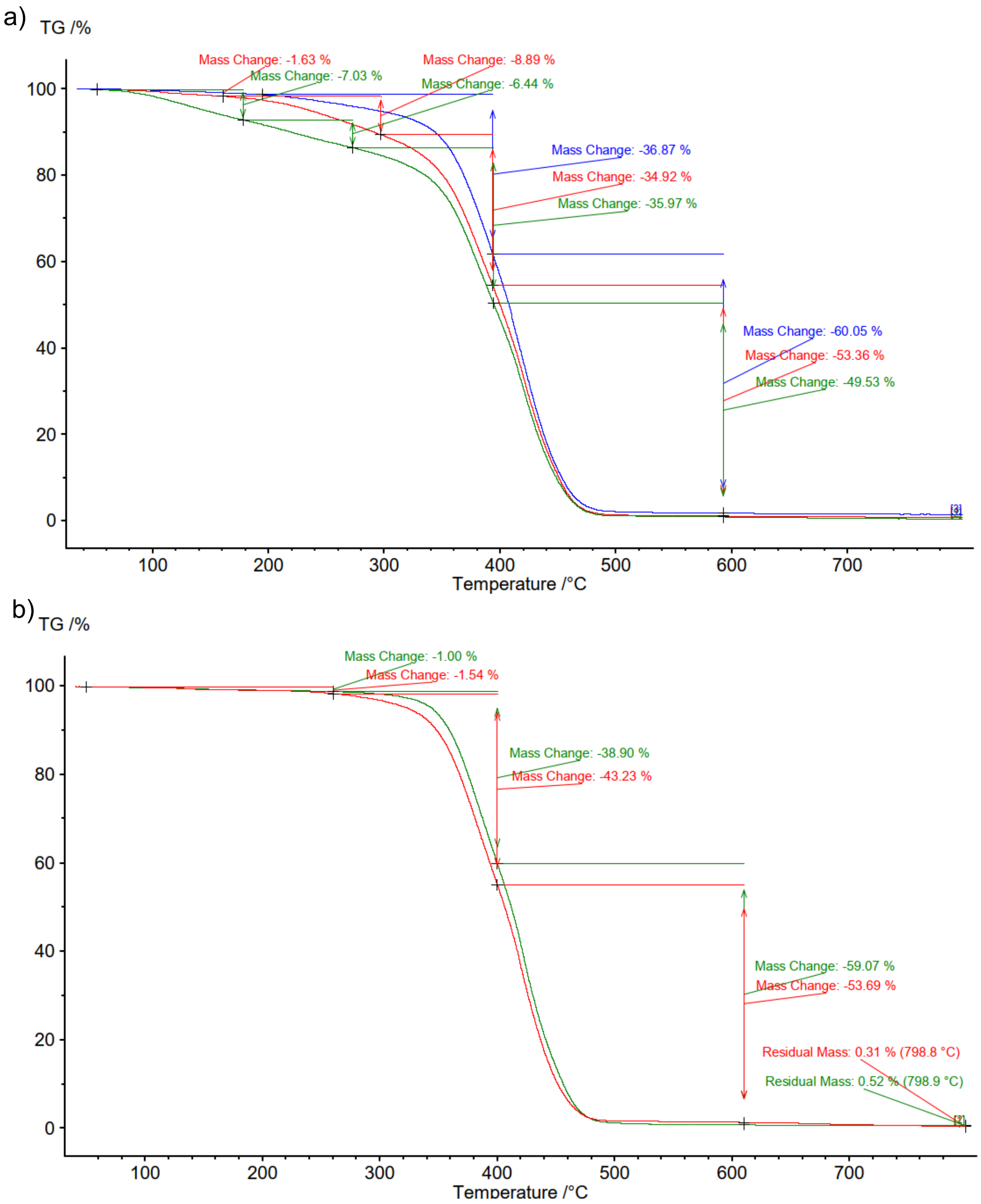

Figure 72: TGA data. a) recipe 8 (25 vol-% DDDA, 25 vol-% PGTA, 30 vol-% ECC, 20 vol-% PEG), 2 h $scCO_2$ tests without co-solvent (red), with EasyClean (green) and with ethanol (blue). b) Recipe 8, 4 h extraction with ethanol co-solvent (red) and 24 h extraction without co-solvent (green).

The efficiency of extraction with ethanol is also shown in Figure 72 b between a recipe 8 sample after 24 h $scCO_2$ extraction time without co-solvent and after 4 h extraction with ethanol as co-solvent. Their results are quite similar to each other, but there is still a difference in the extraction of mass as was shown in Table 14. Based on this, the use of co-solvent can speed up the extraction process for this recipe, but flaw examination and co-solvent flow optimization should be done in addition.

The effects of ethanol as a co-solvent on recipes 9 and 10 and the effect of isopropanol as co-solvent for recipe 10 are shown in TGA data in Figure 73 a–b. For recipe 9, no major difference is seen in the TGA curve in a 2 h test with and without ethanol co-solvent. According to the mass decrease data in Table 14, less monomer was extracted with ethanol for this recipe. The TGA should be repeated to confirm changes, as the TGA sample weighs only 10–20 mg and if a presentable sample piece is not chosen, the results may vary.

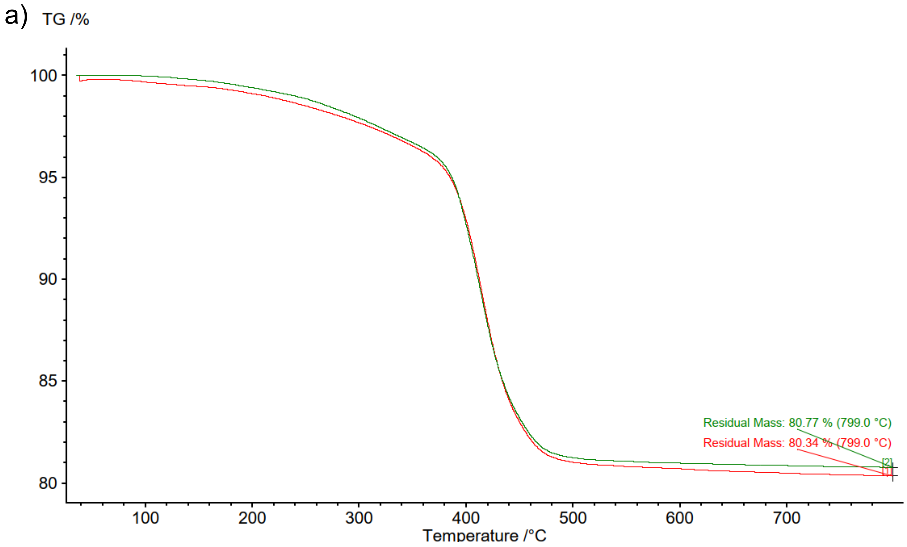

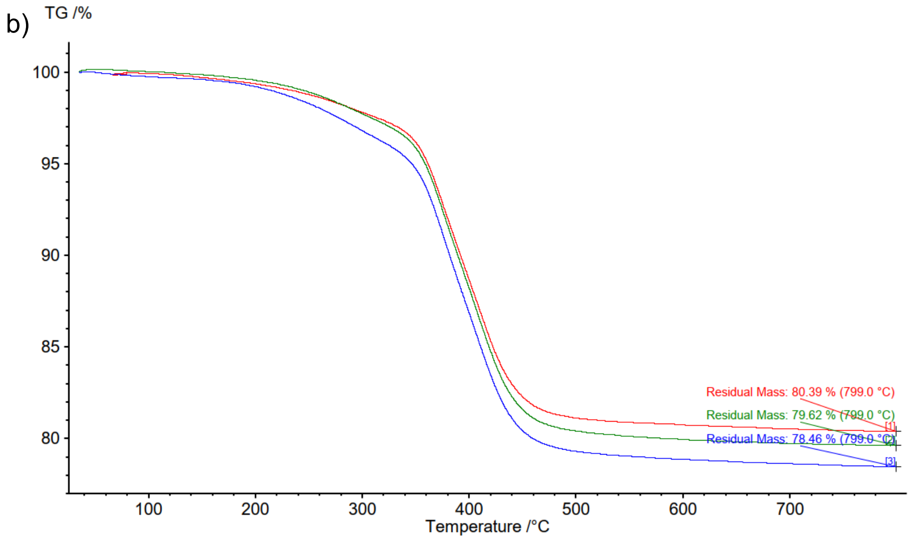

Figure 73: TGA data after $scCO_2$ extraction. a) recipe 9 (50 vol-% alumina, 37.5 vol-% DDDA, 2.5 vol-% PEGMA200, 10 vol-% PEG), 2 h extraction without co-solvent (green) and 2 h with ethanol as co-solvent (red). b) Recipe 10 (50 vol-% alumina, 12.5 vol-% DDDA, 12.5 vol-% PGTA, 15 vol-% ECC, 10 vol-% PEG), 2 h extraction without co-solvent (green), with 2h extraction with ethanol (red) and 2h extraction with isopropanol (blue) as co-solvent.

As already indicated by the mass decrease results in Table 14, for recipe 10 isopropanol was a better solvent compared to ethanol, that in addition caused cracks on the structure. As a conclusion, the use of co-solvent can speed up the $scCO_2$ extraction, but it may not be suitable for all slurry recipes and the choice of co-solvent effects the extraction rate and delamination of samples. Further experiments should be made to make further conclusions.

7.9 Error sources and variables

The major challenge of this thesis was the significant number of variables linked to the whole process from mixing chemicals to a final $scCO_2$ extracted print. The first one of them was the role of the user. Everyone does work tasks slightly differently and this process includes many steps, as described in Chapter 6, in which small details can make a difference. Already the choices of chemicals in the slurry recipe determine what kind of product can be expected. The number and type of different polymerization methods, discussed in Chapter 4, affect the properties of the green body and thus the final part. The mass ratio between fast curing monomers and slow curing monomers or inert additives, the type and amount of photoinitiators or dispersion agent used, all affect the curing process, crosslinking conversion, sample handling and thermal treatment programs.

As presented in Chapters 2 and 3, the type of ceramic powder, its particle size distribution, solid content in slurry and refractive index affect viscosity, conversion, light scattering, penetration depth, mechanical properties, and density. If the slurry is stored before usage, its shelf life also needs to be considered.

Preparation of slurries has many steps as well. The same weighing scale should be used throughout the whole process and the scale should be calibrated before weighing. The scale accuracy and the allowed error in computed amounts of chemicals affect the chemical ratios in the slurry. The measurement error of ±1% of desired substance mass also may change the results. The light-curing chemicals should be kept and handled in a dark room or a room with lighting that does not affect the curing. Contaminations from gloves, fume hoods, chemical canisters, weighing cups and spoons are possible. Contaminations, such as dust, chemical residuals from glassware, or impurities from hands, may lead to the cracks and voids in the parts, that were presented in Subsection 7.3.

The way the chemicals are mixed needs to be controlled; the same time and speed needs to be used for all recipes and sedimentation occurring after the mixing needs to be considered. To neglect the effect of sedimentation, a protocol for mixing after slurry storage should be considered. Air bubbles should be removed by vacuum after mixing to avoid flaws during printing. The homogeneity and size of agglomerates in each slurry should be tested to be sure of the slurry characteristics. Proper mixing after storage, air bubble removal or slurry homogenization studies were not conducted during this thesis, however they should be considered in future studies.

Several aspects affect the printing phase, starting from the 3D CAD file creation. The part geometry, height, wall thickness, area and size of the print affect its mechanical properties and diffusion of substances, as was shown in Chapter 3. The individual layer thickness needs to be chosen correctly in relation to the used light intensity and irradiation time to get sufficient adhesion between the adjacent print layers, as was compared in Figure 48. Supports, holes and drainage holes need to be created based on the part geometry. The light exposure per layer and printer moving speed are important to enable enough curing and moving time for a possibly viscous slurry. Therefore, the slurry viscosity (Figure 53) and curing depth (Appendix 5) need to be measured.

As bottom-up SLA was used, there were challenges with samples falling from the printing platform or having more adhesion to the FEP film than the printing platform. This creates an extra parameter to adjust. The printing platform might need to be treated with a primer (that needs to be carefully removed from the printed green body) or sand-blasted, which can create even too high adhesion to the platform and break the samples when attempting to remove them from the platform. Another way to solve the issue was to cure a layer of slurry covering the whole printing area, but then it must be decided how thick the first base layer needs to be and how to remove it from the green body without breaking the print. If the initial layer is cured by hand, its thickness is not controlled. For Prusa SL1S, the printing platform was made of aluminum and for Cerafab7500, it was glass. These materials have different adhesion properties against slurries used.

In the actual printing phase, contaminations might be induced from the resin tank or printing platform. The light source and its power, the LCD-screen, radiation wavelength and amount of light from sunlight or lamps in the laboratory affect the print result. Air bubbles should be removed once the resin is poured in the resin tank but doing this by hand likely leaves some air bubbles in the slurry. The printer technical details, like resolution and calibration procedures, need to be considered when observing possible flaws in the prints.

It was observed that heating lowers the viscosity of ceramic slurries (Figure 54 in Chapter 7), but the heating the whole printing space including the platform may be challenging, creating a temperature gradient in the slurry. In Prusa SL1S printer, there was also no stirring possibility apart from vat tilting, and the resin tank fill level was much higher than in Lithoz CeraFab7500, which mixes the slurry with a blade after each layer, keeping the slurry thickness between 250 and 350 µm. This makes us note that also the printers are very different, creating different print results. Therefore, it must be considered that the sample characteristics from different printers can also be different and changing printers between recipes must be avoided.

Once the print is ready, it must be removed from the platform carefully. This is done by hand with a blade and is a step in which flaws are very easily created. The print washing procedure was different for Prusa and Lithoz prints. The polymeric Prusa prints were dipped into the washing liquid EasyClean Resin Cleaner for 3 min and rinsed with water. The Lithoz prints containing alumina powder were dipped into dibasic ester in an ultrasonic device for 1 min. Once these green bodies are created, their shelf life may not be long, as was seen in the samples that started “sweating” liquid after some days in storage (Figure 74) and the sample may absorb oxygen, preventing from further post-curing during the pre-conditioning phase prior to thermal debinding.

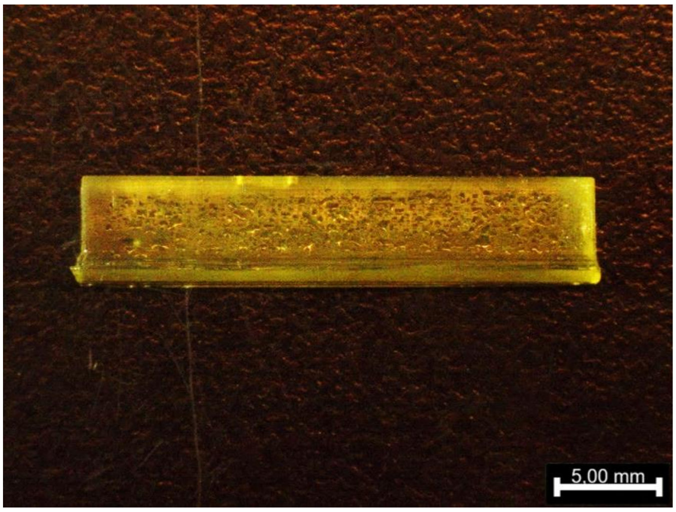

Figure 74: Microscopy image of uncured/inert substances escaping the print after storage.

The green bodies are handled with tweezers and gloves during the rest of the treatments and may collect contaminations from these. This may cause only minor marks on the sample surface (as seen as minor scratches in Figure 47 a), as far as the contamination does not chemically react with the sample. If the green body is stored, it should be placed in a dark container not to cure more due to light exposure. Attention must be paid to the timing of weighing and thermal debinding so that CO_2 possibly adsorbed into the sample, as with Azure Blue samples in Subsection 7.1, has fully left the structure, not causing weighing errors or flaws during thermal debinding.

The $scCO_2$ debinding includes several variables as well. CO_2 is heated before entering the pressure chamber and the pressure is increased up to cylinder pressure by opening the needle valve by hand, as described in the Thar RESS 250 schematic in Subsection 6.1.3. After this, the device increases the pressure with a constant CO_2 flow, but as the density of CO_2 changes dramatically during pressure increase, this phase is not controllable and is different for each test run. Device heaters also overshoot the setpoint temperatures, which causes heating above the desired test temperature for some minutes at an uncontrollable speed. These uncontrollable variables may be the cause for delamination of recipe 6 (Figure 45).

During the $scCO_2$ extraction, the sample is kept at a set temperature and pressure for a selected time. As the solubility of substances with CO_2 is limited, all tests were done with a dynamic CO_2 flow to prevent saturation. The set value for CO_2 flow is however a device setting and its accuracy has not been tested. This makes it difficult to count the co-solvent percentage related to $scCO_2$ when used with a dynamic flow setting, as was done with the co-solvent tests in Subsection 7.8.

As diffusion of $scCO_2$ into the sample starts from the sample surface, sample geometry and test time play an important role in ensuring that dissolvable substances have been removed through the whole structure, as seen in results of different $scCO_2$ extraction times in Subsection 7.3 in Figure 51.

Different substances have different solubility in $scCO_2$, which may affect the removal speed of each substance. For example, a question remains how do the kinetics change once substance A is removed totally and there is still some substance B left? The solvation may be affected if some of the substances create additional phases with $scCO_2$ in the pressure chamber. In addition, clogs and freezing of outlet pipes might affect the removal of $scCO_2$ from the chamber, creating fluctuations in the pressure inside the chamber.

The depressurization phase is better controlled than pressurization in the currently used setup, as it is set as a pressure change per unit of time, controlled by an automated back-pressure regulator (ABPR), but still the pressure and temperature decrease faster during the conversion from $scCO_2$ to CO_2 as the CO_2 density changes rapidly, as introduced in Subsection 2.2.1. During this transformation, it was observed that the samples often “swim” in the liquid CO_2 (Figure 75) in the chamber, especially with the use of ethanol as a co-solvent. The effects of this need to be studied and slower depressurization phase optimized.

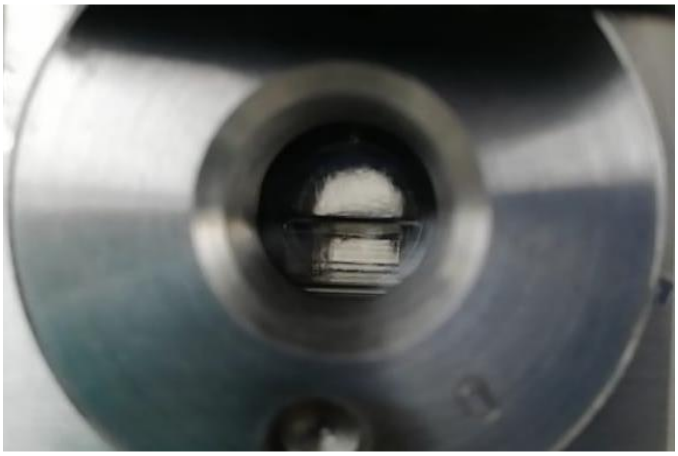

Figure 75: View from Thar RESS250 apparatus pressure chamber window during depressurization from 100 bars to atmospheric pressure.

To make the process used in this thesis repeatable and reliable, very careful instructions and procedure must be followed and more parallel samples used per experiment. More parallel samples, parameter optimization and better organization of a clear test matrix would be needed for quantifying the observed results, but as a proof of concept, the current work has been successful.

8. CONCLUSIONS

The purpose of this thesis was to qualitatively study extraction of substances out of stereolithographically (SLA) printed ceramic parts with the use of supercritical carbon dioxide ($scCO_2$) as a solvent. The aim was to create a way to speed up the thermal debinding process, which makes ceramic manufacturing using SLA economically limited. Hypothetically this could be achieved by removing some of the binder substances prior to pyrolysis, and possibly creating flow channels for the remaining substances to efficiently exit through in the following thermal debinding.

To be economically extracted with $scCO_2$, the solute needs to have weak polarity, low molecular weight, high free volume, flexible molecular backbone with exposed functional groups that are preferably carbonyl, of fluorine. In addition, the substance needs to be non-crosslinked.

In this study, the $scCO_2$ extraction was successfully performed for PEG, uninitiated ECC, PEGMA200, and paraffin oil with different co-solvents, and it was shown to be possible to perform the extraction without creating cracks in the SLA-printed part and the use of right co-solvent can speed the extraction, but further studies are needed to choose a co-solvent that does not cause flaws in the printed part. Based on literature, similar $scCO_2$ extraction procedure has been successfully conducted with hydroxyapatite prints and injection molded ceramic parts, however any similar study with alumina or zirconia powder for SLA-printed parts with PEG or an uninitiated monomer as an extractable binder was not found. Successful extraction gives a promising base to expand the $scCO_2$ extraction studies and to study the extraction method also for printed zirconia parts in the future. Motivation to improve the user safety with the use of $scCO_2$ instead of organic solvents was discussed in Chapter 2, and could be further enhanced with studying i.e., use of plant-derived epoxies or biobased UV-curable caprolactone or lactic acid in the slurry recipes.

In addition, further studies are needed to examine if the $scCO_2$ -exposed parts can be thermally debinded and sintered without cracks, and if the thermal debinding step can be sped up with the $scCO_2$ extraction as a pre-debinding step. The effect of pressure and temperature on the extraction efficiency could be studied further, and to be used in dental applications, it would be important to experiment the effects of $scCO_2$ extraction on the mechanical properties of the ceramic parts.

REFERENCES

[1] Z. Eckel, Z. Chaoyin, J. Martin, A. Jacobsen, W. Carter, and T. Schaedler, “Additive manufacturing of polymer-derived ceramics,” *Science (1979)*, vol. 351, no. 6268, pp. 58–62, Jan. 2016, doi: 10.1126/science.aad2688.

[2] M. N. Rahaman, *Ceramic processing*. CRC Press, 2007. doi: 10.1201/9781315276045.

[3] Z. Z. Fang, *Sintering of Advanced Materials - Fundamentals and Processes*. Woodhead Publishing, 2010. [Online]. Available: https://app.knovel.com/hotlink/khtml/id:kt00926MT3/sintering-advanced-materials/front-matter

[4] J. Deckers, J. Vleugels, and J. P. Kruth, “Additive manufacturing of ceramics: A review,” *Journal of Ceramic Science and Technology*, vol. 5, no. 4. Goller Verlag, pp. 245–260, 2014. doi: 10.4416/JCST2014-00032.

[5] G. Stock, “How to simulate and optimize debinding processes,” Jan. 21, 2020. https://analyzing-testing.netzsch.com/en/blog/2020/how-to-simulate-and-optimize-debinding-processes (accessed Nov. 03, 2022).

[6] C. Valenti *et al.*, “Mechanical properties of 3D-printed prosthetic materials compared with milled and conventional processing: A systematic review and meta-analysis of in vitro studies,” *Journal of Prosthetic Dentistry*. Elsevier Inc., 2022. doi: 10.1016/j.prosdent.2022.06.008.

[7] J. Z. Shen and T. Kosmač, *Advanced ceramics for dentistry*. Waltham, MA: Butterworth-Heinemann, 2014.

[8] Q. Lian, W. Sui, X. Wu, F. Yang, and S. Yang, “Additive manufacturing of ZrO2 ceramic dental bridges by stereolithography,” *Rapid Prototyp J*, vol. 24, no. 1, pp. 114–119, 2018, doi: 10.1108/RPJ-09-2016-0144.

[9] A. Barazanchi, K. C. Li, B. Al-Amleh, K. Lyons, and J. N. Waddell, “Additive Technology: Update on Current Materials and Applications in Dentistry,” *Journal of Prosthodontics*, vol. 26, no. 2, pp. 156–163, Feb. 2017, doi: 10.1111/jopr.12510.

[10] R. López-Píriz *et al.*, “Current state-of-the-art and future perspectives of the three main modern implant-dentistry concerns: Aesthetic requirements, mechanical properties, and peri-implantitis prevention,” *Journal of Biomedical Materials Research - Part A*. John Wiley and Sons Inc., 2019. doi: 10.1002/jbm.a.36661.

[11] S. Tasaki, S. Kirihara, and T. Soumura, “Fabrication of Ceramic Dental Crowns by using Stereolithography and Powder Sintering Process,” *Advanced Processing and Manufacturing Technologies for Structural and Multifunctional Materials V*, vol. 32, no. 8, pp. 141–146, 2011, doi: 10.1002/9781118095379.ch16.

[12] E. Nishikawa, N. Wakao, and N. Nakashima, “Binder Removal from Ceramic Green Body in the Environment of Supercritical Carbon Dioxide with and without Entrainers,” *J Supercrit Fluids*, vol. 4, pp. 265–269, 1991.

[13] J. J. A. Barry *et al.*, “In vitro study of hydroxyapatite-based photocurable polymer composites prepared by laser stereolithography and supercritical fluid extraction,” *Acta Biomater*, vol. 4, no. 6, pp. 1603–1610, 2008, doi: 10.1016/j.actbio.2008.05.024.

[14] V. K. Popov, A. v Evseev, A. L. Ivanov, V. v Roginski, A. I. Volozhin, and S. M. Howdle, “Laser stereolithography and supercritical fluid processing for custom-designed implant fabrication,” *J Mater Sci Mater Med*, vol. 15, pp. 123–128, 2004.

[15] J. M. DeSimone and W. Tumas, *Green Chemistry Using Liquid and Supercritical Carbon Dioxide*. Oxford, UNITED STATES: Oxford University Press, Incorporated, 2003. [Online]. Available: http://ebookcentral.proquest.com/lib/tampere/detail.action?docID=4703192

[16] A. J. Hunt and T. M. Attard, “Green Chemistry Series No. 57 Supercritical and Other High-pressure Solvent Systems: For Extraction, Reaction and Material Processing,” Royal Society of Chemistry, 2018. [Online]. Available: www.rsc.org

[17] T. Chartier, E. Delhomme, J. F. Baumard, P. Marteau, P. Subra, and R. Tufeu, “Solubility, in supercritical carbon dioxide, of paraffin waxes used as binders for low-pressure injection molding,” *Ind Eng Chem Res*, vol. 38, no. 5, pp. 1904–1910, 1999, doi: 10.1021/ie980552e.

[18] J. K. Bal *et al.*, “Swelling of Poly(n-butyl methacrylate) Films Exposed to Supercritical Carbon Dioxide: A Comparative Study with Polystyrene,” *Langmuir*, vol. 32, no. 7, pp. 1716–1722, Feb. 2016, doi: 10.1021/acs.langmuir.5b04436.

[19] M. Champeau, J. M. Thomassin, C. Jérôme, and T. Tassaing, “In situ FTIR micro-spectroscopy to investigate polymeric fibers under supercritical carbon dioxide: CO2 sorption and swelling measurements,” *Journal of Supercritical Fluids*, vol. 90, pp. 44–52, 2014, doi: 10.1016/j.supflu.2014.03.006.

[20] R. v. Shende and S. J. Lombardo, “Supercritical extraction with carbon dioxide and ethylene of poly(vinyl butyral) and dioctyl phthalate from multilayer ceramic capacitors,” *Journal of Supercritical Fluids*, vol. 23, pp. 153–162, Feb. 2002, [Online]. Available: www.elsevier.com/locate/supflu

[21] N. Merilaita, T. Vastamäki, A. Ismailov, E. Levänen, and M. Järveläinen, “Stereolithography as a manufacturing method for a hierarchically porous ZSM-5 zeolite structure with adsorption capabilities,” *Ceram Int*, vol. 47, no. 8, pp. 10742–10748, Apr. 2021, doi: 10.1016/j.ceramint.2020.12.190.

[22] S. Zakeri, T. Vastamäki, M. Honkanen, M. Järveläinen, M. Vippola, and E. Levänen, “Fabrication of self-supporting structures made of washcoat materials (γ-Al2O3-CeO2) by ceramic stereolithography: Towards digital manufacturing of enhanced catalytic converters,” *Mater Des*, vol. 210, Nov. 2021, doi: 10.1016/j.matdes.2021.110115.

[23] T. Vastamäki, “Stereolithography Ceramic 3D-printing,” Tampere University, Tampere, 2019. Accessed: Nov. 03, 2022. [Online]. Available: https://trepo.tuni.fi/handle/123456789/27168

[24] V. Goodship and E. Ogur, *Polymer Processing with Supercritical Fluids*. Shrewsbury, UNITED STATES: iSmithers Rapra Publishing, 2004. [Online]. Available: http://ebookcentral.proquest.com/lib/tampere/detail.action?docID=476896

[25] T. Wu and B. Han, “Supercritical Carbon Dioxide (CO2) as Green Solvent,” in *Green Chemistry and Chemical Engineering*, B. Han and T. Wu, Eds. New York, NY: Springer New York, 2019, pp. 173–197. doi: 10.1007/978-1-4939-9060-3_391.

[26] A. Royer, T. Barriere, and Y. Bienvenu, “Influence of supercritical debinding and processing parameters on final properties of injection-moulded Inconel 718,” *Powder Technol*, vol. 336, pp. 311–317, Aug. 2018, doi: 10.1016/j.powtec.2018.05.047.

[27] Y. Lakhdar, C. Tuck, J. Binner, A. Terry, and R. Goodridge, “Additive manufacturing of advanced ceramic materials,” *Progress in Materials Science*, vol. 116. Elsevier Ltd, Feb. 01, 2021. doi: 10.1016/j.pmatsci.2020.100736.

[28] L. H. Sperling, *Introduction to Physical Polymer Science*. Hoboken, UNITED STATES: John Wiley & Sons, Incorporated, 2005. [Online]. Available: http://ebookcentral.proquest.com/lib/tampere/detail.action?docID=242875

[29] S. Somiya, *Handbook of Advanced Ceramics- Materials, Applications, Processing, and Properties*, vol. 2. Elsevier, 2013. [Online]. Available: https://app.knovel.com/hotlink/pdf/id:kt00BWTI61/handbook-advanced-ceramics/title-page

[30] M. Dehurtevent, L. Robberecht, J. C. Hornez, A. Thuault, E. Deveaux, and P. Béhin, “Stereolithography: A new method for processing dental ceramics by additive computer-aided manufacturing,” *Dental Materials*, vol. 33, no. 5, pp. 477–485, May 2017, doi: 10.1016/j.dental.2017.01.018.

[31] S. Manotham and P. Tesavibul, “Effect of particle size on mechanical properties of alumina ceramic processed by photosensitive binder jetting with powder spattering technique,” *J Eur Ceram Soc*, vol. 42, no. 4, pp. 1608–1617, Apr. 2022, doi: 10.1016/j.jeurceramsoc.2021.11.062.

[32] V. Carnicer, C. Alcázar, M. J. Orts, E. Sánchez, and R. Moreno, “Microfluidic rheology: A new approach to measure viscosity of ceramic suspensions at extremely high shear rates,” *Open Ceramics*, vol. 5, Mar. 2021, doi: 10.1016/j.oceram.2020.100052.

[33] A. Bove, F. Calignano, M. Galati, and L. Iuliano, “Photopolymerization of Ceramic Resins by Stereolithography Process: A Review,” *Applied Sciences (Switzerland)*, vol. 12, no. 7. MDPI, Apr. 01, 2022. doi: 10.3390/app12073591.

[34] P. J. Bártolo, Ed., *Stereolithography: Materials, Processes and Applications*. Springer, 2011. doi: 10.1007/978-0-387-92904-0.

[35] S. Jang, S. Park, and C. J. Bae, “Development of ceramic additive manufacturing: process and materials technology,” *Biomedical Engineering Letters*, vol. 10, no. 4. Springer Verlag, pp. 493–503, Nov. 01, 2020. doi: 10.1007/s13534-020-00175-4.

[36] G. Mitteramskogler *et al.*, “Light curing strategies for lithography-based additive manufacturing of customized ceramics,” *Addit Manuf*, vol. 1, pp. 110–118, Oct. 2014, doi: 10.1016/j.addma.2014.08.003.

[37] H. Wu *et al.*, “Effect of the particle size and the debinding process on the density of alumina ceramics fabricated by 3D printing based on stereolithography,” *Ceram Int*, vol. 42, no. 15, pp. 17290–17294, Nov. 2016, doi: 10.1016/j.ceramint.2016.08.024.

[38] T. R. Crompton, *Thermal Methods of Polymer Analysis*. Shrewsbury: Smithers Rapra, 2013. [Online]. Available: http://libproxy.tuni.fi/login?url=https://search.ebscohost.com/login.aspx?direct=true&AuthType=cookie,ip,uid&db=e000xww&AN=561955&site=ehost-live&scope=site

[39] S. Zhang, I. A. Sutejo, J. Kim, Y. J. Choi, C. W. Gal, and H. S. Yun, “Fabrication of Complex Three-Dimensional Structures of Mica through Digital Light Processing-Based Additive Manufacturing,” *Ceramics*, vol. 5, no. 3, pp. 562–574, Sep. 2022, doi: 10.3390/ceramics5030042.

[40] Y. Pan *et al.*, “Effect of Holding Time During Sintering on Microstructure and Properties of 3D Printed Alumina Ceramics,” *Front Mater*, vol. 7, Apr. 2020, doi: 10.3389/fmats.2020.00054.

[41] S. Zakeri, M. Vippola, and E. Levänen, “A comprehensive review of the photopolymerization of ceramic resins used in stereolithography,” *Additive Manufacturing*, vol. 35. Elsevier B.V., Oct. 01, 2020. doi: 10.1016/j.addma.2020.101177.

[42] T. Chartier, M. Ferrato, and J.-F. Baumard, “Influence of the Debinding Method on the Mechanical Properties of Plastic Formed Ceramics,” *J Eur Ceram Soc*, vol. 15, pp. 899–903, Mar. 1995.

[43] A.-K. Hofer, A. Kocjan, and R. Bermejo, “High-strength lithography-based additive manufacturing of ceramic components with rapid sintering,” *Addit Manuf*, vol. 59, p. 103141, Nov. 2022, doi: 10.1016/j.addma.2022.103141.

[44] I. Denry and J. R. Kelly, “Emerging ceramic-based materials for dentistry,” *Journal of Dental Research*, vol. 93, no. 12. SAGE Publications Inc., pp. 1235–1242, Dec. 25, 2014. doi: 10.1177/0022034514553627.

[45] John. A. Hyatt, “Liquid and Supercritical Carbon Dioxide as Organic Solvents,” *Journal of Organic Chemistry*, vol. 49, 1984.

[46] A. Kaleva, “Zinc Surface Functionalization: Artificial Patination with CO2,” Tampere University, Tampere, 2021. Accessed: Nov. 03, 2022. [Online]. Available: https://urn.fi/URN:ISBN:978-952-03-1876-5

[47] M.-A. Porter, “Effects of Binder Systems for Metal Injection Moulding,” Luleå University of Technology, Luleå, 2003.

[48] T. Chartier, E. Delhomme, J. F. Baumard, P. Marteau, and R. Tufeu, “Extraction of binders with supercritical carbon dioxide,” *Key Eng Mater*, no. 136 PART I, pp. 4–7, 1997, doi: 10.4028/www.scientific.net/kem.132-136.4.

[49] S. P. Nalawade, F. Picchioni, and L. P. B. M. Janssen, “Supercritical carbon dioxide as a green solvent for processing polymer melts: Processing aspects and applications,” *Progress in Polymer Science (Oxford)*, vol. 31, no. 1. Elsevier Ltd, pp. 19–43, 2006. doi: 10.1016/j.progpolymsci.2005.08.002.

[50] S. G. Kazarian, “Polymer Processing with Supercritical Fluids,” *Polymer Science*, vol. 42, pp. 78–101, 2000.

[51] T. Chartier, M. Ferrato, and J. E. Baumardat, “Supercritical Debinding of Injection Molded Ceramics,” *J Am. Ceram. Soc*, vol. 78, pp. 1787–92, 1995.

[52] T. Chartier, E. Delhomme, and J. F. Baumard, “Mechanisms of binder removal involved in supercritical debinding of injection moulded ceramics,” *Journal de Physique III*, vol. 7, no. 2, pp. 291–302, 1997, doi: 10.1051/jp3:1997122.

[53] Y. H. Kim, Y. W. Lee, J. K. Park, C. H. Lee, and J. S. Lim, “Supercritical carbon dioxide debinding in metal injection molding (MIM) process,” *Korean Journal of Chemical Engineering*, vol. 19, no. 6, pp. 986–991, 2002, doi: 10.1007/BF02707221.

[54] F. Bordet, T. Chartier, and J.-F. Baumard, “The Use of Co-Solvents in Supercritical Debinding of Ceramics,” *Journal of The European Ceramic Society - J Eur Ceram Soc*, vol. 22, pp. 1067–1072, Jul. 2002, doi: 10.1016/S0955-2219(01)00398-3.

[55] M. A. McHugh and V. J. Krukonis, “Supercritical Fluid Extraction (2nd Edition).” Elsevier, 1994. [Online]. Available: https://app.knovel.com/hotlink/toc/id:kpSFEE0001/supercritical-fluid-extraction/supercritical-fluid-extraction

[56] H. Liu *et al.*, “Role of supercritical carbon dioxide (scCO2) in fabrication of inorganic-based materials: a green and unique route,” *Science and Technology of Advanced Materials*, vol.

22, no. 1. Taylor and Francis Ltd., pp. 695–717, 2021. doi: 10.1080/14686996.2021.1955603.

[57] MarketsandMarkets Research Private Ltd., “3D Printing Ceramics Market,” Apr. 2021. https://www.marketsandmarkets.com/Market-Reports/3d-printing-ceramic-market-26085601.html (accessed Nov. 03, 2022).

[58] All3DP, “The Best Ceramic 3D Printers of 2022,” Jan. 04, 2022. https://all3dp.com/2/ceramic-3d-printer-ceramic-3d-printing/ (accessed Nov. 03, 2022).

[59] H. Wu *et al.*, “Fabrication of dense zirconia-toughened alumina ceramics through a stereolithography-based additive manufacturing,” *Ceram Int*, vol. 43, no. 1, pp. 968–972, Jan. 2017, doi: 10.1016/j.ceramint.2016.10.027.

[60] T. Chartier *et al.*, “Influence of irradiation parameters on the polymerization of ceramic reactive suspensions for stereolithography,” *J Eur Ceram Soc*, vol. 37, no. 15, pp. 4431–4436, Dec. 2017, doi: 10.1016/j.jeurceramsoc.2017.05.050.

[61] Z. Xing, W. Liu, Y. Chen, and W. Li, “Effect of plasticizer on the fabrication and properties of alumina ceramic by stereolithography-based additive manufacturing,” *Ceram Int*, vol. 44, no. 16, pp. 19939–19944, Nov. 2018, doi: 10.1016/j.ceramint.2018.07.259.

[62] J. M. Suominen *et al.*, “Three-dimensional printing of zirconia: characterization of early stage material properties,” *Biomater Investig Dent*, vol. 6, no. 1, pp. 23–31, Dec. 2019, doi: 10.1080/26415275.2019.1640608.

[63] P. Robles Martinez, A. W. Basit, and S. Gaisford, “The History, Developments and Opportunities of Stereolithography,” in *3D Printing of Pharmaceuticals*, A. W. Basit and S. Gaisford, Eds. Cham: Springer International Publishing, 2018, pp. 55–79. doi: 10.1007/978-3-319-90755-0_4.

[64] Prusa Research a.s., “Photopolymer Resin Safety Data Sheet.” Jan. 15, 2020.

[65] T. Drost, S. Reimann, M. Frentzen, and J. Meister, “Effectiveness of photopolymerization in composite resins using a novel 445-nm diode laser in comparison to LED and halogen bulb technology,” *Lasers Med Sci*, vol. 34, no. 4, pp. 729–736, Jun. 2019, doi: 10.1007/s10103-018-2651-1.

[66] LightLab Sweden AB, “What is UV light?,” 2021. https://www.purefize.com/about-uv-light/ (accessed Nov. 03, 2022).

[67] 3D HUBS B.V., “What is SLA printing?,” 2022. https://www.hubs.com/knowledge-base/what-is-sla-3d-printing/ (accessed Nov. 03, 2022).

[68] C. Hinczewski, S. Corbel, and T. Chartier, “Ceramic Suspensions Suitable for Stereolithography,” *J Eur Ceram Soc*, vol. 18, pp. 583–590, 1998.

[69] C. J. Bae, A. Ramachandran, K. Chung, and S. Park, “Ceramic stereolithography: Additive manufacturing for 3D complex ceramic structures,” *Journal of the Korean Ceramic Society*, vol. 54, no. 6, pp. 470–477, Nov. 2017, doi: 10.4191/kcers.2017.54.6.12.

[70] RheoSense, “What is the viscosity of...?,” Jun. 06, 2017. https://blog.rheosense.com/what-is-the-viscosity-of (accessed Nov. 03, 2022).

[71] M. Hartmann, “Lithography-based Ceramic Manufacturing (LCM)- a bottom-up DLP-Technology,” 2022. https://euroceram.org/en/eu/bottom-up-process (accessed Nov. 03, 2022).

[72] Z. Xing, H. Zhou, W. Liu, J. Nie, Y. Chen, and W. Li, “Efficient cleaning of ceramic green bodies with complex architectures fabricated by stereolithography-based additive manufacturing via high viscoelastic paste,” *Addit Manuf*, vol. 55, Jul. 2022, doi: 10.1016/j.addma.2022.102809.

[73] N. Kovacev, S. Li, and K. Essa, “Effect of the preparation techniques of photopolymerizable ceramic slurry and printing parameters on the accuracy of 3D printed lattice structures,” *J Eur Ceram Soc*, vol. 41, no. 15, pp. 7734–7743, Dec. 2021, doi: 10.1016/j.jeurceramsoc.2021.08.052.

[74] R. Menzel, Ed., “Linear Interactions Between Light and Matter,” in *Photonics: Linear and Nonlinear Interactions of Laser Light and Matter*, Berlin, Heidelberg: Springer Berlin Heidelberg, 2007, pp. 93–171. doi: 10.1007/978-3-540-45158-7_3.

[75] F. A. Obaid and A. M. Al-Rahim, “Imaging of 2D Seismic Data Using Time Migration of Ajeel Oilfield, Central of Iraq Western Desert-Iraq View project Seismic inversion and attribute enhancement View project,” 2020, doi: 10.13140/RG.2.2.21505.28003.

[76] C. Sun and X. Zhang, “The influences of the material properties on ceramic micro-stereolithography,” *Sensors and Actuators A*, vol. 101, pp. 364–370, Jul. 2002.

[77] L. Chen *et al.*, *Advances in Condensed Matter Optics*. Berlin/Boston, GERMANY: De Gruyter, Inc., 2014. [Online]. Available: http://ebookcentral.proquest.com/lib/tampere/detail.action?docID=1524410

[78] H. Moosmüller and J. A. Ogren, “Parameterization of the aerosol upscatter fraction as function of the backscatter fraction and their relationships to the asymmetry parameter for radiative transfer calculations,” *Atmosphere*, vol. 8, no. 8. MDPI AG, Jul. 25, 2017. doi: 10.3390/atmos8080133.

[79] M. Ilie, J. C. Kneip, S. Matteï, A. Nichici, C. Roze, and T. Girasole, “Laser beam scattering effects in non-absorbent inhomogenous polymers,” *Opt Lasers Eng*, vol. 45, no. 3, pp. 405–412, 2007, doi: 10.1016/j.optlaseng.2006.07.004.

[80] C. Qian, K. Hu, J. Li, P. Li, and Z. Lu, “The effect of light scattering in stereolithography ceramic manufacturing,” *J Eur Ceram Soc*, vol. 41, no. 14, pp. 7141–7154, Nov. 2021, doi: 10.1016/j.jeurceramsoc.2021.07.017.

[81] S. P. Gentry and J. W. Halloran, “Absorption effects in photopolymerized ceramic suspensions,” *J Eur Ceram Soc*, vol. 33, no. 10, pp. 1989–1994, Sep. 2013, doi: 10.1016/j.jeurceramsoc.2013.03.004.

[82] B. Oezkan, F. Sameni, S. Karmel, D. S. Engstrøm, and E. Sabet, “A systematic study of vat-polymerization binders with potential use in the ceramic suspension 3D printing,” *Addit Manuf*, vol. 47, Nov. 2021, doi: 10.1016/j.addma.2021.102225.

[83] E. Johansson, O. Lidström, J. Johansson, O. Lyckfeldt, and E. Adolfsson, “Influence of resin composition on the defect formation in alumina manufactured by stereolithography,” *Materials*, vol. 10, no. 2, 2017, doi: 10.3390/ma10020138.

[84] S. Eränen, “Silicon Dioxides,” in *Handbook of Silicon Based MEMS Materials and Technologies*, Elsevier Inc., 2010, pp. 137–148. doi: 10.1016/B978-0-8155-1594-4.00008-5.

[85] J. Schweiger, D. Bomze, and M. Schwentenwein, “3D Printing of Zirconia–What is the Future?,” *Curr Oral Health Rep*, vol. 6, Dec. 2019, doi: 10.1007/s40496-019-00243-4.

[86] T. Chartier *et al.*, “Additive manufacturing to produce complex 3D ceramic parts,” *Journal of Ceramic Science and Technology*, vol. 6, no. 2. Goller Verlag, pp. 95–104, Jun. 01, 2015. doi: 10.4416/JCST2014-00040.

[87] T. Chartier, A. Badev, Y. Abouliatim, P. Lebaudy, and L. Lecamp, “Stereolithography process: Influence of the rheology of silica suspensions and of the medium on polymerization kinetics - Cured depth and width,” *J Eur Ceram Soc*, vol. 32, no. 8, pp. 1625–1634, Jul. 2012, doi: 10.1016/j.jeurceramsoc.2012.01.010.

[88] R. R. Braga, R. Y. Ballester, and J. L. Ferracane, “Factors involved in the development of polymerization shrinkage stress in resin-composites: A systematic review,” *Dental Materials*, vol. 21, no. 10, pp. 962–970, 2005, doi: 10.1016/j.dental.2005.04.018.

[89] L. F. M. da Silva, A. Öchsner, and R. D. Adams, Eds., *Handbook of Adhesion Technology*, 2nd ed., vol. 2. Berlin: Springer, 2011.

[90] W. Brockmann, P. L. Geib, J. Klingen, and B. Schröder, *Adhesive Bonding: Materials, Applications and Technology*. Weinheim: Wiley-VCH, 2009.

[91] E. M. Petrie, *Handbook of Adhesives and Sealants*, 2nd ed. New York: McGraw-Hill Education, 2007. [Online]. Available: https://www.accessengineeringlibrary.com/content/book/9780071479165

[92] A. Thakur and A. G. Tesfay, “Adhesion Characterization of micro components fabricated by Micro stereo lithography,” *REST Journal on Emerging trends in Modelling and Manufacturing*, vol. 3, no. 1, pp. 1–6, 2017, [Online]. Available: www.restpublisher.com/journals/jemm

[93] R. D. Adams, “17.5 Strength and Durability,” in *Adhesive Bonding - Science, Technology and Applications*, Woodhead Publishing. [Online]. Available: https://app.knovel.com/hotlink/pdf/id:kt00C5Y5I1/adhesive-bonding-science/boats-and--strength-durability

[94] S. Ebnesajjad and A. H. Landrock, *Adhesives Technology Handbook (3rd Edition)*, 3rd ed. Elsevier, 2015. [Online]. Available: https://app.knovel.com/hotlink/toc/id:kpATHE0004/adhesives-technology/adhesives-technology

[95] K. G. Swift and J. D. Booker, *Manufacturing Process Selection Handbook*. Oxford: Butterworth-Heinemann, 2013. [Online]. Available: http://libproxy.tuni.fi/login?url=https://search.ebscohost.com/login.aspx?direct=true&AuthType=cookie,ip,uid&db=nlebk&AN=486522&site=ehost-live&scope=site

[96] L. Butterfield *et al.*, “Morphology and Thermomechanical Properties in Epoxy Acrylate Interpenetrated Networks,” *Macromol Symp*, vol. 365, no. 1, pp. 59–66, Jul. 2016, doi: 10.1002/masy.201650012.

[97] T. Sarbu, T. Styranec, and E. J. Beckman, “Non-fluorous polymers with very high solubility in supercritical CO2 down to low pressures,” *Nature*, vol. 405, no. 6783, pp. 165–168, 2000, doi: 10.1038/35012040.

[98] C. D. Wick, J. I. Siepmann, and D. N. Theodorou, “Microscopic origins for the favorable solvation of carbonate ether copolymers in CO2,” *J Am Chem Soc*, vol. 127, no. 35, pp. 12338–12342, Sep. 2005, doi: 10.1021/ja0510008.

[99] N. S. Muralisrinivasan, *Basics of Polymers : Materials and Synthesis*. New York, [New York] [222 East 46th Street, New York, NY 10017]: Momentum Press, 2016. [Online]. Available: http://libproxy.tuni.fi/login?url=https://search.ebscohost.com/login.aspx?direct=true&AuthType=cookie,ip,uid&db=e000xww&AN=1135117&site=ehost-live&scope=site

[100] Y.-W. Mai and Z.-Z. Yu, “12.5 Types of Rubber-Clay Nanocomposite,” in *Polymer Nanocomposites*, Woodhead Publishing. [Online]. Available: https://app.knovel.com/hotlink/pdf/id:kt007CWNZA/polymer-nanocomposites-2/types-rubber-clay-nanocomposite

[101] R. A. Pethrick, “10.2.6.4 Chemically Amplified Negative Resists,” in *Polymer Science and Technology for Scientists and Engineers*, Whittles Publishing. [Online]. Available: https://app.knovel.com/hotlink/pdf/id:kt00U65A16/polymer-science-technology/chemically-amplified

[102] A. S. H. Makhlouf, “20.3 Additives and Pigments,” in *Handbook of Smart Coatings for Materials Protection*, Elsevier. [Online]. Available: https://app.knovel.com/hotlink/pdf/id:kt00U7Y8I2/handbook-smart-coatings/additives-pigments

[103] P. Cognard, “5.2.1.1 UV-Curable Acrylate Resins,” in *Handbook of Adhesives and Sealants, Volume 2 - General Knowledge, Application of Adhesives, New Curing Techniques*, Elsevier. [Online]. Available: https://app.knovel.com/hotlink/pdf/id:kt008S1MOJ/handbook-adhesives-sealants-3/uv-curable-acrylate-resins

[104] T. Şucu and M. P. Shaver, “Inherently degradable cross-linked polyesters and polycarbonates: Resins to be cheerful,” *Polymer Chemistry*, vol. 11, no. 40. Royal Society of Chemistry, pp. 6397–6412, Oct. 28, 2020. doi: 10.1039/d0py01226b.

[105] J.-P. Fouassier, J. Laleve, J. Lalevée, and J. Laleve, *Photoinitiators for Polymer Synthesis : Scope, Reactivity, and Efficiency*. Weinheim, GERMANY: John Wiley & Sons, Incorporated, 2012. [Online]. Available: http://ebookcentral.proquest.com/lib/tampere/detail.action?docID=1048249

[106] L. W. McKeen, “Film Properties of Plastics and Elastomers (3rd Edition).” Elsevier, 2012. [Online]. Available: https://app.knovel.com/hotlink/toc/id:kpFPPEE001/film-properties-plastics/film-properties-plastics

[107] R. Nomoto, “Effect of Light Wavelength on Polymerization of Light-cured Resins,” *Dent Mater J*, vol. 16, no. 1, pp. 60–73, 1997, doi: 10.4012/dmj.16.60.

[108] M. A. Tehfe, F. Louradour, J. Lalevée, and J. P. Fouassier, “Photopolymerization reactions: On the way to a green and sustainable chemistry,” *Applied Sciences (Switzerland)*, vol. 3, no. 2, pp. 490–514, Jun. 2013, doi: 10.3390/app3020490.

[109] “Merck,” Nov. 03, 2022. https://www.sigmaaldrich.com/FI/en/ (accessed Nov. 03, 2022).

[110] J. Lange, N. Altmann, C. T. Kelly, and P. J. Halley, “Understanding vitrification during cure of epoxy resins using dynamic scanning calorimetry and rheological techniques,” *Polymer (Guildf)*, vol. 41, 2000.

[111] B. I. Suh, L. Feng, / David, H. Pashley, and F. R. Tay, “Factors Contributing to the Incompatibility Between Simplified-step Adhesives and Chemically-cured or Dual-cured Composites. Part III. Effect of Acidic Resin Monomers,” *J Adhes Dent*, vol. 5, no. 4, pp. 267–282, 2003.

[112] C. J. Bae and J. W. Halloran, “Influence of residual monomer on cracking in ceramics fabricated by stereolithography,” *Int J Appl Ceram Technol*, vol. 8, no. 6, pp. 1289–1295, Nov. 2011, doi: 10.1111/j.1744-7402.2010.02578.x.

[113] P. Gill, T. T. Moghadam, and B. Ranjbar, “Differential Scanning Calorimetry Techniques: Applications in Biology and Nanoscience,” *Journal of Biomolecular Techniques*, vol. 21, pp. 167–193, 2010.

[114] R. Hardis, J. L. P. Jessop, F. E. Peters, and M. R. Kessler, “Cure kinetics characterization and monitoring of an epoxy resin using DSC, Raman spectroscopy, and DEA,” *Compos Part A Appl Sci Manuf*, vol. 49, pp. 100–108, 2013, doi: 10.1016/j.compositesa.2013.01.021.

[115] P. Y. Bruice, *Organic chemistry*. Pearson Education, 2016.

[116] I. L. de Camargo, M. M. Morais, C. A. Fortulan, and M. C. Branciforti, “A review on the rheological behavior and formulations of ceramic suspensions for vat photopolymerization,” *Ceram Int*, vol. 47, no. 9, pp. 11906–11921, May 2021, doi: 10.1016/j.ceramint.2021.01.031.

[117] "Sarbio 6201 Difunctional Methacrylate Monomer Safety Data Sheet." Sartomer Arkema, Dec. 13, 2019.

[118] A. Bagheri and J. Jin, "Photopolymerization in 3D Printing," *ACS Applied Polymer Materials*, vol. 1, no. 4. American Chemical Society, pp. 593–611, Apr. 12, 2019. doi: 10.1021/acsapm.8b00165.

[119] "Sarbio 5300 Trifunctional Acrylate Safety Data Sheet." Sartomer Arkema, Mar. 08, 2016.

[120] "Sarbio 5201 1,10 Decanediol Diacrylate Safety Data Sheet." Sartomer Arkema, Jul. 02, 2019.

[121] M. Sangermano, W. Carbonaro, G. Malucelli, and A. Priola, "UV-cured interpenetrating acrylic-epoxy polymer networks: Preparation and characterization," *Macromol Mater Eng*, vol. 293, no. 6, pp. 515–520, Jun. 2008, doi: 10.1002/mame.200800020.

[122] J. Parameswaranpillai, N. Hameed, J. Pionteck, and E. M. Woo, *Handbook of Epoxy Blends*. Springer Nature, 2017. doi: 10.1007/978-3-319-40043-3.

[123] A. Vitale, M. Sangermano, R. Bongiovanni, P. Burtscher, and N. Moszner, "Visible light curable restorative composites for dental applications based on epoxy monomer," *Materials*, vol. 7, no. 1, pp. 554–562, 2014, doi: 10.3390/ma7010554.

[124] W. Miao, J. W. Halloran, and D. E. Brei, "Suspension polymerization casting of lead zirconate titanate, part I: Acrylamide hydrogel system," *J Mater Sci*, vol. 38, no. 12, pp. 2571–2579, Jun. 2003, doi: https://doi.org/10.1023/A:1024466014836.

[125] Z. Wang, C. Huang, J. Wang, and B. Zou, "Development of a novel aqueous hydroxyapatite suspension for stereolithography applied to bone tissue engineering," *Ceram Int*, vol. 45, no. 3, pp. 3902–3909, Feb. 2019, doi: 10.1016/j.ceramint.2018.11.063.

[126] I. L. de Camargo, R. Erbereli, H. Taylor, and C. A. Fortulan, "3Y-TZP DLP additive manufacturing: Solvent-free slurry development and characterization," *Materials Research*, vol. 24, no. 2, 2021, doi: 10.1590/1980-5373-MR-2020-0457.

[127] C. S. Sodré, P. P. A. C. Albuquerque, C. P. Isolan, R. R. Moraes, and L. F. Schneider, "Relative photon absorption determination and the influence of photoinitiator system and water content on C=C conversion, water sorption/solubility of experimental self-etch adhesives," *Int J Adhes Adhes*, vol. 63, pp. 152–157, Dec. 2015, doi: 10.1016/j.ijadhadh.2015.09.005.

[128] I. v. Khudyakov, "Fast photopolymerization of acrylate coatings: Achievements and problems," *Progress in Organic Coatings*, vol. 121. Elsevier B.V., pp. 151–159, Aug. 01, 2018. doi: 10.1016/j.porgcoat.2018.04.030.

[129] M. Benelmekki, "Introduction," in *Nanomaterials*, IOP Publishing, 2019. doi: 10.1088/2053-2571/ab126dch1.

[130] Aptia Engineering, "The basic scientific principles of solvent extraction for hemp processors," Aug. 19, 2020. https://aptiaengineering.com/2020/08/19/science-overview-of-solvent-extraction/ (accessed Nov. 03, 2022).

[131] Y.-P. Sun, *Supercritical fluid technology in materials science and engineering: synthesis, properties, and applications*. New York: Marcel Dekker, 2002.

[132] H.-S. Byun, "Phase Behavior of Poly(ethylene glycol) in Supercritical CO2 , C3H6, and C4H8," *J. Ind. Eng. Chem*, vol. 12, no. 6, pp. 893–899, 2006.

[133] R. B. Yoganathan, R. Mammucari, and N. R. Foster, "Dense gas processing of polymers," *Polymer Reviews*, vol. 50, no. 2, pp. 144–177, Apr. 2010, doi: 10.1080/15583721003698846.

[134] F. Rindfleisch, T. P. DiNoia, and M. A. McHugh, "Solubility of Polymers and Copolymers in Supercritical CO2," *J Phys Chem*, vol. 100, no. 38, pp. 15581–15587, Jan. 1996, doi: 10.1021/jp9615823.

[135] S. G. Kazarian, M. F. Vincent, F. v Bright, C. L. Liotta, and C. A. Eckert, "Specific Intermolecular Interaction of Carbon Dioxide with Polymers," *J Am Chem Soc*, vol. 118, no. 7, pp. 1729–1736, Jan. 1996, doi: 10.1021/ja950416q.

[136] J. G. Drobny and A. L. Moore, *Fluoroelastomers handbook: the definitive user's guide and databook*. Norwich, N.Y: William Andrew, 2005.

[137] A. Mouahid, H. Bouanga, C. Crampon, and E. Badens, "Supercritical CO2 extraction of oil from Jatropha curcas: An experimental and modelling study," *Journal of Supercritical Fluids*, pp. 2–11, Nov. 2018, doi: 10.1016/j.supflu.2017.11.014.

[138] J. Speight, "13.3.2 Paraffin Oil," in *Handbook of Industrial Hydrocarbon Processes*, Elsevier. [Online]. Available: https://app.knovel.com/hotlink/pdf/id:kt0090TM7M/handbook-industrial-hydrocarbon/paraffin-oil

[139] Master Organic Chemistry, “General Chemistry Review,” 2022. https://www.masterorganicchemistry.com/ (accessed Nov. 03, 2022).

[140] A. B. A. de Azevedo, P. Mazzafera, R. S. Mohamed, S. A. B. Vieira De Melo, and T. G. Kieckbusch, “Extraction of caffeine, chlorogenic acids and lipids from green coffee beans using supercritical carbon dioxide and co-solvents,” vol. 25, no. 03, pp. 543–552, [Online]. Available: www.abeq.org.br/bjche

[141] Thermo Scientific, “Basic Organic Functional Group Reference Chart.” https://www.thermofisher.com/blog/materials/a-gift-for-you-an-ftir-basic-organic-functional-group-reference-chart/ (accessed Nov. 03, 2022).

[142] E. Moore, *Fourier Transform Infrared Spectroscopy (FTIR) : Methods, Analysis, and Research Insights*. Hauppauge, New York: Nova Science Publishers, Inc, 2016. [Online]. Available: http://libproxy.tuni.fi/login?url=https://search.ebscohost.com/login.aspx?direct=true&AuthType=cookie,ip,uid&db=e000xww&AN=1419216&site=ehost-live&scope=site

[143] Dental Image Therapy Centres, “What are the different parts of the tooth?,” Jul. 20, 2022. https://www.dentalimage.ca/ask-a-dentist/what-are-the-different-parts-of-the-tooth (accessed Nov. 03, 2022).

[144] Z. Liu *et al.*, “Additive manufacturing of hydroxyapatite bone scaffolds via digital light processing and in vitro compatibility,” *Ceram Int*, vol. 45, no. 8, pp. 11079–11086, Jun. 2019, doi: 10.1016/j.ceramint.2019.02.195.

[145] D. M. Davis, R. M. Watson, and M. E. Packer, “Single tooth crowns supported on hydroxyapatite coated endosseous dental implants: a prospective 5-year study on twenty subjects,” *Int Dent J*, vol. 54, no. 4, pp. 201–205, 2004, [Online]. Available: http://europepmc.org/abstract/MED/15335090

[146] T. Sirisoam, C. Saelee, S. Thiansem, and S. Punyanitya, “Characteristic, Microstructure and Properties of Dense Hydroxyapatite Ceramic from Cockle Shell for Biomaterials,” *Materials Science Forum*, vol. 940, pp. 3–7, Dec. 2018, doi: 10.4028/www.scientific.net/MSF.940.3.

[147] K. Chu, C. Zhao, and F. Ren, “Measuring fracture toughness of human dental enamel at small scale using notched microcantilever beams,” *Biosurf Biotribol*, vol. 7, no. 4, pp. 228–232, Dec. 2021, doi: 10.1049/bsb2.12022.

[148] MatWeb, “Material Property Data: Alumina, 98%, Al2O3.” https://www.matweb.com/search/QuickText.aspx?SearchText=zirconia (accessed Nov. 03, 2022).

[149] J. Yan, B. Taskonak, and J. J. Mecholsky, “Fractography and fracture toughness of human dentin,” *J Mech Behav Biomed Mater*, vol. 2, no. 5, pp. 478–484, Oct. 2009, doi: 10.1016/j.jmbbm.2008.12.002.

[150] H. R. Rezaie, H. B. Rizi, M. M. Rezaei Khamseh, and A. Öchsner, *Advanced Structured Materials A Review on Dental Materials*, vol. 123. Springer Nature, 2020. doi: https://doi.org/10.1007/978-3-030-48931-1.

[151] Finnish Standards Association SFS, “Glass in building - Procedures for goodness of fit and confidence intervals for Weibull distributed glass strength data, SFS-EN 12603.” SFS, Apr. 22, 2003.

[152] A. Ioannidis, D. Bomze, C. H. F. Hämmerle, J. Hüsler, O. Birrer, and S. Mühlemann, “Load-bearing capacity of CAD/CAM 3D-printed zirconia, CAD/CAM milled zirconia, and heat-pressed lithium disilicate ultra-thin occlusal veneers on molars,” *Dental Materials*, vol. 36, no. 4, pp. e109–e116, Apr. 2020, doi: 10.1016/j.dental.2020.01.016.

[153] Z. Mei *et al.*, “Determination of Hardness and Fracture Toughness of Y-TZP Manufactured by Digital Light Processing through the Indentation Technique,” *Biomed Res Int*, vol. 2021, 2021, doi: 10.1155/2021/6612840.

[154] M. Revilla-León, N. Al-Haj Husain, L. Ceballos, M. Özcan, and M. Dent, “Flexural strength and Weibull characteristics of stereolithography additive manufactured versus milled zirconia,” *J Prosthet Dent*, vol. 125, no. 4, pp. 685–690, 2020, doi: https://doi.org/10.1016/j.prosdent.2020.01.019690.

[155] A. C. Branco *et al.*, “Tribological performance of the pair human teeth vs 3D printed zirconia: An in vitro chewing simulation study,” *J Mech Behav Biomed Mater*, vol. 110, Oct. 2020, doi: 10.1016/j.jmbbm.2020.103900.

[156] W. Wang, H. Yu, Y. Liu, X. Jiang, and B. Gao, “Trueness analysis of zirconia crowns fabricated with 3-dimensional printing,” *J Prosthet Dent*, vol. 121, no. 2, pp. 285–291, 2018, doi: https://doi.org/10.1016/j.prosdent.2018.04.012.

[157] M. Dehurtevent *et al.*, "Effect of build orientation on the manufacturing process and the properties of stereolithographic dental ceramics for crown frameworks," *J Prosthet Dent*, vol. 125, no. 3, p. 453, 2020, doi: https://doi.org/10.1016/j.prosdent.2020.01.024.

[158] W. Wang and J. Sun, "Dimensional accuracy and clinical adaptation of ceramic crowns fabricated with the stereolithography technique," *J Prosthet Dent*, vol. 125, no. 4, pp. 657–663, 2020, Accessed: Nov. 03, 2022. [Online]. Available: https://doi.org/10.1016/j.prosdent.2020.02.032

[159] "Sartomer EMEA ," Jul. 04, 2022. https://emea.sartomer.arkema.com/en/product-finders/ (accessed Nov. 03, 2022).

[160] M. Arner, *Statistical Robust Design : An Industrial Perspective*. Somerset, UNITED KINGDOM: John Wiley & Sons, Incorporated, 2014. [Online]. Available: http://ebookcentral.proquest.com/lib/tampere/detail.action?docID=1603266

[161] "Poly(ethylene glycol)." Sigma-Aldrich, Apr. 20, 2020. Accessed: Nov. 03, 2022. [Online]. Available: https://www.sigmaaldrich.com/FI/en/product/aldrich/202398

[162] "3,4-Epoxycyclohexylmethyl 3,4-epoxycyclohexanecarboxylate." Sigma-Aldrich, Sep. 27, 2019. Accessed: Nov. 03, 2022. [Online]. Available: https://www.sigmaaldrich.com/FI/en/product/aldrich/407208

[163] "Phenylbis(2,4,6-trimethylbenzoyl)phosphine." Sigma-Aldrich, Sep. 11, 2019. Accessed: Nov. 03, 2022. [Online]. Available: https://www.sigmaaldrich.com/FI/en/product/aldrich/511447

[164] ChemicalBook, "Phenolic epoxy resin," 2017. https://www.chemicalbook.com/ProductChemicalPropertiesCB32131152_EN.htm (accessed Nov. 03, 2022).

[165] Alfa Chemistry, "Glyceryl propoxy triacrylate," 2022. https://www.alfa-chemistry.com/glyceryl-propoxy-triacrylate-cas-52408-84-1-item-170206.htm (accessed Nov. 03, 2022).

[166] TCI America, "1,10-Bis(acryloyloxy)decane (stabilized with MEHQ)." https://www.tcichemicals.com/GR/en/p/B2937 (accessed Nov. 03, 2022).

[167] O. Dugauguez, "Application of unconventional methods on Inconel 718 MIM components," Université Bourgogne Franche-Comté; Universidad autonóma de Madrid, Madrid, 2020. [Online]. Available: https://tel.archives-ouvertes.fr/tel-02550981

[168] J. Schawe, R. Riesen, J. Widmann, M. Schubnell, and U. Jörimann, "Interpreting DSC Curves, Part 1: Dynamic Measurements." Jan. 2000. Accessed: Nov. 03, 2022. [Online]. Available: https://www.mt.com/de/en/home/applications/Application_Browse_Laboratory_Analytics/Application_Browse_thermal_analysis/TA_UserCom.html#publications

[169] J. Fang, L. Zhang, D. Sutton, X. Wang, and T. Lin, "Needleless melt-electrospinning of polypropylene nanofibres," *J Nanomater*, vol. 2012, 2012, doi: 10.1155/2012/382639.

[170] A. Brangule, R. Šukele, and D. Bandere, "Herbal Medicine Characterization Perspectives Using Advanced FTIR Sample Techniques – Diffuse Reflectance (DRIFT) and Photoacoustic Spectroscopy (PAS)," *Front Plant Sci*, vol. 11, Apr. 2020, doi: 10.3389/fpls.2020.00356.

[171] K. Pandey, R. Kumar, V. Saraswat, M. Kumar, and K. Awasthi, "Functionalized and engineered nanochannels for gas separation," *Pure and Applied Chemistry*, vol. 90, Jan. 2017, doi: 10.1515/pac-2017-0712.

[172] M. G. González, J. C. Cabanelas, and J. Baselga, "Applications of FTIR on Epoxy Resins - Identification, Monitoring the Curing Process, Phase Separation and Water Uptake," in *Infrared Spectroscopy - Materials Science, Engineering and Technology*, InTech, 2012. doi: 10.5772/36323.

[173] W. Reusch, "Infrared Spectroscopy," May 05, 2013. https://www2.chemistry.msu.edu/faculty/reusch/virttxtjml/spectrpy/infrared/infrared.htm (accessed Nov. 03, 2022).

APPENDIX 1: PRELIMINARY TEST DATA

Changes in Prusa Azure Blue Tough resin thickness *b* and height *h* as a result of $scCO_2$ exposure. t=0 is the time immediately after $scCO_2$ exposure.

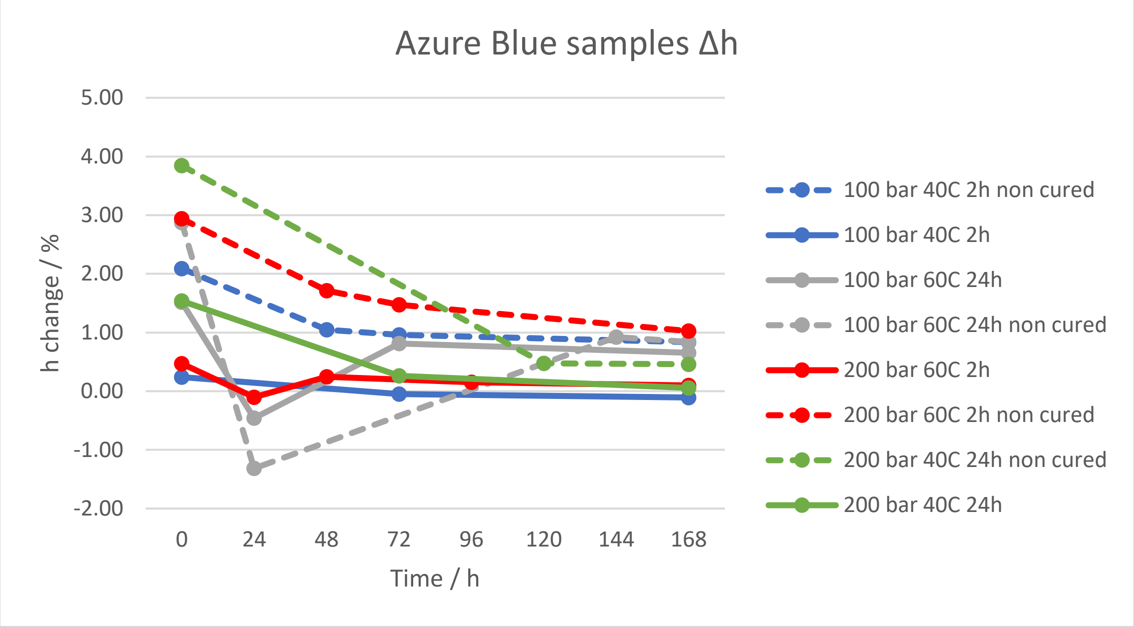

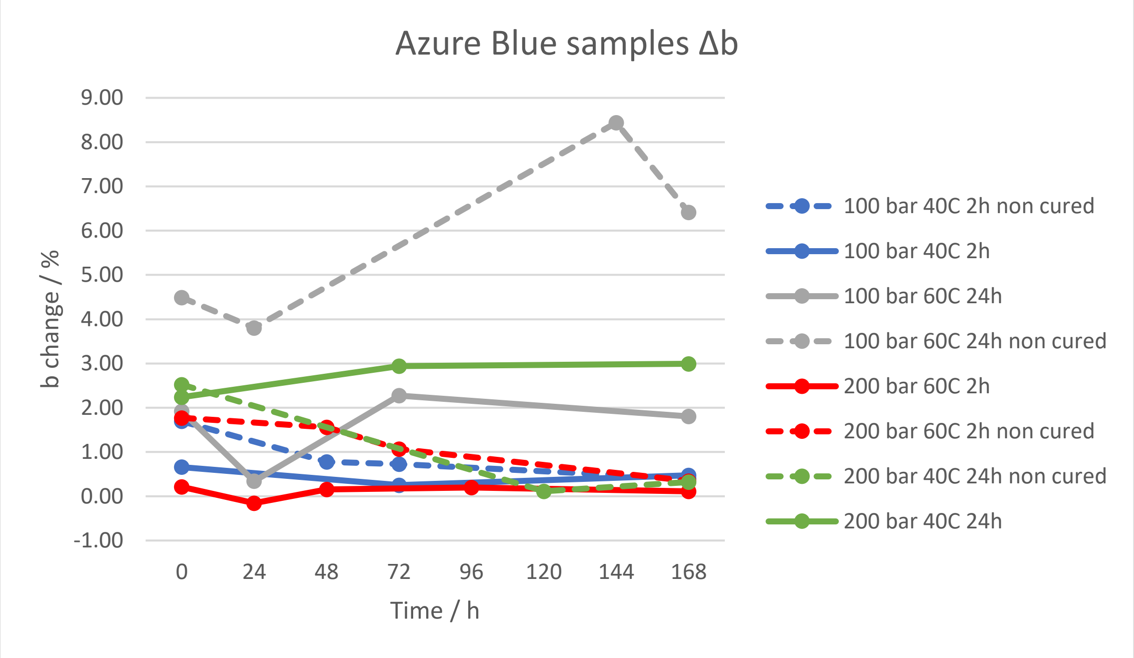

FTIR graphs of DDDA and Lithoz Lithalox HP500 green body before and after $scCO_2$ extraction for 1.5 h in 100 bars and 40°C, with PerkinElmer Spectrum 2 with wave number range 500-4000 cm-1 with 24 scans.

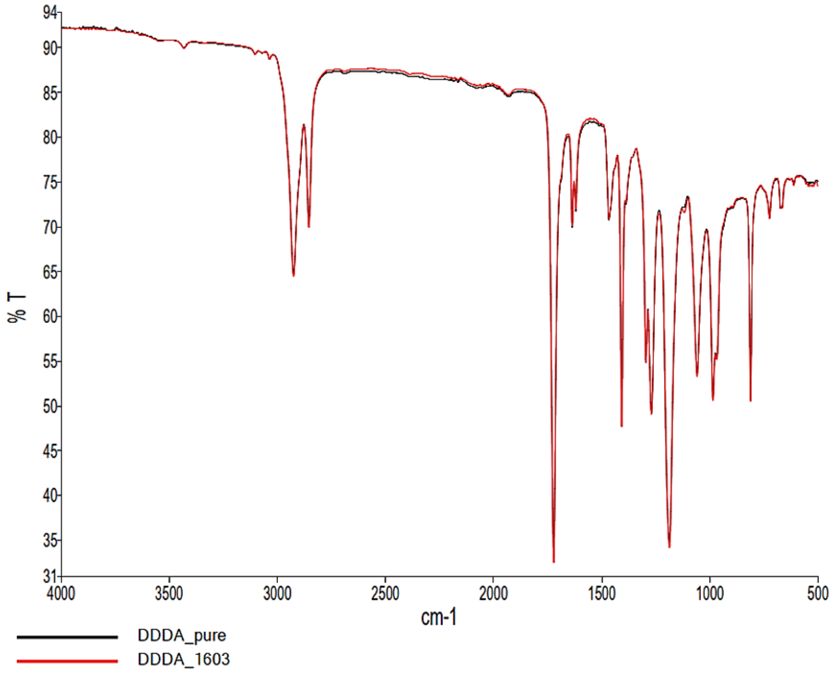

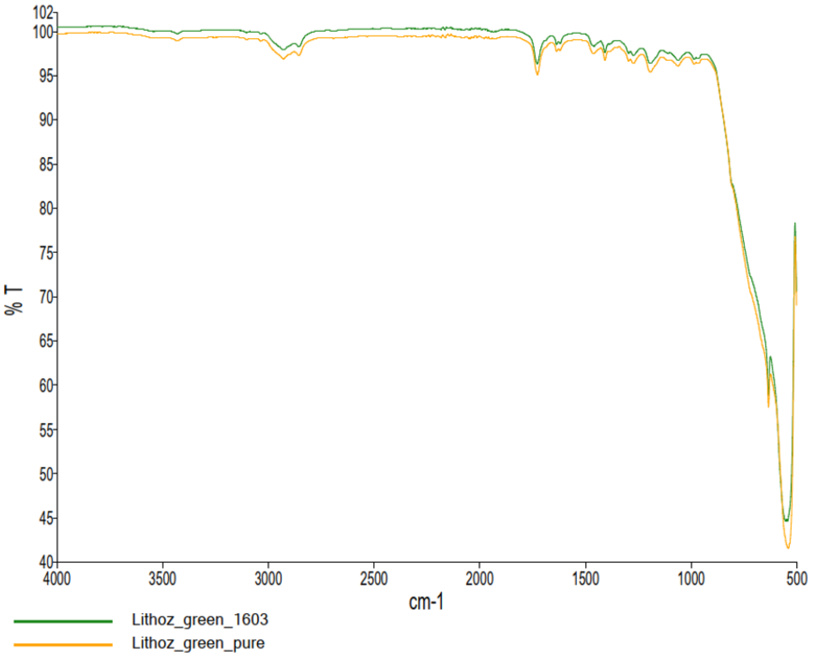

APPENDIX 2: OPTICAL MICROSCOPY IMAGES OF AS PRINTED AND SCCO$_2$ TREATED SAMPLES

Optical stereomicroscopy images with Leica MZ7.5.

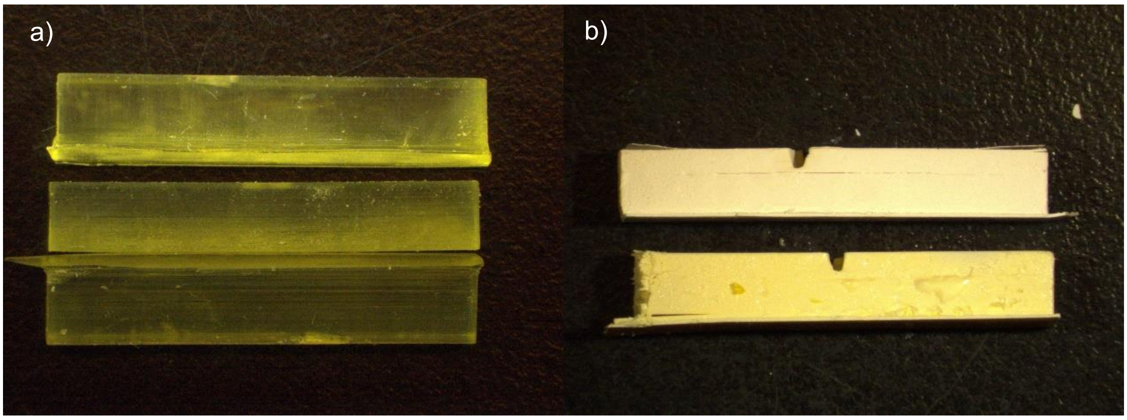

Figure 76: Optical microscopy images of a) recipes 6 (up), 8 (middle) and 7 (down) before scCO$_2$ exposure. b) recipe 9 before (down) and after 5 h scCO$_2$ exposure (up).

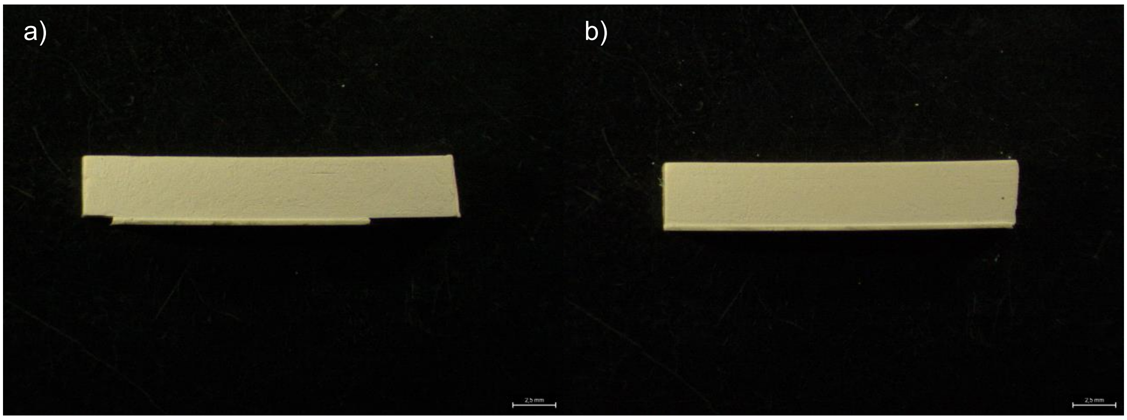

Figure 77: Optical microscopy images of recipe 10 after 2 h (a) and 5 h (b) scCO$_2$ exposure.

APPENDIX 3: FRACTURE SURFACES WITH STEREOMICROSCOPE

Optical stereomicroscopy images with Leica MZ7.5.

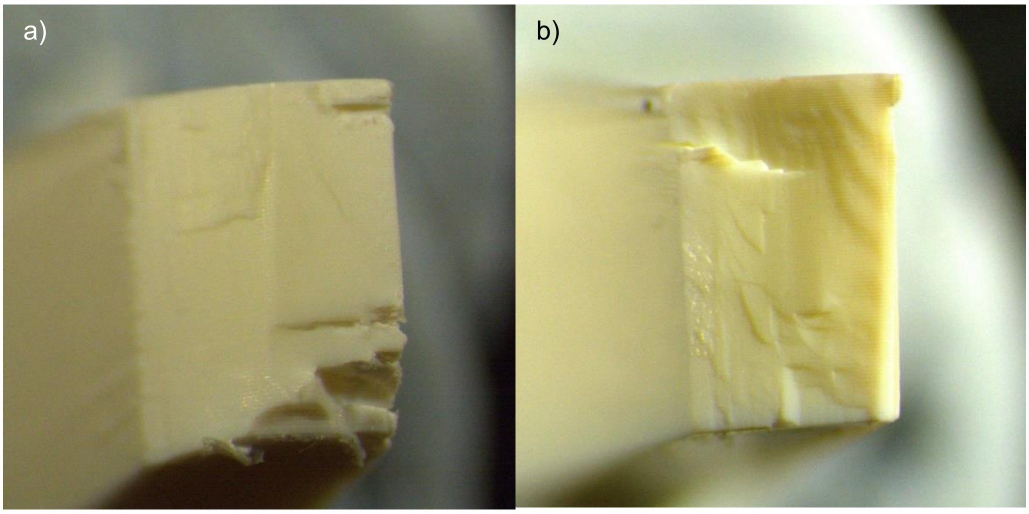

Figure 78: Optica microscopy images of fracture surfaces of recipe 5 (a) after 24h and recipe 8 (b) after 5 h scCO$_2$ *exposure. 64x magnification.*

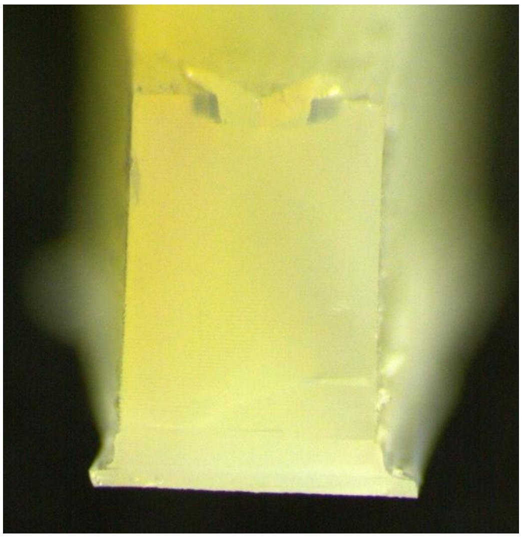

Figure 79: Optical microscopy image of recipe 8 fracture surface after 2 h scCO$_2$ *exposure with ethanol as co-solvent. 64x magnification.*

APPENDIX 4: ELECTRON MICROSCOPY IMAGES OF PRINTED POLYMER RESINS

Scanning electron microscopy images with Jeol JSM-IT500, 15 kV voltage.

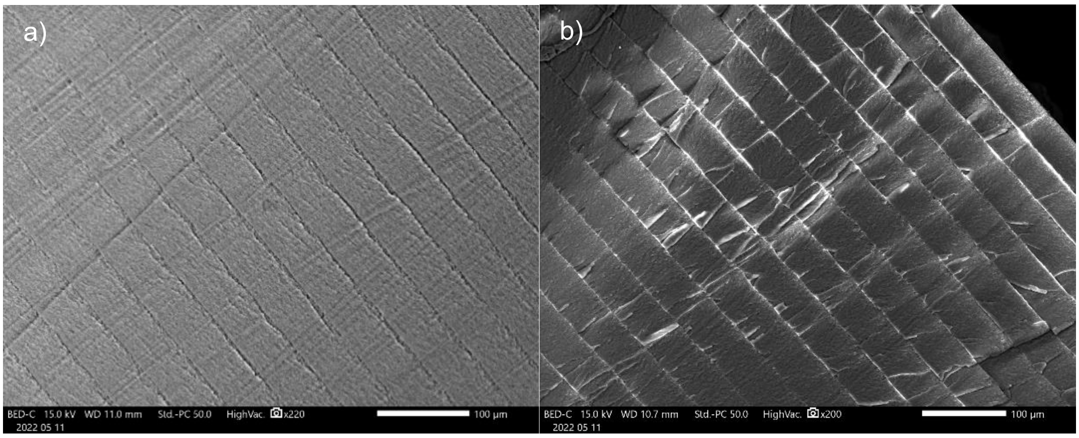

Figure 80: Back-scattering electron (BSE) images with 220x and 200x magnification of recipe 3 fracture surfaces.

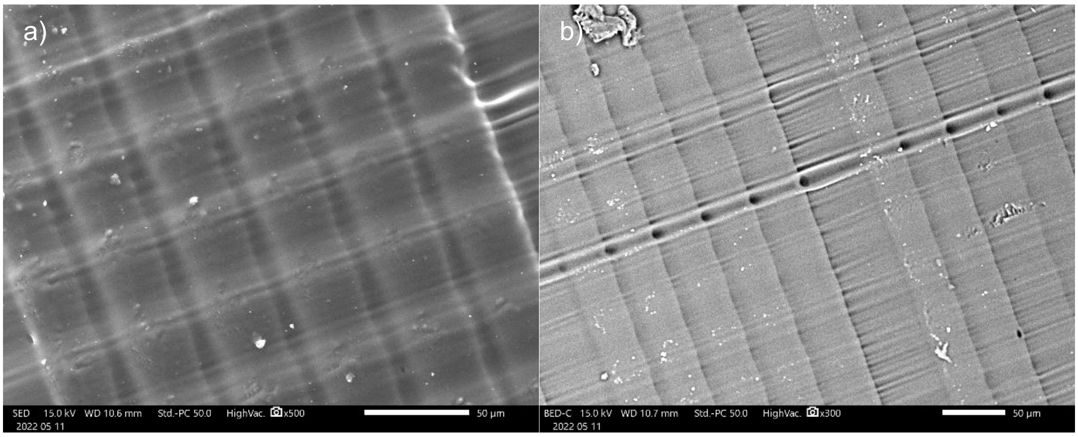

Figure 81: Secondary electron (SE) (a) image with 500x magnification and BSE (b) image with 300x magnification of recipe 8 sample surface.

APPENDIX 5: VISCOSITY, MASS CHANGES, DIMENSION CHANGES AND CURING DEPTH

Viscosity measurements of resins 5 and 8, slurries 9 and 10, and Lithoz Lithalox HP500 slurry at room temperature and at 40 °C measured with Anton Paar MCR 301 rotational rheometer, with a shear rate sweep from 0.1 to 1000 1/s, using a plate-plate geometry.

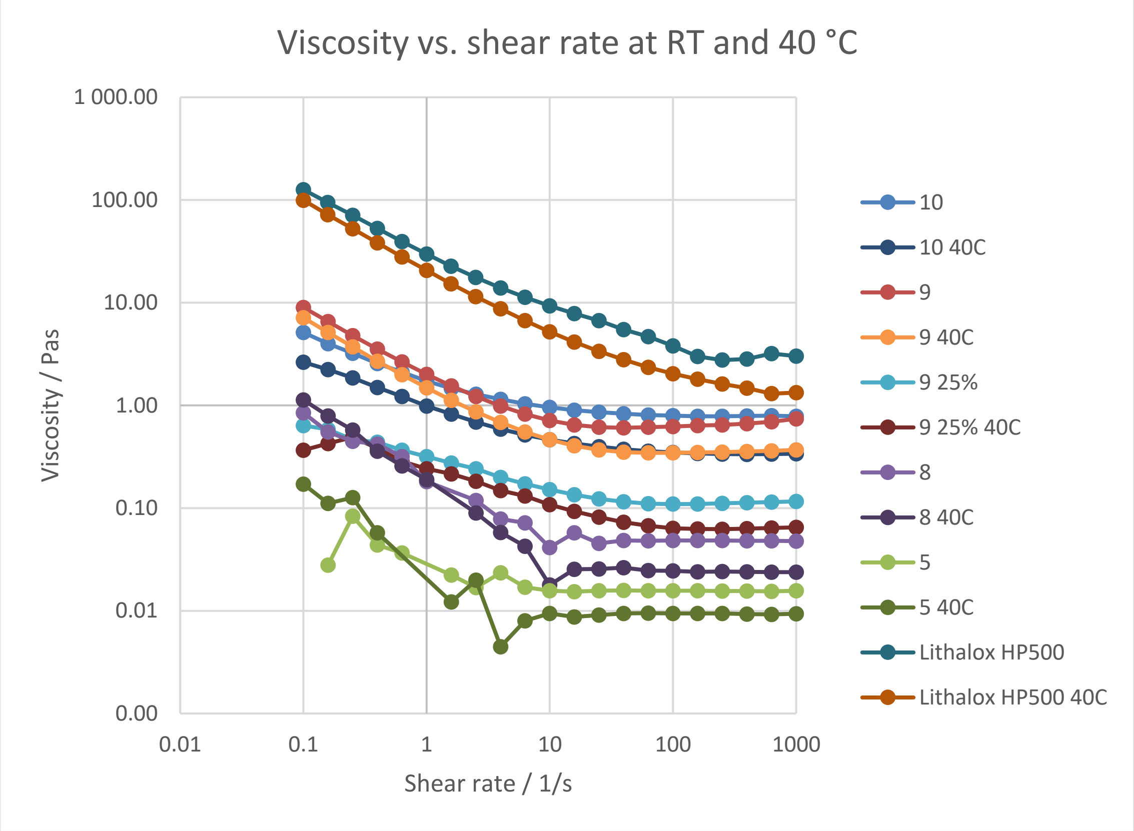

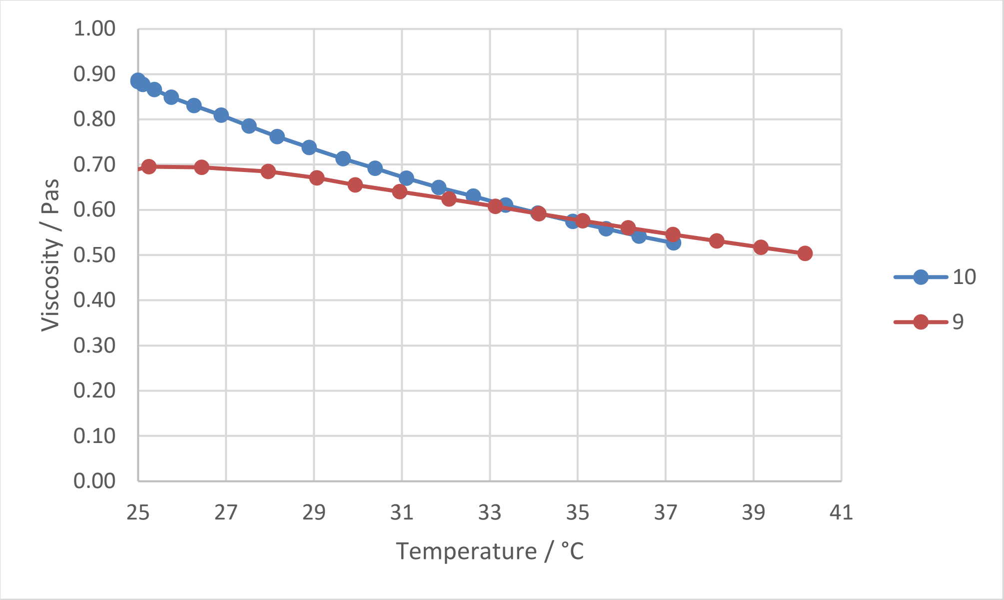

Table 15: Mass changes (% of monomer mass) due to $scCO_2$ exposure for varying times.

Recipe	2h	5h	24h
2			-11.10
3			-3.65
4	-18.36		
5	-15.75		-25.60
6			-20.88
7			-20.00
8	-30.00	-41.00	-51.00
9	-29.68	-32.98	-37.30
10	-38.37	-34.15	-49.25

Table 16: Dimension (h height, b thickness, L length) and density changes after 24h $scCO_2$ exposure.

Recipe	Δh %	Δb %	ΔL %	Δρ %
2	-1.34	3.29	-1.15	-11.94
3	0.91	-0.12	-0.78	-3.66
5	-3.00	-3.12	-2.64	-18.69
6	-1.79	-3.82	-3.86	-12.84
7	-3.39	-4.20	-3.71	-10.34
8	-12.34	-9.53	-10.52	-26.07
9	-1.17	-0.12	-1.78	-6.47
10	-4.66	-2.37	-3.74	-6.06

Curing depth measurement results for recipes 1-10.

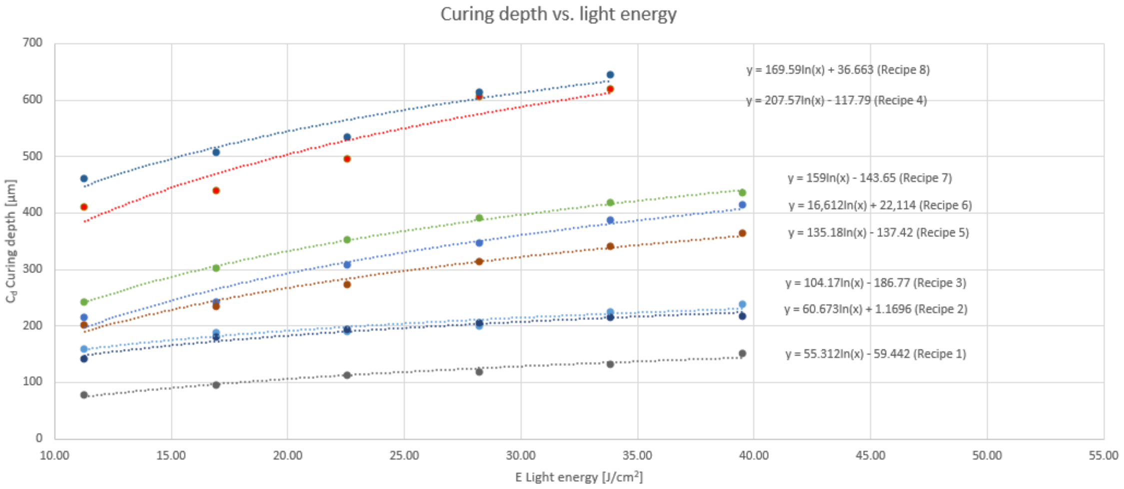

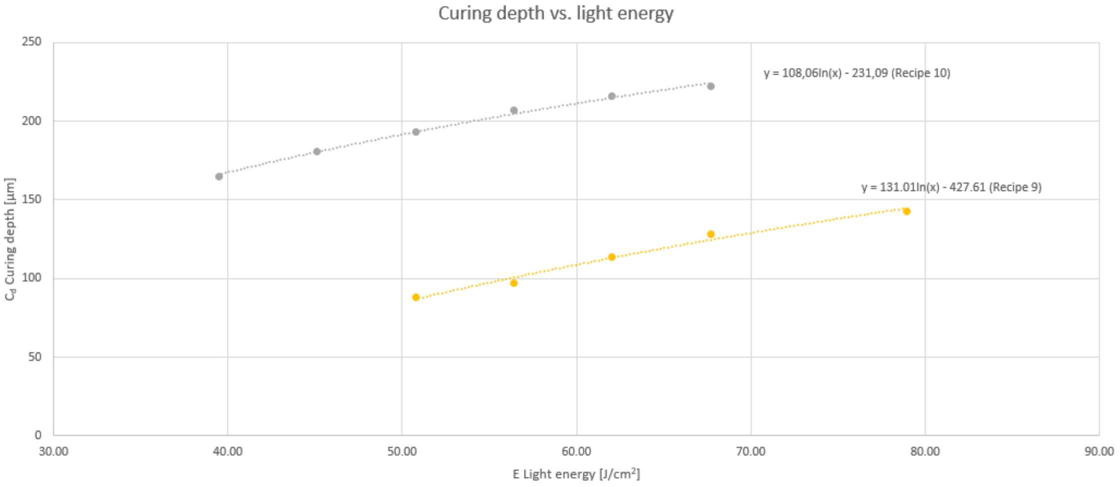

APPENDIX 6: TGA DATA

Thermogravimetric analysis with Netzsch TGA 209F3 Tarsus from room temperature to 600-800°C with 10 K/min heating rate in nitrogen gas atmosphere.

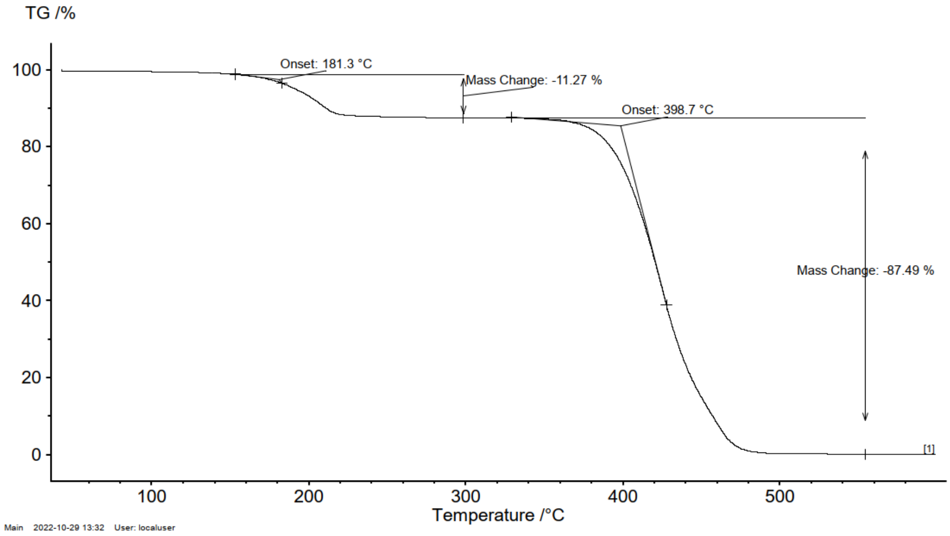

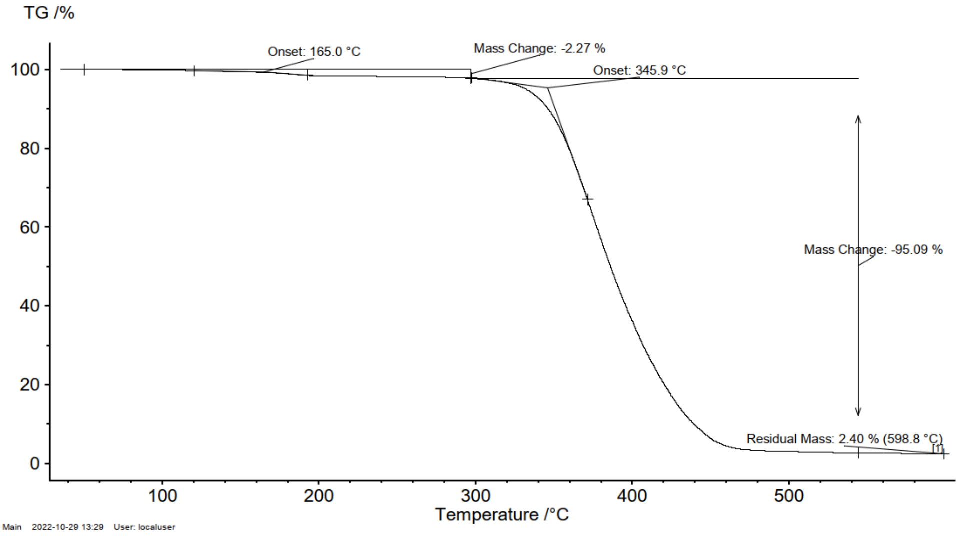

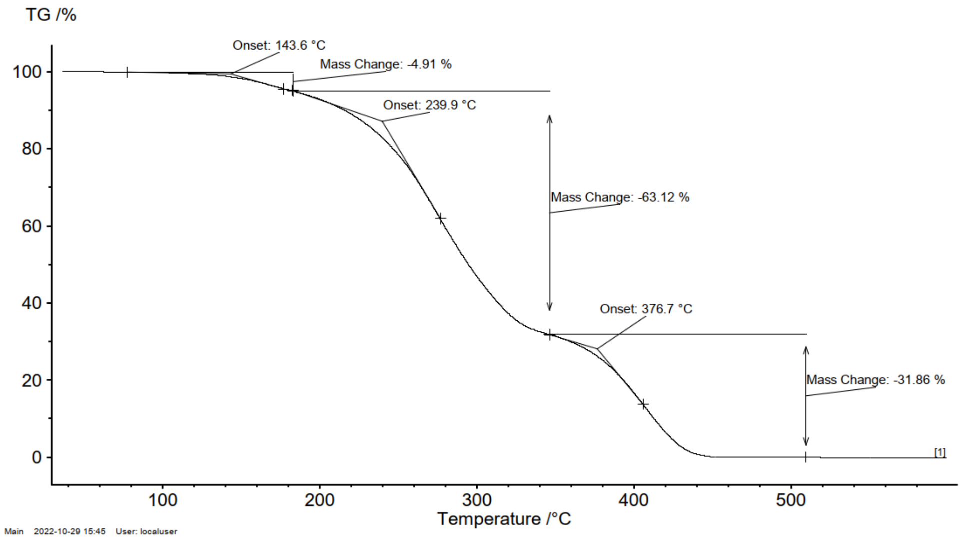
TG /%
100
80
60
40
20
0
Onset: 143.6 °C
Mass Change: -4.91 %
Onset: 239.9 °C
Mass Change: -63.12 %
Onset: 376.7 °C
Mass Change: -31.86 %
[1]
100
200
300
400
500
Temperature /°C
Main 2022-10-29 15:45 User: localuser

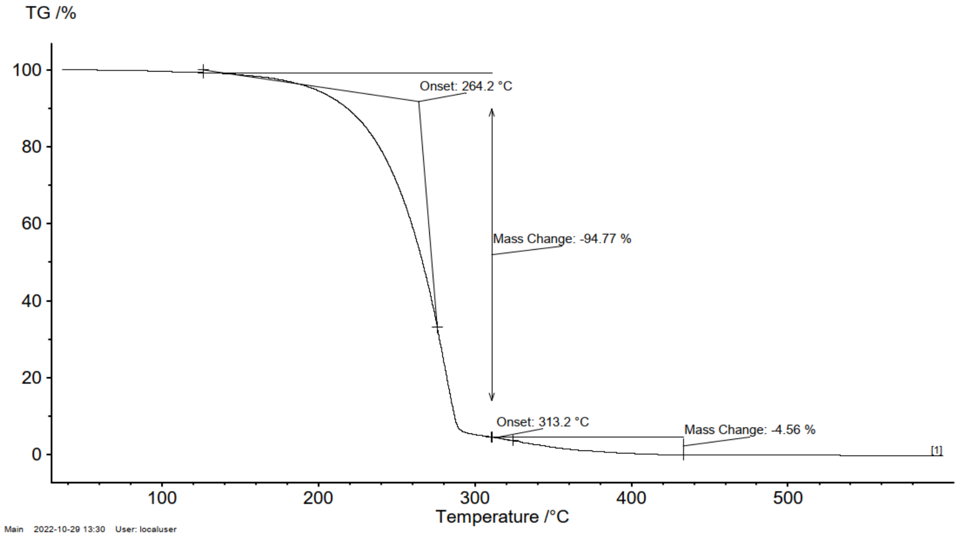
TG /%
100
80
60
40
20
0
Onset: 264.2 °C
Mass Change: -94.77 %
Onset: 313.2 °C
Mass Change: -4.56 %
[1]
100
200
300
400
500
Temperature /°C
Main 2022-10-29 13:30 User: localuser

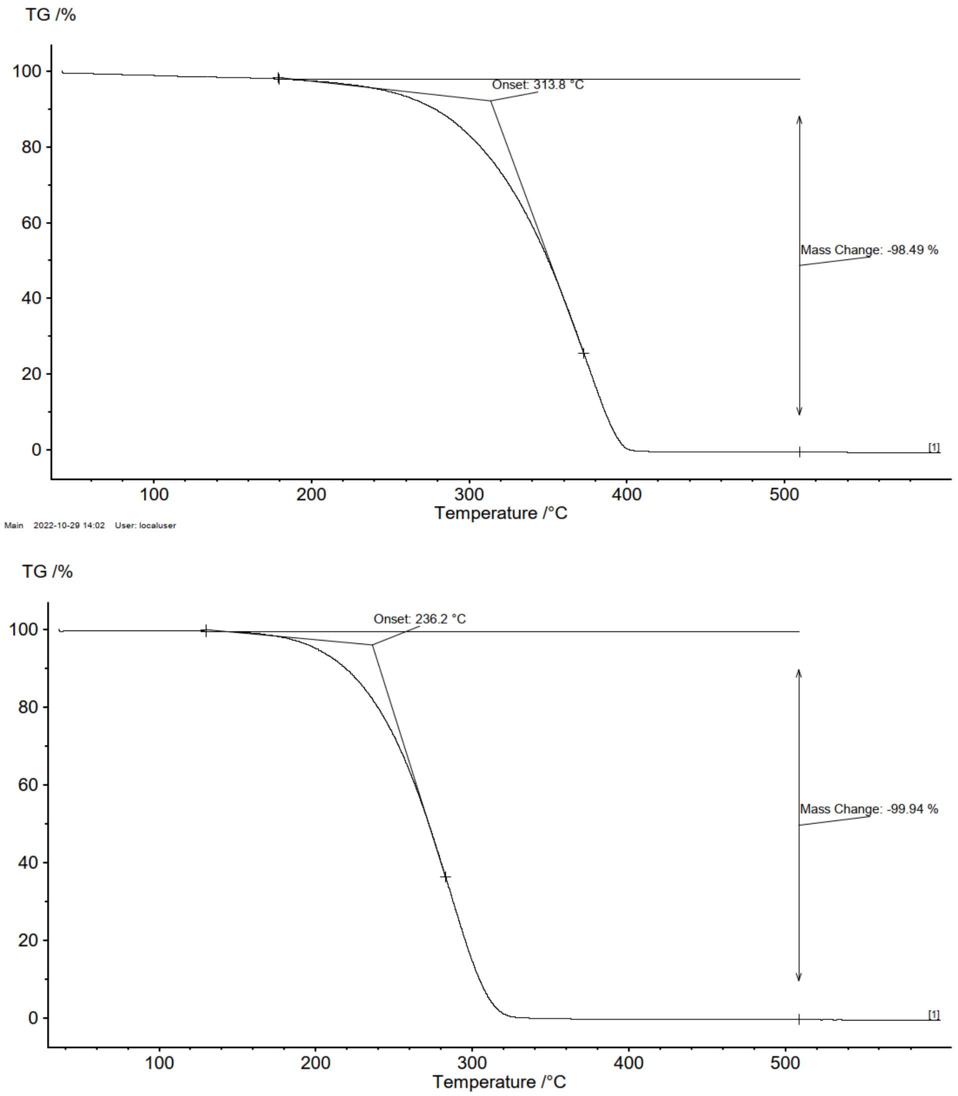

Figure 82: TGA curves from up to down: DDDA, PGTA, PEGMA200, ECC, PEG400, paraffin oil.

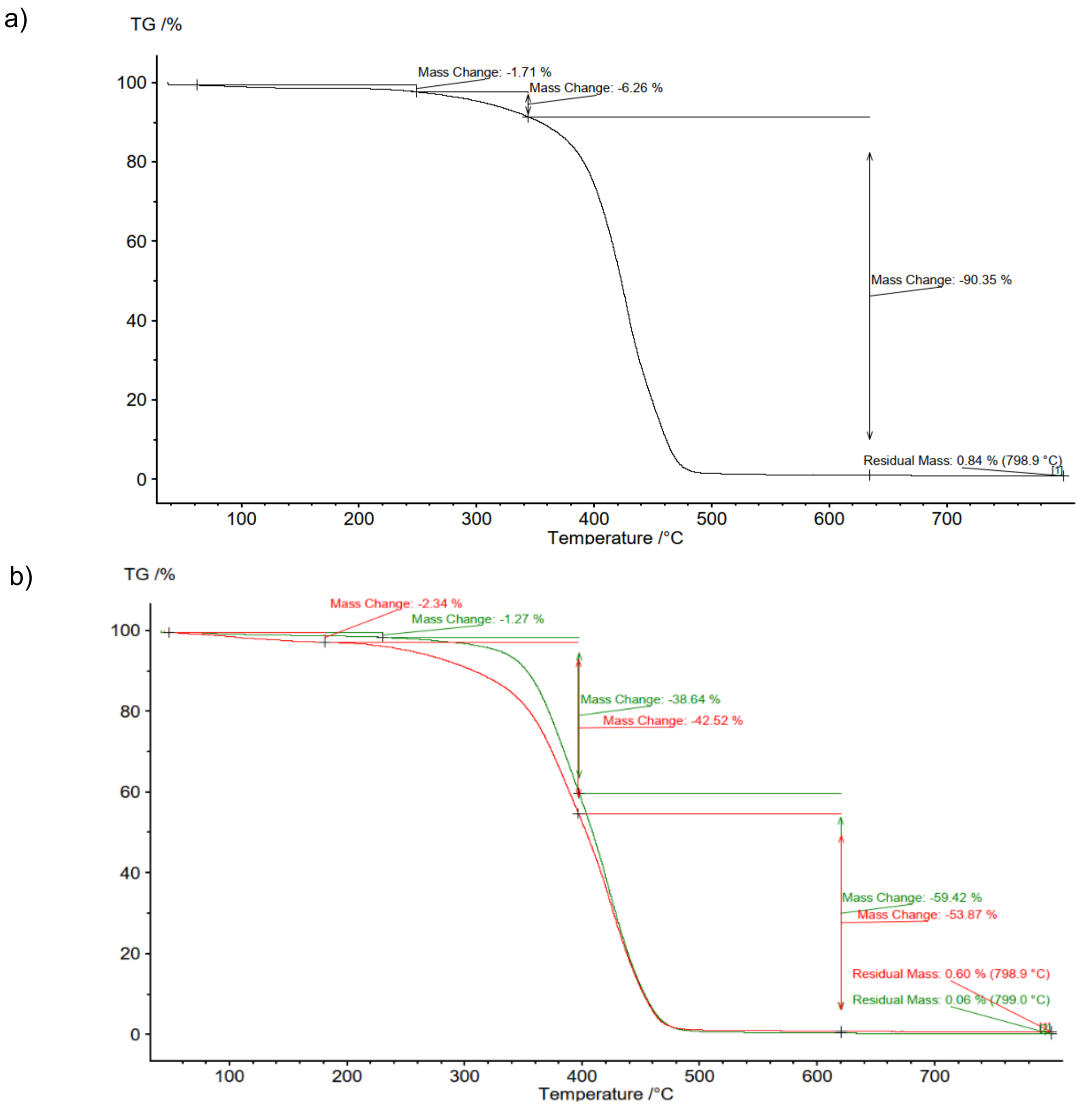

Figure 83: a) recipe 5 after 2h $scCO_2$ extraction. b) recipe 6 TGA curves of print (red) and 24h exposed $scCO_2$ (green) samples.

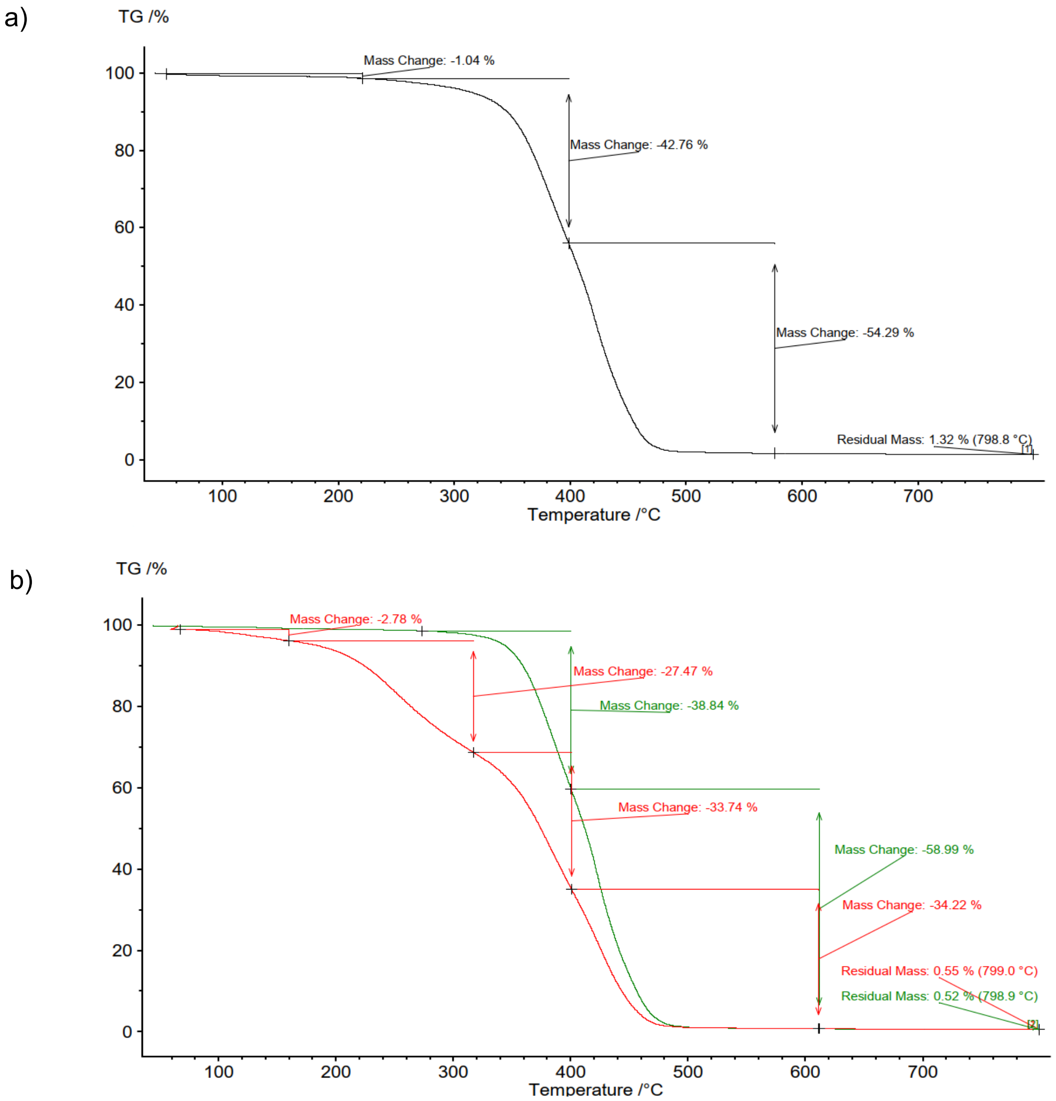

Figure 84: Recipe 8 TGA curves of 5h (black, a), b) print (red) and 24h exposed scCO$_2$ (green) samples.

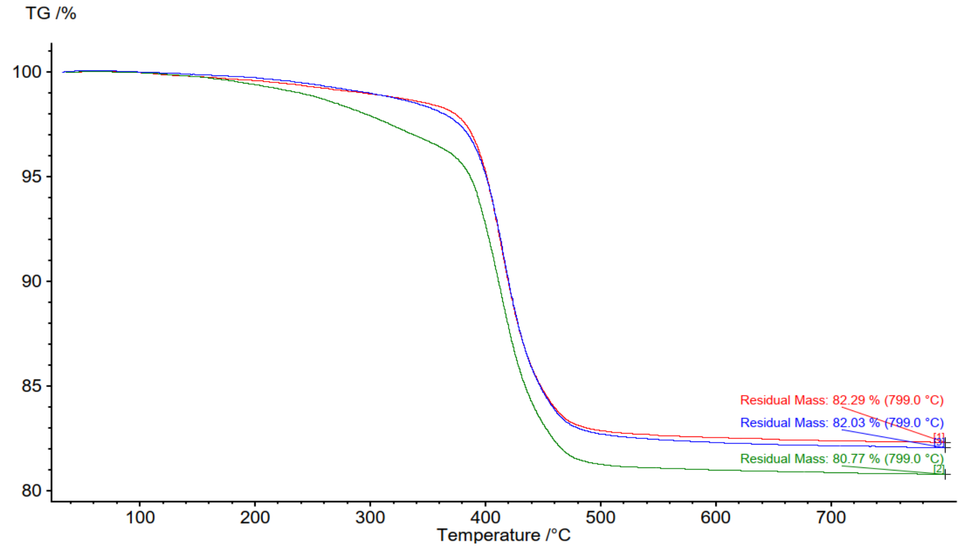

Figure 85: TGA data, recipe 9 2 (green), 5 (blue) and 24 h (red) $scCO_2$ extraction.

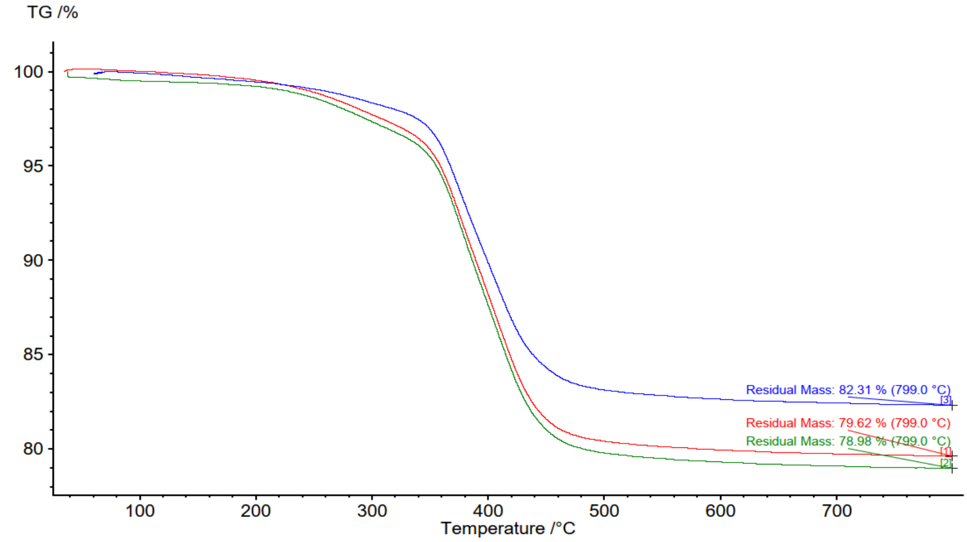

Figure 86: TGA data, recipe 10 2 (green), 5 (red) and 24 h (blue) $scCO_2$ extraction.

APPENDIX 7: DSC DATA

Differential scanning calorimetry results with Netzsch DSC 214 Polyma in nitrogen atmosphere, with 10 K /min heating rate.

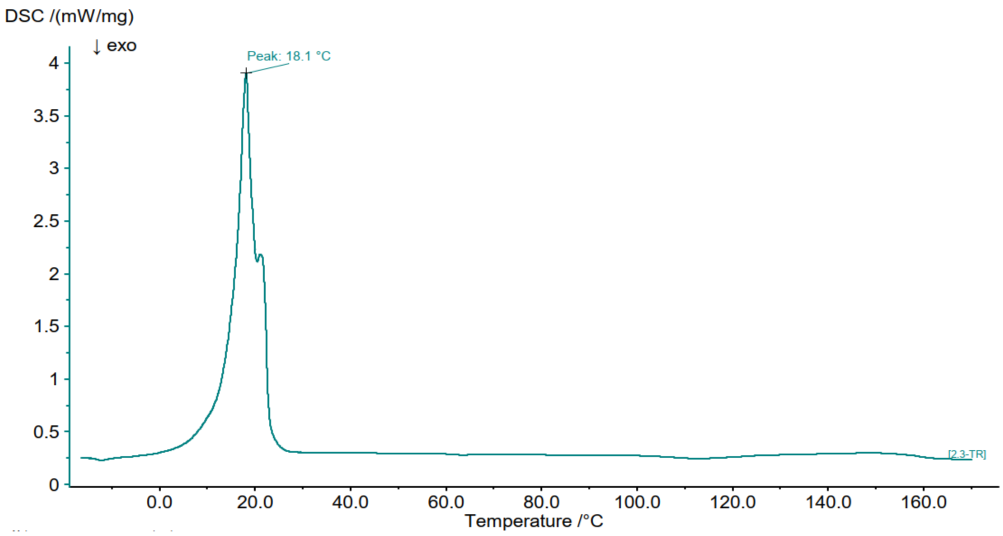

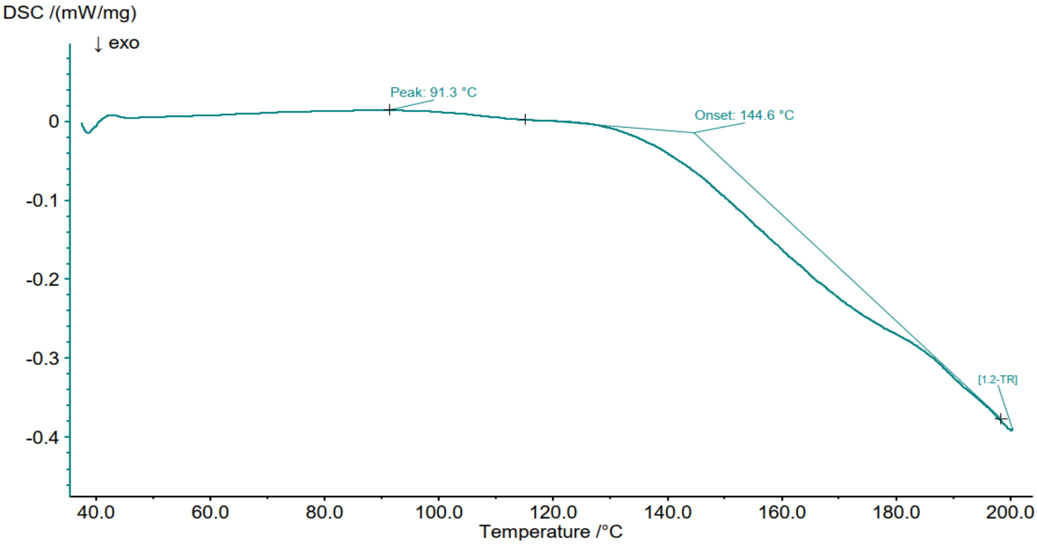

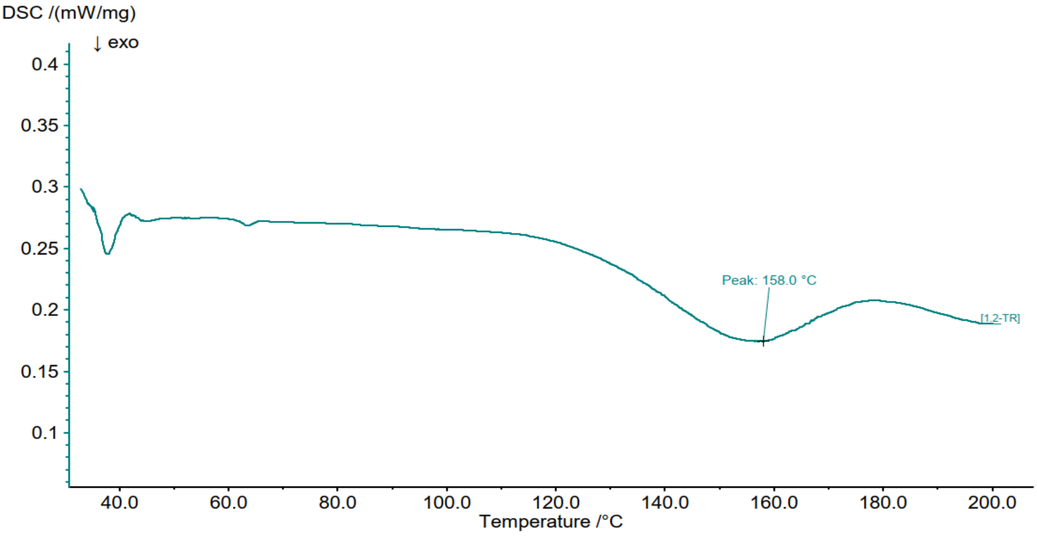
DSC /(mW/mg)
↓ exo
0.4
0.35
0.3
0.25
0.2
0.15
0.1
Peak: 158.0 °C
[1.2-TR]
40.0
60.0
80.0
100.0
120.0
140.0
160.0
180.0
200.0
Temperature /°C

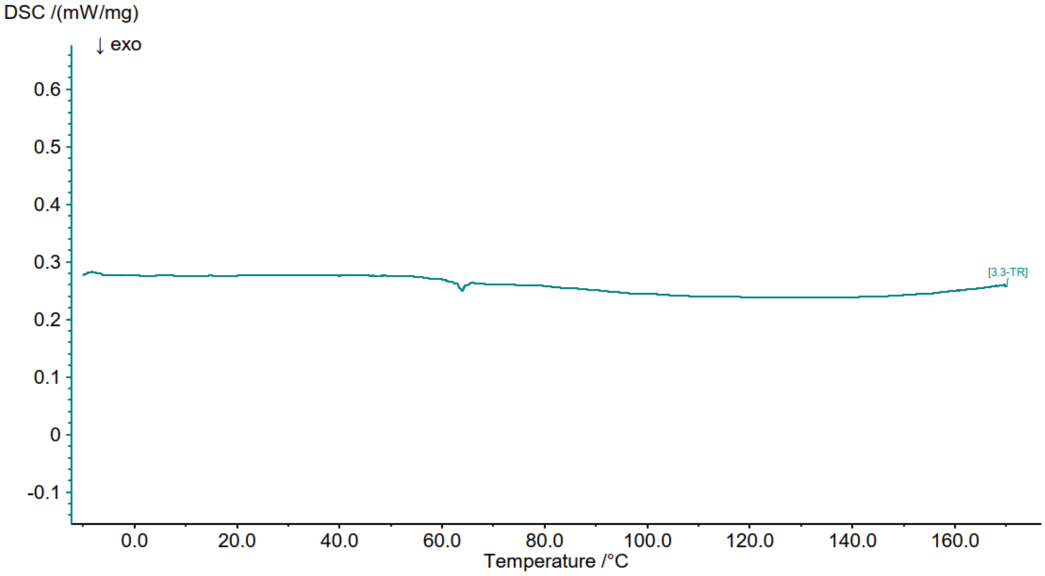
DSC /(mW/mg)
↓ exo
0.6
0.5
0.4
0.3
0.2
0.1
0
-0.1
[3.3-TR]
0.0
20.0
40.0
60.0
80.0
100.0
120.0
140.0
160.0
Temperature /°C

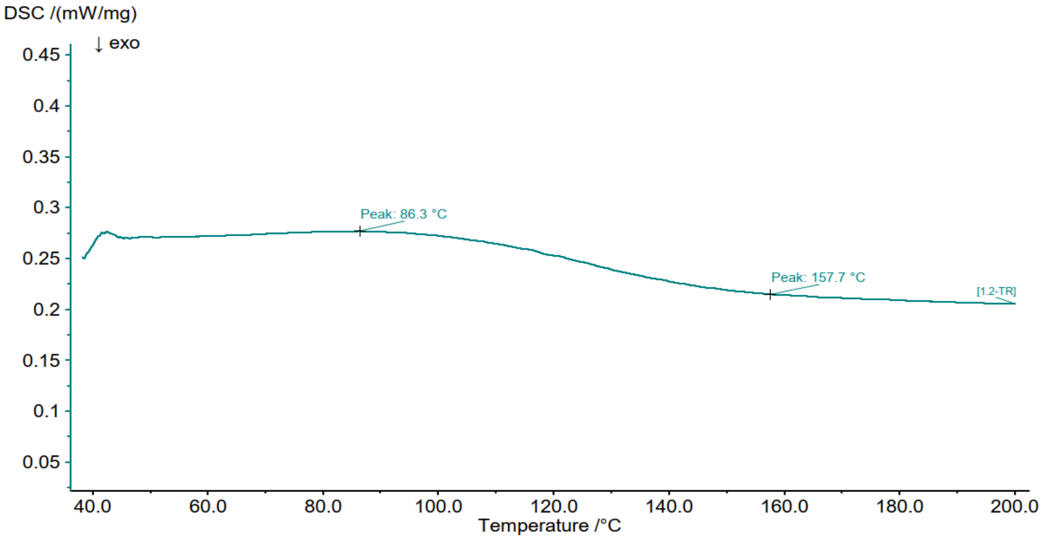

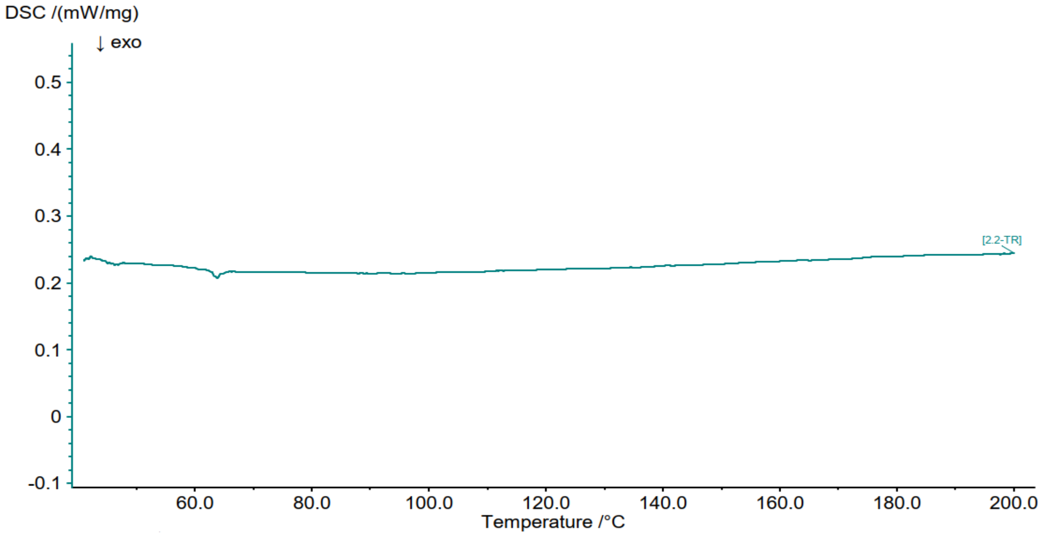

Figure 87: DSC curves up to down: DDDA, PGTA, PEGDMA200, ECC, PEG and paraffin oil.

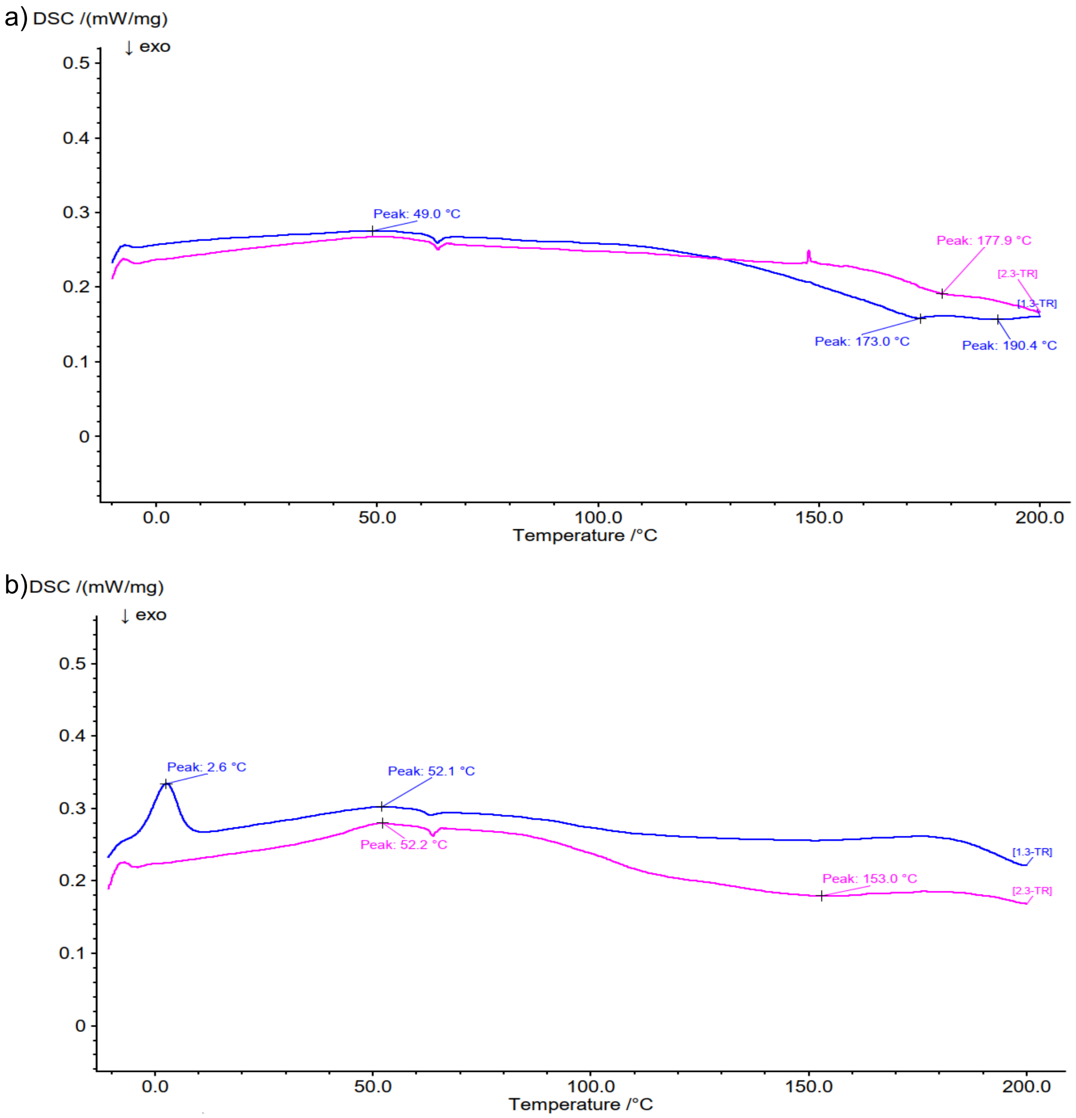

Figure 88: DSC data a) recipe 4 print (blue) vs. 2h (pink). b) recipe 6 print (blue) and 24 h (pink).

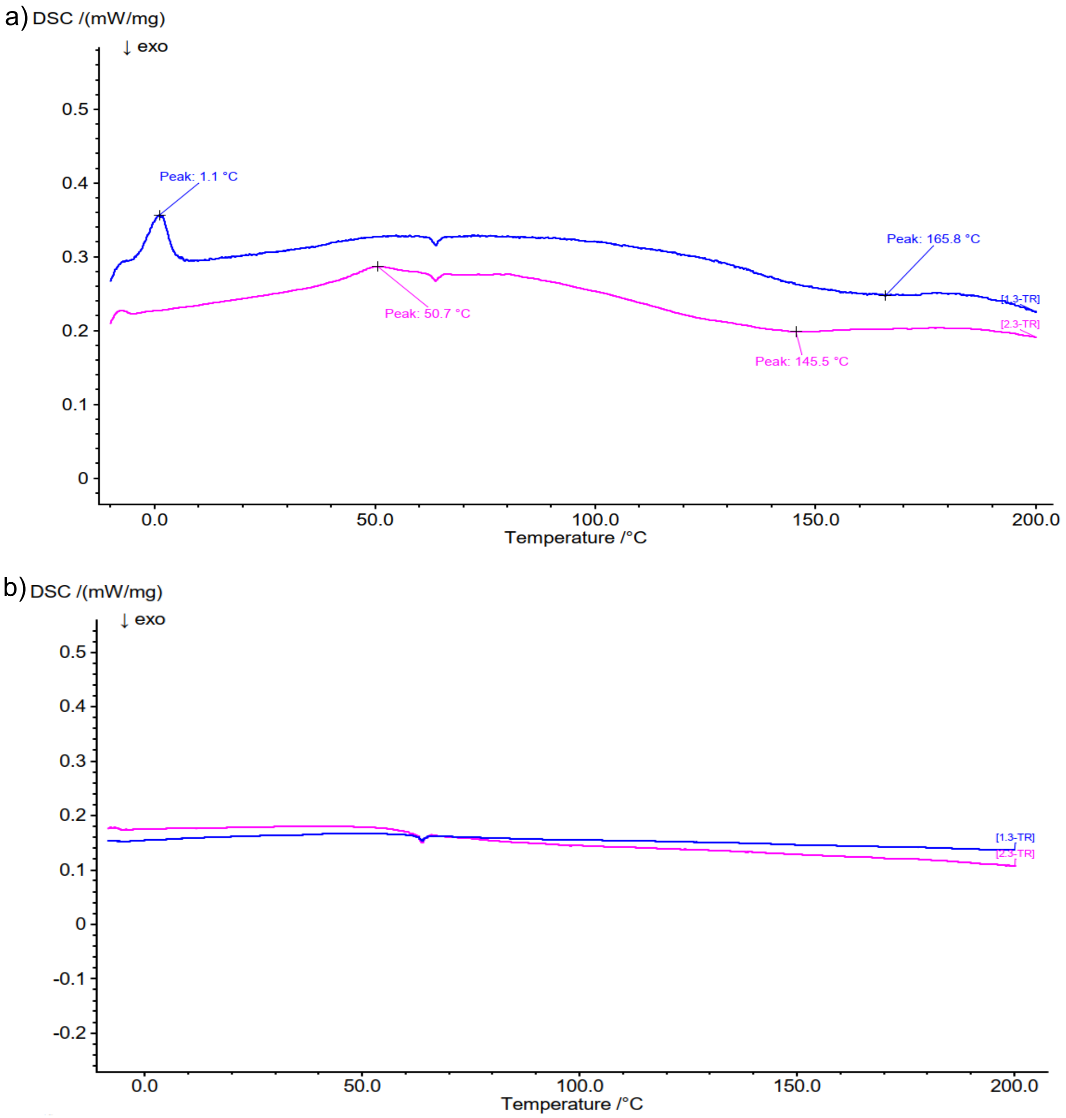

Figure 89: DSC data a) recipe 7 print (blue) and 24 h (pink). b) recipe 9 2h (pink) and 2h with ethanol (blue).

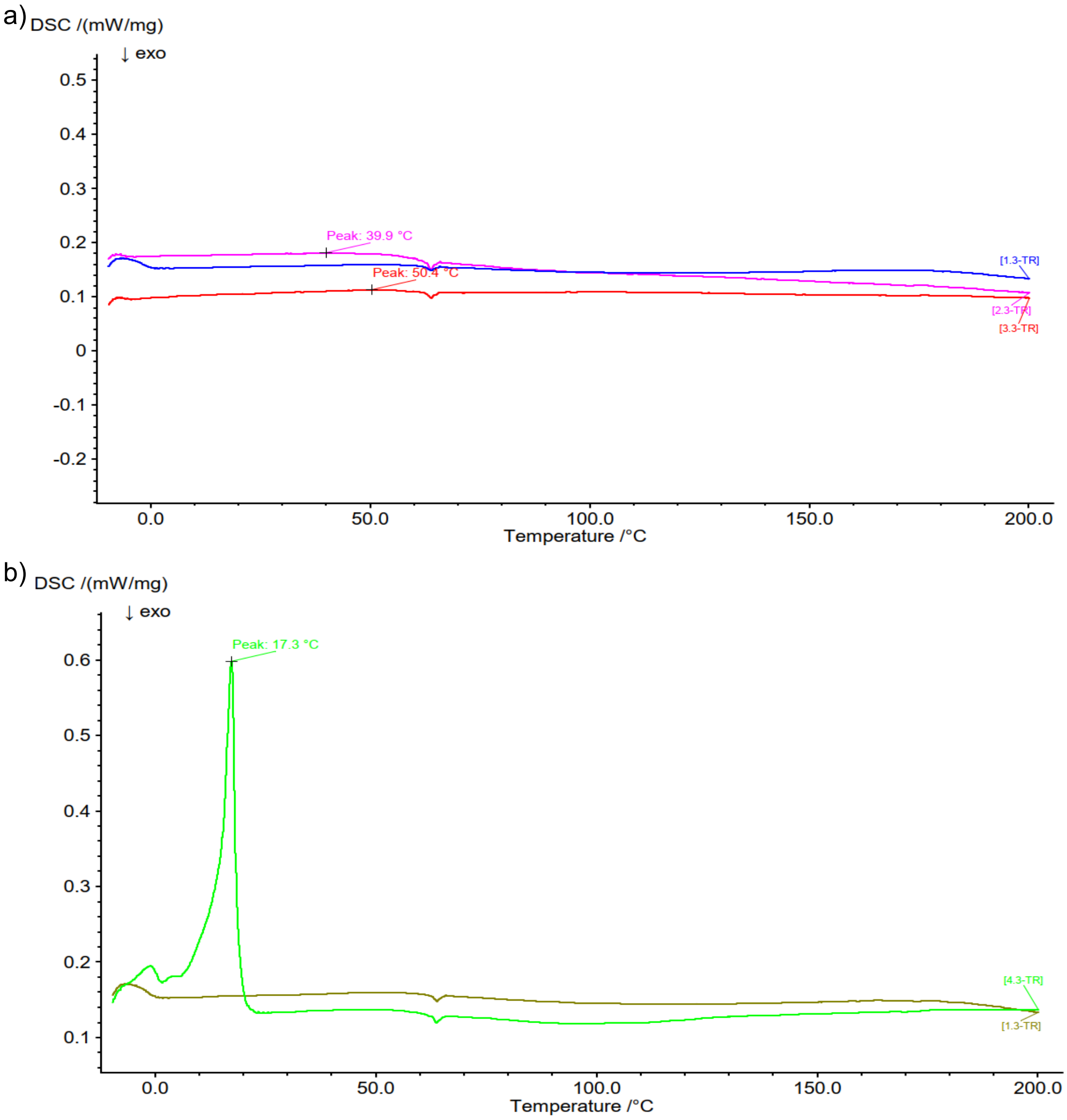

Figure 90: DSC data a) recipe 9 print (blue), 2 h (pink), 24 h (red). b) slurry (light green) and print (dark green).

APPENDIX 8: FTIR DATA

Fourier-transformation infrared measurement data measured with PerkinElmer Spectrum 2 with wave number range 500-4000 cm^{-1} with 24 scans.

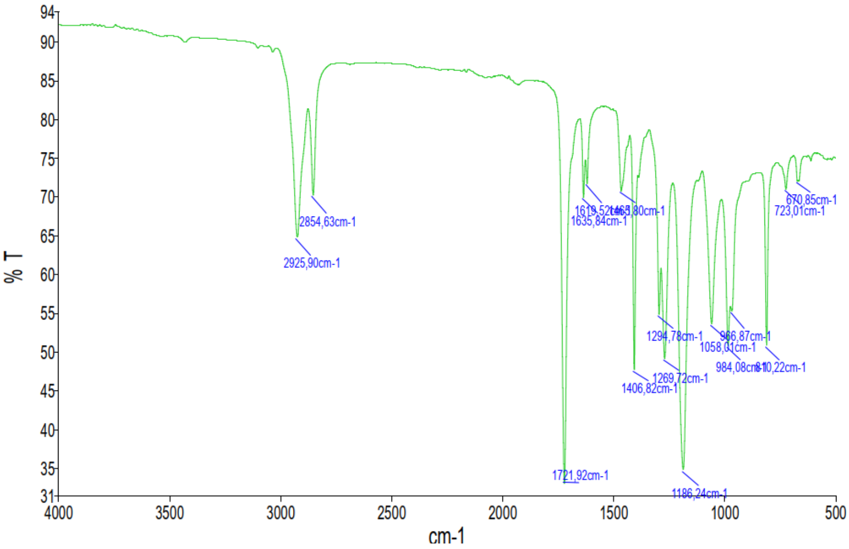

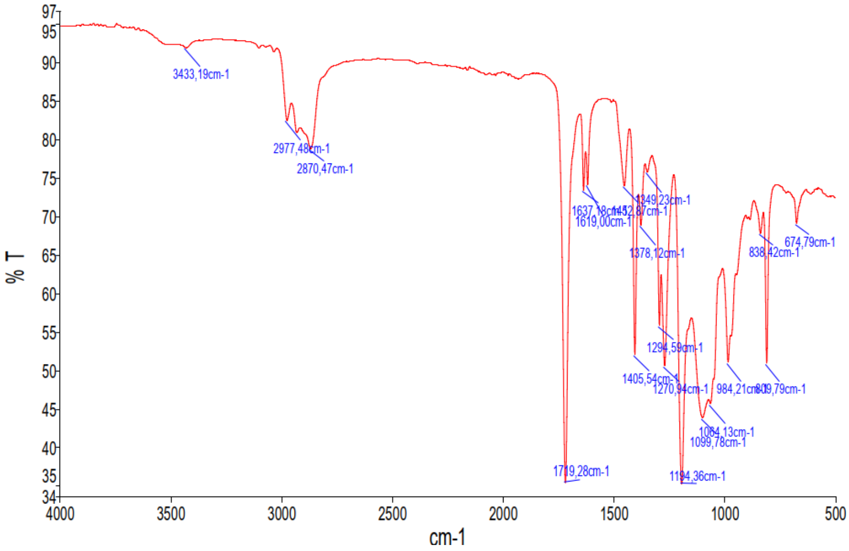

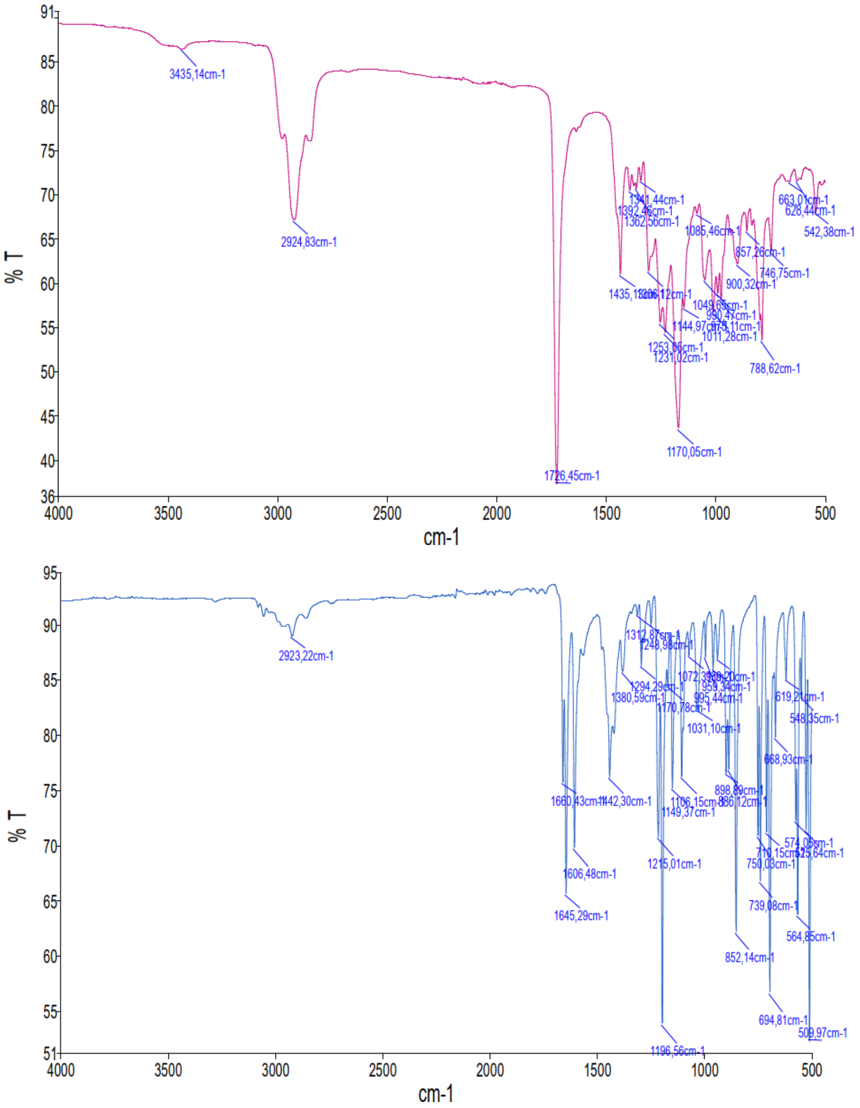

Figure 91: FTIR data from up to down: DDDA, PGTA, ECC and BAPO.